DoKDoK 2012

07th – 11th October 2012, Schloss Oppurg, Germany

PROCEEDINGS

Abbe School of Photonics, Jena, Germany

Imprint

DoKDoK 2012 – Proceedings

Editor-in-Chief and Conference Chair: Thomas Kaiser (Thomas.Kaiser.1@uni-jena.de)
Print: Friedrich-Schiller-Universität Jena – Reprotechnik
The DokDoK Logo was created by Martin Schaffer

Abbe School of Photonics
Friedrich-Schiller-Universität Jena
Physikalisch-Astronomische-Fakultät
Max-Wien-Platz 1
07743 Jena
Germany

Contents

Editorial Note

Our century is often said to be the century of the photon. Emerging optical technologies and concepts have tremendously changed the face of the world in many branches of everyday life as optical communication, amazing applications for the laser in fabrication and medicine, microoptical components for imaging or solid state lighting to name just a few. As doctoral students, we are not just silent witnesses of this development but we are right at the heart of the research that shapes tomorrow.

Those past achievements wouldn't have been possible without the seminal work of thousands of doctoral students around the world who carry out the vast majority of the research load under the guidance of their supervisors. A tremendous amount of specialized knowledge and experience is accumulated which should be regarded as a huge potential to be set free. Especially other doctoral students at the same level of knowledge and in a similar career and personal situation can benefit from the exchange of ideas in a scientific, professional and personal way.

DoKDoK was intended to serve exactly this goal when started in 2011. After this event, many new collaborations and scientific exchange developed among the doctoral students, jobs in industry were found and we were sure that this conference had to be established as a permanent event. This year's **DoK**DoK retains last year's established format but includes some additional features. First to mention is the conference site. The marvelous castle in Oppurg provides an inspiring surrounding for the conference. As last year, the housing is directly at the conference site. Talks are all presented in plenary sessions and last nearly half an hour to give every participant the chance to communicate as much of his research as possible. Posters are present all the time and allow for in-depth discussions.

In addition to last year, we are happy that we could include a broader range of topics, such as publishing and career opportunities, which are of particular importance to young scientists. With Prof. Martijn de Sterke we not only have won a world leading scientist as our first keynote speaker but also the Editor-in-Chief of Optics Express, a well-known journal in our field. As long-standing leader of the Central Department for Optics Design and Simulation at the company Carl Zeiss, Prof. Herbert Gross especially will address the perspectives of young scientist in industry.

Last but not least, I would also like to thank our numerous sponsors that have made **DoK**DoK 2012 possible. I wish all of us an exciting conference with many fruitful discussions that give a good perspective to a successful continuation in 2013.

Thomas Kaiser, General Conference Chair

Keynote Speakers

Prof. Martijn de Sterke

Martijn de Sterke received the M.Eng degree in Applied Physics from the University of Delft in the Netherlands, and his PhD in Optics from the University of Rochester in the USA. After postdoctoral work at the University of Toronto in Canada, he joined the School of Physics at the University of Sydney, where he is now a Professor in Physics working in the area of optics and photonics, particularly Nonlinear Optics, Fiber Optics and Photonic Crystals. He has been the Editor-in-Chief of the Journal Optics Express since 2007. Martijn de Sterke was the 1999 winner of the Pawsey Medal of the Australian of Sciences and has been a Fellow of the Optical Society of America since 2003.

Martijn willl also be available for a chat at the Welcome Reception on Sunday, where he will talk about his work as Editor-in-Chief of Optics Express. This is a good oppurtinity to gain insight into the world of scientific publishing. Maybe you will also get some useful hints for the next paper you try to publish!

Prof. Herbert Gross

Herbert Gross has studied and graduated at the University of Stuttgart, Germany, where he received the Dr.-Ing. degree with a work on the propagation of higher order modes through optical systems in 1996. Since 1998 he has had various teaching assignments at the University of Aalen, Germany, the École Polytechnique Fédérale de Lausanne (EPFL), Switzerland, and the Technical University Ilmenau, Germany. As a ”practical theoretical” physicist, he was leading the Central Department for Optics Design and Simulation of Carl Zeiss since the mid-1990s, until he joined the Friedrich-Schiller-University in Jena in 2012.

As a physicist in a leading key position in industry, Herbert Gross gained a lot of expriences which are especially useful for young scientists. In his talk he will provide insight into this exciting world.

Conference Schedule Overview

Time	Su - Oct 7	Mo - Oct 8	Tu - Oct 9	We - Oct 10	Th - Oct 11
		Keynote 1	**Ses 6 (Heraeus)**	**Keynote 2**	**Ses 10**
		Martijn de Sterke	**Optical Materials & - Processing**	**Herbert Gross**	**Bragg Gratings**
9:00 AM		*"Why evanescent modes*	*NN (Heraeus)*	*"Physicists in Industry"*	Richter
9:25 AM		*matter"*	Just		Elsmann
9:50 AM			Rothhardt		Mörbitz
10:15 AM			Döring		Voigtländer
	Arrival & Registration	**Ses 3**		**Ses 7**	**Ses 11**
		Plasmonics		**Nanostructured Materials**	**Microscopy**
11:00 AM		Filter	**Social Day**	Zimmermann	Jost
11:25 AM		Klein		Vetter	Kielhorn
11:50 AM		Walther	*TBA*	Wiesendanger	Ott
12:15 PM				Falkner	
1:00 PM	**Lunch**	**Lunch**		**Lunch**	
	Ses 1	**Ses 4 - Coupled waveguides**		**Ses 8 (Leoni)**	
	Optical Metrology I	**and resonators**		**Fibers + Fiber Lasers**	
2:00 PM		Spittel		*NN (Leoni)*	
2:25 PM	Schulze	Stützer		Jansen	
2:50 PM	Schaffer	Schmidt		Otto	
3:15 PM	Fuchs	Kaiser		Flamm	
	Ses 2	**Ses 5**		**Ses 9**	
	Ultrashort Dynamics	**Optical Metrology II**		**Lithium Niobate Waveguides**	
4:00 PM	Bierbach	Seise		Krösen	
4:25 PM	Eilenberger	Chemnitz		Bin Hasan	
4:50 PM	Möller	Wuchrer		Sergeyev	
6:00 PM	**Welcome Reception**	**Poster Session (Asphericon)**		**Conference Dinner**	
	Editor Chat with M. de Sterke	*NN (Asphericon)*			
		NN (Gründerzentrum FSU)			

Schedule can be subject to change

Conference Schedule

Sunday, 07th October 2012

01 – Optical Metrology I

Chair: Matthias Falkner

14:25 CHRISTIAN SCHULZE
Institute of Applied Optics, Friedrich-Schiller-Universität, Jena, Germany
"Measuring wavefronts using modal decomposition"

14:50 MARTIN SCHAFFER
Institute of Applied Optics, Friedrich-Schiller-Universität, Jena, Germany
"Recent advances in laser speckle based structured illumination stereophotogrammetry"

15:15 SILVIO FUCHS
Institute of Optics and Quantum Electronics, Friedrich-Schiller-Universität, Jena, Germany
"Optical Coherence Tomography using broad-bandwidth XUV and soft x-ray radiation"

02 – Ultrashort Dynamics

Chair: Christian Vetter

16:00 JANA BIERBACH
Institute of Optics and Quantum Electronics, Friedrich-Schiller-Universität, Jena, Germany
"Intense Attosecond Pulses from Relativistic Surface Plasmas"

16:25 FALK EILENBERGER
Institute of Applied Physics, Friedrich-Schiller-Universität, Jena, Germany
"Imaging Cross Correlator FROG: Space-Time Retrieval of Ultrashort Complex Electric Fields"

16:50 MAX MÖLLER
Institute of Optics and Quantum Electronics, Friedrich-Schiller-Universität, Jena, Germany
"Single-shot carrier-envelope phase measurement based on stereographic above-threshold ionization in the multi-cycle regime"

18:00 **Welcome Reception**

Possibility to chat with Prof. Martijn de Sterke, the Editor-in-Chief of Optics Express

Monday, 08th October 2012

Keynote I

9:30 PROF. MARTIJN DE STERKE
University of Sydney, Australia
"Why evanescent modes matter"

10:45 Short Break

03 – Plasmonics
Chair: Thomas Kaiser

11:00 ROBERT FILTER
Institute of Condensed Matter Theory and Solid State Optics, Friedrich-Schiller-Universität, Jena, Germany
"Controlling Light-Matter-Interactions using Nanoantennas"

11:25 ANGELA KLEIN
Institute of Applied Physics, Friedrich-Schiller-Universität, Jena, Germany
"Controlling plasmonic hot-spots by interfering Airy beams"

11:50 BENNY WALTHER
Institute of Applied Physics, Friedrich-Schiller-Universität, Jena, Germany
"Multi-wavelength holograms made of plasmonic metamaterials "

12:30 Lunch Break

04 – Coupled waveguides and resonators
Chair: Robert Filter

14:00 RON SPITTEL
Institute of Photonic Technology, Friedrich-Schiller-Universität, Jena, Germany
"Equivalent step-index model of multifilament core fibers"

14:25 SIMON STÜTZER
Institute of Applied Physics, Friedrich-Schiller-Universität, Jena, Germany
"Superballistic transport and anomalous diffusion in inhomogeneous lattices"

14:50 CARSTEN SCHMIDT
Institute of Applied Physics, Friedrich-Schiller-Universität, Jena, Germany
"Characteristics of optical modes in coupled disk microresonators"

15:15 THOMAS KAISER

Institute of Applied Physics, Friedrich-Schiller-Universität, Jena, Germany

"Light propagation in plasmonic nanoparticle loaded waveguides"

15:40 Short Break

05 – Optical Metrology II

Chair: Martin Schaffer

16:00 BARBARA SEISE

Institute of Photonic Technology, Friedrich-Schiller-Universität, Jena, Germany

"Fluorescence based DNA detection of pathogens with magnetic beads"

16:25 MARIO CHEMNITZ

Institute of Applied Physics, Friedrich-Schiller-Universität, Jena, Germany

"Parametric fiber optical amplifier for spectrally high-resolved coherent anti-Stokes Raman spectro-microscopy"

16:50 ROLAND WUCHRER

Fraunhofer Institute for Nondestructive Testing, Dresden, Germany

"Filter-based spectrometer for optical wavelength shift sensors"

18:00 **Asphericon Poster Session**

Asphericon Company Presentation
Presentation Gründerzentrum FSU Jena

Tuesday 09th October 2012

06 - Heraeus Session on Optical Materials & - Processing

Chair: Daniel Richter

9:00 DR. HOFMANN
Heraeus
"Heraeus Company Presentation"

9:25 FLORIAN JUST
Institute of Photonic Technology, Friedrich-Schiller-Universität, Jena, Germany
"Powder sintering process for the manufacturing of novel, highly efficient laser fibers"

9:50 CAROLIN ROTHHARDT
Fraunhofer Institute for Applied Optics and Precision Engineering, Jena, Germany
"Fabrication of a Faraday Isolator by plasma-activated bonding"

10:15 SVEN DÖRING
Institute of Applied Physics, Friedrich-Schiller-Universität, Jena, Germany
"Analysis of the hole formation in ultrashort pulse laser deep drilling"

11:30 Lunch

Social Day

We will visit some sights in the nearby town of Pößneck.

13:00 (optional) visit of the local chocolate factory (with selling on-site)

14:00 Start of the official Social Day Program.
Further information will be provided.

In the evening we close this day in the traditional local restaurant "Ratskeller".

Wednesday, 10th October 2012

Keynote II

9:30 PROF. HERBERT GROSS
Friedrich-Schiller-Universität, Jena, Germany
"Physicists in industry"

10:45 Short Break

07 – Nanostructured Materials
Chair: Falk Eilenberger

11:00 FELIX ZIMMERMANN
Institute of Applied Physics, Friedrich-Schiller-Universität, Jena, Germany
"Ultrashort pulse induced nanogratings and their fundamental structure"

11:25 CHRISTIAN VETTER
Institute of Applied Physics, Friedrich-Schiller-Universität, Jena, Germany
"Femtosecond-Laser Induced Nanogratings - A versatile Platform for Birefringent Polarization Control"

11:50 SAMUEL WIESENDANGER
Institute of Condensed Matter Theory and Solid State Optics, Friedrich-Schiller-Universität, Jena, Germany
"Front and rear side photonic structures in silicon solar cells"

12:15 MATTHIAS FALKNER
Institute of Applied Physics, Friedrich-Schiller-Universität, Jena, Germany
"How to characterize comprehensively highly dispersive metamaterials with optical activity"

12:40 Lunch

08 – Leoni Session on Optical Fibers and Fiber Lasers
Chair: Thomas Kaiser

14:00 NN
Leoni
"Leoni Company Presentation"

14:25 FLORIAN JANSEN
Institute of Applied Physics, Friedrich-Schiller-Universität, Jena, Germany
"Ytterbium-doped large-pitch fibers"

14:50 HANS-JÜRGEN OTTO

Institute of Applied Physics, Friedrich-Schiller-Universität, Jena, Germany

"Mode instabilities in high-power fiber-laser systems"

15:15 DANIEL FLAMM

Institute of Applied Optics, Friedrich-Schiller-Universität, Jena, Germany

"Selective excitation of higher-order modes in optical fibers using a spatial light modulator"

15:40 Short Break

08 – Lithium Niobate Waveguides

Chair: Reinhard Geiss

16:00 SEBASTIAN KRÖSEN

Institute for Applied Physics, Westfälische Wilhelms- Universität, Münster, Germany

"Integration of Functional Optical Devices in Lithium Niobate Wafers by Direct Femtosecond Laser Writing"

16:25 SHAKEEB BIN HASAN

Institute of Condensed Matter Theory and Solid State Optics, Friedrich-Schiller-Universität, Jena, Germany

"Quadratic Frequency Conversion In Plasmonic Slot Waveguides"

16:50 ANTON SERGEYEV

Institute of Applied Physics, Friedrich-Schiller-Universität, Jena, Germany

"Optimisation and application of the second-harmonic waveguiding in lithium niobate nanowires"

18:00 **Conference Dinner** and **Official Welcome of the new ASP doctoral students**

Thursday 11th October 2012

10 – Bragg Gratings

Chair: Ria Krämer

9:00 DANIEL RICHTER
Institute of Applied Physics, Friedrich-Schiller-Universität, Jena, Germany
"Illustration of the Ewaldsphere with a twodimensional fs pulse written volume Bragg grating (VBG)"

9:25 TINO ELSMANN
Institute of Photonic Technology, Friedrich-Schiller-Universität, Jena, Germany
"Inscription of first order Volume-Bragg-Gratings in a non-photosensitive material by using femtosecond-pulses with a wavelength of 400 nm"

9:50 JULIA MÖRBITZ
FBGS Technologies GmbH, Jena, Germany
"Fabrication and characterization of a "continuous Fiber Bragg Grating fiber" using Draw Tower Grating Technology"

10:15 CHRISTIAN VOIGTLÄNDER
Institute of Applied Physics, Friedrich-Schiller-Universität, Jena, Germany
"Femtosecond laser inscribed mode filter for few mode fibers"

10:40 Short Break

11 – Advanced Microscopy

Chair: Angela Klein

11:00 AURELIE JOST
Institute of Photonic Technology, Friedrich-Schiller-Universität, Jena, Germany
"Fast Structured Illumination Microscopy"

11:25 MARTIN KIELHORN
Institute of Photonic Technology, Friedrich-Schiller-Universität, Jena, Germany
"Spatio-angular microscopy"

11:50 JOHANNES OTT
Department of Medical Engineering and Biotechnology, Ernst-Abbe-University of Applied Sciences, Jena, Germany
"Development of an Optical System to Monitor a Cell Based Lab-On-A-Chip In Vitro Assay"

12:15 Official Closing of the Conference

Poster Contributions

ALAEE, RASOUL
Institute of Condensed Matter Theory and Solid State Optics, Friedrich-Schiller-Universität, Jena, Germany

"Complete light absorption in extremely coupled plasmonic nanostructure"

DIETRICH, KAY
Institute of Applied Physics, Friedrich-Schiller-Universität, Jena, Germany

"Chiral Nanomaterial Fabrication by means of On-Edge Lithography"

FASOLD, STEFAN
Institute of Applied Physics, Friedrich-Schiller-Universität, Jena, Germany

"Plasmonic Moiré Magnifier"

GEISS, REINHARD
Institute of Applied Physics, Friedrich-Schiller-Universität, Jena, Germany

"Lithium Niobate Nanowaveguides fabricated by IBEE"

GERMER, SUSETTE
Institute of Ion-Beam Physics and Materials Research, Helmholtz-Center Dresden-Rossendorf , Dresden, Germany

"Basic structures of integrated photonic circuits for smart biosensor applications"

GRÄFE, MAXIMILIAN
Institute of Applied Optics, Friedrich-Schiller-Universität, Jena, Germany

"Design of ultrafast fluorescence spectroscopy for axial resolution of fluorophore distribution with low numerical apertures for ophthalmologic application"

HARTUNG, ALEXANDER
Institute of Photonic Technology, Friedrich-Schiller-Universität, Jena, Germany

"Applicability of input coupling taper transitions for supercontinuum generation"

HEISEL, PER-CHRISTIAN
Institute of Photonic Technology, Friedrich-Schiller-Universität, Jena, Germany

"UV fs-laser pulse durations from autocorrelation measurements in CaF2"

JAHN, MARTIN
Institute of Physical Chemistry, Friedrich-Schiller-Universität, Jena, Germany

"Lipophilic sensor layers for SERS-based detection of water-insoluble substances"

KARRAS, CHRISTIAN
Institute of Photonic Technology, Friedrich-Schiller-Universität, Jena, Germany

"The impact ionization coefficient in dielectric materials revisited"

KLINER, ANDREA
Fraunhofer Institute for Applied Optics and Precision Engineering, Friedrich-Schiller-Universität, Jena, Germany

"Adiabatic Tapers"

KRÄMER, RIA
Institute of Applied Physics, Friedrich-Schiller-Universität, Jena, Germany

"Inscription of fiber Bragg gratings in a 120 core fiber with ultrashort pulses"

LORENZ, ADRIAN
Institute of Photonic Technology, Friedrich-Schiller-Universität, Jena, Germany

"Comparison of different design concepts for large mode area optical fibers"

LU, HUI WEN
Institute of Photonic Technology, Friedrich-Schiller-Universität, Jena, Germany

"Fast High-Resolution Fluorescence Microscopy by Nonlinear Structured Illumination"

MAASS, JACQUELINE
Carl Zeiss Jena GmbH, , Germany

"Flexible Simulation Tool for Talbot - Lithography to Fabricate Various Three-dimensional Microstructures"

PRATER, KARIN
Institute of Applied Physics, Friedrich-Schiller-Universität, Jena, Germany

"Vortex Light Bullets: a Discrete Revolution"

RATZSCH, STEPHAN
Institute of Applied Physics, Friedrich-Schiller-Universität, Jena, Germany

"Properties of titanium oxide deposited by atomic layer deposition as a coating for highly efficient transmission grating"

SARAVI, SINA
Institute of Applied Physics, Friedrich-Schiller-Universität, Jena, Germany

"Slow light in lithium niobate photonic crystal slab waveguides"

ZIERBOCK, SOPHIE
Institute of Physical Chemistry, Friedrich-Schiller-Universität, Jena, Germany

"Surface enhanced Raman spectroscopy (SERS) for the detection of ecological harmful arrearages of sewage water"

ZÜRCH, MICHAEL
Institute of Optics and Quantum Electronics, Friedrich-Schiller-Universität, Jena, Germany

"Highly nonlinear interaction of laser beams with angular orbital momentum"

Abstracts

(first authors are in alphabetical order)

Complete light absorption in extremely coupled plasmonic nanostructure

Rasoul Alaee[*1], Christoph Menzel[1], Uwe Huebner[2], Ekaterina Pshenay-Severin[3], Thomas Pertsch[3], H.-G. Meyer[2], J. Popp[2], Carsten Rockstuhl[1], and Falk Lederer[1]

[1]*Institute of Condensed Matter Theory and Solid State Optics, Abbe Center of Photonics, Friedrich-Schiller-Universität Jena, D-07743 Jena, Germany*

[2]*Institute of Photonic Technology (IPHT), PO. Box 100239, 07702 Jena, Germany*

[3]*Institute of Applied Physics, Abbe Center of Photonics, Friedrich-Schiller-Universität Jena, Max-Wien-Platz 1, D-07743 Jena, Germany*

[*]Corresponding Author: *rasoul.alaee@uni-jena.de*

Abstract

The complete absorption of light by plasmonic nanostructures promises tremendous applications in, e.g., thermal emitters, plasmonic sensors, and solar cells. The prefect absorption can conceptionally be achieved by suppressing the transmission and reflection channels for the illumination. The question is how to design and implement structures that reach that goal. We focuss here on a realization of such perfect absorbers employing the idea of extreme coupling in plasmonic absorbers and explore the device numerically and experimentally.

INTRODUCTION

Metamaterials are subwavelength engineered composite materials which have sparked enormous research interest in the past decade since they promise to control light propagation at the nanoscale. Recently, the concept of perfect absorption based on metamaterials has been introduced at microwave, terahertz, infrared and visible frequencies [1, 2, 3, 4]. These absorbers consists of periodically arranged metallic nanostructures, an optically thick metallic ground plate, and a dielectric spacer in between. Generally, transmission through the ground plate is almost zero. Thus, in order to capture the total incoming light by the absorber, the reflection should be suppressed by optimizing the geometry of nanostructure. The underlying physics of complete light absorption in the plasmonic metamaterials can be explained in terms of near field or far field interaction. In the case of near field interaction, the metallic nanostructure is very close to the ground plate and the structure will capture the whole incoming electromagnetic energy at the resonance frequency due to the critical coupling [3]. In contrast, at far field interaction i.e. the ground plate is far from the nanostructure, the coupling between the them is negligible and the complete absorption can be expressed in terms of destructive interference of direct reflection and multiple reelection [4].

The aim of this work is to investigate the extreme coupling between plasmonic nanostructures at nanoscale for the purpose of perfect absorption and to explore the physics of the device [5]. The regime of extremely coupling is accessed by choosing a dielectric spacer between of absorber that is only in the order of few nanometers and it can be fabricated by atomic layer deposition (ALD).

NUMERICAL AND EXPERIMENTAL RESULTS

The structure under consideration as well as the SEM image of the fabricated sample is shown in Fig. 1 (a) and (b). The geometrical parameters are given in the legend of the figure. The structure is periodic in x and y direction with periodicity P. The dielectric deposited onto the metal is fused silica with permittivity 2.25. The measured and simulated reflection spectra at normal incidence are shown in Fig. 2 (a). The result shows that the measured reflection is in excellent agreement with the simulated spectrum. The discrepancy is owing to the surface roughness of the fabricated structure. The structure supports different modes

at 130 THz , 320 THz and 410 THz. Figure 1 (b) and (c) show antisymmetric current distribution at corresponding resonance frequencies. We experimentally and numerically will show that the fabricated absorber is almost independent of angle of incidence and the first mode can be excited at higher angle.

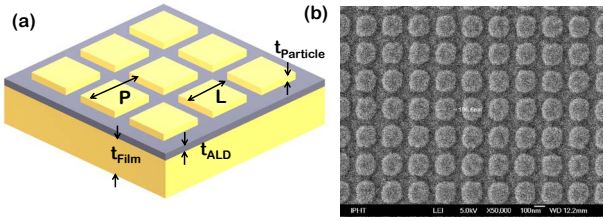

Figure 1: Geometry of the structure under consideration. (a) Schematic of a metamaterial perfect absorber. (b) SEM-image of the fabricated sample. Geometrical parameters of the sample are: $t_{\mathrm{ALD}} = 3.5\,\mathrm{nm}$, $t_{\mathrm{particle}} = 30\,\mathrm{nm}$, $t_{Film} = 10\,\mathrm{nm}$, $L = 195\,\mathrm{nm}$, and $P = 250\,\mathrm{nm}$.

To conclude, we have investigated an extreme coupling in the plasmonic nanostructure by taking the advantage of atomic layer deposition fabrication technique. The result shows that strong coupling can lead to an extremely low resonance frequency. Moreover, the structure supports higher antisymmetric modes that will generate the higher mode absorption.

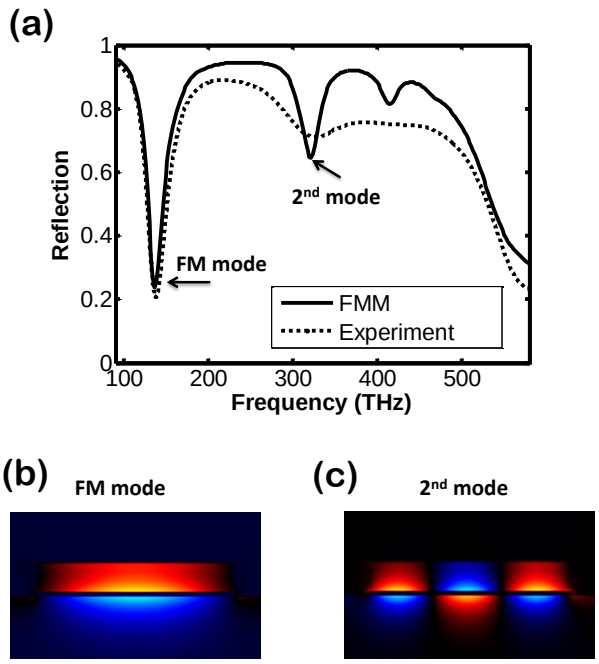

Figure 2: (a) Measured and simulated reflection spectra of the metamaterial perfect absorber at normal incidence. (b) and (c) Current distribution for the fundamental mode and the second mode of absorber, respectively.

[1] K. Aydin, V. E. Ferry, R. M. Briggs, and H. A. Atwater, Nat. Commun. **2**, 517 (2011).

[2] N. I. Landy, S. Sajuyigbe, J. J. Mock, D. R. Smith, and W. J. Padilla, Phys. Rev. Lett. **100**, 207402 (2008).

[3] C. Wu, B. Neuner, G. Shvets, J. John, A. Milder, B. Zollars, and S. Savoy, Phys. Rev. B **84**, 075102 (2011).

[4] H. T. Chen, Optics Express **20**, 7165 (2012).

[5] C. Menzel, R. Alaee, E. Pshenay-Severin, C. Helgert, A. Chipouline, C. Rockstuhl, T. Pertsch, and F. Lederer, Opt. Lett. 37, 596 (2012).

Intense Attosecond Pulses from Relativistic Surface Plasmas

Jana Bierbach[*1,2], Christian Rödel[1,2], Mark Yeung[3], Brendan Dromey[3], Thomas Hahn[4], Arpa Galestian Pour[1], Silvio Fuchs[1,2], Georg Pretzler[4], Matthew Zepf[3], Gerhard G. Paulus[1,2]

[1] *Institute of Optics and Quantum Electronics, Friedrich Schiller University, Max-Wien-Platz 1, 07743 Jena, Germany*

[2] *Helmholtz-Institute Jena, Fröbelstieg 3, 07743 Jena, Germany*

[3] *Centre for Plasma Physics, School of Mathematics and Physics, Queen's University Belfast, BT7 1NN, United Kingdom*

[4] *Institute for Laser- and Plasmaphysics, Heinrich Heine University Düsseldorf, Universitätsstraße 1, 40225 Düsseldorf, Germany*

[*] Corresponding Author: *jana.bierbach@uni-jena.de*

Abstract

Surface High Harmonic Generation (SHHG) from solid density plasmas is thought to be a promising source of intense XUV pulses with attosecond pulse duration. We report on the efficiency of the relativistic process of SHHG, measured in a series of experiments at the 40 TW laser system "'Jeti"' at the university of Jena. Our experimental findings are compared to established theory and to particle-in-cell simulations. A strong influence of the plasma scale length on the efficiency is found, which can be controlled by an adequate enhancement of the laser pulse contrast using a plasma mirror or second harmonic generation. We record XUV pulse energies in the μJ range and efficiencies of $\approx 10^{-5}$. Thus, in terms of pulse energy surface high-harmonic generation is becoming a competetive source to HHG in gases. Hence, we demonstrate the first consecutively measured relativistic SHHG at a repetition rate of 10 Hz yielding an average power of 10 μW in the spectral range between 26 nm to 52 nm.

Introduction

The generation of high harmonics of the fundamental laser field is the most prominent way to generate ultrashort pulses providing the shortest available temporal resolution of the order of attoseconds. High-harmonic generation on solid surfaces (SHHG) using relativistic laser intensities exploits nonlinear phenomena in fully ionized relativistic plasmas and can overcome the intensity limitations of the HHG process in gases. In SHHG, laser pulses are focused onto a surface to an amplitude of the normalized laser vector potential of

$$a = \frac{eE}{\omega m_e c} = \sqrt{\frac{I\lambda^2}{1,37 \cdot 10^{18} \frac{W\mu m^2}{cm^2}}} \gg 1, \qquad (1)$$

thus leading to a relativistic electron oscillation at the surface. After the solid material is ionized by prepulses or the rising slope of the main pulse, a dense plasma-vacuum boundary exceeding the critical density is created and reflects the incident laser pulse. For relativistic intensities the dominant process of harmonic generation is often described by the simplified but intuitive model of the "'relativistically oscillating mirror"' (ROM) [1]. Within the framework of this model the electrons at the plasma surface are oscillating with relativistic velocity whereas the oscillations amplitude and phase are coupled to the driving laser field component. While being reflected off the relativistically moving plasma surface the laser wave experiences a periodic phase modulation. In a simplified description this can be understood in terms of a relativistic Doppler up-shift, generating in each laser cycle one attosecond pulse with a broad and continuous spectrum up to a maximum frequency

$$\omega_{ro} \approx \sqrt{8}\gamma^3 \omega_0. \qquad (2)$$

Due to the periodicity of this process a train of attosecond pulses is emitted from the plasma surface, exhibiting a broad harmonic spectrum. In the ultra-relativistic limit ($a_0 \gg 1$) an extended version of the ROM model predicts a spectral power law of the harmonic radiation [1]

$$\eta(\omega) \propto \left(\frac{\omega}{\omega_0}\right)^{-\frac{8}{3}}. \qquad (3)$$

From these equations high efficiencies, e.g. 10^{-4} for the 30^{th} harmonic, are expected. Moreover the ROM process is not limited in intensity as it is the case for gas harmonics. Therefore SHHG in the relativistic regime is thought to be a promising source of intense attosecond XUV pulses with pulse energies orders of magnitude higher than the current state-of-the-art. In fact, using ultra-relativistic intensities it has been shown that bright harmonics up to keV photon energies can be generated [2].

EFFICIENCY OF RELATIVISTIC SURFACE HIGH HARMONICS

Until now, it has generally been accepted that achieving sufficiently steep density gradients for ROM harmonics is the major challenge. Thereby, the plasma scale length L_p, describing the distance of the 1/e-decay of an exponential electron density profile, depends on the laser pulse contrast. Thus the density gradient can be controlled by an adequate enhancement of the contrast using a plasma mirror or second harmonic generation. In our experiments at the Jeti laser system we apply different plasma mirror targets to achieve various contrast settings [3]. The pulse energy of SHHG is investigated using an imaging XUV spectrometer, which was calibrated at a synchrotron facility. Surprisingly, the strongest harmonic emission is recorded for an intermediate contrast ($L_p \approx \lambda/5$, s. Fig. 1) yielding, e.g. 2.7 μJ for the 21st harmonic (equavalent to an efficiency of 10^{-5}). For a higher laser pulse contrast and shorter plasma scale length, respectively, a decrease in harmonic signal is observed. Consequently, the harmonic efficiency can be optimized by careful control of the laser pulse contrast and the resulting plasma scale length. Our findings are confirmed by particle-in-cell simulations and are discussed theoretically [4].

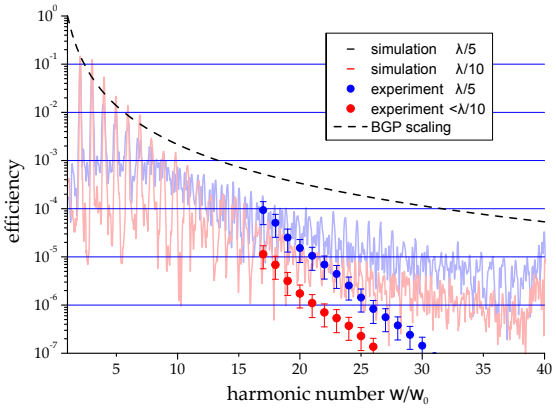

Figure 1: Experimental efficiencies (circles) are compared to spectral densities from 1D PIC simulations (lines) for different plasma scale lengths (density $n_e = 200n_c$, exponential density profile). The experimental efficiencies have been normalized to a pulse energy of 250mJ (energy that is focused to $a_0 > 1$). In the ultra-relativistic limit the efficiencies are given by eq. (3).

In addition, we demonstrate the first consecutively measured relativistic surface high-harmonic generation at a repetition rate of 10 Hz [5]. We report on an average power of 10 μW in the spectral range of 51 nm to 26 nm. The capability of producing stable and intense high-harmonic radiation from relativistic surface plasmas may facilitate experiments on nonlinear ionization or the seeding of free-electron lasers.

[1] T. Baeva et al., *Theory of high-order harmonic generation in relativistic laser interaction with overdense plasma*, (Phys. Rev. E **74**, 046404, 2006).

[2] B. Dromey et al., *Bright Multi-keV Harmonic Generation from Relativistically Oscillating Plasma Surfaces*, (Phys. Rev. Lett. **98**, 085001, 2007).

[3] C. Rödel et al., *High repetition rate plasma mirror for temporal contrast enhancement of terawatt femtosecond laser pulses by three orders of magnitude*, (Appl. Phys. B. **103**, 295, 2011).

[4] C. Rödel et al., *Harmonic Generation from Relativistic Plasma Surfaces in Ultra-steep Plasma Density Gradients*, (submitted, preprint available at arXiv:1205.6821v1).

[5] J. Bierbach et al., *Generation of 10 μW relativistic surface high harmonic radiation at a repetition rate of 10 Hz*, (to be published in New Journal of Physics).

Parametric fiber optical amplifier for spectrally high-resolved coherent anti-Stokes Raman spectro-microscopy

Mario Chemnitz[1,*], Martin Baumgartl[1], Cesar Jauregui[1], Tobias Meyer[2], Benjamin Dietzek[2], Jürgen Popp[2], Jens Limpert[1], Andreas Tünnermann[1,3]

[1] *Friedrich-Schiller-Universtity Jena, Institute for Applied Physics, Albert-Einstein-Str. 15, 07745 Jena, Germany*

[2] *Institute of Photonic Technology, Albert-Einstein-Str. 9, 07745 Jena, Germany*

[3] *Fraunhofer Institute for Applied Optics and Precision Engineering, Albert-Einstein-Str. 7, 07745 Jena, Germany*

[*] Corresponding Author: *mario.chemnitz@uni-jena.de*

Abstract

We present a quasi alignement-free fiber-based optical parametric amplifier for coherent anti-Stokes Raman scattering (CARS) in (non-)biological samples. The wavelength tuneable, narrowband generation of CARS pump and Stokes pulses is based on four-wave-mixing in photonic crystal fibers. With its performance in CARS spectro- and microscopy the compact fiber system directly competes with table-top optical parametric bulk systems.

Introduction

Coherent anti-Stokes Raman scattering (CARS) names the scattering of photons at molecular vibrational modes excited by two well-defined frequency separated fields. Thus CARS spectro-/microscopy provides the possibility of label-free acquisition of chemical selective information of molecular systems making it competitive to well-applied fluorescence microscopy methods. Due to the higher demands concerning bandwidth and tunability expensive, table-spanning Titanium-Sapphire (Ti:Sa) lasers or Ti:Sa pumped optical parametric oscillators (OPO) were the means of choice for CARS imaging up to now [1].

We designed an all-fiber optical parametric amplifier (FOPA) providing a tuneable three-band output for CARS applications in biochemistry and medicine. The generation of the necessary new wavelengths is done by amplification of an extern seed signal using four-wave mixing (FWM) in photonic crystal fibers (PCF). Besides the theoretical outline of the process of four-wave-mixing, possibilities for improving the output spectrum in view of tunablity and spectral resolution are discussed and demonstrated. Examples for the successful usage of the presented setup in doing CARS spectro-/microscopy are shown.

Theoretical aspects

The third-order nonlinear process of (degenerately pumped) FWM works most efficiently by conserving energy $2\omega_p = \omega_s + \omega_i$ (see inset of fig. 1) and momentum $2k_p = k_s + k_i + 2\gamma P_p$ both together known as phase-matching [2]. The designable effective refractive index of PCFs, which can be calculated numerically, enables phase-matching over a wide wavelength region.

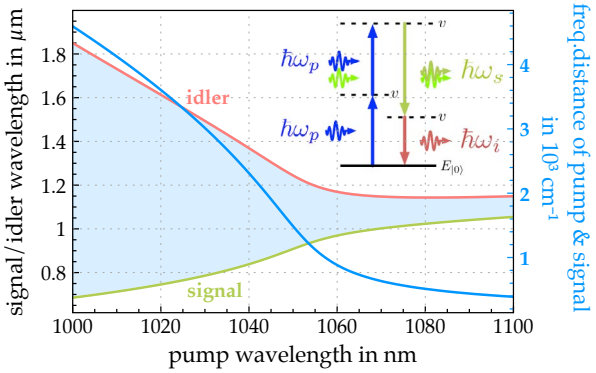

Figure 1: Signal/idler wavelength and frequency distance between signal and pump in dependence on pump wavelength for perfect phase-matching in a PCF. Inset: energy scheme for a FWM process

In our simulations we investigated several PCFs having their zero-dispersion-wavelength close to the Ytterbium spectral emission of our used laser systems. Phase-matching curves like in fig. 1 and further gain calculations predict a wide range of output wavelengths tuneable by wavelength variation of pump and input seed signal. Frequency distances between pump and signal of 500 to 4000cm^{-1} can be expected addressing most Raman-active molecular modes.

Experimental setup

The upper part of fig. 2 shows the principle setup of the FOPA. The FWM process is driven by an amplified, mode-locked fiber oscillator, which emits 140ps broad pulses around 1038nm with few kilowatt peak power [3]. The amplification of a tuneable, continuous Ti:Sa output signal is used to prove the whole spectral parametric gain accessibility.

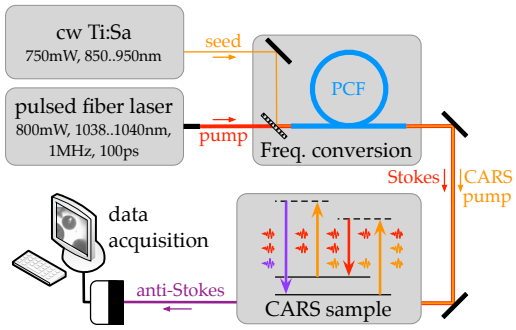

Figure 2: Principle of our experimental setup for CARS spectro-/microscopy

Like visible in fig. 3 the FOPA supplies three clearly separated wavelength bands whereby signal and idler have a very small bandwidth of below 1cm^{-1} due to the narrowband seeding. The gain bandwidth and the wavelength tuning range, respectively, is comparable to the spectrum of unseeded optical parametric generation (grey spectrum in fig. 3) affording several hundred inverse centimetres in bandwidth. Accordingly the potential spectral resolution of the FOPA exceeds the one of commercially available OPO systems [4] for comparable tuning bandwidths.

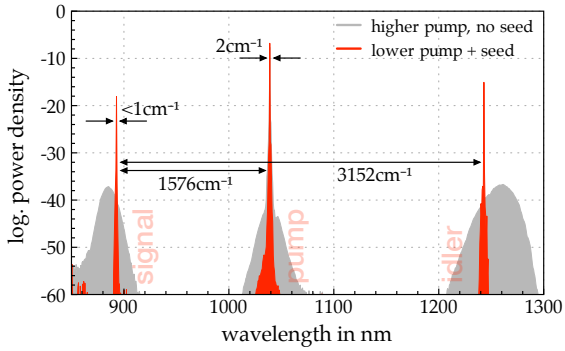

Figure 3: Output spectrum of the FOPA system with (red) and without (grey) an input seed

CARS spectro-/microscopy

The principle of the setup of CARS experiments is pictured in fig. 2. Due to the high spectral resolution Raman resonances with a bandwidth of below 10cm^{-1} could be resolved. Furthermore imaging of biological samples like aorta wall tissue (fig. 4) could be realised. Varying the excitation frequency lead to deeper view inside of the biochemical structure of the tissues.

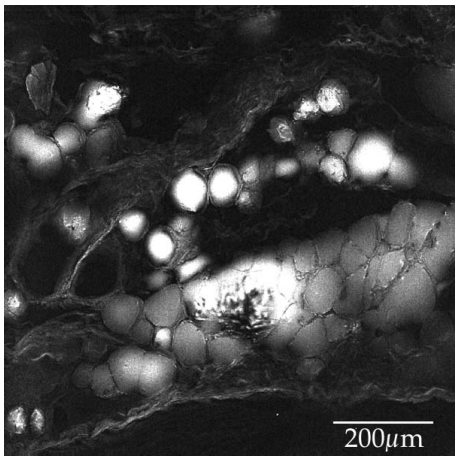

Figure 4: CARS microscopic picture of a rabbit aorta wall excited at 2930cm^{-1} (CH stretching mode)

[1] C. L. Evans, X. S. Xie, *Annual Review of Analytical Chemistry* **1**, 883 (2008).

[2] G. P. Agrawal, *Nonlinear fiber optics* (Academic Press, 2001).

[3] M. Baumgartl, *et al.*, *Optics Express* **20**, 4484 (2012).

[4] APE, fs/ps MHz OPOs (2012).

Chiral Nanomaterial Fabrication

by means of On-Edge Lithography

Kay Dietrich*, E.-Bernhard Kley and Andreas Tünnermann

Abbe Center of Photonics, Institute of Applied Physics,
Friedrich-Schiller University Jena, Max-Wien-Platz 1, 07743 Jena

*Corresponding Author: *dietrich.kay@uni-jena.de*

Abstract

In our contribution we report about a novel method concerning efficient fabrication of a chiral nanomaterial by on-edge lithography enhancing the application spectrum of electron beam lithography. The functionality of the proposed method is demonstrated showing SEM micrographs of the fabricated chiral metallic nanoparticle array. Furthermore, investigating polarization dependent far-field transmittance measurements reveals both the fabrication process and optical properties of the chiral nanostructure.

INTRODUCTION

One of the most striking arguments in doing scientific research is the opportunity to find novel effects never noticed in nature before. Metamaterials offer a whole bunch of fascinating optical effects like cloaking, negative refraction or superlensing worth to investigate [1]. This class of materials consists of tiny nanostructures, usually metallic, where the structure is equal or less in size in comparison to the operating wavelength. The fact that shape and size of the nanostructures have major impact on its functionality leads to the brilliant possibility in tailoring the metamaterials optical properties.

Chiral metamaterials, the structure mirror image cannot superimpose the original structure by means of rotational transformation operations, are a subclass and sensitive to effects depending on circular polarization [2]. One of the most obvious chiral geometry is the helix. Being either left or right handed the amount of absorbed light by such a helix structure coincides with the polarization state of light, which is left (LCP) or right circular polarized (RCP), respectively. Gansel *et al.* have published a work investigating in a simulation the influence of helix parameter changes on the resulting optical transmittance spectra [3]. They even successfully managed to fabricate such a structure by means of direct laser writing (DLW) with small helix

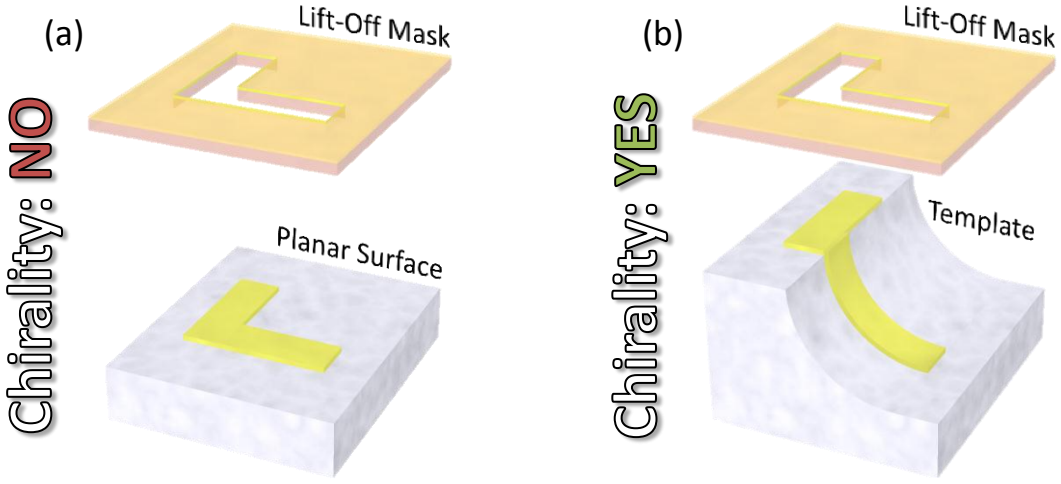

Figure 1: Sketch of a lift-off process for a 2D-L shaped hole-mask written and developed on either (a) a planar surface resulting in a 2D-L pattern without chirality or (b) a pre-structured surface (template) resulting in a 3D-L pattern with chirality. Lift-off mask and substrate are sketched with distance to each other due to a simpler insight.

dimensions sufficient for an operation in the mid-infrared region [4].

SCOPE

Despite the helix structure seems to be a perfect shape, the DLW patterning system is limited concerning writing speed, space and resolution, which means a huge handicap for efficient production. Scientists already applied other fabrication methods yielding in different shaped chiral nanostructures [5, 6], but the efficient fabrication of a chiral nanomaterial on larger scales remains unaccomplished. Thus we have developed a novel technique called on edge lithography (OEL) being efficient and capable for chiral nanostructure fabrication on larger scales. Furthermore, involving electron beam lithography (EBL) during fabrication, the structure sizes are small enough pushing the operation of the presented chiral pattern into the near-infrared region.

EXPERIMENTAL ISSUES

The main idea of OEL is applying EBL to resist spun on a pre-structured surface in the following stated as template. Thus we transfer the problem of three-dimensional shaped patterns from the lithography system towards the template. A proposed template may one offering a wavelike or corrugated profile (fig. 1b). While structures attached to a planar surface remain two-dimensional (2D) (fig. 1a), structures attached to a convenient template do not. They are finally three-dimensional (3D) like sketched in figure 1(b), though a 2D-L shaped void mask for shadow evaporation has been used. We will present polarization dependent far-field transmittance spectra indicating the OEL technique is capable of efficient chiral nanoparticle fabrication (fig. 2). Secondary, fabrication specific deviations from the proposed structure and their impacts on the optical properties will be investigated and discussed.

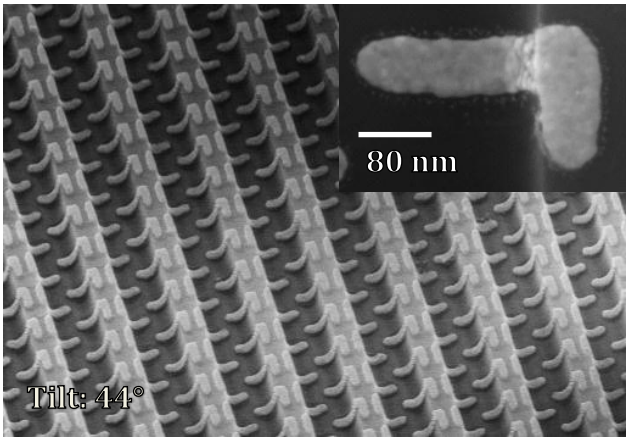

Figure 2: Tilted view SEM micrograph of the fabricated 3D-L particle array. The inset shows a magnified view from top of a single gold 3D-L particle. The position accuracy of the particle at the grating bar is noteworthy.

[1] G. Goussetis, A. Feresidis and A. Harvey, Journal of Modern Optics 57, 1-16 (2010).

[2] B. Wang, J. Zhou, T. Koschny, M. Kafesaki and C. Soukoulis, J. Opt. A: Pure Appl. Opt. 11 (2009).

[3] Justyna K. Gansel et al., Optics Express 18, No. 2, 1059 (2010).

[4] Justyna K. Gansel et al., Science 325, 1513 (2009).

[5] Zhang et al., Phys. Rev. Lett. 102, 023901 (2009).

[6] C. Helgert et al., Microelectron. Eng., "A dedicated multilayer technique for the fabrication of three-dimensional metallic nanoparticles", in press, (2012).

[7] The authors gratefully acknowledge support by the German Federal Ministry of Education and Research grant 03IS2101A (PhoNa).

Analysis of the hole formation in ultrashort pulse laser deep drilling

Sven Döring[*1], Tobias Ullsperger[1], Sören Richter[1], Andreas Tünnermann[1,2], and Stefan Nolte[1,2]

[1] *Institute of Applied Physics, Abbe Center of Photonics, Friedrich-Schiller-Universität Jena, Albert-Einstein-Straße 15, 07745 Jena, Germany*

[2] *Fraunhofer Institute for for Applied Optics and Precision Engineering, Albert-Einstein-Straße 7, 07745 Jena, Germany*

[*] Corresponding Author: *sven.doering@uni-jena.de*

Abstract

We present a detailed experimental study of the hole formation process during ultrashort pulse laser deep drilling in silicon by in-situ imaging. The influence of the focus position and the pulse energy are evaluated with respect to the achievable hole depth and shape. Our observations show three characteristic phases of the drilling process for all parameters with a standard deviation of depth and size in the order of several percent. The achievable hole depth can be increased up to a factor of 2 by optimizing the focus position, while minimizing statistical variations.

Introduction

Ultrashort laser pulses with a typical pulse duration below 10 ps enable burr and melt free manufacturing of microsize structures in a large variety of materials, e.g. metals, glass, polymers and ceramics, which cannot or may only be achieved with extraordinary effort by conventional techniques [1]. Consequently, a fundamental understanding of the formation process of the ablated structures is required to develop and optimize industrial applications. Previous investigations studied the ablation behaviour at the surface, revealing the fluence (pulse energy per irradiated area) as the primary parameter which determines the material specific ablation rate and threshold [1, 2]. However, the pulse propagation and material removal characteristics are different for structures with high aspect ratio, especially percussion drilled holes, where the hole diameter is similar to the laser spot size.

We developed an in-situ investigation technique to directly observe the formation of the hole shape during laser drilling of a silicon sample [3]. This enables a direct analysis of the hole's depth as well as its longitudinal section (shape) according to the number of applied pulses in a material, which is opaque for the drilling radiation and therefore behaves similar to a metal.

In this study, we analyze the laser drilling process with respect to the statistical varition of the hole's depth and shape and how this can be influenced by the process parameters pulse energy and focal position.

Experimental Setup

In our experiments, laser drilling is performed by 8 ps pulses at 1030 nm inside a crystalline silicon sample. At the same time, the sample is transilluminated with a second laser at a wavelength close to the band edge of silicon and the hole's silhouette is projected onto a standard CCD camera.

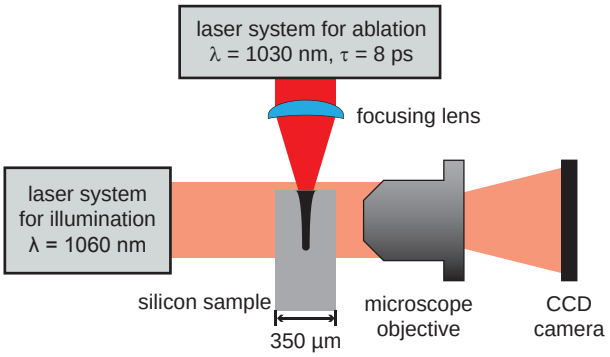

Figure 1: In-situ imaging setup.

A lens with a focal length of 100 mm is used for focussing, which results in a focal spot size of $d_0 \approx 27\,\mu\text{m}$ and a Rayleigh length $z_R = \pi d_0^2/4\lambda \approx 600\,\mu\text{m}$, typical for micromachining applications. The focus position is varied between $z = -3z_R$ and $z = +3z_R$ with respect to the sample surface for two different pulse energies, 30 µJ and 125 µJ. For each set of parameters ten holes are drilled for a statistical analysis of the hole depth and section area.

Results

The evolution of the hole depth for a pulse energy of $E_P = 30\,\mu J$ and focus at the sample surface is shown in fig. 2 for ten repetitions of the drilling process.

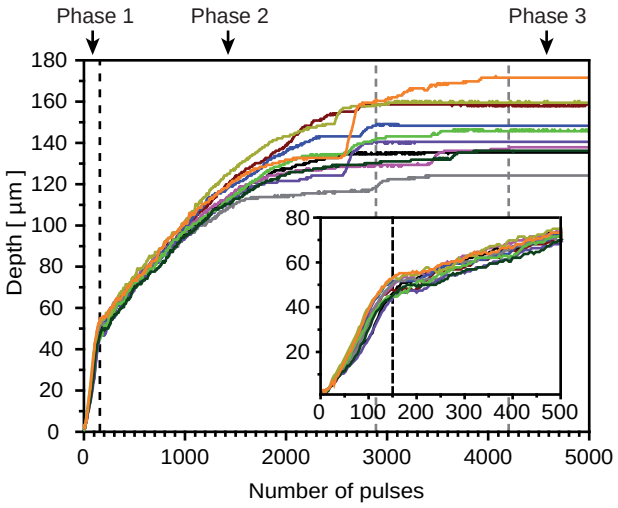

Figure 2: Depth evolution for drilling with $E_P = 30\,\mu J$ and focus at the sample surface. Multiple holes show the statistical variation of the process.

Three phases of the drilling process can be distinguished with a clear transition between phase 1 and 2, marked by a sudden drop in the ablation rate at approximately 150 pulses. In phase 1, a taper-shaped capillary is excavated. In the following second phase, ablation additionally occurs in transverse direction leading to the formation of bulges along the side walls and even bending of the hole. Intermediate periods without forward drilling but predominant transversal growth can be observed at every instant during phase 2. These occur most likely due to internal reflections within the hole capillary. The final stop of forward drilling is different for every hole and ranges between 2,900 and 4,200 pulses in this example, afterwards only the hole diameter may increase slightly. The relative standard deviation in depth is approximately 10% at the end of phase 1 and also in the final state.

This principal behavior in depth evolution is typical for all process parameters under investigation. However, absolute values of depth and size change accordingly. Already for a slight raise of the focus position above the surface to $z = +\frac{1}{2}z_R$, the maximum achievable depth decreases by a factor of 0.8, independent of the pulse energy. Further defocussing enhances this effect. The divergent beam in this case enlarges the irradiated area and expands the hole's taper to a funnel shape with large entrance diameter, see left part of fig. 3.

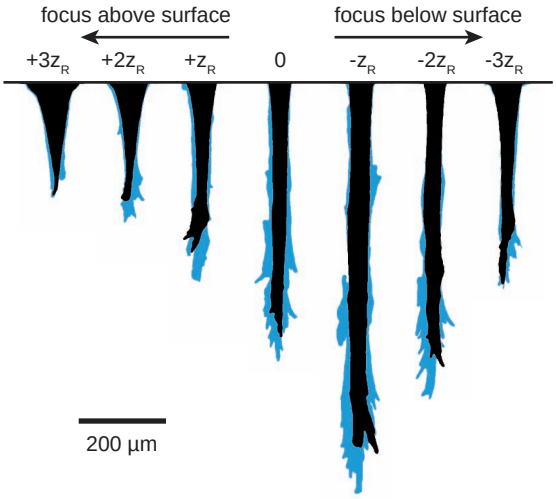

Figure 3: Final hole shape for drilling with $E_P = 125\,\mu J$ at different focus positions. Black shades show typical hole shapes, light blue shades all observed variations.

In contrast, a position of the focus below the surface can increase the achievable depth, see right part in fig. 3. The optimized focus position was determined around $z = -z_R$. The effect is most distinct in phase 1 and for low pulse energies with a factor of up to 1.8 and reaches a factor of 1.6 at the final hole depth. Simultaneously, the relative standard deviation of the achieved depth is reduced to 5%. Similar results are obtained for the section area. This effect can be attributed to lower propagation losses due to adaption of the convergent beam to the tapered shape of the growing hole. Nevertheless, inappropriate defocussing, e.g. to $z = -3z_R$, leads to a funnel shaped hole geometry wih reduced depth.

[1] D. Breitling, A. Ruf, F. Dausinger, *Proc. of SPIE* **5339**, 49 (2004).

[2] S. Nolte *et al., J. Opt. Soc. Am. B* **14**, 2716 (1997).

[3] S. Döring, S. Richter, A. Tünnermann, S. Nolte, *Applied Physics A* **105**, 69 (2011).

Imaging Cross Correlator FROG: Space-Time Retrieval of Ultrashort Complex Electric Fields

Falk Eilenberger[*1], Alex Brown[1], Stefano Minardi[1], and Thomas Pertsch[1]

[1]*Institute of Applied Physics, Abbe Center of Photonics, Friedrich-Schiller-Universität, Max-Wien-Platz 1, 07745 Jena*

[*]Corresponding Author: *falk.eilenberger@uni-jena.de*

Abstract

We present *i*XFROG, a method for the three-dimensional retrieval of the amplitude and phase of spatiotemporal electric fields with femtosecond resolution. The method is based on established imaging cross-correlation techniques (*i*XCorr) and the robust FROG method for retrieval of complex pulses. It is implemented into a robust and inline setup, which can be added to an *i*XCorr.

INTRODUCTION

The measurement and characterization of femtosecond optical pulses is one of the most sophisticated measurement tasks carried out in photonic labs, because femtosecond pulses are among the shortest events that are generated arbitrarily and reproducibly. Advanced self-referencing measurement techniques, such as SPIDER [1], FROG [2], or MIIPS [3] are now routinely used to characterize ultrashort pulses of known spatial structure, such as those with a defined mode profile emitted by laser sources.

However, ultrashort sources and experiments are moving away from the classical concept of a 1D single-mode structure. Consequentially pulse trains become more complex in space and time, probing deep into the realm of ultrafast spatiotemporal dynamics [4-6]. All the above mentioned methods are, however, unsuitable for the characterization of spatiotemporally complex wavepackets.

Here we present a new method, imaging cross-correlation frequency-resolved, optical gating (*i*XFROG) for the characterization of such fields. The method is based on an imaging cross correlation technque (*i*XCorr) [7, 8] and extends this method towards improved temporal resolution and for the first time demonstrates 3D phase retrieval.

FUNDAMENTALS

XFROG [9] retrieves a complex amplitude $A(t)$ of an optical pulse by measurement of the spectrally resolved cross correlation (XCorr) $I(\omega,\tau)$ with a known gate pulse $G(t)$, such that

$$I(\omega,\tau)=\left|\int A(t)G^{*}(t-\tau)\exp(-i\omega t)\,dt\right|^{2} \qquad (1)$$

In practice sum-frequency (SF) generation in a $\chi^{(2)}$ crystal with the delayed gate pulse is used to generate the XCorr followed by a spectrometer. If no known gate pulse is at hand a delayed copy of the pulse itself or even an unknown gate pulse [10] can be used. $I(\omega,t)$ contains the same kind of dual time-frequency information as a musical score sheet.

Reconstruction of the complex field $A(t)$ is achieved iteratively by means of generalized projections [2], somewhat similar to the technique used for the construction of computer generated holograms. This algorithm is robust against noise, partially due to its vast redundancy – one measures N^2 data points to retrieve $2N$ results.

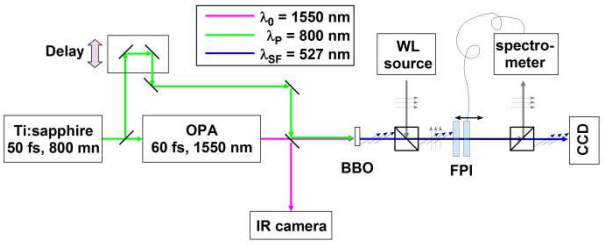

Figure 1 Drawing of the experimental setup.

For the construction of spatiotemporal fields $A(x,y,t)$ we record a spectrogram at each point in space $I(x,y,\omega,\tau)$ and use the XFROG algorithm for each pixel (x,y). To resolve the relative ambiguity of the absolute phase we can reconstruct a phase plane $\theta_0(x,y;\tau_0)$ at any given delay τ_0, i.e. with a Shack-Hartmann sensor [11], which will be implemented in the future. Consideration has to be given to the recording of the N^4, data points, of which a

large subspace (i.e. all spatial pixels (x, y) for a given pair (ω, τ)) should be recorded in parallel and along all other parameters as fast as possible.

EXPERIMENTAL SETUP

The experimental implementation of the iXFROG is depicted in Figure 1. A short pulse of known temporal structure is split. One part is used in an experiment, undergoing nonlinear, spatiotemporal reshaping which is to be measured. It is imaged onto a BBO crystal. The other part serves as the reference with tunable delay. It is short in time and fills the complete aperture of the crystal homogeneously.

The BBO is cut and oriented for SF generation. The SF field containing the spatial structure (x, y) of the wavepacket at a given delay τ is imaged onto a CCD camera, which records a set of pictures while the delay stage scans through the range of delays. Coarse spectral filtering along the ω axis is achieved by interference filters with 10 nm resolution. Fine filtering with a resolution 1 nm of is achieved by a tunable Fabry-Perot-Interferometer (FPI) built from two mirrors on piezo positioners. It is auto-aligned to maintain parallelity and proper transmission wavelength by a feedback loop of a cross-polarized white-light source and a spectrometer.

RESULTS

Figure 2 displays the first three dimensionally reconstructed field, representing the field of the pulse leaving an OPA. Figure 2 (a) displays the spatial intensity, while subfigures (b) and (d) contain the measured and retrieved Spetcrogramm at the pixel position denoted with the cross in (a). Subfigure (c) contains the reconstructed intensity and phase at both points denoted in Figure 2 (a). Although the temporal shape of the pulse intensity is seen to be equal we reveal a variation in the phase evolution across the pulse front and a delay in the centre.

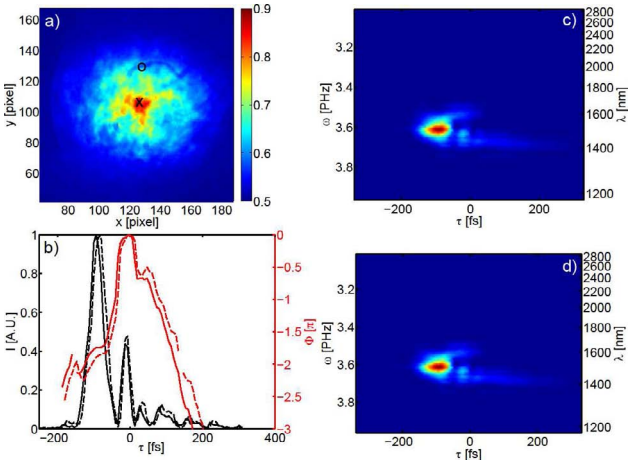

Figure 2 Pulse reconstructed by iXFROG. (a) Measured spatial energy density. (b) Reconstrcuted intensity and phase at the points marked in (a) with cross (dashed) and circle (solid). (c) Measured spectrogramm at the position marked with the cross. (d) Retrieved spectrogram.

CONCLUSIONS

We present iXFROG, a method for the complete retrieval of ultrashort spatiotemporal electric fields, with femtosecond resolution. Key element is a tunable FPI as a spatially non-distorting wavelength-selective element. We demonstrate first results of the reconstruction of a highly chirped pulse.

[1] C. Iaconis and I. Walmsley, Opt. Lett. **23**, 792 (1998).

[2] R. Trebino, *Frequency-Resolved Optical Gating: The Measurement of Ultrashort Laser Pulses* (Kluwer Academic Publishers, 2002).

[3] V. V. Lozovoy, I. Pastirk, and M. Dantus, Opt. Lett. **29**, 775 (2004).

[4] P. Di Trapani *et al.*, Phys. Rev. Lett. **91**, 093904 (2003).

[5] F. Eilenberger *et al.*, Opt. Express **19**, 23171 (2011).

[6] S. Minardi *et al.*, Phys. Rev. Lett. **105**, 263901 (2010).

[7] M. A. C. Potenza *et al.*, Optics Communications **229**, 381 (2004).

[8] S. Minardi, J. Trull, and M. A. C. Potenza, Journal of Holography and Speckle **5**, 85 (2009).

[9] S. Linden, H. Giessen, and J. Kuhl, physica status solidi (b) **206**, 119 (1998).

[10] K. W. DeLong, R. Trebino, and W. E. White, J. Opt. Soc. Am. B **12**, 2463 (1995).

[11] B. Platt, Journal of Refractive Surgery **17**, 573 (2001).

Inscription of first order Volume-Bragg-Gratings in a non-photosensitive material by using femtosecond-pulses with a wavelength of 400 nm

Tino Elsmann[*1], Alexander Hartung[1], Manfred Rothhardt[1], Hartmut Bartelt[1], Matthias Falk[2], and Hansruedi Moser[2]

[1]*Institute of Photonic Technology, Albert-Einstein-Straße 9, 07745 Jena, Germany*

[1]*FISBA OPTIK AG, Rorschacher Straße 268, CH-9016 St. Gallen, Switzerland*

[*]Corresponding Author: *tino.elsmann@ipht-jena.de*

Abstract

Volume-Bragg-Gratings were inscribed in glass by using a femtosecond-pulses to overcome the limitation of photosensitive materials. For inscription a wavelength of 400 nm was chosen to fabricate first order gratings. The fabrication itself was done holographically using a Talbot interferometer. The grating structure was analyzed by external Bragg reflection. Further investigations on the grating like absorption measurements, microscopic imaging and heating experiments were done.

INTRODUCTION

In general, a Bragg-grating is a structure of alternating refractive index or absorption properties which now are commonly used in fiber optics. Depending on its geometrical and physical parameters a Bragg-grating reflects only a special part of the incoming spectrum. The aim of our work was to demonstrate that the inscription technique for Fiber-Bragg-Gratings using a Talbot-interferometer can also be applied to fabricate grating structures inside bulk material, so called Volume-Bragg-Gratings (VBGs). Such VBGs can be applied in micro optical setups like diode lasers as narrowband filters or as external resonator [1], but also in other setups as an internal resonator or as a chirped grating for pulse compression [2, 3].

EXPERIMENTAL SETUP AND RESULTS

The grating structure can be fabricated easily by illuminating the material with an interference pattern which is generated by a pure two-beam-interference. Regions with a high intensity undergo a higher change in their optical properties than the regions of low or zero intensity, which generates alternating properties. This concept is based on an intrinsic photosensitivity of the material to illumination, but most of the glasses show no photosensitivity to moderate laser intensities. But for different applications often user adapted materials are necessary, which cannot be chosen with respect to their photosensitivity. To overcome this limitation a femtosecond laser system was used to generate the interference pattern. It provides pulses with duration of 135 fs at 800 nm. Due to these short pulses, high peak powers are reached (more than 20 GW) and therefore nonlinear absorption occurs and thus multi-photon absorption becomes likely. To demonstrate this advantage of using fs-pulses we used a non-photosensitive glass for our experiments (S-TIH53 from OHARA). This material is used for diode laser applications because of its very high refractive index of 1.81 at 1.1 µm wavelength.

Due to the high refractive index of the glass material a short laser wavelength is necessary to inscribe first order gratings for a target Bragg wavelength λ_{Bragg} in the typical wavelength region of diode lasers in the order of 1060 nm.

The resonance wavelength of the grating, the Bragg wavelength λ_{Bragg}, depends on the effective refractive index of the material n_{eff}, the wavelength of the inscription laser λ_{laser} and the angle ϑ between the two interfering beams (see Fig. 1):

$$\lambda_{Bragg} = \frac{n_{eff}\,\lambda_{laser}}{\sin(\vartheta)} \qquad (1)$$

Thus we used a frequency-doubled Ti:Sa-amplified laser with a corresponding λ_{laser} of 400 nm.

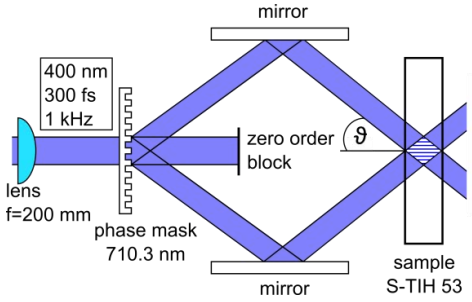

Figure 1: Talbot interferometer setup. The first diffraction orders are superposed to generate an interference pattern inside the bulk sample.

The interference pattern was generated in a Talbot interferometer due to several advantages. In this setup the sample is placed far away from the beam splitter (phase mask) so that a replacement of the samples does not affect the stability of the adjustment. Furthermore it is possible to inscribe gratings deep inside the sample volume. Another advantage of the Talbot interferometer is the tunability of λ_{Bragg} by rotating the mirrors (see Fig. 1).

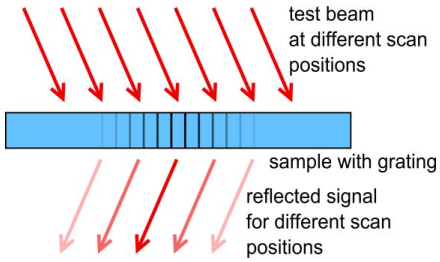

Figure 2: Top view of the grating characterization by the external Bragg reflection method.

After the inscription the VBGs were analyzed using the external Bragg reflection method [4]. For this purpose the samples were illuminated with a test laser of moderate power (HeNe, 10 mW at 633 nm). Only for a particular angle of 63.0° Eq. (1) is fulfilled and the incoming beam is reflected under the same angle at the other side of the sample (see Fig. 2).

We examine the angular dependence of the reflected intensity and found a maximum in the expected region at (62.9±0.2)°. We also recognized an asymmetric reflectivity profile of the gratings which corresponds very well to the beam profile of the inscription laser. The maximum modulation of refractive index inside the material was estimated to be $2.5 \cdot 10^{-5}$ by measuring the transmitted and reflected intensity.

The estimation for the refractive index modulation assumes a phase grating, but there are also other kinds of gratings possible with no modulation in refractive index and poor transmission properties. A surface grating was foreclosed by taking microscope images from the front and back surface of the illuminated samples. No change of the surface was observed. Another kind of grating is an absorption grating. To rule out this type of grating we have removed any change in absorption by an annealing process at temperatures of 300°C. After the annealing process the grating was still observable which indicates a phase structure as origin of the observed diffraction effect.

CONCLUSION

We demonstrated the applicability of the grating inscription technique using a Talbot-interferometer for fabrication of VBGs inside the high refractive index glass S-TIH53. For inscription of first order gratings we used fs-pulses at a wavelength of 400 nm. The grating structure was investigated by using the external Bragg reflection method. With this technique a clear proof of a grating structure, a measurement of the local reflectivity profile and the estimation of the modulation of refractive index was possible. Further investigations foreclosed other kinds of material modifications than the preferred index change. Thus, a phase grating was successfully produced.

Funding by the Thuringian Ministry of Education, Science and Culture and FISBA OPTIK AG is gratefully acknowledged.

[1] G. Steckman, W. Liu, Chr. Moser, F. Havermeyer, J. Sel. Topics Quantum Electron. **13**, 672 (2007).

[2] K. Kawamura, M. Hirano, D. Takamizu, T. Kamiya, and H. Hosono, Appl. Phys. Lett. **84**, 311 (2004).

[3] K.-H. Liao, M.-Y. Cheng, V. I. Smirnov, L. Glebov, and A. Galvanauskas, Opt. Express **15**, 4876 (2007).

[4] P. A. Krug, R. Stolte, and R. Ulrich, Opt. Lett. **20**, 1767 (1995).

How to characterize comprehensively highly dispersive metamaterials with optical activity

M. Falkner[1,*], E. Pshenay-Severin[1], C. Helgert[1], C. Menzel[2], C. Rockstuhl[2], F. Lederer[2], and T. Pertsch[1]

[1]*Institute of Applied Physics and*
[2]*Institute of Condensed Matter Theory and Solid State Optics*
Abbe Center of Photonics, Friedrich-Schiller-Universität Jena,
Max Wien Platz 1, 07743 Jena, Germany

[*]Corresponding Author: *Matthias.Falkner@uni-jena.de*

Abstract

We introduce a novel experimental scheme to characterize the transmission characteristics of optical metamaterials in amplitude and phase. The approach reveals all properties of the respective Jones matrix entirely on experimental grounds and was verified to be highly accurate. The presented Jones matrix formalism lifts issues associated with the assignment of effective properties to heterogeneous metamaterials and provides a straightforward, yet accurate description. Thus it is not required to resort on numerical simulations to disclose properties of metamaterials, for which the geometrical details of the considered structures or their material properties are often known with insufficient precision. We show how to discuss the pertinent properties of optical metamaterials once the Jones matrix is determined, and exemplarily present measurements of giant optical activity in a chiral metamaterial. The proposed experimental scheme enables the complex far-field characterization of a very broad class of generally dispersive and/or optically active media.

INTRODUCTION

The extraordinary optical behavior of artificial metamaterials is governed by the resonant nature of their constitutive elements. Recent developments in nanostructure technology enabled the fabrication of metamaterials composed of complex three-dimensional nanostructures [1]. This significant progress requires revising standard theoretical and experimental approaches for the characterization of optical properties of metamaterials. This holds particularly in the visible spectral domain where the mesoscopic size of the constituting nanostructures is not much smaller than the wavelength of light and the occurring strong spatial dispersion results in contradictive predictions when using the standard effective material parameters [2].

EXPERIMENTAL METHOD

Here we advance the experimental characterization of the far-field properties of optical metamaterials on the basis of an adapted Jones matrix formalism [3] which can disclose the transmission of light trough any optically active metamaterial by

$$\begin{pmatrix} E_x' \\ E_y' \end{pmatrix} = \begin{pmatrix} T_{xx} & T_{xy} \\ T_{yx} & T_{yy} \end{pmatrix} \begin{pmatrix} E_x \\ E_y \end{pmatrix}. \quad (1)$$

Since the four coefficients T_{ij} of the Jones matrix are in general complex-valued, interferometric measurements are necessary for their full experimental acquisition. For this purpose we developed a modified Jamin-Lebedeff-interferometer based on white-light Fourier-transform spectral interferometry in frequency domain (Fig. 1) which facilitates measurements of complex transmission and reflection coefficients for wavelengths from 600 nm to 1700 nm [4].

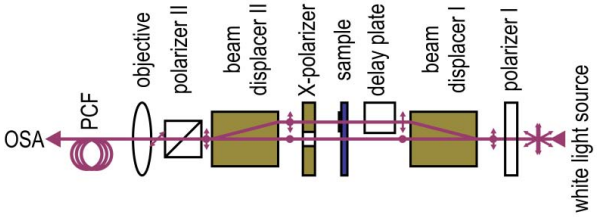

Figure 1: Sketch of the interferometric setup.

To measure the complex functions T_{ij}, a signal and a reference beam in the interferometer are cross-polarized, using birefringent crystals and polarization optics. The data acquisition comprises

two measurements for each orthogonal polarization of the illuminating wave $[(E_x, 0)$ and $(0, E_y)]$ with the X-polarizer rotated to +45° or -45° with respect to the optical axis and relative to the incident polarization on the investigated sample and a known reference sample (Fig. 1). From this data, we can unambiguously access the absolute phase delay of each single coefficient of the Jones matrix. The accuracy of the method with respect to the optical phase delay was verified to be 20 mrad.

EXPERIMENTAL RESULTS

To demonstrate the strength of the approach, the method was applied to a chiral metamaterial composed of so-called loop-wire nanostructures [1] shown in Fig. 2a. The excellent agreement between the measured and simulated amplitudes and phases of T_{ij} is demonstrated in Fig. 2b-e.

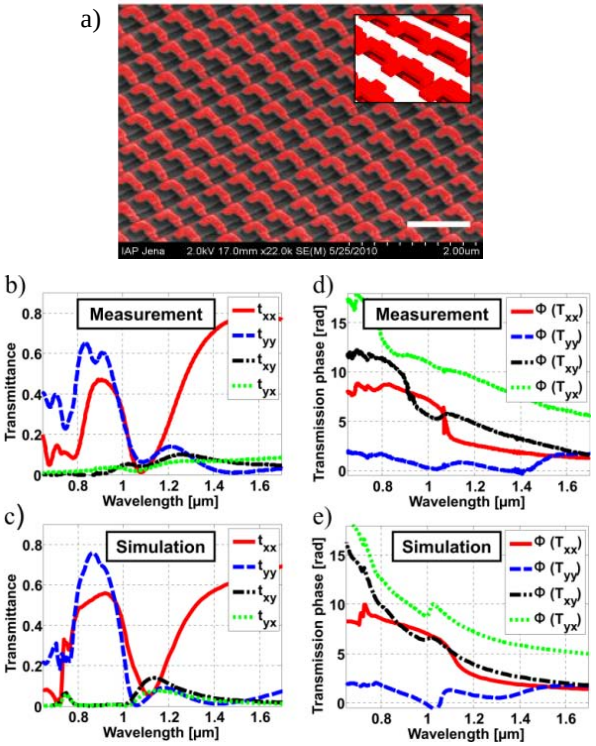

Figure 2: (a) False-colored, tilted view scanning electron microscopy image of the loop-wire metaatoms. The scale bar is 1 µm. The inset shows a corresponding sketch of the metaatoms without the supportive dielectric grating structure. (b) Measured and (c) simulated transmittances, (d) measured and (e) simulated transmission phase delays of the chiral nanostructured surface. The different colors indicate the four entries of the Jones matrix.

Thus, the developed experimental technique discloses for the first time the full complex transmission response for wavelengths from 600 nm to 1700 nm and allows for unambiguous quantification of, amongst others, circular dichroism, circular birefringence and polarization eigenstates of the chiral metamaterial across this broad spectral range. Specifically, the polarization output upon exciting the structure with an arbitrary input can be predicted immediately. It is shown that the fabricated loop-wire metamaterial exhibits giant optical activity for all wavelengths measured. Particularly, we found pure circular birefringence, i.e. a rotation of the polarization azimuth of linearly polarized light exceeding 50° at a wavelength around 1,08 µm. Normalized to the thickness of the metamaterial, this corresponds to a specific rotation of 3,3 • 10^5 °/mm which is, to the best of our knowledge, larger than that of any linear, passive and reciprocal medium reported to date.

CONCLUSION

In summary, we will present a novel interferometric scheme which allows for the direct measurement of the complex Jones matrix in the visible and near-infrared spectral domain, applicable not only to optical metamaterials, but rather to a very general class of dispersive media. The performance of the setup was demonstrated at a chiral metamaterial and reveals its giant optical activity.

[1] C. Helgert, E. Pshenay-Severin, M. Falkner, C. Menzel, C. Rockstuhl, E.-B. Kley, A. Tünnermann, F. Lederer, and T. Pertsch, Nano Letters **11**, 4400-4 (2011).

[2] C. R. Simovski, Optics and Spectroscopy **107**, 726-753 (2009).

[3] C. Menzel, C. Rockstuhl, and F. Lederer, Physical Review A **82**, 1-9 (2010).

[4] E. Pshenay-Severin, F. Setzpfandt, C. Helgert, U. Hübner, C. Menzel, A. Chipouline, C. Rockstuhl, A. Tünnermann, F. Lederer, and T. Pertsch, Journal of the Optical Society of America B **27**, 660 (2010).

Plasmonic Moiré Magnifier

Stefan Fasold*[1], Thomas Paul[2], Thomas Pertsch[1]

[1] *Institute for Applied Physics, Abbe Center of Photonics, Friedrich-Schiller-Universität, 07745 Jena*

[2] *Institute of Condensed Matter Theory and Solid State Optics, Abbe Center of Photonics, Friedrich-Schiller-Universität, 07745 Jena*

*Corresponding Author: *stefan.fasold@uni-jena.de*

Abstract

Moiré pattern are well known to be observable, e.g. in digital imaging, whenever two periodic structures do overlap each other. We will use this effect to magnify subwavelength plasmonic structures and to make them visible in the optical domain.

Introduction

Lord Rayleigh was the first person who described the Moiré pattern in 1874 [1] since this time a lot of groups exploited this topic. Especially in the 1960's and 1970's a lot of papers appeared ([1], [2]) and in the last years it was tried to use this approach to look at subwavelength structures ([3], [4]).
In contrast to other imaging techniques like scanning near field microscopy, the application of Moiré patterns promises to process an entire sample in a single operation. No scanning is needed at all. Additionally the resolution of the Moiré pattern only depends on the accuracy of the production and is not limited by physical laws.
However, the Moiré effect can only be exploited for periodically arranged structures, and the application to a single object is not possible.

Principles of Moiré Magnification

Moiré Effect. The Moiré effect is a special manifestation of the Alias effect and it appears whenever two periodic structures do overlap with each other. The first structure is usually referred to be the "sample" and the second one is called the "view grid".

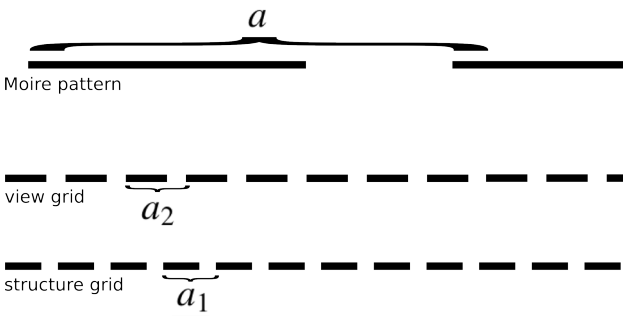

Figure 1: simplified picture of the Moiré effect; the system is illuminated from below and the Moiré pattern can be measured in the far field

Consider for example two one-dimensional transmission gratings with periods a_1 and a_2. When, in a simple picture, light consecutively propagates through both of these elements, then the transmitted light distribution will exhibit periodic features with a periodicity of:

$$a = \frac{a_1 a_2}{|a_1 - a_2|}$$

Thus, the difference between the periods a_1 and a_2 determines the magnification of the optical signal.

Outlook Our aim is to map the nearfield of plasmonic objects with other plasmonic particles which complicates this easy picture from above because of interactions between the grids.
In [4] the effect was shown by using a grid of fluorescence nanoparticles as view grid to map an array of squared gold nanoparticles (figure 2).

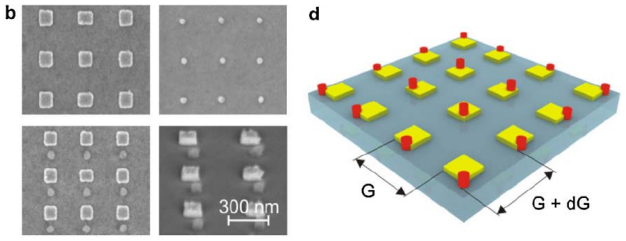

Figure 2: experimental setup with squared gold nanoparticles (yellow) and fluorescence nanoparticles (red) as view grid; the structure itself is the nearfield of the gold nanoparticles; on the left SEM pictures of the particles are shown [4]

With the help of the Moiré effect it was possible to map the nearfield of the gold nanoparticles with a feature size much smaller then the excitation wavelength around 700*nm* (figure 3).
Using nanoantennas instead of fluorescence particles should increase the signal strength and with the help of the Moiré magnifier it should be possible to map the near field of arbitrary nanoparticles and to investigate even macromolecules like DNA if they are arranged in a grid.

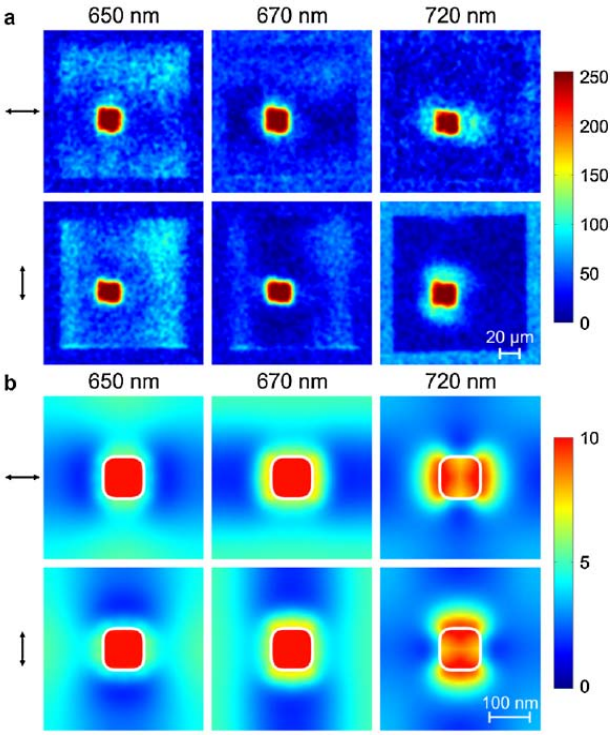

Figure 3: a) experimental realization of the Moiré effect, b) calculations for a single particle for different excitation wavelength and polarization directions of the excitation [4]

[1] G. Oster, M. Wasserman, C. Zwerling, *Journal of the optical society of america* **54** (1964).

[2] R. McCurry, *Journal of Applied Physics* **37** (1966).

[3] Z. Liu, S. Durant, H. Lee, *OPTICS LETTERS* **32** (2007).

[4] D. Koller, U. Hohenester, A. Hohenau, *PRL* **104** (2010).

Controlling Light-Matter-Interactions using Nanoantennas

Robert Filter[*1]

[1]*Institute of Condensed Matter Theory and Solid State Optics, Abbe Center of Photonics, Friedrich-Schiller-Universität Jena, Max-Wien-Platz 1, D-07743, Germany*

[*]Corresponding Author: *robert.filter@uni-jena.de*

Abstract

The possibility to design optical near-fields using nanoantennas lead to incredible new possibilities to control light-matter-interactions. In this contribution, two applications will be reviewed: The possibility to excite dipole-forbidden transitions in quantum systems and the use of graphene nanoantennas to selectively and tunably enhance molecular emissions. Both approaches have direct implications for molecular spectroscopy.

INTRODUCTION

Ever since Hertz described in 1887 the emission of electromagnetic radiation from dipole antennas, a pertinent question has been to fabricate them such that they may interact with light at optical frequencies, a spectral domain of paramount importance for many applications. To achieve this goal, antennas have to be downscaled in their critical dimensions to a few hundreds of nanometers to match the wavelength of the visible. More than a century later, this spectral domain has been reached due to recent advances in nanofabrication and characterization techniques [1]. Later on, experiments have demonstrated the outstanding abilities of such nanoantennas including the directive emission of quantum systems or the modification of radiative rates at which such systems emit light [2,3]. So, the advance of nanotechnology has drastically changed our understanding of matter. Concepts that seemed to be carved in stone are challenged and new insight is paving the way for once inconceivable applications.

In this contribution, two concepts shall be introduced exploiting the unique possibilities to control light-matter-interactions using nanoantennas. First, the possibility to excite dipole-forbidden transitions will be reviewed. Implications for secondary processes important for spectroscopic measurements will be discussed. Thereafter, the exceptional characteristics of graphene will be shown to enable the selective and tunable enhancement of molecular emissions.

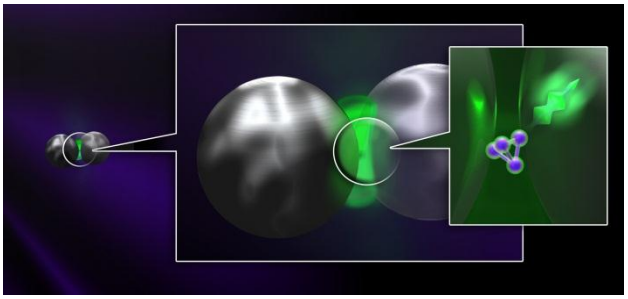

Figure 1: Left: a plane wave (purple) scatters two close silver nanospheres. Middle: molecules in-between undergo a dipole-forbidden excitation resulting in a luminescence signal at a lower wavelength (green). Right: excitation and emission of a single molecule.

EXCITATION OF DIPOLE-FORBIDDEN TRANSITIONS USING NANOANTENNAS

Usually visible light cannot induce dipole-forbidden transitions in quantum systems. The reason is that it is effectively a dipolar field on molecular scales and all higher order contributions are much weaker. In the presence of nanoantennas, this scenario changes dramatically - higher order multipole contributions of the fields can be enhanced by several orders of magnitude compared to free space. This leads to a huge increase of rates for dipole-forbidden transition rates, see [4].

This effect strongly influeces the interaction of the quantum system to the excitation field. In addition, the presence of the nanoantenna also hugely effect secondary processes like subsequent relaxations, see

Fig. 1. The reason is the so-called Purcell effect: in an inhomogeneous environment, the emission rate of a quantum system changes. This radiative enhancement is proportional to the mode volume and the quality factor of a resonator. Plasmonic systems allow extremely small mode volumes. So, in their vicinity, enhancements of molecular relaxations can be several orders of magnitude compared to free space.

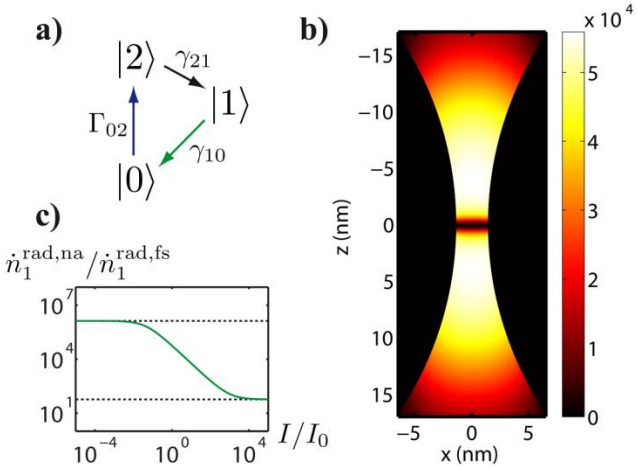

Figure 2. a) Scheme of the quantum mechanical system that is placed in the vicinity of the nanoantenna. b) Local enhancement of the luminescence, i.e. $\dot{n}_1^{rad,na}/\dot{n}_1^{rad,fs}$, in the x-z-plane. Because of saturation, the enhancement is not as strong as expected from the quadrupole enhancement alone. c) Luminescence enhancement as a function of the intensity at x = 0 nm, z = 4 nm.

Overall, the luminescence of the system depends strongly on the position of the quantum system and the geometry of the nanoantenna itself. Regarding a three-level system, such an excitation-relaxation process reveals that the luminescence enhancement in the vicinity of a certain nanoantenna with respect to free space strongly depends on the intrinsic properties of the quantum system and the intensity of the excitation field. It can be calculated from limiting cases that only for small intensities the quadrupole enhancement effectively results in a strong luminescence enhancement, see Fig. 2. Hence the nanoantenna influences the entire dynamics of the quantum system. Understanding this process is of vital importance for spectroscopic measurements.

TUNABLE GRAPHENE ANTENNAS FOR SELECTIVE EMISSION ENHANCEMENTS

Graphene is a perfect material to taylor light-matter-interactions. This material provides an incredibly high conductivity for wavelengths down to approximately ten microns. Since graphene is only a one-atom thick layer, the supported symmetric surface plasmon polaritons have extremely small wavelengths compared to their free-space pendants. This leads to subwavelength resonant structures and implies possible enhancements of molecular transitions of seven order of magnitude or more [5]. These numbers would be directly sufficient to justify applications of graphene antennas for sensing devices. But this is still not the end of the story. Because of the so-called electric field effect, the conductivity of graphene can be tuned to a certain extent. This property enables a tunable enhancement of molecular transitions. Furthermore, a careful choice of antenna geometry can be used to restrict the radiative enhancement of a molecule to a single wavelength. Then, spectrally weak features can be made the dominant contribution providing extremely useful new possibilities in molecular spectroscopy, see [6].

In conclusion new paths were outlined to use nanoantennas to taylor light-matter-interactions enabling amazing new applications.

[1] P. Mühlschlegel, et al., Science **308**, 1607 (2005), passage after R. Filter, et al., Physical Review B **85**, 125429 (2012).

[2] A. G. Curto et al., Science **20**, 930 (2010).

[3] P. Anger, et al., Physical Review Letters **96**, 113002 (2006).

[4] R. Filter, et al., submitted, preprint available at arxiv.org/abs/1110.3927.

[5] F. H. L Koppens, et al., Nano Letters **11**, 3380 (2011).

[6] R. Filter, et al., in preparation.

Selective excitation of higher-order modes in optical fibers using a spatial light modulator

Daniel Flamm, Christian Schulze, and Michael Duparré

Institute of Applied Optics, Fröbelstieg 1, 07745 Jena, Germany

*Corresponding Author: *daniel.flamm@uni-jena.de*

Abstract

A procedure for the selective excitation of several higher-order modes in optical fibers is presented. By using a spatial light modulator (SLM), the complex field of the respective mode is shaped and properly imaged onto the facet of the fiber. The SLM's ability to rapidly refresh the encoded transmission function enables to excite different modes and their superpositions in real-time. The working principle is tested using a conventional step-index large mode area (LMA) fiber and recording the output near-field intensity.

Introduction

The possibility to stable excite higher order modes in optical fibers may result in both novel and useful fields of application, like e.g. optical transmission using supermodes [1], or on the other hand in the unintended degradation of the beam quality of the emerging laser light, see e.g. mode instabilities in high-power fiber lasers [2].
The presented procedure enables to selectively excite higher order modes and their phase dependent superposition in multi mode fibers. Hence, laser beam shaping at the fiber output becomes possible in a controlled manner. The specific mode excitation in combination with the analysis of their propagation behavior in amplitude and phase, represents a measuring instrument to characterize in detail the multi-mode fiber under test which is intended to be used for both single-mode or multi-mode operation.

Shaping complex mode fields

Based on the knowledge about the spatial field distribution of the set of modes guided in the fiber under test $\{\psi_l(\mathbf{r})\}$, we generate the respective modal fields by employing digital holograms on a liquid-crystal-on-silicon-based SLM. The task is to encode the complex valued transmission function of the respective lth order mode field distribution $T(\mathbf{r}) = \psi_l(\mathbf{r}) = A(\mathbf{r})\exp[\mathrm{i}\Phi(\mathbf{r})]$ into a phase hologram $H(\mathbf{r}) = \exp[\mathrm{i}\Psi(A,\Phi)]$ with given unit amplitude transmittance and certain phase modulation $\Psi(A,\Phi)$. The phase modulation $\Psi(\mathbf{r})$ provides the same information as the original transmission function $T(\mathbf{r})$ in a certain diffraction order. In this work, we use the coding technique proposed by V. Arrizón *et al.* [3]. To image the generated optical field with required scale parameters in the input plane of the fiber a $4f$-setup is necessary. This ensures the coupling of the intended optical field without a curved phase distribution due to the free space propagation.

Setup

The experimental setup is depicted in Figure 1 and consists mainly of two $4f$-arrangements. After the SLM is illuminated with a linearly polarized plane wave at 1064 nm the first $4f$-lens combination images the shaped beam in the plane of the input fiber facet. The scaling parameters of the encoded LP modes as well as the focal lengths of the Fourier lens and the microscope objective are chosen to fit the core size of a step-index LMA fiber ($V = 7$). The length of the fiber under test, being carefully placed into the setup to avoid stress or external distortions, is only ≈ 4 cm. The second $4f$-lens combination images the magnified near-field intensity of the fiber end facet in the plane of the CCD camera.

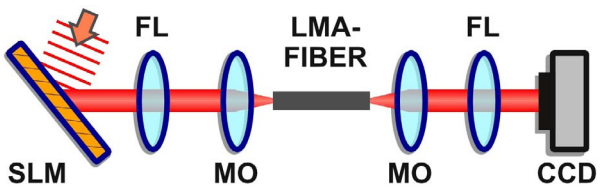

Figure 1: Experimental Setup. SLM, spatial light modulator; FL, Fourier lens; MO, microscope objective.

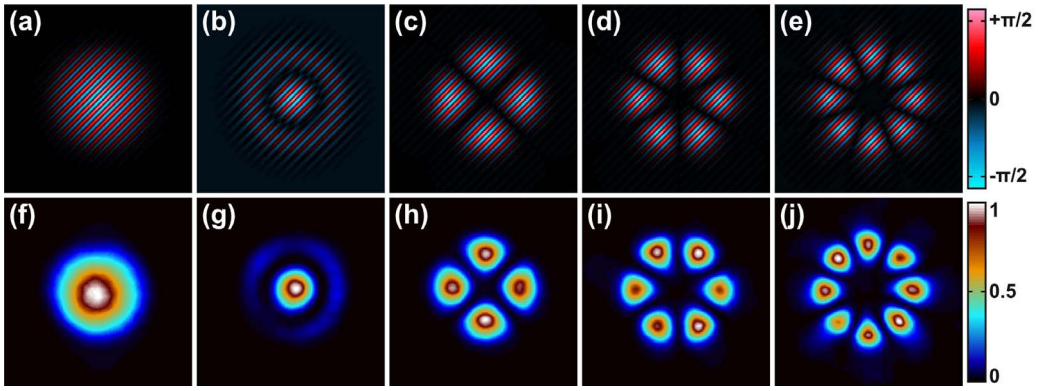

Figure 2: (a)-(e) Phase modulations $\Psi(\mathbf{r})$ for the generation of the modes LP_{01}, LP_{02}, LP_{21e}, LP_{31e}, and LP_{41e} with the SLM in the first order of diffraction. (f)-(j) Corresponding near-field intensities measured in the plane of CCD.

The SLM used in our setup is the Hamamatsu LCoS X10468-03 with 800×600 pixels of pitch $20\,\mu m$ and calibrated for a 2π phase shift at 1064 nm.

Measurement results

In Figure 2 (a)-(e), the phase modulations $\Psi(\mathbf{r})$ are depicted to generate the optical fields of modes LP_{01}, LP_{02}, LP_{21e}, LP_{31e}, and LP_{41e} with the SLM in the first order of diffraction. The quality of the diffracted beams using the coding technique of V. Arrizón *et al.* [3] is excellent (not shown here) and has already been investigated regarding mode purities by T. Ando *et al.* [4]. The diffraction efficiency of the procedure is only in the range of some percent. The corresponding measured near-field intensity distributions of the fiber are plotted in Figure 2 (f)-(j). By evaluating the zero intensity node lines of the measured intensity distributions, these high-quality results can be assigned to the modes being intended for excitation. Though the measured intensities seem to agree accurately with the corresponding LP modes, a detailed classification can only be achieved by employing a technique for modal decomposition [5, 6]. The SLM's ability to refresh its phase modulation enables to switch the modes being guided in the waveguide with up to 60 Hz.

Outlook

We presented an easy procedure to selectively excite higher-order modes and their phase dependent superpositions in optical fibers. Depending on the SLM's refresh rate a fast switch of the modal power content becomes possible. The required equipment mainly consists of the digital hologram and an adapted imaging system. The combination of the procedure with a mode analysing technique enables to determine the modal transfer function of the fiber. The procedure can be applied to arbitrary waveguides with an accessible set of eigenmodes.

[1] C. Xia, N. Bai, I. Ozdur, X. Zhou, G. Li, *Opt. Express* **19**, 16653 (2011).

[2] F. Stutzki, *et al.*, *Opt. Lett.* **36**, 4572 (2011).

[3] V. Arrizón, U. Ruiz, R. Carrada, L. A. González, *J. Opt. Soc. Am. A* **24**, 3500 (2007).

[4] T. Ando, Y. Ohtake, N. Matsumoto, T. Inoue, N. Fukuchi, *Opt. Lett.* **34**, 34 (2009).

[5] T. Kaiser, D. Flamm, S. Schröter, M. Duparré, *Opt. Express* **17**, 9347 (2009).

[6] D. Flamm, D. Naidoo, C. Schulze, A. Forbes, M. Duparré, *Opt. Lett.* **doc. ID 164710** (posted 1 May 2012, in press).

Optical Coherence Tomography using broad-bandwidth XUV and soft x-ray radiation

Silvio Fuchs[*1,2], Alexander Blinne[1], Christian Rödel[1,2], Ulf Zastrau[1], Vinzenz Hilbert[1], Martin Wünsche[1], Jana Bierbach[1], Eckhart Förster[1,2], and Gerhard Paulus [1,2]

[1] *Institute of Optics and Quantum Electronics, Friedrich-Schiller University of Jena, Max-Wien-Platz 1, 07743 Jena, Germany*

[2] *Helmholtz Institute Jena, Helmholtzweg 4, 07743 Jena, Germany*

[*] Corresponding Author: *silvio.fuchs@uni-jena.de*

Abstract

We present a novel approach to extend optical coherence tomography (OCT) to the extreme ultraviolet (XUV) and soft X-ray (SXR) spectral range. As a consequence, the theoretical resolution limit of XUV coherence tomography (XCT) is in the order of nanometers. We performed an experiment at synchrotron sources and found the expected properties concerning resolution and penetration depth confirmed.

Introduction

Optical coherence tomography (OCT) is a well-established method to retrieve three-dimensional, cross-sectional images of biological samples in a non-invasive way using near-infrared radiation. The axial resolution of OCT is in the order of the coherence length $l_c \propto \lambda_0^2/\Delta\lambda_{\mathrm{FWHM}}$ which depends on the central wavelength λ_0 and the spectral width (FWHM) $\Delta\lambda_{\mathrm{FWHM}}$ of a light source. As a consequence, the axial resolution only depends on the spectrum rather than the geometrical properties of the radiation. OCT with broadband visible and near-infrared sources typically reaches axial (depth) resolutions in the order of a few micrometers [1]. Within the last decade and in conjunction with the quickly developing sector of advanced material design, the scale length of interest has dropped from micrometers to a few nanometers. The method presented here takes advantage of the fact that the coherence length can be significantly reduced if broadband XUV and SXR radiation is used. Microscopy using XUV and SXR radiation has regularly ineluctable practical restrictions imposed by the optics and sources available in this regime. Coherence tomography with short wavelength has the potential to circumvent some of these limitations. A major limitation of XUV radiation is the absorption within a few tens or hundreds of nanometers depending on the actual composition of the material and the wavelength range. Consequently, XUV coherence tomography (XCT) can only display its full capabilities when used in the transmission windows of the sample materials. For instance, the silicon transmission window (30-99 eV) corresponds to a coherence length of about 12 nm assuming a rectangular spectrum and an absorption length of about 200 nm, thus suggesting applications for semiconductor inspection. In the water window at 280-530 eV as defined by the K absorption edges of carbon and oxygen, respectively, a coherence length as short as 3 nm can be achieved and highlights possible applications of XCT for life sciences.

Setup

Typically, a OCT device in the near-infrared spectral range consists of a Michelson-type interferometer in which one mirror is the sample [2]. The image can be captured by measuring the spectral intensity of each component of the broad bandwidth light source (Fourier-domain OCT) or by scanning the reference arm length of the interferometer (time-domain OCT). We used a variant of Fourier-domain OCT setup that completely avoids a beamsplitter [3, 4], see Fig. 1. For the present proof-of-principle experimental setup broadband synchrotron light was focused on the surface of the sample. The samples are one-dimensional structured layer systems consisting of materials with sufficient absorption lengths in the spectral ranges used, e.g., silicon or boron carbide. The reflected intensity is measured either with a grating spectrometer, consisting of a gold transmissinon grating and a toroidal mirror (spectrometer-based OCT), or with a

photo diode (swept-source OCT). The top layer reflection assumes the role of a reference beam. Merely a Fourier transform of the reflected spectrum needs to be computed for retrieving the structural information. A 3D image can be captured by scanning the focus point over the sample.

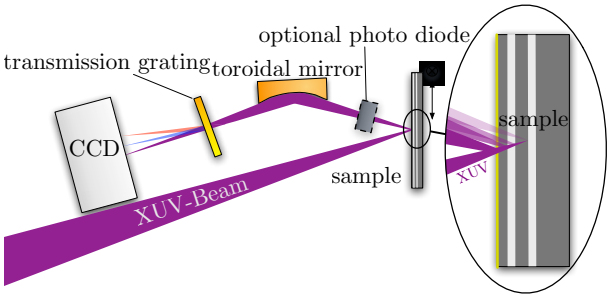

Figure 1: Proposed common-path Fourier-domain OCT setup in the XUV spectral range.

Measurement

Different samples were investigated at the synchrotron facilities DESY (Deutsches Elektronen-Synchrotron, Hamburg) and BESSY (Berliner Elektronenspeicherring-Gesellschaft für Synchrotronstrahlung) in the water and silicon transmission window. Both swept-source OCT with a photo diode and spectrometer-based OCT with the grating spectrometer were performed. We found the expected values in resolution and penetration depth confirmed.

In Fig. 2 the XCT-signal of two 5-nm gold layers separated by a silicon layer, buried under 120 nm silicon and a gold top layer is shown. The spectrum was recorded with a grating spectrometer. It can be seen that the peak width is about 15 nm, which corresponds to the coherence length of broadband radiation in the silicon transmission window. The two peaks at 120 nm and 140 nm are the two buried gold layers and they appear clearly seperated from each other.

Conclusion

We report on the extension of Optical Coherence Tomography using extreme ultraviolet and soft x-ray radiation and demonstrate an axial resolution of nanometers. The experimental results strongly suggests its application as a new non-invasive tomographic method to investigate nanometer-scale structures of layered systems and simple three-dimensional samples by lateral raster scanning.

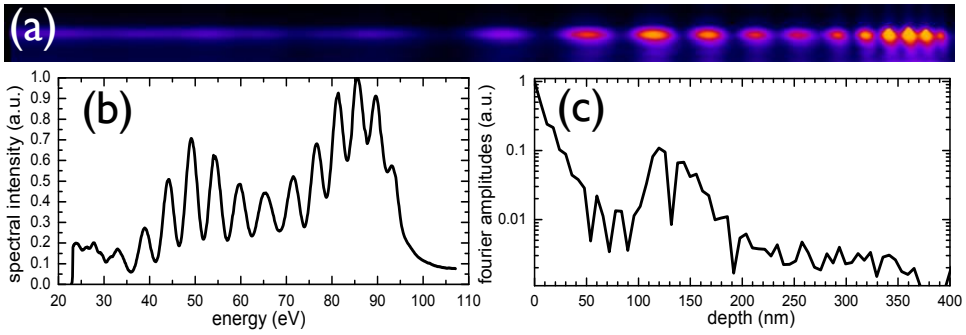

Figure 2: XCT signal of two 5-nm gold layers separated by a silicon layer, buried under 120 nm silicon and a gold top layer. (a) CCD image of the grating spectrometer, (b) lineout from (a) and rescaled to energy units, (c) fourier transform of (b) shows depth structure of the sample

[1] D.Huang et al., *Science* **254**, 1178-1181 (1991).

[2] W. Drexler and J. G. Fujimoto, *Optical Coherence Tomography* (Springer Verlag, Berlin, 2008).

[3] S. Fuchs et al., *Appl. Phys. B* **106**, 789-795 (2012).

[4] G. G. Paulus and C. Rödel, *Short-wavelength coherence tomography* (US Patent 20080212075)

Lithium Niobate Nanowaveguides fabricated by Ion-BeamEnhanced Etching

Reinhard Geiss*, Holger Hartung, Frank Schrempel, Ernst-Bernhard Kley, Thomas Pertsch, Andreas Tünnermann

Institute of Applied Physics, Abbe Center of Photonics,
Friedrich-Schiller-Universität Jena, Max-Wien-Platz 1, 07743, Jena, Germany
**Corresponding Author: geiss@iap.uni-jena.de*

Abstract

$LiNbO_3$ nanoscale waveguides allow for highly efficient frequency conversion mediated by strong spatial confinement of waveguide modes. Their fabrication is facilitated through ion-beam enhanced etching. The required mask is patterned by electron-beam lithography. Subsequent wet etching results in a grid of freestanding nanowires that are further manipulated for optical testing.

Nanoscale waveguides fabricated in media with strong quadratic nonlinearity such as lithium niobate ($LiNbO_3$) allow for highly efficient frequency conversion and harmonic generation. The strong spatial confinement of the waveguide mode significantly enhances the nonlinear interactions. At the same time, phase matching of the nonlinear processes can be precisely adjusted by dispersion engineering, i.e. modification of the waveguide geometry.[1] Such $LiNbO_3$ nanowires used as nanoscale second harmonic (SH) light sources have great potential as luminescent markers for imaging applications in life science.[2]

The fabrication of the nanowires was facilitated through ion-beam enhanced etching of $LiNbO_3$, which is a technique originally developed for the fabrication of freestanding photonic crystal membrane structures.[3] In a first step the mask for ion beam irradiation is patterned into layers of chromium and fused silica by means of electron beam lithography, RIE and ICP-RIE dry etching. The mask layout contains a large number of homogenous grating structures, where the individual grating ridges represent the final nanowires. The irradiation with argon ions is carried out in a series with different energies and fluencies to homogeneously damage the crystal in the unmasked regions from the sample surface down to the desired depth. After removal of the masking layer the sample is irradiated with helium ions forming a buried damaged layer at a depth of about 500 nm. Now, the sample is etched in diluted hydrofluoric acid. Since the etch rates of ion-beam irradiated and bulk $LiNbO_3$ differ significantly, the damaged crystal is removed, resulting in freestanding grids of nanowires (Fig.1).

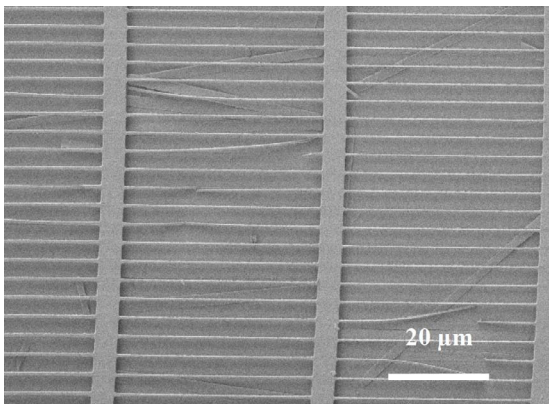

Figure 1: Grid of lithium niobate nanoscale waveguides. The grating structure was fabricated by means of ion-beam enhanced etching.

The nanowires typically have cross section areas of 300 nm by 500 nm at a length of 50 µm. The smallest wire has an equivalent diameter of about 180 nm at a length of 5 µm (Fig.2).

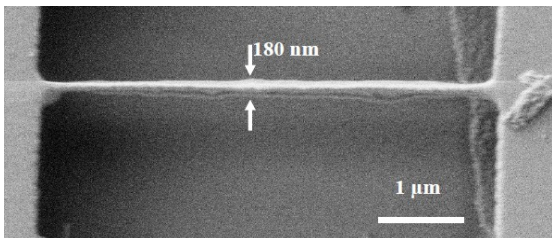

Figure 2: Lithium niobate nanoscale waveguide with an equivalent diameter of 180 nm and a length of 5 µm.

Compared to chemically synthesized nanowires2 the fabrication here is completely deterministic with just minor deviations in shape throughout the respective batch. To make the nanowires accessible for optical testing on a neutral substrate the sample

is first sonicated in Ethanol. A droplet of this nanowire solution is then brought onto an ITO coated silica wafer where processing and manipulation was continued using FIB milling in combination with a micro manipulator needle (Fig.3).

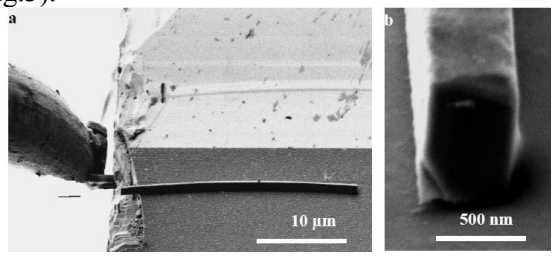

Figure 3: a) FIB micro manipulator needle placing a lithium niobate nanoscale waveguide on a fused silica substrate for optical testing. b) Cross section of the nanowaveguide: 500 nm by 600 nm

.

Samples thus prepared are illuminated with a laser at 1.55 µm resulting in generation and waveguiding of the SH. Those results give a first proof of the nanowires' capabilities as SH light sources. They give access to the investigation of the physics of nonlinear effects in nanoscale waveguides.

---

[1] A.S. Solntsev et al., Applied Physics Letters, 98, 231110 (2011)

[2] C. Hsieh et al., Optics Express, 17, 2880 (2009)

[3] H. Hartung et al., Optical Materials, 33, 19 (2010)

Basic structures of integrated photonic circuits for smart biosensor applications

S. Germer[*1], L. Rebohle[1], W. Skorupa[1] and M. Helm[1]

[1]*Institute of Ion-Beam Physics and Materials Research (FWI), Helmholtz-Center Dresden-Rossendorf (HZDR), Dresden, Germany*

[*]Corresponding Author: *s.germer@hzdr.de*

Abstract

Integrated optics concerns mainly the generation, guiding, and detection of light. Especially biosensing needs systems that incorporate electrical, electronic, and photonic devices for the detection of harmful substances, like synthetic oestrogens or plasticizers. We present here recent developments in the integration of our Si-based light emitter into a photonic circuit for a planar optical waveguide-based biodetection system.

INTRODUCTION

The growing demand for sensitive biochemical sensors in the environmental control, medicine or process technology results in the development of integrated sensors, which should show a high resolution over a wide concentration regime. They should be very fast, highly selective and sensitive as well small and cheap. In our first approach we deal with the integration of our Si-based light emitting device (LED), as light source, into a photonic circuit for detection of harmful biological substances, like synthetic estrogens or plasticizers in drinking water. Light injection into a waveguide is commonly obtained by using an external source coupled to the guide by systems, such as an optical fiber, a microscope objective, or a prism by total internal reflection. For simplifying this injection process, we built Si-based LEDs which have a metal-oxide-semiconductor (MOS) structure, in which the oxide film contains group-IV and rare earth elements, incorporated by ion-beam synthesis [1, 2].

EXPERIMENTAL

Our concept bases upon a Si-based photonic circuit which consists of the integrated LED, a newly fabricated dielectric strip-waveguide below a bioactive layer and a receiver. The Si-based LED exhibits strong electroluminescence, tunable from the visible up to the UV region depending on the rare-earth element (e.g. Gd, Tb, Eu, Nd, Er). For example, an Er implanted LED operates in the infrared range and a Tb doped one is suitable for the visible spectral region. The dielectric strip-waveguide has a Si_3N_4 or SiON core with cross sections between 50 and 1µm, in which the light should be guided, and a cladding of SiO_2. The receiver should be a photodiode (e.g. Ge, Si). Currently, the Si-based LEDs are already available and best efficiencies are achieved by Tb implantation with an external quantum efficiency of 16% and a corresponding power efficiency of 0.3%. LOCOS (local oxidation of silicon) processing and an additional layer of SiON were applied to the device in order to improve the electrical stability and operation time. In this work, we are concentrating on the development and characterization of the dielectric waveguides. For the theoretical analysis we are using a finite element simulation software (FlexPDE). The fabrication of the waveguides was done by plasma enhanced chemical vapor deposition (PECVD), photolithography and electron beam lithography. Manufactured waveguides were analyzed by scanning electron microscope (SEM). Furthermore, a new measurement setup is built up, which enables future transmission measurements and the inspection of the beam profiles as well as the damping factors of the structures in dependence on their cross sections.

RESULTS AND DISCUSSION

Obtained SEM results enabled an improvement of the fabrication recipe of the waveguides by using an additional Al-masking during the reactive ion etching (RIE), which protects against undercutting and allows better definite waveguide structures.

Moreover, it was found out, that the choice of too high plasma energy did destroy the smaller guides, while a low power did result in non-satisfying waveguide end faces. In preparation of the beam profiling, mode profiles as well as resonance frequencies were calculated according to the cross sections of the structures with the software FlexPDE. In the future, the theoretical calculations are going to be compared with the experimental results of the transmission and beam profiling measurements. Moreover, the Si-based LED should be coupled with the waveguide by e.g. Bragg grating.

CONCLUSION

Finally, this lab-on-a-chip system is showing a high potential to become an all-round applicable integrated sensor system, without using any external light sources, relay lenses, which is why it should be lightly portable and customizable.

[1] L. Rebohle, C. Cherkouk, S. Prucnal, M. Helm, W. Skorupa, Vacuum 83, 24 (2009)

[2] L. Rebohle, T. Gebel, R.A. Yankov, T. Trautmann, W. Skorupa, J. Sun, G. Gauglitz, R. Frank, Optical Materials 27, 1055 (2005)

Design of ultrafast fluorescence spectroscopy for axial resolution of fluorophore distribution with low numerical apertures for ophthalmologic application

Maximilian Gräfe*[1], Andreas Hoffmann[1] and Christian Spielmann[1,2]

[1] *Institut für Optik und Quantenelektronik, Friedrich-Schiller-Universität Jena, Max-Wien-Platz 1, 07743 Jena, Germany*

[2] *Helmholtz-Institut Jena, Fröbelstieg 3, 07743 Jena, Germany*

*Corresponding Author: *maximilian.graefe@uni-jena.de*

Abstract

A new method for resolving the fluorophore distribution along the propagation direction of a laser-beam is presented. For reaching spatial resolution of several tens of micrometers the time dependent fluorescence signal is sampled in the fs-regime by using a technique similar to fluorescence upconversion applying optical parametric amplification. Thus this approach is applicable to fluorescence spectroscopy in the human eye.

Introduction

Common techniques for scanning a tissue in X-, Y- and Z-direction like confocal or nonlinear microscopy typically make use of strong focusing due to high numerical apertures (NA).

However there are applications like *in vivo* investigations of the human retina where high NAs can not be used and high intensities like those for nonlinear processes have to be prevented. One example where such techniques are needed is the work of the group of Schweitzer [1] and Hammer [2] in the ophthalmologic clinic in Jena.

Thus a new method was developed for scanning the axial fluorophore distribution by a time resolved measurement.

Theoretical background

Fluorescence of molecules is composed of 3 steps: The absorption of typically UV or VIS photons, fast internal conversion and emission of photons in the VIS or IR with a fluorophore specific exponential decay [3]. Treating the excitation and emission process as a three-level system one can derive the photon flux as given in Eq. (1) [4].

$$\Phi_F(t) \sim \left[1 - \exp\left(-\left(\frac{1}{\tau_{IC}} - \frac{1}{\tau_F}\right)t\right)\right] \cdot \exp\left(-\frac{t}{\tau_F}\right) \quad (1)$$

In this equation τ_{IC} is the time constant of internal conversion and τ_F the fluorescence lifetime. This is the flux of just one fluorescing point. Additionally the influence of the spatial extension of a volume probe has to be considered. This is shown in Fig. 1

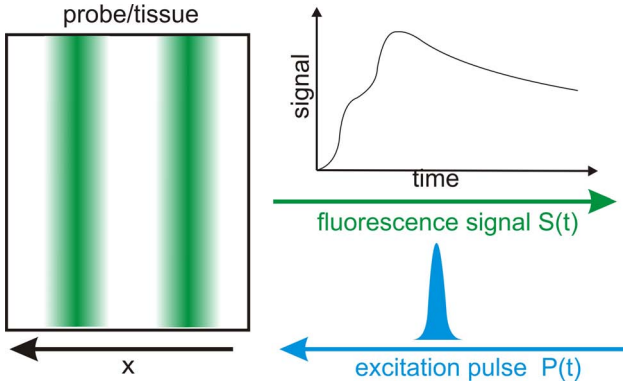

Figure 1: Illustration of origin of fluorescence signal of a volume probe

The excitation pulse $P(t)$ propagates through the tissue, excites time dependent the axial fluorophore distribution $\rho_{fl}(x)$ which emits the photons described in Eq. (1). The result is the convolution of those functions:

$$\mathscr{F}((S(t)) = \mathscr{F}(\Phi_F(t)) \times \mathscr{F}(\rho_{fl}(z)) \times \mathscr{F}(P(t)) \quad (2)$$

The characteristic information to be measured is the stepped slope in Fig. 1. In theory the deconvoluted distribution is limited by the pulse duration and can be distorted by the influence of the constant τ_{IC}.

Experimental Setup

The experimental setup is shown in Fig 2. Pulses at the central wavelength of 800nm, pulse energy of 0.9mJ, pulse duration of 75fs (FWHM) and a repetition rate of 1kHz from the output of a CPA-System (Spectra Physics Spitfire®) are frequency doubled through a BBO and split into two beams.

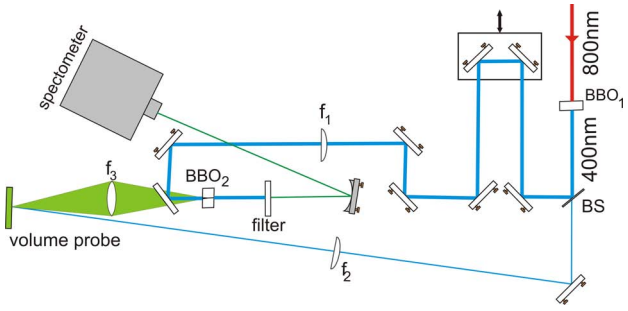

Figure 2: Experimental setup to sample the signal of the fluorescing volume probe in the femtosecond regime

One part, acting as gate pulse, is guided through a delay stage and is then focused using f_1 to get a 0.5mm beam diameter in BBO_2 to prevent damaging and to get a large enough interaction cross section. The second one is focused by f_2 into the sample and excites the fluorophores. The fluorescence is collected and focussed by f_3 into BBO_2 too. Due to incoherence the accessible focal spot of fluorescence is much larger than the diffraction limit of Gaussian beams.

For gating the fluorescence optical parametric amplification is used. This principle of amplifying fluorescence ultrasensitive by OPA already was demonstrated in [5, 6] (gain up to 10^6) and delivers in comparison to the more common used sum frequency generation [7] a high signal gain.

Using one pulse as gate induces for the instrument response function another convolution [4].

Conclusion

A method is presented which allows it to measure an axial distribution of fluorophores in a sample. Additional this has in comparison to the common fluorescence upconversion (with sum frequency generation) a much higher gain since for sum frequency generation every fluorescence photon can create only one SFG-photon but for OPA it is just an initiator for the amplification process.

Furthermore this technique does not need any strong focussing and can be driven with linear excitation and that way with low intensities.

Outlook

The overall aim of this technique is to apply it to the human eye and resolve the fluorophores in the retina in a scale of 10μm. Therefore further investigations have to be carried out with a temporal resolution of 30fs. Also the questions of dispersion compensation for the length of the human eye and whether this process can be driven with an intensity preventing damaging of the retina in combination with applicable exposure times for *in vivo* measurements have to be answered.

[1] D. Schweitzer et al., *Klinisches Monatsblatt Augenheilkunde* **222**, 396 (2005)

[2] Hammer et al., *Ophthalmologe* **101**, 1189 (2004)

[3] J. R. Lakowicz, *Principles of Fluorescence Spectroscopy* (Springer, New York, 2006).

[4] A. C. Bhasikuttan and T. Okada *J. Phys. Chem. B* **108** (34), 12629 (2004)

[5] Han et al. *J. Opt. Soc. Am. B* **24** (7), 1633 (2007)

[6] Chen et al. *J. Opt. Soc. Am. B* **26** (8), 1627 (2009)

[7] Zhao et al. *Phys. Chem. Chem. Phys.* **7**, 1716 (2005)

Applicability of input coupling taper transitions for supercontinuum generation in nanoscale all-normal dispersion optical fibers

Alexander Hartung*, Alexander Heidt, Hartmut Bartelt

Institute of Photonic Technology
Albert-Einstein-Straße 9, 07745, Germany

*Corresponding Author: *alexander.hartung@ipht-jena.de*

Abstract

Supercontinuum generation in nanoscale all-normal dispersion optical fibers requires special attention concerning the input coupling of light due to the small core size. Preceding taper transitions along which the fiber core gradually decreases from microscale to nanoscale dimensions facilitates the input coupling regarding efficiency and stability. The influence of these taper transitions on the subsequent supercontinuum generation in the nanoscale optical fiber is discussed in detail and appropriate taper shapes with minimized influence are proposed.

INTRODUCTION

Supercontinuum generation is the generation of light with a very broad spectral bandwidth. The spectral broadening is governed by a multitude of participating nonlinear effects which in total define the overall supercontinuum properties like spectral homogeneity or pulse-to-pulse stability. Supercontinuum generation in optical fibers instead of bulk media takes advantage of a very long interaction length, a small spot size and the adjustment of the chromatic dispersion by waveguide dispersion.

Typically, supercontinuum generation in optical fibers relies on anomalous dispersion and numerous nonlinear optical effects related to optical solitons. The most prominent effects are soliton self-steepening, soliton fission, and soliton self-frequency shift. Supercontinua generated by soliton-related effects can have a very broad spectral bandwidth exceeding an optical octave. Apart from this, soliton-related supercontinua suffer from a very low pulse-to-pulse correlation, large spectral intensity fluctuations and from the breakup of the injected pulse into multiple output pulses. Thus, they are not utilizable for more sophisticated applications.

Recently, a new method for the generation of high quality supercontinua was demonstrated based on optical fibers featuring only low normal dispersion values over an extended spectral range but no anomalous dispersion [1]. The utilization of these so called all-normal dispersion (ANDi) optical fibers prevents soliton-related nonlinear optical effects and accompanied drawbacks like the breakup of the input pulse into multiple output pulses or the high noise sensitivity. In the normal dispersion range only self-phase modulation and four-wave mixing contribute to the spectral broadening and lead to smooth spectra, single pulse conservation and high pulse-to-pulse correlation.

Pulse preserving supercontinuum generation initially was demonstrated employing photonic crystal fibers with a core diameter around 2 µm. Nanoscale suspended-core fibers and cylindrically symmetric nanofibers with a core diameter around 0.5 µm can provide ANDi behavior, as well.

The small core size of nanoscale fibers prevents the common input coupling scheme by a converging lens. Instead a special input coupling technique applying an optical fiber taper, a fiber sections with decreasing diameter, is required to achieve reasonable efficiency and reliability. These fiber tapers have to meet certain requirements concerning energy conservation and nonlinear pulse propagation which set opposed demands concerning the length of the fiber taper. We investigate various shapes of fiber tapers and discuss under which conditions they meet the aforementioned requirements and therefore are suitable for input coupling purposes concerning supercontinuum generation in nanoscale ANDi optical fibers.

ADIABATICITY OF OPTICAL FIBER TAPERS

Energy conservation of light propagating along a fiber taper is governed by the adiabaticity criterion

$$\Omega \leq (\beta_1 - \beta_2) r / 2\pi. \quad (1)$$

It determines an upper limit of the local taper angle Ω as a function of the local taper radius *r* and the local propagation constants β_1 and β_2 of the involved fiber modes. Thereby β_1 is the propagation constant of the fundamental mode whose energy is to be conserved and β_2 the propagation constant of the next higher order mode.

Figure 1 shows two selected taper shapes derived from (1) for a step index fiber from initial 125 µm in diameter down to an ANDi fiber diameter of 0.45 µm. The adiabatic taper shape is the overall shortest one satisfying (1) but its preparation is quite challenging. The exponential taper shape is significantly longer than the adiabatic one but can be prepared with reasonable effort. Both taper shapes meet the requirement concerning energy conservation. Likewise taper shapes for suspended-core optical fibers can be established. The remaining question is if the considered taper shapes satisfy the requirements concerning nonlinear pulse propagation as well.

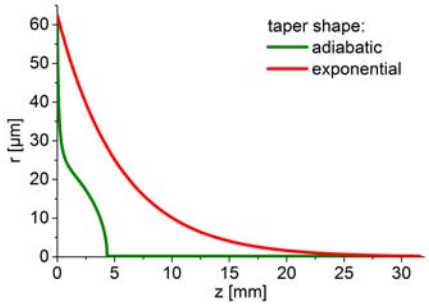

Figure 1: Variation of radius *r* along axial direction *z* for two fiber tapers of a step index fiber satisfying the requirements concerning energy conservation.

NONLINEAR PULSE PROPAGATION IN OPTICAL FIBER TAPERS

Using fiber tapers for input coupling purposes includes the risk for early nonlinear effects within the fiber taper at undesired core diameter and hence undesired dispersion behavior. For an optimal exploitation of the properties of the nanoscale fiber with its enhanced nonlinearity and special ANDi behavior the fiber taper should be as short as possible to prevent any nonlinear effects within. As opposed to this, a minimum taper length is required for energy conservation reasons to satisfy the adiabaticity criterion (1).

Figure 2 shows the spectral evolution of an ultrashort high intensity pulse along the two fiber tapers shown in figure 1 and along an additional nanoscale section of the fiber. The initial pulse parameters are 100 fs pulse duration and 25 kW peak power. The vertical white line indicates the end of the taper and the beginning of the nanoscale fiber.

Apparently, pulse propagation along the adiabatic taper (Fig. 2a) does not reveal any early spectral broadening and leads to a homogeneous and broadband supercontinuum within the nanoscale fiber. Pulse propagation along the exponential taper (Fig. 2b) is accompanied by spectral broadening resulting in a distorted supercontinuum with locally varying intensity distribution and narrowed bandwidth. Likewise pulse propagation in suspended-core fiber tapers is discussed.

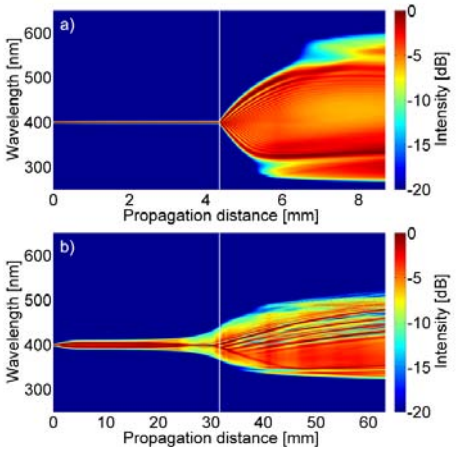

Figure 2: Spectral evolution along the fiber taper and the nanoscale fiber for a) the adiabatic taper shape and b) the exponential taper shape.

SUMMARY

We discussed the influence of fiber tapers for input coupling purposes on the supercontinuum generation in nanoscale ANDi optical fibers. Therefore different taper shapes satisfying energy conservation where investigated regarding their influence on nonlinear pulse propagation. Appropriate taper shapes satisfying both requirements are proposed.

Funding by the Thuringian Ministry of Education, Science and Culture (EFRE program) is gratefully acknowledged.

[1] A. M. Heidt, A. Hartung, G. W. Bosman, P. Krok, E. G. Rohwer, H. Schwoerer, and H. Bartelt, "Coherent octave spanning near-infrared and visible supercontinuum generation in all-normal dispersion photonic crystal fibers," Optics Express **19**, 3775-3787 (2011).

Quadratic Frequency Conversion In Plasmonic Slot Waveguides

Shakeeb Bin Hasan*[1], Carsten Rockstuhl[1], Thomas Pertsch[2], Falk Lederer[1]

[1]*Institute for Condensed Matter Theory and Solid State Optics, Abbe Center of Photonics, Friedrich-Schiller-Universität Jena Max-Wien-Platz* 1, 07743, *Jena, Germany*

[2]*Institute of Applied Physics, Abbe Center of Photonics, Friedrich-Schiller-Universität Jena, Max-Wien-Platz* 1, 07743, *Jena, Germany*

*Corresponding Author: *shakeeb-bin.hasan@uni-jena.de*

Abstract

We present theoretical study on the quadratic nonlinear frequency conversion in plasmonic slot waveguides. By manipulating the geometrical cross-section of the dielectric core, it is shown that phase-matched frequency conversion can be achieved. This is exploited toward quantifying the parametric amplification of modes taking into account realistic material parameters.

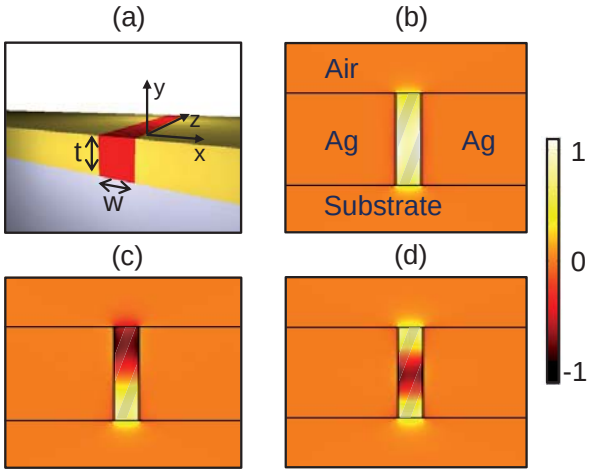

Figure 1: (a) Schematic illustration of the metallic slot waveguides. (b-d) Modal distribution of the x-component of Electric field according to the coordinate frame shown in (a) for mode order M= $0,1,2$ respectively [2].

Introduction

Subwavelength confinement afforded by plasmonic waveguides has long held the promise of enhancing nonlinear interactions at moderate power levels. Most of the studies in past have been dedicated to plasmonic waveguides guiding light in only one transverse dimension perpendicular to the propagation direction. They include the simplest as well as hybrid metal-insulator-metal (MIM) slot waveguides for demonstrating nonlinear effects such as phase-matched second harmonic generation [1] and plasmon solitons in a cubic medium [4]. In this study, we stretch the scope of our investigation to 3D metallic slot waveguides [5] having a dielectric core possessing quadratic nonlinearity. These waveguides support a multitude of plasmonic modes in contrast to even and odd symmetric modes supported by the simple 2D MIM waveguides (Fig. 1). Taking degenerate second harmonic (SH) generation as a referential caser, we demonstrate the applicability of the concept of modal phase-matched $\chi^{(2)}$ interaction between guided modes at fundamental harmonic (FH) and second harmonic (SH).

Numerical results

We assume the substrate to be a dielectric with permittivity $\varepsilon_r = 1.96$, metal is silver, dielectric core to be $LiNbO_3$ and cladding to be air. FH is tuned to $\lambda_0 = 1.55\mu m$. In degenerate SHG, the phase-mismatch factor is given by $\Delta n'_{\mathrm{LM}} = n'_{\mathrm{eff,M}}(2\omega) - n'_{\mathrm{eff,L}}(\omega)$ where $n'_{\mathrm{eff,k}}(\omega)$ is the real part of the effective mode index of order k at angular frequency ω. Considering monomode (L = 0 [Fig. 1(b)]) behavior at the defined FH, we solved the coupled mode equations presented in [6] to analyze the propagation of SH modes in the waveguide which is pumped at FH power of 1W. The conversion efficiency is defined for the output of computation as $\eta_M = \frac{max[Power_{\mathrm{M}}(2\omega,z)]100\%}{Power(\omega,z=0)^2\kappa_{\mathrm{M}}(2\omega)}$ where $\kappa_{\mathrm{M}}(2\omega)$ symbolizes the linear propagation length of SH mode order M

in the unit of cm.

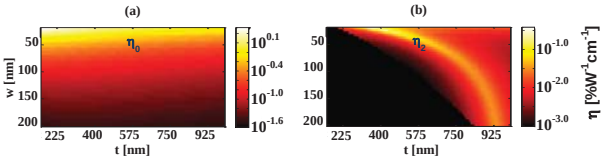

Figure 2: Nonlinear conversion efficiency η_M of the SH mode order M = 0 (a) and M = 2. Input pump power of FH is equal to 1W. Black area denotes regions in the parameter space where the plasmonic mode is cut-off. [3]

Conversion efficiency of SH modes for mode orders 0 and 2 is mapped in Figure 2. This corresponds to the modes shown in Fig. 1(b) and (d). Conversion into mode order 1 [Fig. 1(c)] is not included owing to the fact that its E_x component has an anti-symmetric profile which results in poor coupling with the symmetric mode (Fig. 1a) at FH. The bright line showing an enhancement in η_M in Fig. 2(b) actually coincides with the phase matching line where $\Delta n'_{0M}$ is equal to zero.

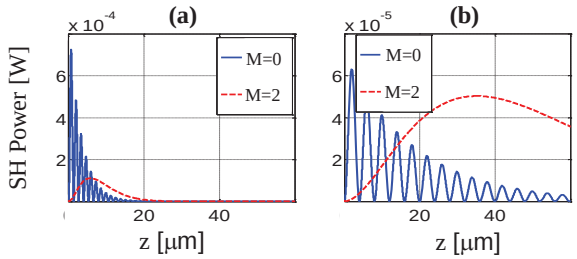

Figure 3: Evolution of power in SH modes of order M with propagation with input pump of 1W power at FH. (a) w = 20nm, t = 360nm. (b) w = 200nm, t = 929nm [3].

Thanks to the presence of damping in metals chosen frequencies, full energy conversion into SH modes is not possible even when modes are perfectly phase-matched. This highlights the need for a careful evaluation for designing practical devices between minimizing the phase-mismatch or enhancing the mode overlap between FH and SH. The former is in general achievable between modes of different orders. But for the latter, we get optimum results when modes of the same order interact at both FH and SH. To signify this point, Fig. 3 shows the simultaneous propagation of modes at phase-matched configurations taken from Fig. 2(b). Evidently, the SH mode of order M = 0 can be more useful for short-distance operation despite having a phase-mismatch. Mode of order M = 2 can become a more desirable option when larger propagation distances are necessary.

Conclusion

The possibility of modal phase-matching in plasmonic slot waveguides has the potential of being a major step forward toward realizing useful optical devices based on quadratic nonlinearity at nano-scale. In the present design, this is achieved at aspect ratios which might not be realistic with the present technology. Since our aim was only to demonstrate the proof of concept, we didn't pay attention to possibly engineer the material parameters in order to achieve more realistic geometrical parameters. One direct application of this work would be to investigate the problem of parametric amplification of plasmonic mode through SH pump. This can potentially lift the problem of small propagation lengths of plasmonic modes to practically acceptable limits.

[1] A. R. Davoyan, I. V. Shadrivov, Y. S. Kivshar, Opt. Express **17**, 20063–20068 (2009).

[2] S. B. Hasan, C. Rockstuhl, T. Pertsch, F. Lederer, Accepted for publication in JOSAB.

[3] S. B. Hasan, C. Rockstuhl, T. Pertsch, F. Lederer, in CLEO: QELS-Fundamental Science, OSA Technical Digest (Optical Society of America, 2012), paper QTu1F.6.

[4] E. Feigenbaum, M. Orenstein, Opt. Lett. **32**, 674–676 (2007).

[5] L. Liu, Z. Han, S. He, Opt. Express **13**, 6645–6650 (2005).

[6] Z. Ruan, G. Veronis, K. L. Vodopyanov, M. M. Fejer, S. Fan, Opt. Express **17**, 13502–13515 (2009).

UV fs-laser pulse durations from autocorrelation measurements in CaF_2

P.-C. Heisel[*1], T. Zeuner[1], W. Paa[1] and H. Stafast[1,2]

[1]*Institute of Photonic Technology, Albert-Einstein-Straße 9, 07745 Jena, Germany*

[2]*Friedrich Schiller University Jena Faculty of Physics and Astronomy*

[*]Corresponding author: *per-christian.heisel@ipht-jena.de*

Abstract

For the determination of UV femtosecond laser pulse durations we use the autocorrelation technique based on two photon absorption (TPA) in CaF_2. To picture TPA of 197 nm laser radiation we measure either the energy transmission through a sample or the laser induced fluorescence (LIF) of self trapped excitons (STE) at 278 nm. Both ways yield second order autocorrelations, which are easy to analyze and allow to derive the real pulse lengths being about 370 fs in our case.

Introduction

By steadily downsizing the dimensions of semiconductor devices via laser lithography, laser wavelengths down to the UV have attracted industrial and research interest.

Unfortunately, conventional methods (e. g. SHG autocorrelation) for the determination of the UV fs laser pulse durations fail, since no transparent materials are available for wavelength below about 150 nm. Therefore it is necessary to use other detection methods to investigate the length of used laser pulses in a preferably easy way. Thus in recent years TPA based autocorrelation techniques have been established: in 1991 Le Blanc et al. [1] reported on single-shot measurements in the alkaline earth fluorides BaF_2 and CaF_2. Although they pointed out the advantages of BaF_2 compared to the more common CaF_2, both materials were found to be suitable TPA media. Latest publications by Homann et al. [2] show a broad overview of manifold TPA media and give evidence which crystal should be used in which wavelength regime for most exact results. But they explicitly found no signals in CaF_2, which is inconsistent with the mentioned previous work and our own measurements.

Our group focuses on autocorrelation measurements in CaF_2 at 197 nm. CaF_2 is a commonly used, readily available material and therefore a suitable medium for TPA measurements. Both above mentioned procedures, energy transmission or STE-LIF, provide consistent results in pulse length measurements with a good signal to noise ratio.

TPA based autocorrelation measurements even work in liquid media: Reuther et al. showed results for *in situ* pulse length determination in fluids [3], showing, however, interactions between the incident laser radiation and photolysis products, influencing the autocorrelation.

Experimental Setup

A Coherent Mira900F oscillator provides pulses at the fundamental wavelength of 785 nm of about 130 fs pulse width. These pulses are amplified by a Quantronix Titan regenerative fs-amplifier. The fourth harmonic 197 nm pulses are achieved by sum frequency generation in β-BBO. At 197 nm pulse energies up to 9 µJ are available for measurements.

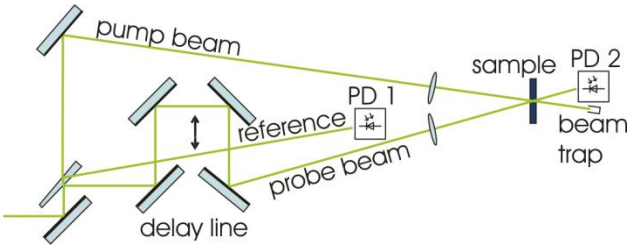

Fig. 1: Experimental setup for pump-probe measurements; for autocorrelation measurements the sample is replaced by a CaF_2 crystal.

The main advantage of the autocorrelation setup is the possibility to be installed easily and quickly in each existing pump-probe setup to determinate the real pulse length in a sample, simply by replacing the sample by a CaF_2 crystal (Fig. 1).

Physical background

CaF_2 is an alkaline earth fluoride with an energy gap of E_g = 11.5 eV [4]. We assume that single photon absorption at 197 nm (6.3 eV photon energy) is negligible. Thus the transmission T is given by

$$T = \frac{1}{1 + \beta z I(x,y,t)},$$

with β being the two photon absorption coefficient, z the sample thickness and I the incident laser intensity. The energy transmission is given by

$$T_{TPA}(z) = \frac{1}{E} \int_{-\infty}^{\infty} \int_{A} \frac{I(x,y,t)}{1 + \beta z I(x,y,t)} dA\, dt.$$

For $\beta z I(x,y,t) \ll 1$ the integrand can be developed in a series and approximated by its linear part providing a second order autocorrelation function, easy to analyze.

Considering that for Gaussian pulses the second order autocorrelation is broadened by factor $\sqrt{2}$ compared to the correlated pulses, their width can be determined via the autocorrelation function width.

Excitation of an electron from the CaF_2 valence to the conduction band produces an electron-hole pair (exciton). By self trapping it can form a metastable defect of the crystal structure called self trapped exciton (STE). The STE decay occurs within 1 µs, showing a characteristic fluorescence at 278 nm. Its intensity is proportional to the TPA and can be used for autocorrelation measurements.

Results and Discussion

Both methods yield the same UV pulse lengths: (362 ± 25) fs by the energy transmission experiments and (375 ± 20) fs by STE-LIF measurements (Fig. 2). The broadening from 130 fs fundamental pulses to about 370 fs at the fourth harmonic presumably happens in the frequency tripler and quadrupler units.

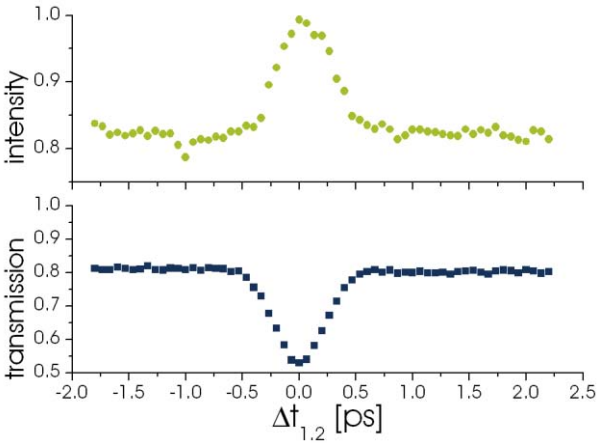

Fig. 2: Measured autocorrelation functions by using the STE-LIF in intensity (upper part, green) or the energy transmission through the crystal (lower part, blue)

Summarizing we can use a simple autocorrelation setup to determine pulse lengths of UV fs-pulses in a reliable way. Our concern, to establish an easy and efficient method for pulse duration measurements under manifold experimental conditions has been verified.

[1] S. P. Le Blanc, G. Szabo and R. Sauerbrey, Femtosecond single-shot phase-sensitive autocorrelator for the ultraviolet (Opt. Lett., 16:1508-1510, 1991)

[2] C. Homann, N. Krebs, E. Riedle, Convenient pulse length measurement of sub-20-fs pulses down to the deep UV via two-photon absorption in bulk material (Appl. Phys. B, 104:783-791, 2011)

[3] A. Reuther, A. Laubereau, D. N. Nikogosyan, A simple method for the in situ analysis of femtosecond UV pulses in the pump-probe spectroscopy of solutions (Opt. Commun., 141:180-184, 1997)

[4] R. Lindner, Bildungs- und Relaxationsdynamik von Self-Trapped Excitons in Erdalkalifluoriden (Wissenschaft und Technik Verlag Berlin, 2000).

Lipophilic sensor layers for SERS-based detection of water-insoluble substances

Martin Jahn[1], Dana Cialla[1,2], Karina Weber[1,2], and Jürgen Popp[*1,2]

[1]*Institute of Physical Chemistry and Abbe Center of Photonics, Friedrich-Schiller-University Jena, Helmholtzweg 4, 07743 Jena, Germany*

[2]*Institute of Photonic Technology (IPHT), Albert-Einstein-Strasse 9, 07745 Jena, Germany*

[*]Corresponding Author: *juergen.popp@uni-jena.de*

Abstract

The most common substrates for surface enhanced Raman spectroscopy (SERS) are metallic colloids in aqueous solution. Therefore, SERS-based detection schemes are limited to water-soluble analyte molecules. Here, we present a technique for the detection of water-insoluble substances based on a lipophilic sensor layer. Hence, water-insoluble molecules are enriched in the vicinity of nanostructured metal surfaces.

INTRODUCTION

Surface enhanced Raman spectroscopy (SERS) is a fast, non-destructive and versatile tool for the analysis of chemical and biological specimens that combines the high specificity of Raman spectroscopy with the near-field enhancement in the proximity of metallic nanostructures [1]. Metallic colloids in aqueous solution, which are the most commonly used SERS-substrates, are limited to the investigation of water-soluble analyte molecules. However, for applications, such as the analysis of food or pharmaceutical products, the detection of water-insoluble substances is of great interest.

In this contribution, we present metallic nanostructures with a lipophilic sensing layer for the detection of water-insoluble analyte molecules via SERS. For the preparation of these sensing layers aliphatic hydrocarbons are the material of choice.

SERS SUBSTRATES

In order to fabricate SERS-substrates several top-down and bottom-up techniques are available. The great benefit of top-down methods like electron beam lithography (EBL) is the high reproducibility of such manufactured structures and the ability to realize almost every desired nanostructure design. However, the high technical effort has to be taken into account [2].

Another way to produce plasmonic active nanoparticles on large areas is the enzymatic generation of silver nanoparticles (EGNP) [3]. This technique, which was established in our group, is based on the enzymatically growth of silver nanoparticles by the use of horseradish peroxidase. Thereby, the enzyme is bond via a biotin streptavidin complex to a DNA double strand, which is immobilized onto the surface of the substrate. The advantage of the resulting desert rose like structures is their easy and fast production process as well as

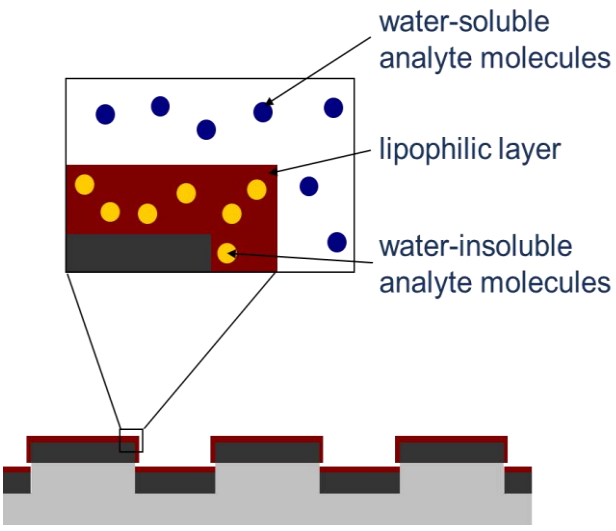

Fig. 1 Sketch of a lithographic manufactured substrate with a lipophilic sensor layer and its working principle

the possibility of a quality check due to an electrical resistance measurement.

LIPOPHILIC SENSOR LAYERS

For first investigations, the sensor layers for the detection of water-insoluble substances were applied on lithographic manufactured substrates (Fig. 1). Therefore, via self-organization a coating of hydrocarbons is formed onto the surface of the metallic nanostructures. Due to its lipophilic behavior water-insoluble analyte molecules were enriched in the sensor layer close to the plasmonic active surface. Hence, strong SERS-signals from these molecules are expected. In contrast, water-soluble substances are not enriched in the coating, which leads to a vanishingly small contribution to the measured signal. This approach might be a contribution towards the fractionation of water-soluble and water-insoluble substances with a combined SERS read-out.

ACKNOLEDGEMENTS

Funding of the research projects ‘QuantiSERS’ and ‘Jenaer Biochip Initiative 2.0’ within the framework ‘Unternehmen Region – InnoProfile Transfer’ from the Federal Ministry of Education and Research, Germany (BMBF) is gratefully acknowledged.

[1] D. Cialla, A. März, R. Böhme, F. Theil, K. Weber, M. Schmitt, and J. Popp, Anal. Bioanal. Chem. **403**, 27 (2012).

[2] D. Cialla, J. Petschulat, U. Hübner, H. Schneidewind, M. Zeisberger, R. Mattheis, T. Pertsch, M. Schmitt, R. Möller, and J. Popp, ChemPhysChem **11**, 1918 (2010).

[3] K.K. Strelau, T. Schüler, R. Möller, W. Fritsche, and J. Popp, ChemPhysChem **11**, 394 (2010).

Ytterbium-doped large-pitch fibers

F. Jansen[*1], F. Stutzki[1], C. Jauregui[1], J. Limpert[1,2], A. Tünnermann[1,2]

[1]*Institute of Applied Physics, Abbe Center of Photonics, Friedrich-Schiller-Universität Jena, Albert-Einstein-Straße 15, 07745 Jena, Germany*

[2]*Helmholtz Institute Jena, Fröbelstieg 3, 07743 Jena, Germany*

[*]Corresponding Author: *jansen@iap.uni-jena.de*

Abstract

Higher-order mode delocalization in large-pitch fibers ensures effective single-mode operation at high output powers and very large mode areas. We demonstrate how this new class of fibers offers unprecedented robustness against thermal effects. Furthermore, we outline new strategies to improve the fiber design.

INTRODUCTION

Fiber lasers and amplifiers are the active medium of choice, wherever high gain, high efficiency and single-transverse-mode beam quality are required. During the past decade, the output power of continuous-wave and pulsed fiber laser systems has risen to the kilowatt range. However, the propagation of tightly confined radiation in the fiber core over long fiber lengths facilitates the onset of nonlinear effects such as stimulated Raman scattering, stimulated Brillouin scattering or self-phase modulation. The development of advanced large mode area (LMA) fiber designs mitigates these limitations firstly by providing large mode-field diameters (MFDs) and, secondly, by shortening the fibers thanks to a larger rare-earth-doped area.
Unfortunately, the traditional single-transverse-mode fiber designs cannot be further scaled since they have reached some technically challenging fiber-production parameters. For instance, step-index fibers require a decreasing numerical aperture with increasing core diameters to remain single-transverse-mode and, thus, they are limited by the technologically attainable index step. The situation is similar in effective-index-guiding photonic crystal fibers, where the limiting parameter is the minimum hole size that can be fabricated. Recently, several more elaborate fiber concepts have been shown, mostly based on resonance effects where higher-order modes (HOMs) are coupled out of the core, thus leading to an effective single-mode operation. However, any such resonant design is strongly affected by thermal waveguide changes that become prominent in very large mode area (VLMA) fibers. Therefore, there is a strong need for new robust effective single-mode operation principles.

LARGE-PITCH FIBERS

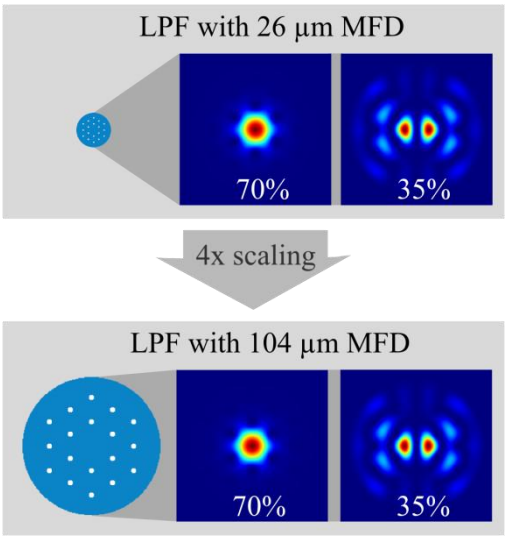

Figure 1: The proportional scaling of an LPF reveals a constant overlap with the doped region for the fundamental mode and the HOM.

Large-pitch fibers (LPFs) fulfil the desired effective single-mode operation by a new concept: the delocalization of higher-order modes [1]. This innovative working principle encompasses an intrinsically improved seed signal coupling to the fundamental mode of the LPF and a strong preferential gain for the fundamental mode. Both combine to provide a stable effective single-mode operation not only in an amplifier configuration but

also as a laser oscillator. The concept is very robust against fabrication tolerances as it features a non-resonant approach. Additionally, as it is shown in Fig. 1, it allows for a proportional scalability to larger dimensions while maintaining the delocalization properties. Figure 1 illustrates the modal properties of an LPF scaled by a factor of 4, i.e. with MFDs of 26 µm and 104 µm, respectively. The HOM delocalization effect is maintained for both designs with a core overlap of 70% for the fundamental mode and 35% for the HOM with the second largest core overlap. Note that the difference between these two fibers is that the pitch has been increased from 15 µm to 60 µm, but the relative hole diameter has been left constant at 0.2, corresponding to a proportional scaling. Thus, unlike any other fiber design, scaling LPFs is not restricted by current fabrication limits.

Thus, this concept has enabled the largest effectively single-mode fiber demonstrated to date: an active LPF with a core diameter of 135 µm which has enabled a Q-switched fiber laser system with 26 mJ pulse energy, 130 W average power and diffraction limited beam quality [2].

The unique scalability of LPFs was exploited in a detailed experimental study on thermal effects in high-power fiber lasers. These thermal effects cannot be neglected any longer for very large MFDs exceeding 50 µm [3]. Quantum defect heating leads to the formation of a thermal index profile that causes the modes to shrink in diameter. Furthermore, this thermal gradient can even change the complete set of guided modes.

In our contribution, we will illustrate that the LPF concept is not only able to robustly deal with thermal waveguide changes but that it can even benefit from this effect over a wide parameter range. With these properties, LPFs appear to outclass resonant VLMA fiber concepts, in which a changing waveguide severely affects the resonance condition required to ensure single-mode operation.

Due to the excellent scaling properties of LPFs, the mode field area is no longer the crucial limitation for high power fiber laser systems. In its place, mode instabilities at high average powers currently limit any further performance increase of fiber lasers. LPFs have already increased the mode instability threshold by a factor of about 3 due to their strong effective single-mode operation [4]. Nevertheless, mode instabilities are the main limitation for any fiber design to date. Therefore, further design improvements have to focus on substantially increasing the mode instability threshold. We will demonstrate design concepts with improved delocalization, which are optimized for an increase of the mode instability threshold. Here, reducing the symmetry of the waveguide structure is a possible way of further increasing the delocalization. In Fig. 2 the hole arrangement of an LPF with increased delocalization is shown together with the fundamental mode and a HOM.

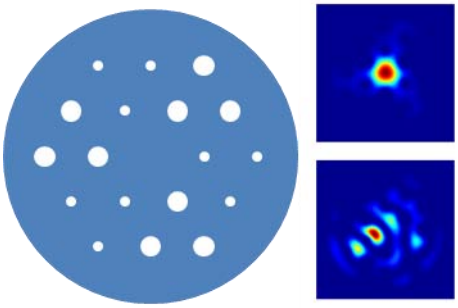

Figure 2: An asymmetric hole arrangement increases the delocalization in LPFs.

The research leading to these results has received funding from the German Federal Ministry of Education and Research (BMBF), the Helmholtz-Institute Jena (HIJ), the European Research Council (FP7/2007-2013 and 240460 "PECS") and the Thuringian Ministry for Economy, Labour and Technology (TMWAT 2011 FGR 0103). Additionally, F.J. acknowledges financial support by the Abbe School of Photonics Jena.

[1] J. Limpert et. al., Light: Science & Applications 1 (2012)

[2] F. Stutzki et. al., Opt. Lett. **37**, 1073-1075 (2012)

[3] F. Jansen et. al., Opt. Express **20**, 3997-4008 (2012)

[4] F. Stutzki et. al., Opt. Lett. **36**, 689-691 (2011)

Fast Structured Illumination Microscopy

Aurélie Jost*[1,2], Ronny Förster[2], Hui-Wen Lu[2], Kai Wicker[1,2] and Rainer Heintzmann[1,2]

[1] *Institute of Physical Chemistry, Lessingstraße 1, 07743 Jena, Germany*

[2] *Institute of Photonic Technologies (IPHT), Albert-Einstein-Straße 9, 07745 Jena, Germany*

*Corresponding Author: *aurelie.jost@ipht-jena.de*

Abstract

Structured Illumination Microscopy (SIM) distinguishes itself from the other super-resolution techniques by its potentially much faster imaging rate. However it requires the acquisition of several frames, which limits its speed. We develop a fast system based on a Spatial Light Modulator (SLM). We aim at an acquisition speed of 10 frames per seconds.

INTRODUCTION

Fluorescence microscopy is a very successful method for imaging biological samples. It offers a wide choice of different methods, each suitable for one particular application. Resolution describes the smallest distance between two point sources in the sample whose images, known as point spread function (PSF), can be separated. Abbe showed that this distance is given by $d = \lambda/2NA$, where λ is the wavelength of the light and NA is the numerical aperture of the objective. In a conventional wide-field fluorescence microscope, d is about 200nm.

So-called super-resolution methods have been developed recently [1]. They bypass the diffraction limit and image structures well under 100nm [2]. Structured Illumination Microscopy (SIM) is one of them [3, 4]. A demonstration of the resolution enhancement in a commercial SIM is provided in figure 1.

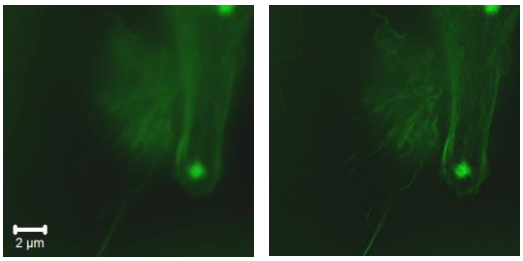

***Figure 1** - Resolution enhancement of the Elyra S1 commercial microscope. Left: wide-field. Right: SIM image. Sample: F-Actin of THP-1 cells labelled with Alexa Phalloidin – 639.*

PRINCIPLE OF STRUCTURED ILLUMINATION MICROSCOPY

Structured Illumination Microscopy (SIM) utilises the Moiré effect to produce lateral resolution enhancement. This phenomenon occurs when exciting the sample with a high frequency sinusoidal illumination pattern. It results in a down modulation of the high frequency components in the sample, shifting them back into the support of the Optical Transfer Function (OTF) of the microscope. Thanks to this effect, linear SIM achieves a two-fold lateral resolution enhancement as compared to conventional wide-field microscopy.

In a classical implementation, the sinusoidal modulation of the light is the result of 2 beam interference. A mechanical grating acts as an illumination mask.

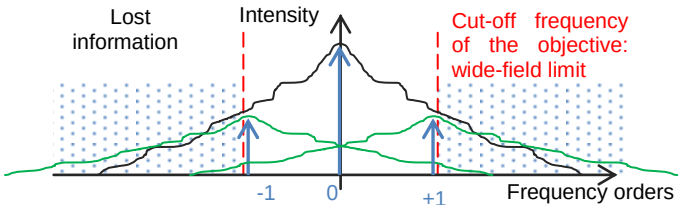

***Figure 2** – Lateral resolution enhancement. The Fourier Transformed sample information (black) is convolved with the Fourier Transform of the illumination pattern (blue). This results into additional object components (green) at the position of the + and – first orders respectively.*

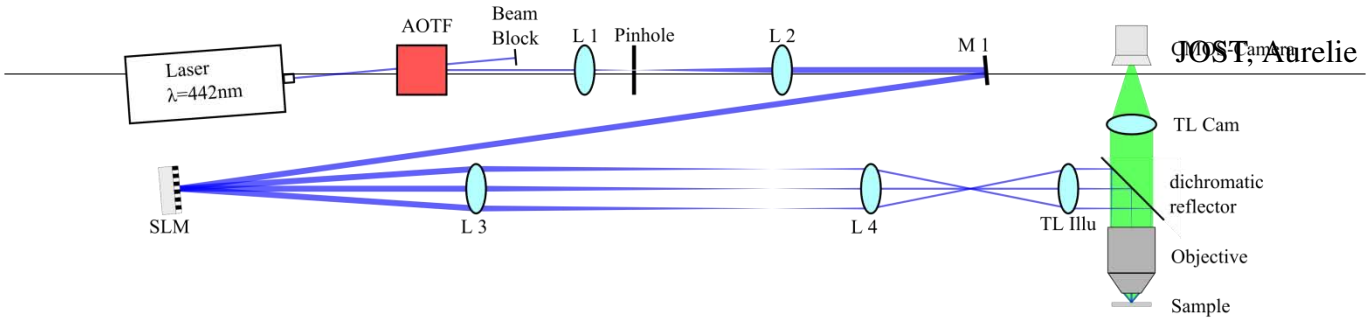

***Figure 3** – Current set-up. The acousto-optic tunable filter (AOTF) acts as a fast shutter. The spatial light modulator (SLM) produces 3 diffraction orders that interfere in the sample plane.*

The Fourier Transform of the illumination pattern yields 3 peaks, which will be convolved with the Fourier Transformed sample information. See figure 2. Thus, one raw image contains the information of 3 components. In order to be able to separate them, it is necessary to acquire 3 raw images, each at different position of the grating in sample space (different phase steps), to reconstruct one final high resolution image. Besides, isotropic resolution enhancement requires repeating this procedure in 2 other orientation of the grating. Finally, one super-resolution image requires 9 raw images minimum. Indeed, in a more complicated but also higher-performance case, 3 beams interference instead of 2 is used to produce the illumination, and 5 phase stepped images are acquired in each direction.

The power of SIM is that, because it is a wide-field method, it can be potentially significantly faster than conventional microscopy techniques that are point-scanning. However, the need to acquire several frames limits its speed.

OUR IMPROVEMENTS

We saw that for the reconstruction of super-resolution SIM images, the shifting of the grating is necessary. They are however time-consuming and therefore the use of a Spatial Light Modulator (SLM) is preferable to that of a mechanical grid. The SLM is a computer-driven optoelectronical device and enables a fast change of the grating position.

The fast structured illumination setup that we built is inspired by the work of Gustafsson and coworkers [5] and is depicted in figure 3. The core component is the fast SLM, which is illuminated by a collimated laser beam at 442nm. It produces 3 diffracted beams, the 0 and the + and – 1st orders. Secondly, the camera must be fast as well. We use a state-of-the-art complementary metal-oxyde-semiconductor (CMOS) camera.

The global set-up includes several electrical components. Its performance depends not only on the speed of each device, but also on the triggering of all parts. We use a micro-controller board driven by a program that synchronizes the different devices.

Indeed there are still at least 2 other important devices that require synchronization and fast operation. They do not directly influence the acquisition speed, but are crucial for image quality and grating contrast. First, a fast polarization control system will be included in near future. Second, an acousto-optical tunable filter (AOTF) controls the exposure.

ACHIEVEMENTS AND OUTLOOK

During the first year of this project, we successfully built the system and tested it using a fluorescent plane sample. There are still many measurements that remain to be done, for instance characterizing the illumination polarization and the modulation contrast of the grating, as well as using the system to acquire SIM images of both fixed and living cells. The preliminary results are very encouraging since we demonstrated an image acquisition rate of 136Hz for a 200 x 200 pixels image. This is 10 times faster than the commercial system Elyra-S1 by Zeiss [6].

[1] Betzig & co, Science **313**, 1642, (2006).

[2] S. Hell, J. Wichmann, Optics Letters OSA **19**, 780, (1994).

[3] M. Gustafsson, Journal of Microscopy **198**, 82, (2000).

[4] R. Heintzmann, C. Cremer, Proceedings of SPIE **3568**, 185, (1999).

[5] M. Gustafsson & co, Biophysical Journal **94**, 4957, (2008).

[6]http://www.zeiss.de/C1256CFB00332E16/0/5F02A12AC0F5C3C6C12578A90034E974/$file/60-1-0016_e_elyra.pdf (22.05.2012).

Powder sintering process for the manufacturing of novel, highly efficient laser fibers

Florian Just*, Stephan Grimm, Martin Leich, Matthias Jäger, and Hartmut Bartelt

Institute of Photonic Technology Jena, Albert-Einstein-Straße 9, 07745 Jena, Germany

*Corresponding Author: *florian.just@ipht-jena.de*

Abstract

The reactive powder sintering process for silica glass is a new method to produce rare earth doped fused silica with very high purities. We show how to manufacture the material and explain its main properties compared to material from the well established MCVD technique.

Introduction

Alternative manufacturing processes for glass are required for the implementation of novel fiber laser concepts, such as extra-large mode area (X-LMA) fiber lasers, multi-core fiber lasers, gain-guided fiber lasers, short-pulse fiber lasers, or Bragg fiber lasers based on highly-doped fused silica glasses. Established gas-phase processes, such as modified chemical vapor deposition (MCVD), reach their limits in the production of these materials. This not only pertains to the required quantities but also to certain quality criteria. During a multi-year development in cooperation with the Heraeus Quarzglas GmbH an innovative powder sintering process for silica glass (RePuSil) was developed [1] to provide materials for the implementation of novel concepts.

Preparation

The starting point is a suspension of nanoparticles made of silicon dioxide. The dopants are attached reactively to the surface and further processed into a granulate (Fig. 1).

Figure 1: Doped powder and the resulting green body.

The glass powder is pressed into a porous body and is purified and compressed during multiple steps. Afterwards, vitrification at high temperatures follows inside a special tube that enables the provision of fiber core material in the form of compact glass rods. This makes this process an useful addition to MCVD.

Material properties

Thanks to the availability of homogeneous rods of different compositions and properties (refractive index, thermal expansion, viscosity, active/passive doping) different fiber designs can be flexibly implemented using a preform made up of individual rods (Fig. 2).

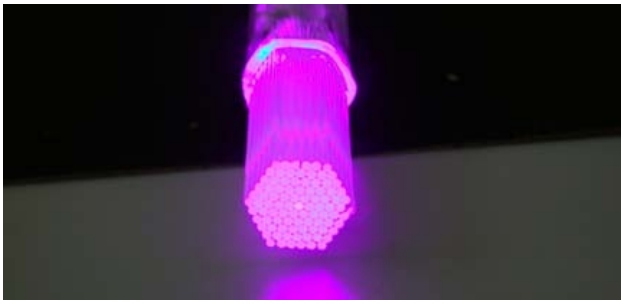

Figure 2: Stacked fiber preform with doped core.

For the first time, the possibility exists to homogeneously manufacture fused silica-based laser glasses for many different IR wavelengths with the required purities in quantities of 10 g to 100 g. In this manner, additional functionalities, such as the breaking of symmetry to increase pump efficiency, maintain stress birefringence, and multi-core structures (Fig. 3) to lower the number of modes, can be easily implemented. This technology is particularly suitable to produce large fiber laser cores in which the radial

and lateral indices of refraction can be adjusted reproducibly and homogeneously (Fig. 4). The absolute difference of the index of refraction to the fused silica buffer can be adjusted from ca. +0.01 to −0.005.

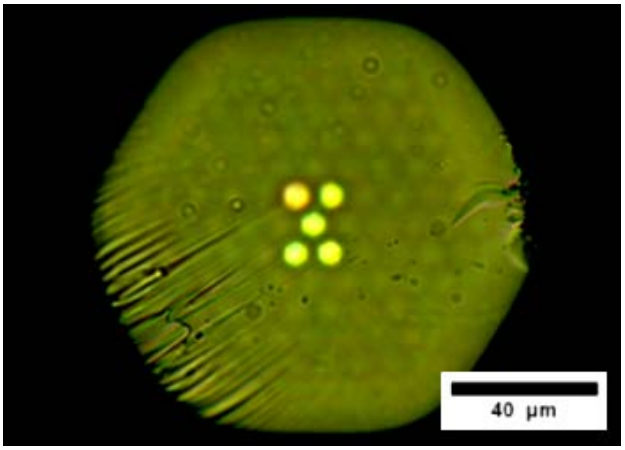

Figure 3: Fiber with 5 active cores.

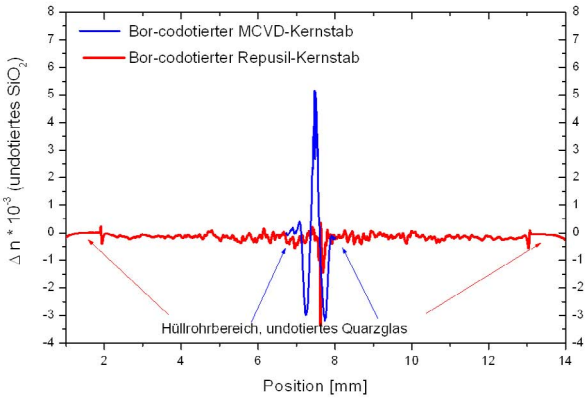

Figure 4: Comparison of refractive index profiles of core material produced by MCVD and RePuSil.

Additional elements lowering the refractive index (boron and fluorine) can be well-defined and homogeneously co-doped in order to compensate the increases caused by aluminum and rare earths. This fulfills the requirements for the implementation of novel single-mode LMA fibers for a further scaling in power by distributing the laser power across a larger laser core. Moreover, nonlinear effects such as stimulated Brillouin scattering (SBS) and stimulated Raman scattering (SRS) are suppressed or reduced. Due to the large laser-active volume in these fibers resulting in smaller lengths, fibers with a moderate residual attenuation can also be used. The described advantages of the process and the materials could be demonstrated by producing and testing different fiber lasers.

Compared to MCVD, RePuSil provides material with nearly identical behavior regarding the fluorescence of the excited Yb-ions and photodarkening caused by pump light. In order to evaluate the laser properties of the fibers, cw tests in a Fabry Perot resonator were made with a pump wavelength of 975 nm. The results (Fig. 5) show an excellent and reproducible efficiency of about 80 % up to 230 W [2].

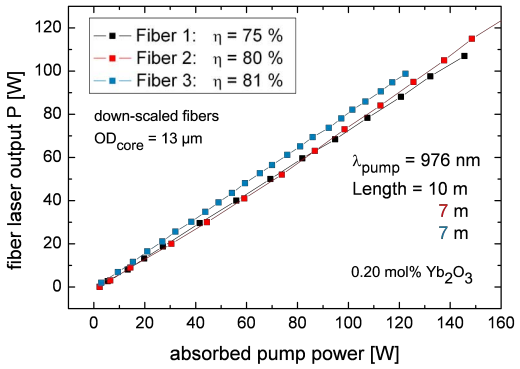

Figure 5: Laser efficiency curves of fibers with a diameter of 300 μm and 13 μm RePuSil laser cores.

APPLICATION

During the ”Falamat” project, fibers with multi-mode X-LMA cores (Ø > 50 μm)were tested for use in high-power fiber lasers. In addition to a high efficiency now comparable to MCVD fibers, power levels of 4 kW from a 1 mm fiber with a beam quality of 6.5 mm mrad were demonstrated by the partner Laserline. This power level was the prerequisite for the application of this type of fibers in lasers used for material processing. First promising tests in welding aluminum and steel have been performed in the automotive industry.

[1] A. Langner, *et al.*, *Proc. SPIE* (2012), vol. 8237, pp. 8237–44.

[2] M. Leich, *et al.*, *Opt. Lett.* **36**, 1557 (2011).

Light propagation in plasmonic nanoparticle loaded waveguides

Thomas Kaiser*[1], Carsten Rockstuhl[2], and Thomas Pertsch[1]

[1]*Institute of Applied Physics and Abbe Center of Photonics, Friedrich-Schiller-Universität Jena, Max-Wien-Platz 1, 07745 Jena, Germany*

[1]*Institute of Condensed Matter Theory and Solid State Optics and Abbe Center of Potonics, Friedrich-Schiller-Universität Jena, Max-Wien-Platz 1, 07745 Jena, Germany*

*Corresponding Author: *thomas.kaiser.1@uni-jena.de*

Abstract

In the field of Nanophotonics / Plasmonics, one distinguishes between the propagating solutions of Maxwell's equations giving rise to a far-field response and the extreme strong and highly localized fields in close vicinity of nanoparticles. We will show how the interaction of the individual localized nanoparticle fields in a standard waveguide geometry is capable of creating unusual propagation properties as negative group velocity or extreme dispersion control by geometrical tuning.

Introduction

Noble metals such as Ag and Au are the key building blocks in Nanophotonics due to their ability to carry highly sub-wavelength localized coupled states of the electromagentic field and the free conduction electrons, the surface plasmon polaritons [1]. In a noble metal nanoparticle, the finite size leads to the formation of localized surface plasmons which can be understood as collective charge oscillation at optical frequencies due to the excitation by an external light field. The shape of the nanoparticle will inherently determine the plasmonic properties by the internal charge dynamics. This will vice versa influence the far field scattering properties dramatically, since the nanoparticle acts as a feeding source for the secondary scattered wave [2].

This working principle allows for the creation of new structures with tunable and unusual electromagnetic properties, as e.g. metamaterials [3]. Here, the plasmonic nanoparticles act as building blocks with designed electromagnetic response. This allowed for the demonstration of effects like artificial magnetism at optical frequencies, negative refraction or cloaking.

Up to date, the collective response of such nanoparticles is mainly studied regarding their far-field response, explorable by plane wave excitation of a nanostructured thin-film. Naturally, the question arises how such particles interact in an integrated optical environment, what eigenmodes exist there and how the propagation properties are influenced.

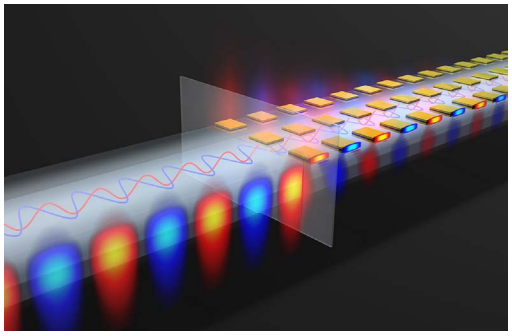

Figure 1: Interface between a bare and a nanoparticle loaded waveguide section with visualized eigenfields.

Propagation properties

The structure we would like to investigate is shown in Fig. 1. A conventional slab waveguide is decorated with nanostructures on top of it. This configuration is easily realized by standard planar e-beam lithography. As nanostructure geometry, we chose so called double cut-plates and -wires. They consist of two 20 nm thin Au sheets, separated by a 40 nm dielectric spacer (usually MgO or MgF_2). Plasmons supported in the upper and lower wire can couple and form a symmetric or anti-symmetric state, respectively, with the current flow being parallel or anti-parallel. In our structure, the nanoparticles are arranged atop a thin (350 nm) high-index (Si_3N_4, $n = 2.0$) dielectric waveguide. The

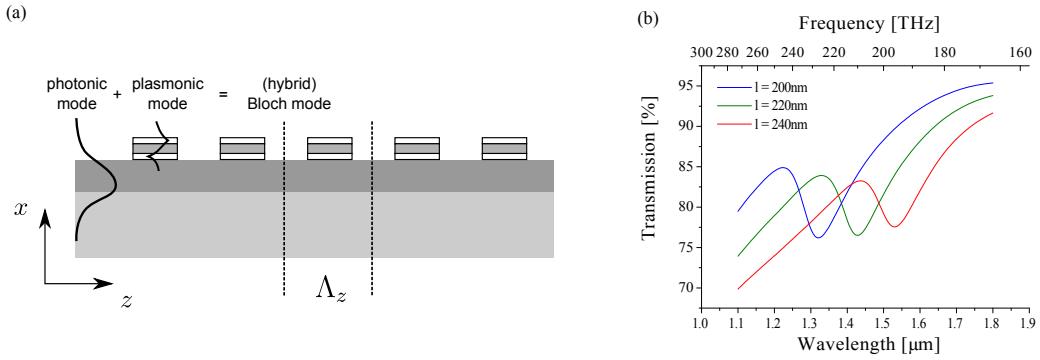

Figure 2: (a) Interaction scheme of the photonic and the plasmonic mode. (b) Transmission spectrum of the double cut-wire, showing the geometric resonance tunability.

high index contrast to the air cladding allows for an efficient excitation of the anti-symmetric plasmonic state in the particle by the fundamental TM waveguide mode. This state is of particular interest since its loop-like current distribution creates the effect of artificial optical magnetism in an optically "dark" quadrupol mode which does not suffer from radiative loss to the far field [2]. This leads to a plasmonic resonance visible in the transmission spectrum which can be tuned by altering the length of the double cut-wires, see Fig. 2.

In such hybrid structures, light propagation is described by Bloch Modes [4]. The dispersion relation (DR) $\omega(k_z)$ hereby is the fundamental aspect which determines the propagation properties. Fig. 3 shows the DR of the aforementioned structure for different lattice constants Γ. The gray area marks the plasmonic resonance. Counterintuitive, a denser array of nanoparticles has only a negligible effect on the dispersion since the excitation is not in phase. If the lattice constant is two large on the other hand, the detrimental effect of the band gap is clearly visible. However, just in between the two regimes, the plasmonic and the Bragg resonance can be balanced. A large redshift is a hint that one approaches the strong coupling regime. Depending on the lattice constant, a dramatic change of the dispersion takes place. The induced resonance now creates spectral regions with flattened, steepened and even backward bent dispersion, associated with a *negative* group velocity [5]. By geometrical tuning, one can now e.g. create a particular value for v_g or the GVD at the frequency of interest.

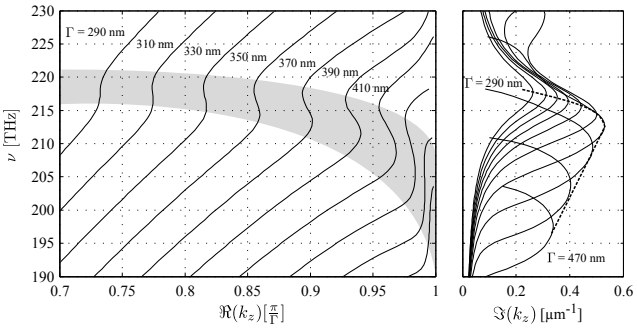

Figure 3: Dispersion relation calculated by a-FMM.

Conclusion

It was shown how the incorporation of plasmonic nanoparticles into conventional waveguide geometries facilitates the possibility to approach extreme regimes of light propagation. The collective response together with a proper design of the single particle resonance allows to create regions with even negative group velocity, allowing for full dispersion control of light propagation.

[1] A. Zayats, I. Smolyaninov, A. Maradudin, *Physics Reports* **408**, 131 (2005).
[2] J. Petschulat, *et al.*, *Optics Express* **18**, 14454 (2010).
[3] W. Cai, V. Shalaev, *Optical Metamaterials: Fundamentals and Applications* (Springer, 2009).
[4] B. Saleh, M. Teich, *Fundamentals of Photonics* (John Wiley & Sons, New York, 1991).
[5] P. Chen, *et al.*, *Physical Review A* **82**, 053825 (2010).

The impact ionization coefficient in dielectric materials revisited

C. Karras*[1, 2], Z. Sun[1], D. N. Nguyen[1], L. A. Emmert[1] and W. Rudolph[1]

[1]*Departement of Physics & Astronomy, University of New Mexico, 1919 Lomas Blvd. NE, Albuquerque, NM 87131, NM, USA*

[2]*Institute of Photonic Technology Albert-Einstein-Str. 9, 07745 Jena*

*Corresponding Author: *christian-karras@ipht-jena.de*

Abstract

Avalanche ionization plays a crucial role in the photoionization of dielectric materials with respect to optical damage. Although it has been investigated closely during the last years, its significance on the ultrashort time scale remains a contentious issue. Here we present UV-pump IR-probe experiment on the fs time scale that allowed us to isolate the avalanche ionization from other major ionization processes, especially multiphoton ionization, electron tunneling, and relaxation into traps and their re-excitation. We show that the assumption of an intensity independent impact ionization factor *a* cannot explain the results. Application of a simple avalanche ionization model within the flux-doubling approximation requires an intensity dependent coefficient *a(I)* to explain the data.

INTRODUCTION

Technical applications based on fs laser pulses, like micromachining and tissue ablation have gained large interest during the last decade [1, 2]. The material removal in this time regime is driven by ionization above a critical electron density threshold [3, 4].

One of the major ionization processes in dielectric materials is avalanche ionization (AI), which leads to an avalanche-like increase in the conduction band (CB) electron density. Although it has been investigated closely during the last years [2, 4, 5] there is little experimental data of how the impact ionization parameter changes with electron density and/or incident pulse energy on the fs time scale. One reason is that in most dielectric materials there are several competing ionization and relaxation processes, such as multiphoton ionization (MPI), tunnel ionization (TI) or electron trapping.

Here we present an experimental setup, which allows us to isolate the impact ionization from its competitive processes. In order to decouple AI from MPI as well as TI, a UV pulse was used to seed electrons into the CB. These electrons were subsequently heated by a succeeding IR pulse and the transmission of this IR pulse as a function of its fluence was measured. The goal was to find the avalanche ionization coefficient *a(I)* in order to explain the transmission measurements.

EXPERIMENTAL SETUP

An amplified fs oscillator was used to create 40 fs pulses at 800 nm with a repetition rate of 10 Hz. After splitting the beam, one component was variably attenuated between 30 nJ and 18 µJ. The second component was frequency tripled (266 nm). The pulse energy could be varied between 1 and 30 µJ. Both beams were focused into an 89 µm thick piece of UV-grade sapphire (α–Al_2O_3, Valley Design, A–plane cut). The beam waists were 32 µm for the UV and 16 µm for the IR–pulses respectively. The sample was mounted on a motorized two-axis translation stage and irradiated under Brewster angle. It was translated after each shot. The transmitted as well as the incident energy of both, the pump and the probe beams were recorded by using photodiodes and a sample–and–hold data acquisition system.

EXPERIMENTAL RESULTS AND DISCUSSION

Figure 1 shows the dependence of the transmitted IR pulse on its input intensity in the presence of UV

pump pulses of different pulse energies. In all cases the delay between the UV and the IR pulses were fixed to be 1 ps. Therefore both, parametric effects due to pulse overlapping as well as relaxation of CB electrons back into the valence band, could be avoided. The CB electron densities were estimated from the two photon absorption of the UV pulse.

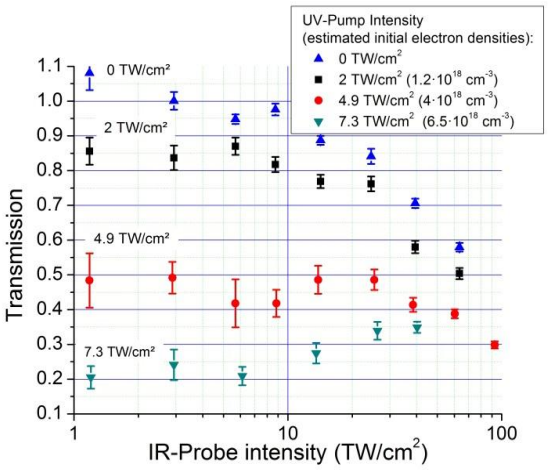

Figure 1: IR transmission for UV-grade sapphire as a function of the input intensity measured 1 ps after the excitation with UV pulses for different UV pulse intensities

For low UV pulse intensities, the transmission behavior of the IR remains constant and drops with increasing IR pulse intensity, where it approaches the transmission of the IR pulse without UV excitation. For strong UV pulses however, the transmission of the IR pulse increases with increasing IR pulse intensity.

ESTIMATION OF THE INTENSITY DEPENDENCE OF THE AVALANCHE COEFFICIENT

In order to relate the experimental results shown in Fig. 1 to the intensity dependence of the avalanche ionization coefficient, pulse propagation through the sample was modeled assuming *a(I)* as functional dependence.
Qualitatively good agreement between experiment and model was achieved assuming *a(I)* according to Fig. 2, UV as well as IR flat top pulses and constant electron densities in propagation direction.

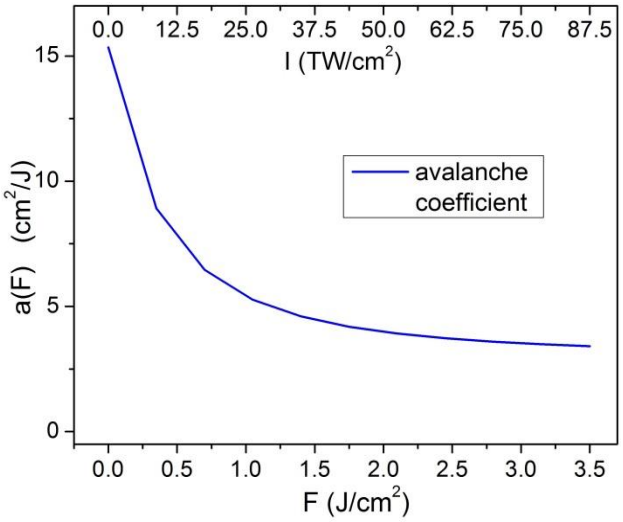

Figure 2: Fluence dependence of the avalanche ionization coefficient for a pulse propagation model fitting the transmission data from Fig.1

CONCLUSION

We studied the transmission of IR fs pulses as a function of the pulse intensity in sapphire in the presence of an UV prepulse providing initial conduction band electrons. Assuming an effective CB electron density with a mean energy, an intensity dependent avalanche ionization coefficient *a(I)* was determined that reproduces the experimental transmission data.

[1] F. H. Loesel, J.P. Fischer, M. H. Götz, C. Horvath, T. Juhasz, F. Noack, N. Suhm, J. F. Bille, "Non-thermal ablation of neural tissue with femtosecond laser pulses", Appl. Phys. B 66, 121 - 128 (1998)
[2] C. Mézel, A. Bourgeade, and L. Hallo, "Surface structuring by ultrashort laser pulses: A review of photoionization models ", Phys. Plasmas 17, 113504 (2010), pp. 113504-1 – 113504-16
[3] B. C. Stuart, M. D. Feit, S. Herman, A. M. Rubenchick, B. W. Shore, and M. D. Perry, "Nanosecond-to-femtosecond laser-induced breakdown in dielectrics", Phys. Rev. B, Vol 53, No. 4 pp. 1749 – 1761 (1996)
[4] L. A. Emmert, M. Mero, and W. Rudolph, "Modeling the effect of native and laser-induced states on the dielectric breakdown of wide band gap optical materials by multiple subpicosecond laser pulses" J. Appl. Phys, 108, 043523 (2010)
[5] P.P. Rajeev, M. Gertsvolf, P.B. Corkum, and D.M. Rayner, "Field Dependent Avalanche Ionization Rates in Dielectrics", Phys Rev. Lett. 102, 083001 (2009)

Spatio-angular microscopy

Martin Kielhorn*[1,2], Susan Cox[2], and Rainer Heintzmann[1,2,3]

[1]*Institute of Photonic Technology, Albert-Einstein Str. 9, 07745 Jena, Germany*

[2]*Randall Division of Cell & Molecular Biophysics, King's College London, NHH, Guy's Campus, London SE1 1UL, U.K.*

[3]*Institute of Physical Chemistry, Friedrich-Schiller-Universität Jena, Helmholtzweg 4, 07743 Jena, Germany*

*Corresponding Author: *kielhorn.martin@gmail.com*

Abstract

Photobleaching and phototoxicity pose a problem in live cell imaging. Excessive excitation light can induce reactive oxygen species in observed organisms. These can disturb signalling pathways and alter the natural response of the sample. We augment a widefield epifluorescence microscope with two spatial light modulators (SLM). These allow illumination with arbitrary patterns. Depending on the distribution of fluorophores a considerable reduction in photobleaching and phototoxicity can be expected.

INTRODUCTION

In a fluorescence microscope excitation light is shone through an objective onto a specimen containing fluorophores. These fluorophores absorb excitation light and subsequently emit photons of lower energy. The fluorescence light of in-focus fluorophores is formed into a sharp image, light from out-of-focus areas deteriorates the image by creating a blurred background.

Nowadays it is common to observe the dynamic properties of fluorescently labelled proteins and extract quantitative information about the structures they form within living cells. The length of the study and the accuracy of the result of a given experiment, however, is limited by photobleaching and light induced toxicity in the biological specimen.

One of the by-products of fluorophore excitation is reactive singlet oxygen. The oxidative stress can lead to cell death or more subtle effects such as the suppression of normal cell signalling functions.

In order to extend experiments in time and to follow the fate of cells over many generations, a substantial reduction illumination would be desired.

In ultra microscopy a thin sheet of excitation light is sent from the side along the focal plane of a widefield microscope. Its results are impressive [1]. However, mounting the samples is difficult and long range objectives are used, which limit the collection angles, detection efficiency and resolution.

In [2] a variant of a confocal microscope is developed, that illuminates the specimen according to local fluorophore concentration. Dim areas are only illuminated until the fluorophore content is confirmed to be below the threshold. Areas with high fluorophore content are only illuminated until a certain photon count is reached. Areas of intermediate brightness are illuminated for the full time. The resulting image is of the same perceived image quality as a conventional confocal image but at much lower dosage.

Temporal focusing (TF) and generalised phase contrast (GPC) have been combined in [3]. For TF the ultra-short excitation pulse is diffracted on a grating in an intermediate image. The spectral components enter along a line on the pupil of the objective and only excite fluorophores in a sheet around the focal plane, where they arrive simultaneously. The GPC allows spatial exposure control in the focal plane.

In [4] a micro-lens-based microscope for simultaneous detection of angular and spatial information about the light returning from the sample is shown. Applying their technique for illumination would give a spatio-angular excitation microscope comparable to ours. It would allow simultaneous exposure of in-focus areas with different angles. However, the micro-lenses define the trade-off between angular and spatial resolution. Our approach is more flexible and better suited as a prototype to establish useful illumination schemes.

SPATIO-ANGULAR MICROSCOPE

Figure 1 shows a schematic of our microscope. A rotating micro-lens array and a light tunnel provide uniform illumination in the plane F'''. SLM1 is an array of torsional micro-mirrors. When the mirrors are tilted, they act as a diffraction grating. The aperture B_1 only transmits the zero order of the grating and the lens L_2 forms an intensity image of SLM1 in P'.

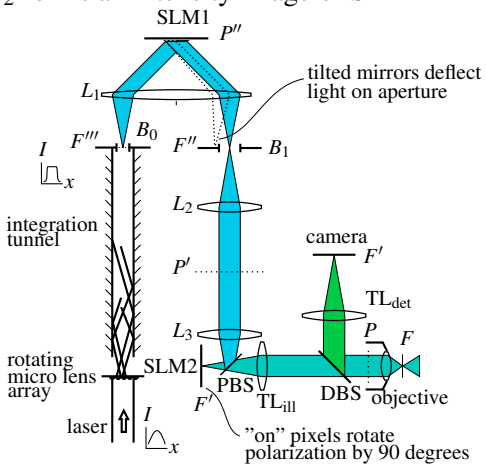

Figure 1: Schematic of our microscope. SLM = spatial light modulator, PBS = polarizing beam splitter, DBS = dichroitic beam splitter, TL = tube lens.

A polarizing beam splitter illuminates SLM2. This display is based on ferroelectric liquid crystals (FLC). The optic axis of the FLC in each pixel has two possible orientations, depending on the applied voltage. On-pixels act as $\lambda/4-$plates and rotate light by 90°. Off-pixel have no effect on the polarization.

SLM1 is imaged into the back focal plane P of the objective. SLM2 is conjugate to the focal plane F in sample space. SLM1 controls the illumination angles while SLM2 selects the area in the sample, that will be illuminated.

The diagram in Figure 2 right, depicts a three-dimensional distribution of beads with 2 μm diameter. The data was obtained by projecting gratings with SLM2 into the specimen and reconstructing optically sectioned slices. After the positions of the beads were known, they were selectively illuminated with SLM1 patterns as shown in 2 left. These patterns were computed by finding areas in the pupil that excite the target bead without exposing out-of-focus beads.

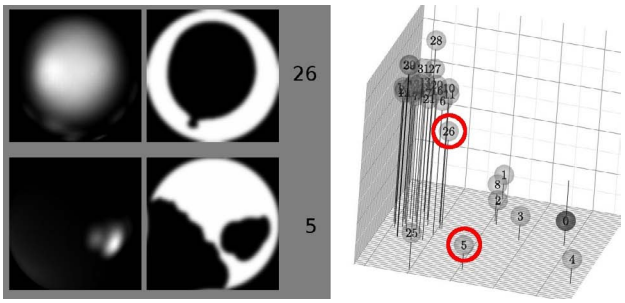

Figure 2: **right:** Sphere model of a sample with three-dimensionally distributed beads. **left:** Optimized SLM1 masks to illuminate bead 26 or bead 5.

A similar approach can be used for time-laps imaging of nuclei in developing embryos. Their structure doesn't change much from one time frame to the next and one could predict the position of the nuclei using the current image stack, while preparing the illumination patterns for the acquisition of the next stack.

CONCLUSION

We built a microscope that can simultaneously control the pattern of the excitation illumination in the pupil P of the objective and the front focal plane F in the specimen.

The two separate displays give the flexibility that is needed in order to investigate illumination strategies while the Heisenberg uncertainty principle prevents tight simultaneous control in the Fourier planes F and P.

Acknowledgements. We thank Jakub Nedbal, Kai Wicker and our project partners at Fraunhofer IPMS (Dresden, Germany), Institut Pasteur (Paris, France), In-Vision (Vienna, Austria) and KLA Tencor (Migdal Ha'emek, Israel). This work was funded by EU FP7 project 215597.

[1] J. Huisken, J. Swoger, F. Del Bene, J. Wittbrodt, E. H. K. Stelzer, *Science* **305**, 1007 (2004).

[2] R. A. Hoebe, *et al.*, *Nature Biotechnology* **25**, 249 (2007).

[3] E. Papagiakoumou, *et al.*, *Nat. Methods* **7**, 848 (2010).

[4] M. Levoy, Z. Zhang, I. McDowall, *Journal of Microscopy* **235**, 144 (2009).

Controlling plasmonic hot-spots by interfering Airy beams

Angela E. Klein,[1,*] Alexander Minovich,[2] Michael Steinert,[1] Norik Janunts,[1] Andreas Tünnermann,[1,3] Dragomir N. Neshev,[2] Yuri S. Kivshar,[2] and Thomas Pertsch[1]

[1] *Institute of Applied Physics, Abbe Center of Photonics, Friedrich-Schiller-Universität Jena, Max-Wien-Platz 1, 07743 Jena, Germany*

[2] *Nonlinear Physics Centre and Centre for Ultrahigh-bandwidth Devices for Optical Systems (CUDOS), Research School of Physics and Engineering, The Australian National University, ACT 0200, Canberra, Australia*

[3] *Fraunhofer Institute of Applied Optics and Precision Engineering, Albert-Einstein-Straße 7, 07745 Jena, Germany*

[*] Corresponding Author: *angela.klein@uni-jena.de*

Abstract

Airy wave packets constitute a special class of nondiffracting waves that accelerate along parabolic trajectories and exhibit self-healing properties. In contrast to other non-diffracting beams like e.g. Bessel beams, Airy beams can also exist in (1+1) dimensions. We demonstrate the generation and near-field mapping of Airy surface plasmon polaritons (SPPs) by specially designed diffraction gratings. By interference of two Airy SPPs, a bright focal spot can be generated. We theoretically and experimentally investigate how the position and the brightness of this hot spot can be controlled by varying the relative positions of the excitation gratings and the phase front of the illuminating beam.

Introduction

Surface plasmon polaritons (SPPs) are electromagnetic waves propagating along metal/dielectric interfaces and exhibit highly localized electromagnetic fields. For applications like light-routing on optical chips and optical addressing of absorbed biomolecules, the generation and manipulation of plasmonic beams is of particular interest. Airy surface plasmons [1, 2] are plasmonic beams that possess remarkable properties such as diffraction-free propagation and a parabolic trajectory. After passing an obstactle, the beam recovers its shape. For one-dimensional wave packets, such as surface plasmon waves, the Airy beams represent the only possible class of non-diffracting beams.

Method

In our experiments we use gratings in the form of rectangular slits in a metal layer to excite surface plasmons (Fig. 1). The grating period along the z axis corresponds to the surface plasmon wavelength, so that SPPs propagating along the z-axes are excited when the gratings are illuminated at normal incidence ($\alpha = 0°$) with a beam polarized along the z axis. Now the grating is subdivided into columns in the x-direction. By selectively shifting the columns along the SPP propagation direction (z axis), the phase of the plasmonic wave packet can be spatially modulated. Phase variations of π are achieved by shifting every second column by half a grating period with respect to the neighboring columns [Fig. 1(d)]. The widths of the columns are chosen to match the zeros of Airy pattern amplitude, as shown in [Fig. 1(b) and (c)]. The resulting interference pattern is characterised by measuring the optical near-field at the sample-surface with fiber-tip based scanning near-field optical microscopy (SNOM).

Results

The generated beams exhibit the main remarkable properties of Airy plasmons, namely self-acceleration, low diffraction and self-healing after passing through surface defects. The measured near-field intensity matches well the theoretical distribution obtained by FDTD simulations. Additional plasmonic excitations

that occur due to imperfect matching of the Airy wavepacket quickly diffract and do not strongly affect the properties of the wavepacket[3].

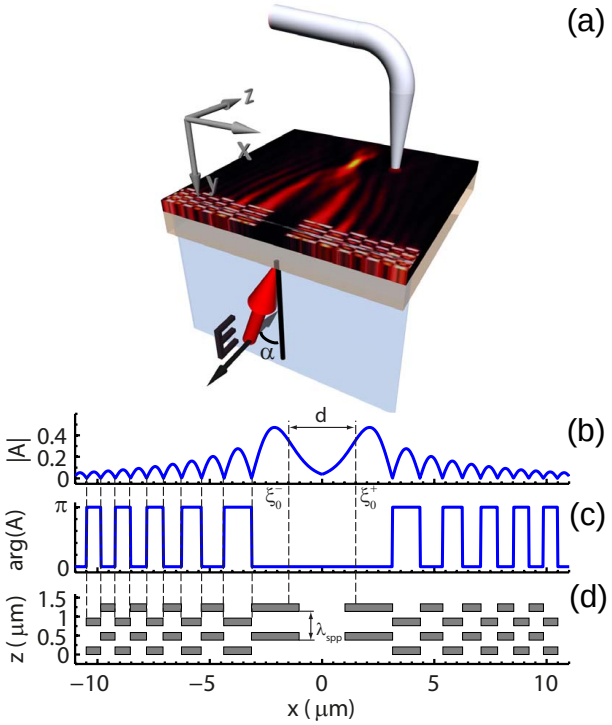

Figure 1: Excitation and interference of Airy plasmons: (a) Schematic of the experimental setup with the mirror symmetric gratings. The gratings are illuminated from the substrate side by a broad Gaussian beam with $\lambda = 784$ nm and polarization along z. (b, c) Absolute value and phase of the amplitude function of the two Airy plasmons. The main lobe half width is $x_0 = 700$ nm. (d) Grating geometry for excitation of Airy plasmons. $\lambda_{SPP} = 764$ nm denotes the SPP wavelength.

Furthermore, we show that a high-intensity spot can be created on a metallic surface by the interference of two Airy plasmons (see Fig. 2). In contrast to hotspots created with the help of nanoantennas, no structuring of the sample in the close vicinity of the sample is necessary. Scanning near-field optical measurements and FDTD-calculations show that the position, shape and brightness of the spot depend on the initial separation distance of the two wavepackets. The high field contrast makes such a high-intensity spot attractive for applications like plasmonic circuitry applications, surface optical tweezers, optical data storage, and biosensing.

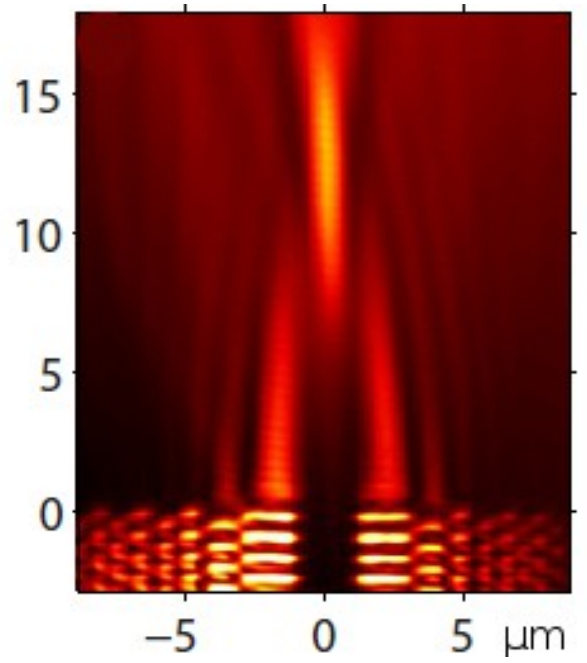

Figure 2: Interference pattern of two plasmonic Airy beams, measured by collection-mode scanning near-field optical microscopy (SNOM)

[1] M. V. Berry, N. L. Balazs, *American Journal of Physics* **47**, 264 (1979).

[2] A. Salandrino, D. N. Christodoulides, *Opt. Lett.* **35**, 2082 (2010).

[3] A. Minovich, *et al.*, *Phys. Rev. Lett.* **107**, 116802 (2011).

Adiabatic Tapers

Andrea Kliner[1], Willi Viehweg[2], Thomas Schreiber[1], Ramona Eberhardt[1] und Andreas Tünnermann[1]

[1]*Fraunhofer Institute for Applied Optics and Precision Engineering, Albert-Einstein-Straße 7, 07745 Jena, Germany*

[2]*University of Applied Sciences Jena, Carl-Zeiss-Promenade2 , 07745 Jena, Germany*

[*]Corresponding Author: *Andrea.kliner@iof.fraunhofer.de*

Abstract

High power fiber laser components are a critical part of monolithic fiber lasers. In this paper we present the characterization results of an adiabatic taper.

INTRODUCTION

Monolithic high power fiber lasers are more and more used in industry and research facilities. The fiber laser component development is an important part of the fiber laser development as they have to be reliable up to several kW without corrupting the good beam quality of fiber lasers. In this contribution we show the manufacture and characterization of an adiabatic taper as an example of a high power fiber laser component that is needed in high power fiber lasers.

ADIABATIC TAPERS

Single-mode performance is a desired behavior in fiber lasers as it is needed for many applications. But single-mode fibers have a low threshold for non-linear effects (NLE) what makes the NLE often the main limiting factor to further increase the power of high power fiber lasers. NLE mainly depend on the power density (power per unit area) and the fiber length. [1] To avoid NLE the fibers have to be short what reduces the pump absorption capabilities. A solution to that are the so-called double clad fibers or large mode area fibers. But bigger fiber cores show usually multi-mode behavior. With the development and utilization of adiabatic tapers it is possible to launch single mode light in multi-mode fibers and still receiving single mode light in the end of the fiber. [2]

EXPERIMENTAL SETUP

In order to fabricate the demonstrator we used the large diameter fusion splicing system (LDS) of the company 3SAE. The LDS uses three electrodes to locally heat the fiber while it is pulled apart to produce the taper. The used fiber was the active fiber 1099sAFO from the IPHT. It has an 18µm core diameter, 375µm inner cladding with an NA of 0,12. The demonstrator fiber was tapered down to 6µm core with an inner cladding of 125 µm. The test setup for the taper is shown in figure 1. We have used a Fiber-Picktailed single-mode laser from Thorlabs to launch ~5mW of 1060 nm light into the fiber. To characterize the taper we used a ccd beam profiler of the company Duma Optronics LTD and measured the power. We used the same setup to characterize the same fiber without tapering it to be able to compare the results.

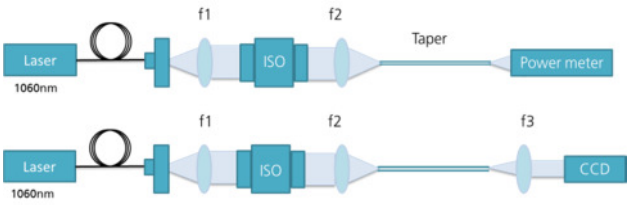

Fig. 1: Test setup for the tapered fibers

Results

The power measurement shows 94% of power throughput. What is a good result but needs to be verified in a high power test setup.

2a)

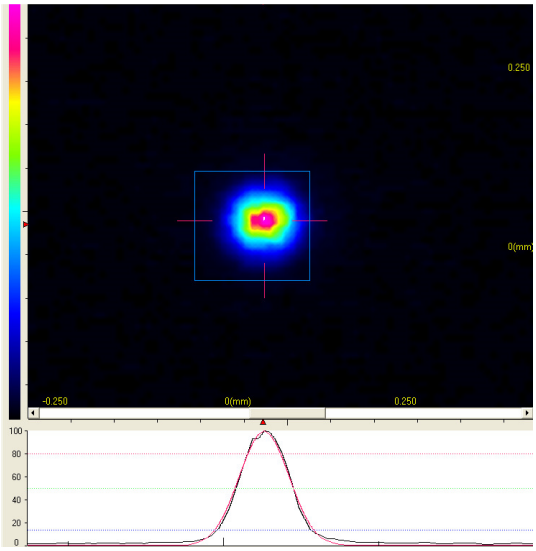

2b)

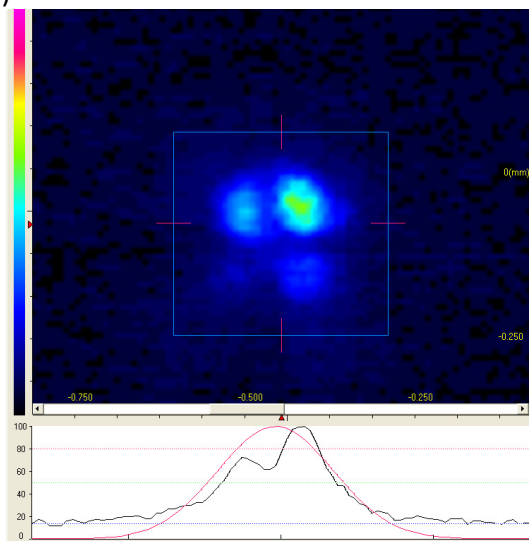

Fig. 2: Beam profile pictures a) beam profile after the taper b) beam profile after the fiber without tapering it.

Figure 2a) shows a nearly Gaussian beam profile. In figure 2b), when the beam profile of the fiber without taper was tested the beam profile shows multi-mode beam output. We have not completed the characterization of the taper but it would include using it in a high power fiber laser to see how thermal behavior is. As fibers with a 20µm core diameter and 400 µm inner cladding diameter are standard fibers this result shows great possibilities for using this technology in high power fiber lasers.

[1] Agraval, Nonlinear Fiber Optics, Academic Press, ISBN 0-12-045140-9
[2] Zellmer, Holger, Dr., 99441 Magdala, Tünnermann, Andreas, Prof. Dr., 07743 Jena, Patent DE10009379C2 25.04.2002

Inscription of fiber Bragg gratings in a 120 core fiber with ultrashort pulses

Ria G. Krämer[1], Christian Voigtländer[1], Jens U. Thomas[1], Roger Haynes[2], Tim A. Birks[3], Andreas Tünnermann[1,4], Stefan Nolte[1,4]

[1]*Institute of Applied Physics, Abbe Center of Photonics, Max-Wien-Platz 1, 07743 Jena, Germany*
[2]*innoFSPEC – Leibniz-Institut für Astrophysik Potsdam, An der Sternwarte 16, 14482 Potsdam, Germany*
[3]*Centre for Photonics and Photonic Materials, Department of Physics, University of Bath, Claverton Down, Bath, BA2 7AY, UK*
[4]*Fraunhofer Institute for Applied Optics and Precision Engineering, Albert-Einstein-Str. 7, 07745 Jena, Germany*

[*]Corresponding Author: *ria.kraemer@uni-jena.de*

Abstract

We present first results of femtosecond inscribed fiber Bragg gratings (FBG) in a 120 core fiber. The multicore FBG were written using the phase mask scanning technique. For all cores the FBG was characterized by measurement of the transmission spectra. We could achieve strong gratings for a large part of the multicore cross-section.

INTRODUCTION

For ground based near-infrared astronomical observations a spectral filtering of the narrow emission line of the atmospheric OH molecules is essential. A solution offers the concept of the "photonic lantern" [1], where light from a multimode fiber is transferred in single mode fibers in which spectral filters in the form of fiber Bragg gratings (FBG) are integrated [2]. In order to reduce complexity and cost, a concept is developed, where the single mode fibers are replaced by a multicore fiber (MCF). Therefore an inscription technique for FBG in a MCF is desired, which provides homogeneous spectral response over all cores. We present first results of the inscription of a FBG in a MCF with 120 cores using femtosecond laser pulses.

INSCRIPTION SETUP

The MCF was developed at the University of Bath [3] in collaboration with innoFSPEC of the Leibnitz Institute of Potsdam. The MCF (see Figure 1(a)) features 120 Ge-doped cores with a diameter of 3.9 µm, which are arranged hexagonal. The cladding diameter is 230 µm. The FBG was inscribed with the femtosecond laser system Spitfire (Spectra Physics) (120 fs pulse duration at 800 nm) using the phase mask scanning technique (Figure 1(b)) [4]. The fs pulses were focused with a cylindrical lens (20 mm focal length) through a phase mask into the fiber.

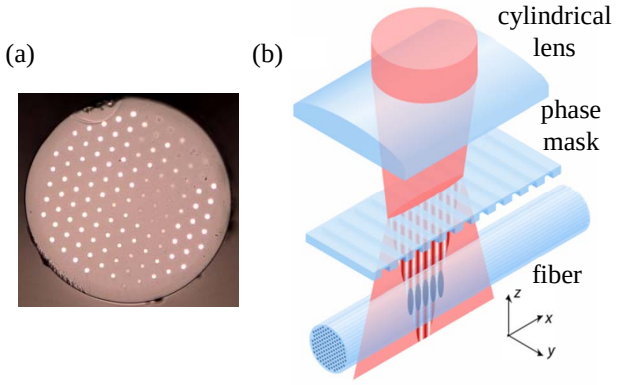

Figure 1: (a) Microscop image of the MCF. (b) Schematic of the phase mask scanning technique.

Since the modification of the refractive index is limited to the focal spot, fiber and phase mask were both moved with respect to the inscription beam to scan over the MCF cross-section, with a total scan area of 200 µm along the y-axis and 230 µm in z-direction.

EXPERIMENTAL RESULTS

In Figure 2 the measurement of the reflectivity as well as the Bragg wavelength of all cores are shown. The red arrow indicates the direction from which the inscription laser was incident. Black circles depict cores where no Bragg reflection could be measured. As one can clearly see, the FBG properties are not evenly distributed over the cross-section of the

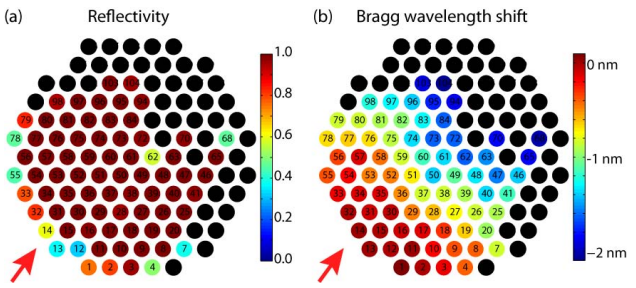

Figure 2: Characterization of the reflectivity (a) and the Bragg wavelength shift of the FBG.

MCF. The upper row of cores with respect to the inscription direction show only low reflectivities, in the center and upper half strong gratings were observed, whereas in the lower part no gratings at all are present. Also, the Bragg wavelength is blueshifted about 2 nm along the inscription direction. We also observed different spectral behavior of the FBG along the cross-section. The cores depicted with green circles in Figure 3(b) show very clean spectral responses with almost no radiation or cladding mode losses (Figure 3(a)). However, cores in the center (red circles) show strong radiation losses as well as a spectral broadened Bragg reflection peak.

We believe the inhomogeneities of the multicore FBG are a result of self-focusing of the inscription beam inside the fiber as well as focusing effects of the curvature of the fiber. Due to these effects, the focus of the inscription beam did not reach the far side of the fiber, hence, the center of the MCF was structured multiple times. This explains the strong radiation losses of the FBG in the center. The strong Bragg wavelength shift can be attributed to wave front aberrations arising at the fiber curvature [5].

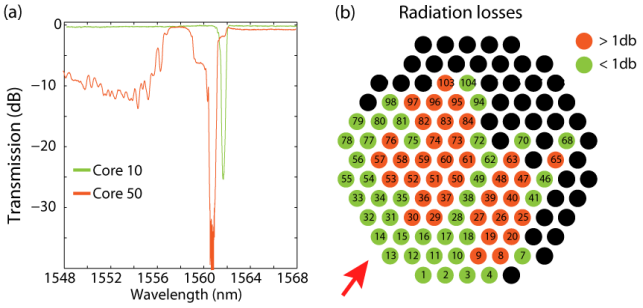

Figure 3: (a) Transmission spectra of two cores of the FBG. (b) Distribution of „clean“ spectral responses (green circles) and position of cores with radiation losses exeeding 1 dB (red circles).

CONCLUSION

We present first results of the femtosecond inscription of fiber Bragg grating in a 120 core fiber. The inhomogeneity of the multicore FBG can be attributed to focusing effects of the curvature of the fiber as well as self-focusing of the inscription beam inside the fiber. Therefore, current work is to circumvent these effects with appropriate adaptions of the inscription setup in order to get a clean and homogeneous spectral response for all cores.

ACKNOWLEDGEMENTS

We acknowledge financial support by the German Federal Ministry of Education and Research (BMBF) under contract No. 13N9687 and the German Research Foundation (DFG). Ria G. Krämer also acknowledges support by the Abbe School of Photonics.

[1] S. Leon-Saval, T. Birks, J. Bland-Hawthorn, M. Englund, Optics Letters **30**, 19 (2005).

[2] J. Bland-Hawthorn, S. C. Ellis, S. G. Leon-Saval, R. Haynes, M. M. Roth, H.-G. Löhmannsröben, A. J. Horton, J.-G. Cuby, T. A. Birks, J. S. Lawrence, P. Gillingham, S. D. Ryder, C. Trinh, Nature Communications **2**, 581 (2011).

[3] T. A. Birks, B. J. Mangan, A. Dìez, J. L. Cruz, D. F. Murphy, Optics Express **20**, 13 (2012).

[4] J. Thomas, C. Voigtländer, R. G. Becker, D. Richter, A. Tünnermann, S. Nolte, Laser & Photon. Rev., doi 10.1002/lpor.201100033 (2012).

[5] C. Voigtländer, R. G. Becker, J. Thomas, D. Richter, A. Singh, A. Tünnermann, S. Nolte, Opt. Mater. Express **1**, 4 (2011).

Integration of Functional Optical Devices in Lithium Niobate Wafers by Direct Femtosecond Laser Writing

Sebastian Kroesen[*1], Raphael Heger[1], Wolfgang Horn[1], and Cornelia Denz[1]

[1] *Institute for Applied Physics, Westfälische Wilhelms- Universität, Corrensstr. 2-4, 48149 Münster, Germany*

[*]Corresponding Author: *s.kroesen@wwu.de*

Abstract

We demonstrate the fabrication of photonic devices in lithium niobate wafers by direct femtosecond laser writing. Low loss type II double line waveguides, 2D-structures as well as multiscan type I waveguides are presented. Furthermore power-splitters, a Mach-Zehnder interferometer and electro-optical tunable Bragg grating waveguides (BGWs) have successfully been integrated to perform optical signal processing at λ = 1.55 μm. Different approaches such as point-by-point integration and burst writing are discussed.

INTRODUCTION

Direct integration of functional optical devices by femtosecond laser writing has emerged as a powerful fabrication technique within recent years [1-3]. The basic principle relies on strongly localized material modification by nonlinear absorption inside the host material. One of the most attractive aspects of this technique is the feasibility of producing three-dimensional refractive index changes simply by translating the material relative to the focal point of the writing beam. Hence, a variety of optical elements such as waveguides, splitters and Bragg Gratings have already been realized. Besides integration in silica glasses it is often desirable to access the unique advantage of high-speed response in electro-optic materials such as lithium niobate, which is widely used in optical communications.

In this contribution we demonstrate integration of various photonic devices in $LiNbO_3$ wafers operating at λ = 1.55μm. High quality low loss waveguides, power splitters and electro-optical tunable devices such as Mach-Zehnder modulators and integrated Bragg grating waveguides (BGWs) are presented.

EXPERIMENTAL SETUP

The experimental setup for the integration and characterization of functional optical devices is depicted in Fig. 1. To induce the refractive index change a Ti:Sa femtosecond laser system at λ = 800 nm with a repetition rate of 1 kHz and 130 fs pulse duration is used. The pulses are attenuated to 250-800 nJ and focused inside the host material using a 100x microscope objective with a NA of 0.9.

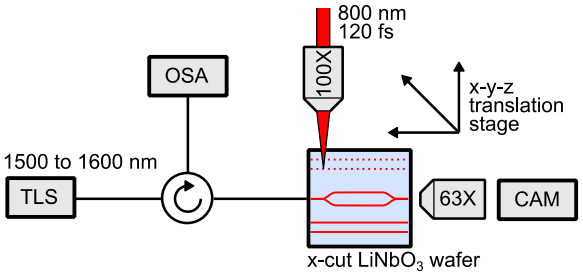

Figure 1: Schematic experimental setup for the integration and characterization of functional optical devices. The samples are but-coupled to a tunable laser source (TLS) or broadband emitting diode and the near-field mode profiles are imaged using an InGaAs camera (CAM). The reflection spectra of integrated Bragg grating waveguides are characterized by an optical spectrum analyzer (OSA).

We use commercially available 3” x-cut Lithium Niobate wafers with a thickness of 500 μm and a x-y-z translation stage (Aerotech). All presented waveguide structures are fabricated approximately 100 μm under the surface. A constant translation velocity of 30 μm/s is used to ensure a sufficient overlap of the refractive index voxels produced by the single laser pulses.

EXPERIMENTAL RESULTS

The origin of type II refractive index modifications inside crystalline materials is mainly caused by a stress field induced by the local volume change inside the laser focus [4]. Hence, a double line structure is required to obtain a guided mode. Fig. 2 (a-b) shows the microscope image of the coupling facet of such a structure and the corresponding near-field mode profile.

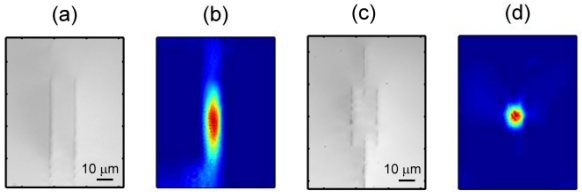

Figure 2: Microscope image of the coupling facet and near-field mode profile of double line (a,b) and quad-waveguide structures (c,d). The horizontal line spacing is 15 µm in both cases.

It is evident that due to the intrinsic asymmetry the mode circularity is rather low. Therefore, a two-dimensional quad-structure consisting of four waveguide lines is suggested to increase the light confinement in the vertical direction (Fig. 2. (c-d)). The presented waveguides exhibit a very low insertion loss of less than 1.3 dB for a 10 mm long waveguide indicating the high quality of the induction technique. These waveguides can be employed to fabricate power splitters and Mach-Zehnder interferometers operating at $\lambda = 1.55$ µm.

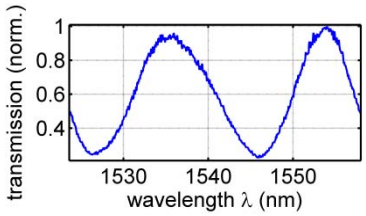

Figure 3: Power transmission of an asymmetric Mach-Zehnder interferometer.

To demonstrate the basic functionality Fig. 3 shows the power transmission of an asymmetric MZI. The interferometer arms exhibit a path length difference that causes constructive and destructive interference at the exit face. Using for instance integrated electrodes fast electro-optical modulation can be employed [5].

One of the key components of optical signal processing, a Bragg grating can be integrated by logging the repetition rate of the laser system to the sample translation, which is shown for various design wavelengths inside the c-band in Fig. 4 (a).

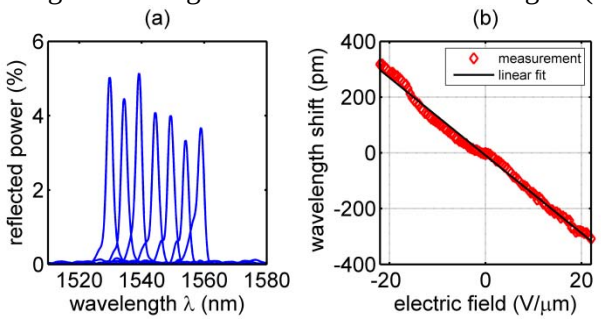

Figure 4: Bragg grating waveguides (BGWs) and electro-optical tuning of the spectral response.

A power reflection of approximately 4 to 6% is achieved with a bandwidth of 2.3 nm. By changing the inscription parameters, the bandwidth could be reduced to less than one nanometer. Furthermore, Fig. 4 (b) demonstrates electro-optical tuning of the central reflection wavelength by $\Delta\lambda = 625$ pm [6].

CONCLUSION

We have successfully demonstrated direct femtosecond integration of functional optical devices in lithium niobate. High quality waveguides, 2D structures, a Mach-Zehnder interferometer and electro-optically tunable Bragg grating waveguides are presented emphasizing prospects of all-integrated signal processing and filtering applications.

[1] J. Thomas et al., Physica Status Solidi (a) **208**, 276 (2011).
[2] G. Della Valle et al., Journal of Optics A: Pure and Applied Optics **11**, 013001 (2009).
[3] R.R. Gattass and E. Mazur, Nat Photon **2**, 219 (2008).
[4] J. Burghoff, S. Nolte, and A. Tünnermann, Applied Physics A **89**, 127 (2007).
[5] Y. Liao, et al., Opt. Lett. **33**, 2281 (2008).
[6] W. Horn, S. Kroesen, and C. Denz submitted to Applied Physics Letters (06 2012)

Comparison of different design concepts for large mode area optical fibers

Adrian Lorenz*, Siegmund Schröter, Matthias Jäger, and Harmut Bartelt

Institute of Photonic Technology, Albert-Einstein-Straße 9, 07745 Jena, Germany

*Corresponding Author: *adrian.lorenz@ipht-jena.de*

Abstract

We present a comparison of different fiber designs with respect to bend sensitivity and effective mode area for high power transmission applications.

INTRODUCTION

In addition to signal transmission, the transport of laser light with high beam quality and power is an important field of application of optical fibers. Single mode fibers are able to transmit light with high beam quality, but the small light guiding core may result in high local intensities. This may lead to undesired nonlinear optical effects (e.g. stimulated Raman scattering) or even to the destruction of the fiber. Scaling of the transmittable power with a larger core diameter requires the reduction of the numerical aperture $NA = \sqrt{n_{core}^2 - n_{clad}^2}$ in order to maintain single mode performance. Technological conditions and weaker light guidance limit the possibilities of reducing the NA. We have therefore investigated how well hihger order modes can be suppressed by bending for fibers which are designed to allow propagation of a few higher modes in addition to the fundamental mode.

BEND SENSITIVITY

Reducing the numerical aperture of a fiber by increasing the radius of the core R_{core} to realize a V-parameter near $V = \frac{2\pi}{\lambda} R_{core} NA = 2.405$ (which is single-mode condition) means that the effective mode index of the fundamental mode n_{eff} gets close to the cladding index n_{clad}: Therefore the confinement of the modes decreases. This results in a high sensitivity to external influences such as bending. Bent fibers can be modeled using modesolvers in combination with a coordinate transformation resulting in an equivalent refractive index profile n_{equ}.

$$n_{equ}(x,y) \approx n_0(x,y) \cdot \left(1 + \frac{x}{R_{eff}}\right). \qquad (1)$$

The undisturbed index profile is denoted by $n_0(x,y)$ and the effective bend radius including photoelastic effects by R_{eff} with x the distance from the fiber center in the bend-plane. The modes resulting from this index distribution are deformed and shifted compared to the modes of a straight waveguide (Fig. 1).

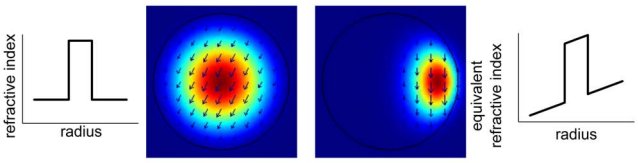

Figure 1: Deformation of mode field due to bending and equivalent index profile.

FIGURE OF MERIT

It is necessary to focus on certain properties for a comparison of different fibers. A measure for suppressing higher order modes is the ratio of higher order mode (HOM) loss to fundamental mode (FM) loss namely:

$$lossratio = \frac{loss(\mathrm{HOM})}{loss(\mathrm{FM})}. \qquad (2)$$

For high power applications it is most important to know whether there is a lower threshold to nonlinear effects due to bend induced mode deformation. This is characterised by the effective mode area

$$A_{eff} = \frac{(\iint |E|^2 dA)^2}{\iint |E|^4 dA} \qquad (3)$$

with E being the electric field of the mode. A way to compare special fibers was proposed by [1] while plotting $lossratio$ against A_{eff} of the bent fiber. Different designs are compared in Fig. 2. The aim is finding a fiber with high effective area and high loss ratio which then is found in the upper right corner of Fig. 2.

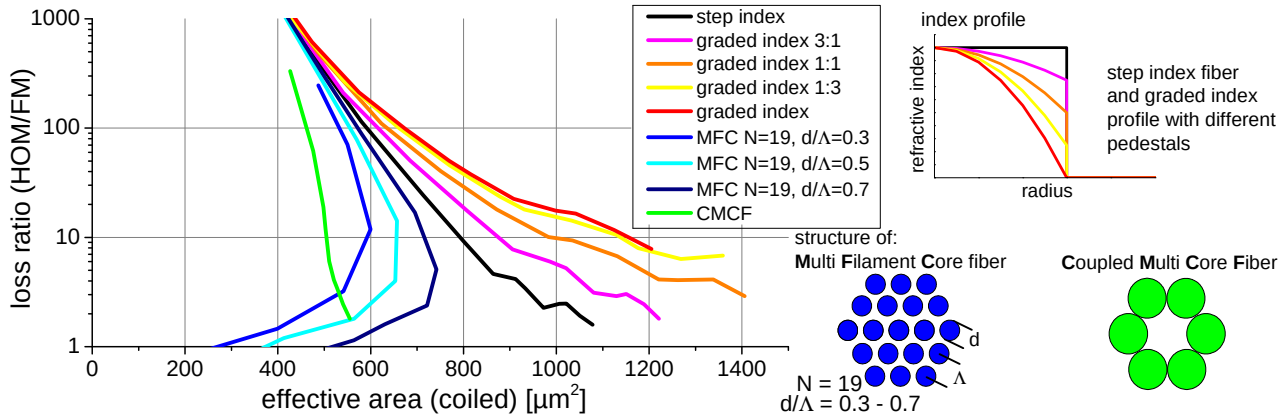

Figure 2: Map plot for different fiber design concepts.

FINDING COMPARABLE FIBERS

Following [1] we use a loss of 0.1 dB/m for the fundamental mode at a fixed bend radius of $R = 15$ cm. The sets of fibers to be compared are generated by scaling the geometry and varying the index difference to meet the given bend loss of the fundamental mode. For example, calculating the bend loss of step index fibers with $R_{core} = 16$ µm and index differences between $3...9 \cdot 10^{-4}$ we find the data shown in Fig. 3. Interpolation for a bend loss of 0.1 dB/m gives the index difference $n_{core} - n_{clad} = 6.03 \cdot 10^{-4}$ in this case. This procedure is repeated for all different fiber-design-families to be considered.

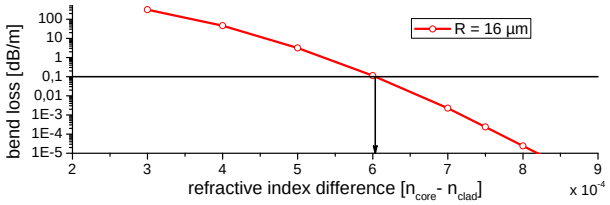

Figure 3: Finding refractive index differences for a given geometry parameter to meet a bend loss of 0.1 dB/m.

Once the set of fibers is found we are also able to compare other properties beyond the loss ratio, such as the shift of the mode field which is important for gain confinement in active fibers.

For comparison we have considered fibers with *step index* and *graded index* profile. Additionally to them there are more structures to be calculated and inserted into the "map" of Fig. 2. For instance one can combine these profiles resulting in *graded index fibers with different pedestals*. Focussing on the question if also multi core fibers are suitable for high power transmission or not leads to the anyalsis of *multi filament core fibers (MFC)* with hexagonal lattice, $N = 19$ cores and d/Λ =0.3 to 0.7 and *coupled multi core fibers (CMCF)* as shown in Fig. 2. Furthermore investigations on other special designs based on microstructured fibers are in progress.

CONCLUSION

We have compared different fiber designs concerning their effective fundamental mode area and their loss ratio for a bent fiber arrangement. Best performance was shown for fibers of graded index type which are closest to the aim of combining high effective area and high loss ratio.

Founding by Thuringian Ministry of Education, Science and Culture (project MOFA and EFRE program) is greatfully acknowledged.

[1] J.M. Fini, *Optics Express* **14**, 2 (2006).

Fast High-Resolution Fluorescence Microscopy by Nonlinear Structured Illumination

Hui-Wen Lu[*2], Ronny Förster[1], Aurélie Jost[1,2], Kai Wicker[1,2], and Rainer Heintzmann[1,2]

[1] *Institute of Photonic Technologies (IPHT), Albert-Einstein-Straße 9, 07745 Jena, Germany*

[2] *Institute of Physical Chemistry, Lessingstraße 1, 07743 Jena, Germany*

[*]Corresponding Author: *hui-wen.lu@ipht-jena.de*

Abstract

With the technique of linear structured illumination microscopy (linear SIM), the resolution can be improved by a factor of 2 compared to conventional wide-field fluorescent microscopy which usually has a limited resolution of ~200 nm in the lateral direction. Further resolution improvement can be achieved by the use of a nonlinear photo-response. This nonlinear photo-response can be obtained by saturating either the on-state or the off-state of a fluorophore.

INTRODUCTION

The high-resolution imaging of living cells is at the heart of interest in biomedical research. The use of electron microscopy is precluded for living cells and fluorescence microscopy is thus the method of choice. It has been shown theoretically and in preliminary experiments that the resolution of light microscopy can be pushed to new limits by the use of a nonlinear photo-response. SIM is a wide-field technique and can produce increased lateral and axial resolution [1]. The use of structured illumination should allow a resolution of < 50 nm when a non-linear dependence is exploited as can be obtained by reversible photoswitching [2]. The photoswitchable dye can be for example mIrisFP, rsEGFP or similar variants. To realize the 50 nm resolution the construction of a fast (> 10 full frames/s) data acquisition setup for structured illumination will be needed. It will be realized with the help of a spatial light modulator (SLM). Besides, new sophisticated algorithms will be needed for a fast reconstruction of high quality images.

PRINCIPLE OF NONLINEAR STRUCTURED ILLUMINATION MICROSCOPY

The resolution of optical systems is limited by the numerical aperture (NA) and the wavelength of light. In frequency space, the resolution of a microscope is represented by the support of the optical transfer function (OTF) which is specified by its cut-off frequency. By projecting a sinusoidally varying pattern into the sample, unresolvable high spatial frequency information is down-modulated into the region of the OTF support of the microscope. In linear SIM, the fluorescent emission intensity depends linearly on the intensity of the illumination pattern. The corresponding fluorescent emission of a sinusoidal structured illumination pattern yields three diffraction orders which mix with the underlying spatial frequencies in the sample in the Fourier plane, see Figure 1. In order to reconstruct the raw data for achieving an isotropic superresolution image in linear SIM, it requires at least three different phase-shift images along all three different orientations of the grating.

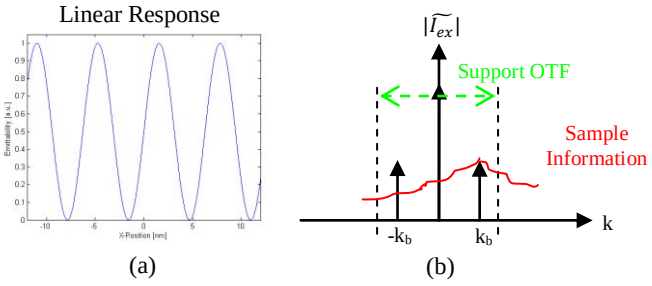

Figure 1 (a) Pattern of the sinusoidal emittability distribution generated by low-intensity patterned excitation. (b) Scheme of the emittability pattern of (a) in Fourier space [3].

Further resolution improvement can be achieved in nonlinear structured illumination microscopy (NLSIM) by saturating either the on-state or the off-state of a photoswitchable dye or a photoswitchable fluorescent protein. The effective illumination

pattern provides a nonlinear photo-response of the fluorescent emission which leads to more higher-order harmonics appearing in the Fourier plane. With this technique substructure information in the sample with even higher spatial frequency is now moved into the region of OTF support and can be resolved by an optical microscope system after image reconstruction, see Figure 2. In theory, the number of higher-order harmonics in NLSIM is in principle infinite which leads to unlimitedly high resolution. In practice, however, the achievable NLSIM resolution will be limited by the signal-to-noise ratio of the raw data [3] [4]. Moreover, the number of images required for a superresolution NLSIM image is much higher than for linear SIM. Consequently, the acquisition time takes longer and more sophisticated algorithms for reconstructing NLSIM image are needed.

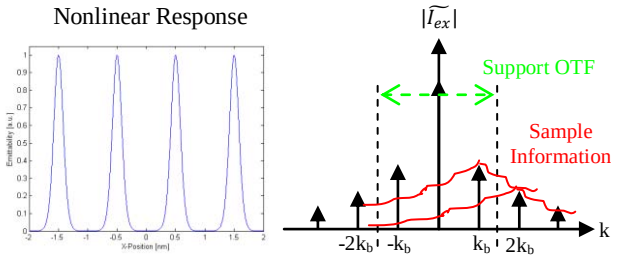

Figure 2 (c) Emittability distribution in real space with off-state saturation of the fluorophore. (d) Corresponding emittability pattern in Fourier space [3].

EXPERIMENTAL SETUP AND INITIAL EXPERIMENT RESULT

A fast (> 10 full frames/s) data acquisition SIM setup is under construction. The aim of the fastSIM system is to replace the grating, which needs mechanical movement, by a spatial light modulator (SLM), see Figure 3. With the help of the SLM, the changing rate of the grating pattern in the sample plane can be up to 1 kHz at most. Accordingly, the acquisition time will be short enough for the imaging of living cells.

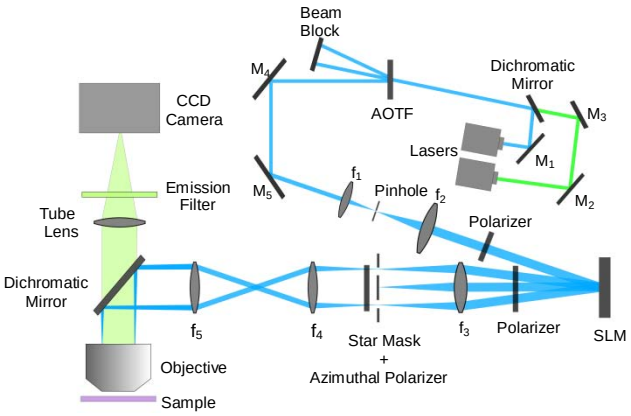

Figure 3 Current setup of the fastSIM system. The acousto-optic tunable filter (AOTF) acts as a fast shutter. The spatial light modulator (SLM) produces structured illumination patterns in the sample plane.

Purified microtubules labeled with Dronpa, a fluorescent photoswitchable protein, have been experimentally tested in a NLSIM system by the work of Gustafsson and coworkers. The resolution can be approximately enhanced down to 41 nm [2]. Other alternatives are mIrisFP and rsEGFP. The initial photoswitching tests of rsEGFP have been done on a comercial SIM system, ELYRA S1, see Figure 4.

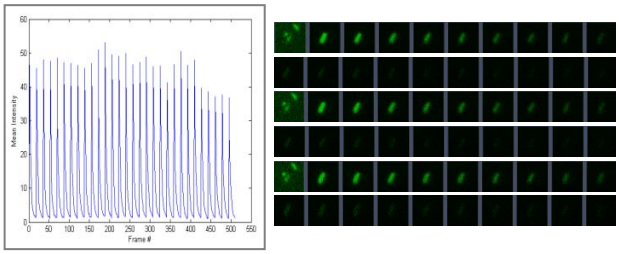

Figure 4 Photoswitching Process of rs-EGFP with 405 nm laser activation and 488 nm laser deactivation.

[1] R. Heintzmann, M. Gustafsson , Reports Nat Photonics **3**: 362-364 (2009).

[2] E. H. Rego et al., PNAS Early Edition 10.1073/pnas. 1107547108 (2011)

[3] R. Heintzmann et al., Opt. Soc. Am. A **19**: 1599-1609 (2002)

[4] M. Gustafsson, PNAS **102**:13081-13086 (2005)

Flexible Simulation Tool for Talbot - Lithography to Fabricate Various Three-dimensional Microstructures

Jacqueline Maaß[*1], Benjamin Ryba[2], Daniel Thomae[2], Oliver Sandfuchs[3], Alexandre Gatto[1], and Robert Brunner[2]

[1]*Carl Zeiss Jena GmbH, Carl-Zeiss-Promenade 10, 07745 Jena, Germany*

[2]*University of Applied Sciences Jena Carl-Zeiss-Promenade 2, 07745 Jena, Germany*

[3]*Hochschule Hamm-Lippstadt, Marker Allee 76-78, 59063 Hamm, Germany*

[*]Corresponding Author: *maass@zeiss.de*

Abstract

The Talbot-effect leads to a self-imaging process in well-defined distances behind a periodic mask pattern which is illuminated with a monochromatic plane-wave. Effectively, various three-dimensional intensity distributions in the Fresnel region can be used for micro- and nano-lithography.

In this contribution we present an effective and flexible modeling approach for the fast calculation of Talbot carpets from initially two-dimensional mask patterns. The introduced numerical algorithm is based on a modified angular-spectrum method, which allows considering boundary effects of the Talbot region from a mask with finite aperture.

For the simulation of micro-optical structures it is necessary to take the fabrication steps into account. Therefore, the three-dimensional intensity distribution behind the mask must be calculated in different media with different complex refraction indices. The second part of the paper discusses the exposure behavior of the photoresist. As a final step in our computation, the developing of the resist is calculated. The result comprises the spatially distributed volume elements within the medium – the microstructure.

---

[1] J. Jope, O. Sandfuchs, A. Deparney, A. Gatto, S. Sinzinger, R. Brunner, DokDok, p. 60 (2011).

[2] J. Maaß, O. Sandfuchs, A. Gatto, R. Brunner, SPIE Photonics Europe [8428-55] (2012).

[3] S. Jeon, J.-U. Park, R. Cirelli, S. Yang, C. E. Heitzmann, P. V. Braun, P. J. A. Kenis, J. A. Rogers, PNAS, Vol. 101, No. 34 (2004).

[4] F. H. Dill, IEEE, Vol. ED-22, No. 7 (1975).

[5] K. H. Toh, A. R. Neureuther, E. W. Scheckler, IEEE Comp.-Aided Design .., Vol. 13, No. 5 (1994).

[6] E. W. Scheckler, N. N. Tam, A. K. Pfau, A. R. Neureuther, IEEE Comp.-Aided Design.., Vol. 12, No. 9 (1993).

[7] R. Liu, J. J. Zheng, H. J. Zhou, Y. C. Tian, G. Liu, L. G. Shen, IEEE Int. Conf. Inf. Acqu. (2007).

Single-shot carrier-envelope phase measurement based on stereographic above-threshold ionization in the multi-cycle regime

Max Möller[1,2], Tim Rathje[1,2], Daniel Adolph[1], A. Max Sayler[1,2], Gerhard G. Paulus[1,2,3]

[1]*Institut für Optik und Quantenelektronik, Friedrich-Schiller-Universität Jena*
Max-Wien-Platz 1, 07743 Jena, Germany

[2]*Helmholtz Institut Jena*
Max-Wien-Platz 1, 07743 Jena, Germany

[3]*Department of Physics, Texas A&M University*
College Station, Texas 77843, USA

[*]Corresponding Author: *max.moeller@uni-jena.de*

Abstract

Polarization gating is used to extend carrier-envelope phase (CEP) measurement based on high-energy above-threshold ionization to the multi-cycle regime. The single-shot CEP precisions achieved are better than 175 and 350 mrad for pulse durations up to 10 fs and 12.5 fs, respectively. Thereby, only 130 µJ of pulse energy are required which opens the door to study and control of CEP-dependent phenomena in ultra-intense laser-matter interaction using optical parametric chirped pulse amplifier based tera- and petawatt class lasers.

INTRODUCTION

Many phenomena in strong-field laser physics and attosecond science are probed and controlled with few-cycle pulses, e.g. high harmonic generation including the generation of attosecond pulses, above-threshold ionization and non-sequential double ionization. As the time dependent electric field dictates the dynamics of strong-field phenomena, a precise characterization of the few-cycle pulses is crucial for understanding and control of the highly non-linear interactions.

The waveform of a Fourier-transform limited Gaussian pulse, $E(t) = E_0 \exp[-2ln2\, t^2/\tau^2]\cos(\omega t + \varphi_{CE})$, is characterized by the peak electric field, E_0, the full-width at half of the maximum (FWHM) duration, τ, the carrier-frequency, ω, and the carrier-envelope phase (CEP). Typically, several devices are used to measure these quantities, e. g. the pulse duration is measured using autocorrelation, frequency resolved optical gating (FROG) or spectral phase interferometry for direct electric field reconstruction (SPIDER) and the CEP is most often characterized and controlled based on f-2f interferometers.

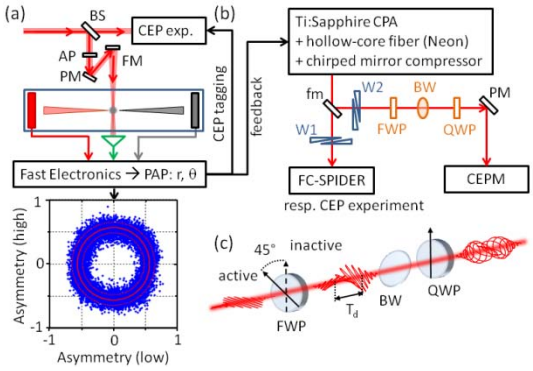

Fig. 1: (a) Illustration of the CEPM. (b) Experimental setup to study the improving effects of polarization gating as function of pulse duration (c) Birefringent optics used to generate laser pulses with polarization gate.

Stereographic above-threshold ionization (ATI) is a recently implemented approach for measuring the CEP and pulse duration of every single-shot in a kHz pulse train of few-cycle pulses simultaneously [1]. The technique facilitates CEP tagging, i.e. measuring the CEP for each laser shot in parallel to another measurement which allows one to probe CEP-dependent phenomena without CEP locking. Alternatively, operating the stereo-ATI measurement

as a carrier-envelope phase meter (CEPM) can be used as basis for CEP locking schemes which improves mid-term (a few second) and long-term (hours) CEP stability. Moreover, the CEPM is a powerful, real-time diagnostic tool for reliable monitoring of intense ultrashort pulses with attosecond sensitivity. So far, the applicability of the CEP measurement is limited to intense linearly polarized few-cycle pulses generated from Ti:sapphire laser sources.

Here we present an implementation of polarization gating (PG) [2] for CEP measurement based on stereo-ATI in the multi-cycle regime [3] and investigate the improvements as function of pulse duration.

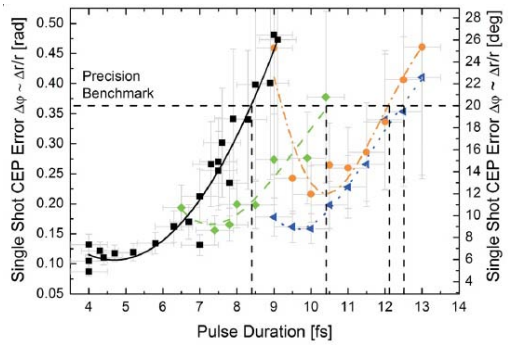

Fig. 2: Achieved single-shot precision as function of pulse duration with inactive and active PG for different gate configurations. The lines are fitted peak functions to guide the eye.

CARRIER-ENVELOPE PHASE METER

The CEPM consists of two opposing time-of-flight electron spectrometers which measure high-energy photoelectron spectra along the polarization axis of the focused laser beam, see Fig. 1 (a). A simple and fast CEP analysis from the photoelectron spectra is achieved by calculating the integrated left-right contrast in the energy-dependent yield of the photoelectrons for two different energy regions using fast electronics. This yields two asymmetry parameters for each laser shot which are the coordinates in the parametric asymmetry plot (PAP), shown in Fig. 2 (a). In this plot, the radial coordinate, r, is a measure for the amplitude of the symmetry which is related to the pulse duration (for linearly polarized pulses), τ, while the angular coordinate, ϑ, belongs to the CEP [1]. The achieved single shot precision of the CEP measurement, $\Delta\varphi$, can be approximated as $\Delta\varphi \cong \Delta r/r$ yielding a single-shot precision of better than 113 mrad for linearly polarized sub-4 femtosecond pulses [4].

POLARIZATION GATING

As the pulse duration increases, the precision of the CEPM decreases, which ultimately limits the operating range of the CEPM in pulse duration to few-cycle pulses, i.e. 8.5 femtoseconds. PG [2,3] allows one to increase the CEP-dependent asymmetries in the left-right ATI spectra from multi-cycle laser pulses and enables a precise single-shot CEP measurement in the multi-cycle regime.

In our experiments, the benefits of PG are studied as function of pulse duration and for different configurations of the PG. Birefringent optics are used to form laser pulses with PG, i.e. to manipulate the incoming laser pulses to exhibit a time-dependent ellipticity that evolves from elliptical to linear to counter-rotating elliptical, see Fig. 1 (c). Fig. 2 shows the achived single-shot precision as function of pulse duration and for different gate configurations.

In conclusion, polarization gating with the CEPM enables precise, single-shot CEP measurement of multi-cycle pulse up to 12.5 femtoseconds pulse duration. The precisions achieved for the CEP measurement with PG are 175 mrad and 350 mrad for pulse durations of 10 femtoseconds and 12.5 femtoseconds, respectively.

[1] T. Rathje, N. G. Johnson, M. Möller, F. Süßmann, D. Adolph, M. Kübel, R. Kienberger, M. F. Kling, G. G. Paulus and A. M. Sayler, J. Phys. B: Mol. Opt. Phys. **45** (2012), 074003 and references there in.

[2] Z. Chang, Phys. Rev. A 7**0**, (2004), 043802

[3] M. Möller, A. M. Sayler, T. Rathje, K. Rühle, G. G. Paulus, Appl. Phys. Lett. **99**, 121108 (2011)

[4] A. M. Sayler, T. Rathje, W. Müller, k. Rühle, R. Kienberger and G. G. Paulus, Opt. Lett. **36** 1-3 (2011)

Fabrication and characterization of a "continuous Fiber Bragg Grating fiber" using Draw Tower Grating Technology

Julia Mörbitz[*1], Eric Lindner[1], Christoph Chojetzki[1], Sven Brückner[2], Manfred Rothhardt[2], Kay Schuster[2] and Hartmut Bartelt[2]

[1]*FBGS Technologies GmbH, Buchaer Straße 6, 07745 Jena, Germany*

[2]*Institute of Photonic Technology (IPHT), Albert Einstein Straße 9, 07745 Jena, Germany*

[*]Corresponding Author: *jmoerbitz@fbgs.com*

Abstract

In this paper we present new technical developments for the fabrication of low reflective fiber Bragg grating (FBG) chains in "continuous FBG fiber" configuration. Such chains consist of several thousand FBGs and are produced by using draw tower grating (DTG®) technology. The length of a fiber including FBGs can exceed 95% of the total fiber length and is therefore also called "all FBG fiber". The chains are interrogated with OFDR measurement devices.

INTRODUCTION

First experimental observations of a periodic refractive index change in optical fibers caused by UV photosensitivity were reported by Hill et al. [1]. The periodic change of the refractive index leads to mode coupling and causes reflection of light with a specific wavelength. A so called fiber Bragg grating acts as a wavelength selective in-fiber-mirror. Early experimental setups showed the possibility of coupling UV light into the front face of a fiber to generate a standing wave forming a FBG. The transverse holographic writing technique, described later by Meltz et al. [2] offered new Bragg grating production opportunities independent of the used writing laser wavelength. In the early nineties, the transverse UV grating writing method was combined with the fiber drawing process [3]. FBGs produced during the fiber drawing have unique properties with respect to their mechanical strength compared to conventional FBGs, due to the fact that the grating writing is done before the fiber is coated. On the other hand, this opens a wide field of applications due to the cost effective fabrication for long chains of fiber Bragg gratings in one line [4]. For DTG® fabrication we use a KrF excimer laser at 248 nm together with a Talbot interferometer configuration [5]. State of the art measurement devices based on wavelength division multiplexing allow interrogation of approximately 160 DTG®s. The measurement principle for distributed sensing with these devices requires knowledge of FBG position. The investigations on measurement devices based on optical frequency domain reflectometry (OFDR) lead to another approach of sensing fiber Bragg grating chains with spatial information [6, 7]. We present the development of arrays comprising of thousands of Bragg gratings with equal wavelengths for sensing applications which are interrogated with OFDR measurement technique.

FABRICATION AND EVALUATION OF LOW REFELCTIVE DTG®s

Due to the unique production process the DTG® reflectivity is affected by the photosensitivity of the fiber preform material and by the exposure conditions (energy density). Because of the continuous movement of the fiber during the drawing process it is necessary to use only a single laser pulse for the grating writing. For the 1550 nm wavelength range a bend insensitive high Germanium doped fiber is used.

OFDR measurements give the possibility for distributed sensing of thousands of Bragg gratings in one single mode fiber with a sub millimeter spatial resolution over dozens of meter of fiber length [6]. Basic components of OFDR devices are a wavelength tunable laser and an in-fiber

interferometer consisting of a static reference arm and the measurement arm represented by the sensing FBG chain. Structural health monitoring is one of the applications which is predestinated for using such chains of thousands of FBGs. Childers et al. represented results of strain load tests in composite structures [7]. Eq. (1) calculates the total reflected light $R_{\%}(n)$ of all gratings. Based on this one can easily estimate the feasible number of sensing points n which is defined by the reflectivity $r_{\%}$ of each grating at the same wavelength:

$$R_{\%}(n) = 100\left(1 - e^{\left(-\frac{r_{\%}}{100}n\right)}\right) \quad (1)$$

By using only 4 standard DTG®s with a reflectivity of 20 % each the total reflectivity is already higher than 50 %. Assuming that the over all reflected light needs to be smaller than 50 % for significant OFDR measurement, the goal of the presented results was reducing the reflectivity of DTG®s in a low bend loss fiber to produce chains with thousands of DTG®s. There are two approaches to lower the reflectivity of the obtained DTG®s: on one hand there is the decreasing of the energy level of the UV laser and on the other hand one has the possibility to minimize the refractive index change by annealing the DTG®s with high temperatures. The used ORMOCER® fiber coating is stable up to temperatures of approximately 200 °C. DTG®s annealed with 200 °C result in a reflectivity of about 1 % which is according to Eq. (1) not low enough for a few hundred OFDR measurable gratings in one line. To achieve reflectivity values of approximately 0.05 % which allow distributed sensing of more than 1000 5 mm long fiber Bragg gratings annealing experiments by varying temperatures from 200 °C to 500 °C were performed. An online annealing process which allows temperatures up to 600 °C before the fiber coating application was implemented to the Draw Tower setup. Figure 1 shows the OFDR measurement of 5000 low reflective 5 mm long DTG®s.

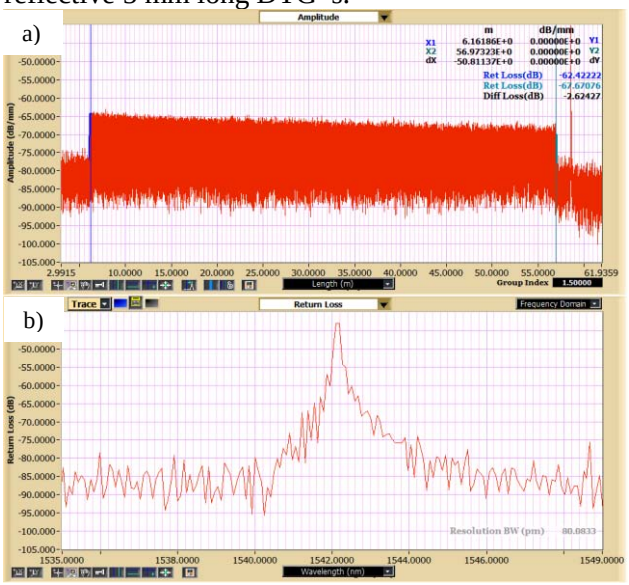

Figure 1: time domain measurement of 5000 low reflective DTG® with Luna OBR 4600 (a), frequency domain spectrum of first DTG® (b)

CONCLUSION

The unique Draw Tower setup provides the possibility to produce several thousand OFDR measureable DTG®s in one fiber chain. To date we were able to achieve grating reflectivity smaller than 0.02 % for 5 mm long DTG®s. The achieved results for low reflective gratings in combination of 10 mm grating length and nominal grating distances of about 10 mm allowed the realization of an "all grating fiber" containing more than 1000 DTG®s.

[1] K.O. Hill et al., Appl. Phys. Lett. **32**, 647-649 (1978).

[2] G. Meltz et al., Optics Lett. **14**, 823-825 (1989)

[3] L. Dong, J. L. Archambault, L Reekie, P. St. J. Russel, and D.N. Payne, Electron. Lett. **29**, 1577-1578 (1993)

[4] V. Hagemann, M.N. Trutzel, L. Staudigel, M. Rothhardt, H.-R. Müller, O. Krumpholz, Elect. Lett. **34**, 211-212 (1998)

[5] E. Lindner, J. Mörbitz, C. Chojetzki, M. Becker, S. Brückner, K. Schuster, M. Rothhardt, and H. Bartelt, Proceedings of the SPIE, Volume **8028**, pp. 80280C-80280C-7 (2011).

[6] M. Froggatt and Jason Moore, Applied Optics, Vol., Issue **10**, pp. 1741-1746 (1998).

[7] B. A. Childers; M. E. Froggatt; S .G. Allison; T C. Moore, Sr.; D. A. Hare; C. F. Batten; D. C. Jegley Proceedings of the SPIE. **4332**, pp.133-142 (2001).

DEVELOPMENT OF AN OPTICAL SYSTEM TO MONITOR A CELL BASED LAB-ON-A-CHIP *IN VITRO* ASSAY

J. Ott, B. Büttner, U. Hofmann, K.-H. Feller

Ernst-Abbe-University of Applied Sciences Jena, Department of Medical Engineering and Biotechnology, Instrumental Analysis Group, Carl-Zeiss-Promenade 2, 07745 Jena, Germany

The trend of lab-on a-chip systems with optical detection moves for the sensitive detection of the signal. Up-to-date in many cases conventional microscopes are used but there is a demand for miniaturized, sensitive optical detection systems tailored for the respective application in order to reduce costs and pave the way for mass production systems. Therefore the aim of this work is to develop a sensitive, miniaturized optical detection system for a lab-on-a-chip system which is designed for the complex analysis of the toxicological impact of chemical substances towards keratinocytes. The system is built-up of a combination of optical and impedimetric detection units, allowing a comprehensive analysis of cellular processes. Stress-induced changes in skin cells become detectable by the use of the keratinocyte cell line HaCaT stably transfected with a stress promoter-reporter-plasmid. The promoter regulates the expression of the reporter gene (green fluorescent protein, GFP) following the exposure to a toxic agent. Hence the optical readout of the fluorescence intensity in dependence on the cellular stress level is possible by means of the green fluorescence of the GFPs. Within this project, the design of a low-cost optical setup for excitation and detection is essential.

The setup consists of a LED light source for the excitation, a dichroic mirror to separate the emission and a single photon counting detector (Figure 1). The beam shaping is realized by 4 plano-convex lenses and one asphere.

Due to the limited space on the lab-on-a-chip the spot size of the excitation light has to be small while the luminous efficiency should be maximized. Therefore the size should not exceed a radius of 1.25 mm in our designed chip system. Since the costs and noise of the highly sensitive single photon counting detector increases strongly with expanding surface, the by fluorescence in all spatial directions emitted light must be focused on a radius of 0.25 mm.

The required parameters have already been determined in ray-tracing simulations and are now standing trial in the experiment. The simulations show that it is possible to focus over 55 % of the excitation light to the cell sample. For the simulation of fluorescence emission a separate source was created. Despite the strong reflections within the chip and the small detector area it was possible to collect around 7 % of the emitted fluorescence light to the detector surface.

A cost-effective system was designed, which meets the requirements of the lab-on-a-chip system with respect to the spot size and characteristics for excitation and detection. The sensitivity of the fluorescence measurement was increased.

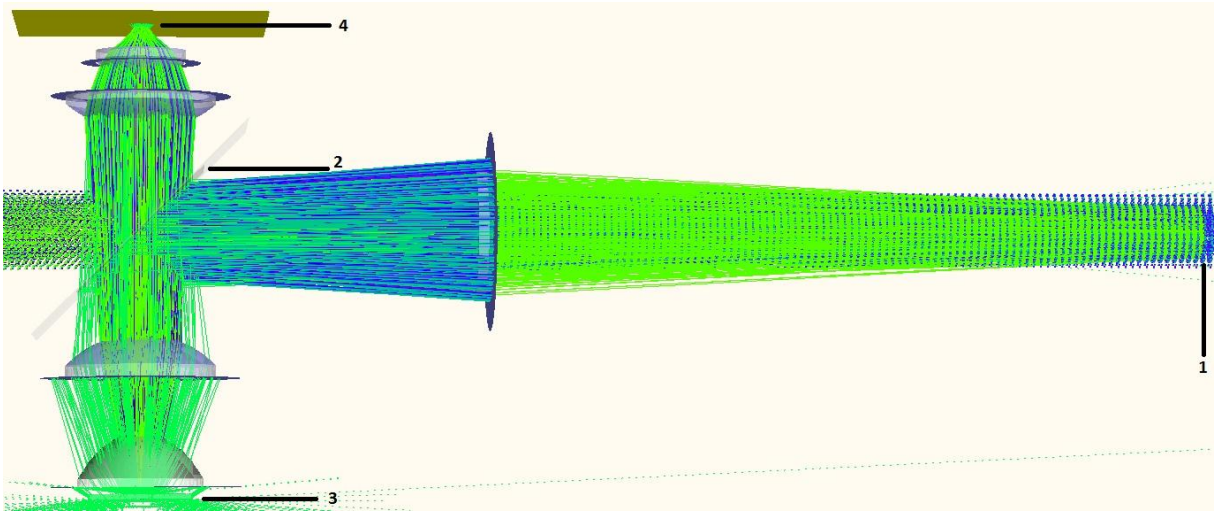

Figure 1: Design of the optical system; (1) high power LED light source for the excitation, (2) dichroic mirror, (3) sample, (4) detection surface

Mode instabilities in high-power fiber-laser systems

Hans-Jürgen Otto[*1], Tino Eidam[1,2], Florian Jansen[1], Fabian Stutzki[1], Cesar Jauregui, Jens Limpert[1,2] and Andreas Tünnermann[1,2,3]

[1] *Friedrich-Schiller-Universität Jena, Abbe School of Photonics, Institute of Applied Physics, Albert-Einstein-Straße 15,07745 Jena, Germany*

[2]*Helmholtz-Institute-Jena, Fröbelstieg 3, 07743 Jena, Germany*

[3]*Fraunhofer Institute for Applied Optics and Precision Engineering, Albert-Einstein-Str. 7, 07745 Jena, Germany*

[*]Corresponding Author: *hans-juergen.otto@uni-jena.de*

Abstract

Latest results in investigating mode instabilities in high-power fiber-laser systems are presented and the current physical understanding of the effect is explained. Additionally, first experimental results of controlling mode instabilities by a periodic excitation of fiber modes are shown.

INTRODUCTION

During the last decade fiber lasers and amplifiers have shown a rapid development in terms of power scaling. This progress has been enabled by the excellent thermal management resulting from the high surface-to-active-volume ratio offered by the fiber geometry. However, this evolution has enabled the possibility to reach power levels where new physical effects become observable for the first time. One prominent phenomenon that has been recently reported is the so-called mode instability (MI) [1]. Up to now, this is the most limiting effect for further scaling the average power of fiber lasers. Thus, it is essential to study MIs in detail in order to develop suitable countermeasures.

MODE INSTABILITIES

Typically, fiber lasers and amplifiers provide an excellent beam quality due to their waveguide properties. In most cases the preferred guided mode is a single nearly Gaussian shaped fundamental mode. For moderate average powers the beam quality is typically independent of the output power. However, by reaching a specific level of average output power the new effect of mode instabilities become observable. Hereby, the former stable beam profile becomes suddenly instable and starts to fluctuate rapidly with time. In the same way, the beam quality degrades due to the presence of higher-order modes (HOMs). When the output power is reduced the effect reverses and the beam profile becomes stable again. Fig. **1** illustrates the observable stable (Fig. **1**(a)) and unstable (Fig. **1**(b)) beam profiles.

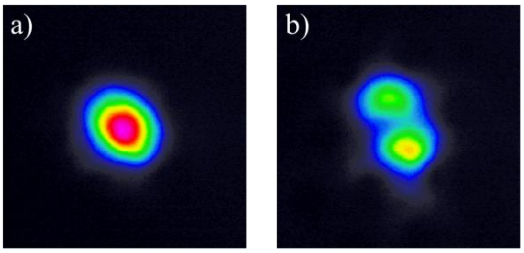

Fig. 1: Transversal output beam profiles. a) Stable beam profile below the power threshold and b) above the threshold.

Because MIs possess a strong temporal dynamic it is compulsory to fully resolve the occurring processes in order to study and understand MIs in detail. The intensity fluctuations of MIs are on a millisecond time scale. Consequently, a camera with a sample rate of several kilohertz has been used to study the temporal dynamics. In Fig. **2** an image series is exemplarily shown of excerpted frames from a high-speed video recorded with 20.000 frames per second. Based on these videos we have shown that the temporal fluctuations are due to a variation of the relative power contents and intermodal phases of the involved modes [2]. Moreover, the fluctuations can be periodic with time or randomized depending on the average output power level[3].

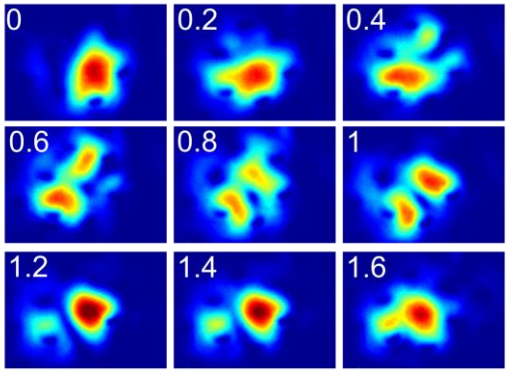

Fig. 2: Excerpted images from the high-speed video in 0.2 ms time steps showing MIs.

PHYSICAL EXPLANATION

State-of-the-art active fibers with large mode-field diameters typically are intrinsic multimode fibers. However, by employing several techniques to reduce the HOM power content an effective single-mode behavior can be achieved. Nevertheless, even a very small amount of power guided in one or more HOMs is sufficient to build up a long-period grating in the fiber core.

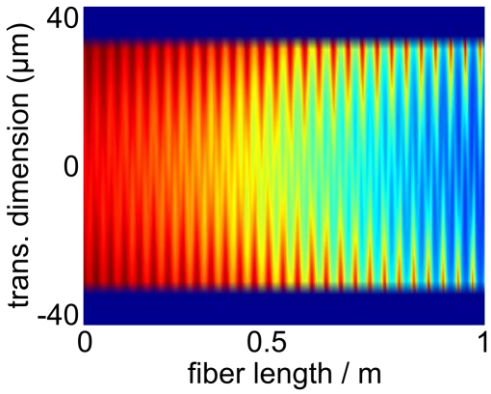

Fig. 3: Transversal slice of the fiber core showing the refractive index oscillations induced by mode beating of the FM and one HOM.

This grating is created via the thermo-optical effect due to the beating of the involved modes while propagating through the fiber and has the right period to provide an energy transfer between the modes. Thus, it is able to cause MIs at high output powers. Fig. 3 gives an impression how this long-period grating can look like.

CONTROLLING

From the theoretical explanation it can be expected that the excitation of the different fiber modes significantly influence MIs due to the corresponding change of the mode beating. Thus, we dynamically change the initial relative modal-power contents on the same time scale as MIs occur. We utilized an acousto-optical deflector (AOD) in order to vary the central position of the seed signal on the fiber core. Thereby, the relative power content of the modes is changed with time. We applied the AOD in a fiber CPA system with a 63 µm core large-pitch fiber as main amplifier. This system becomes unstable for output powers larger than 240 W. In Fig. 4(a) the unstable beam-profile at 390 W is shown. By switching on the AOD and modulating the injected signal the beam becomes clearly more stable as shown in Fig. 4(b).

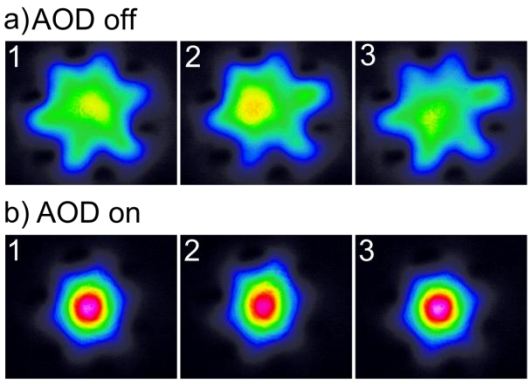

Fig. 4: Image sequences excerpt from a video showing MIs at 390 W of average output power in the case of the AOD: a) switched off and (b) switched on.

We acknowledge funding from ERC Grant agreement n° [240460] and TMBWK under contract PE203-2-1 (MOFA) and contract B514-10061 (Green Photonics). Additionally, F.J. acknowledges financial support by the Abbe School of Photonics Jena.

[1] T. Eidam et. al., "Opt. Express 19, 13218-13224 (2011).

[2] F. Stutzki et. al. , Opt. Lett. 36, 4572-4574 (2011).

[3] H.-J. Otto et. al., accepted for publication in Opt. Express.

[4] C. Jauregui et. al., Opt. Express 20, 440-451 (2012).

Vortex Light Bullets: a Discrete Revolution

Karin Prater[1], Falk Eilenberger[*1], Stefano Minardi[1], and Thomas Pertsch[1]

[1]*Institute of Applied Physics, Abbe Center of Photonics, Friedrich-Schiller-Universität, Max-Wien-Platz 1, 07745 Jena*

[*]Corresponding Author: *falk.eilenberger@uni-jena.de*

Abstract

We present first results on the observation of Vortex Light Bullets in Arrays of Waveguides. These are spatiotemporal, solitary waves of complex spatial symmetry: namely bound states of discrete Light Bullets with an angular momentum, which is shown to stabilize these nonlinear entities against decay. We present thorough simulations of their evolution behavior, discuss excitation strategies and display experimental findings.

INTRODUCTION

Solitons, self-confined wavepackets, in which nonlinearity balances diffraction or dispersion are a main topic of nonlinear optics. They are of great importance as experimentally accessible model systems for various systems in nonlinear physics, and play a central role in the generation of supercontinua [1] and the formation of rogue waves [2].

While, ubiquitous and well-understood in low-dimensional systems, such as optical fibres, higher-dimensional spatiotemporal solitons are a relatively new topic in experimental nonlinear optics. These entities – called Light Bullets – where first observed in arrays of waveguides [3] and exhibit dynamics, which differs significantly from their low-dimensional counterparts. This difference is related to changed stability [4] and evolution [5] properties and direct coupling between spatial, temporal, and nonlinear evolution [6].

While isolated LBs are now regularly excited and understood, we now investigate compound entities, namely spatially bound LB complexes. We analyze threefold symmetric LBs, for which stable solutions have been predicted numerically [7], only if they possess angular charge – i.e. if the phase difference between adjacent waveguides is $2\pi/3$. Such entities are called Vortex Light Bullets (VLBs).

SOLUTIONS AND STABILITY ANALYSIS

We numerically find stationary solutions to the simplified set of discrete-continuous nonlinear Schrödinger equations, containing nearest neighbor coupling, parabolic dispersion and Kerr nonlinearity:

$$-i\frac{\partial A_{nm}(Z,T)}{\partial Z} = \frac{1}{2}\frac{\partial^2 A_{nm}}{\partial T^2} + |A_{nm}|^2 A_{nm} + A_{n+1m} + A_{nm+1} + A_{n-1m} + A_{nm-1} + A_{n+1m+1} + A_{n-1m-1} \quad (1.1)$$

with the ansatz $A_{nm}(Z,T) = a_{nm}(T)\exp ibZ$, where b is a nonlinear parameter. Eq. (1.1) was then solved with a Newton-Raphson-Method, for LBs of various kinds of symmetry. More specifically we look for single LB solutions, solutions with threefold symmetry and no phase shift, dubbed triple LBs and VLBs with threefold symmetry and a $2\pi/3$ phase shift for any rotation of 120 degrees.

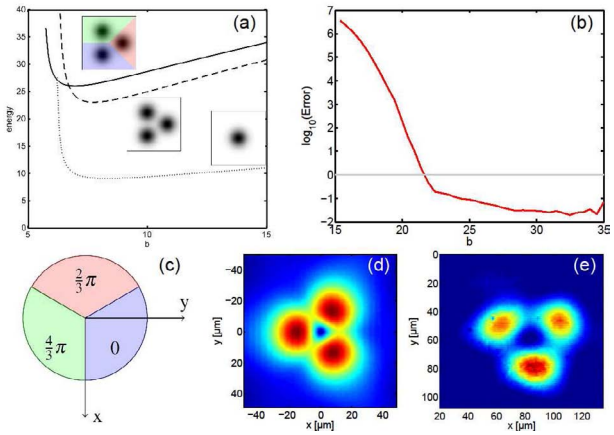

Figure 1 (a) Energy vs. nonlinear phase shift for various LB types. (dotted) Ordinary LBs. (dashed) Triple LBs. (solid) Vortex LBs. (b) Relative deviation of VLBs from stationary solution after $z \approx 2L_C$. Gray line denotes limits of stability. (c) Layout of phase plate for vortex excitation. (d) Simulated focal distribution of light with inserted phase plate. (e) Experimental focal distribution of light with inserted phase plate.

Results are displayed in Figure 1 (a) and show that all three classes of solutions do exist. Stability analysis, however, reveals that triple LBs are always

unstable, whereas VLBs (see Figure 1 (b)) have a range of stability, which we find to be smaller than previously predicted [7]. We further found that VLBs exhibit a new mode of decay, namely fission into three individual LBs with different velocity, and not into linear waves as single LBs do.

Further dynamic simulations, including higher order effects show that the VLB solutions propagate stable for about as long as an ordinary LB does [5]. Furthermore it can be excited by a threefold symmetric, spatially multiplexed Gaussian pulse with a wide range of parameters, as long as their relative phase is approximately $2\pi/3$.

EXCITATION OF VLBs

Excitation of ordinary LBs in arrays of waveguides is surprisingly straightforward: a short pulse is focused into the central core of a waveguide array. It is then self-compressed and supercontinuum generation takes place. A LB is then formed together with a background of dispersing linear waves.

VLBs however require the generation of a threefold-symmetric discrete optical vortex, with a field structure of sufficient overlap with the guided modes of the waveguide array. We shape the wavepacket before focusing onto the array's front facet by means of a threefold symmetric waveplate depicted in Figure 1 (c) with $2\pi/3$ phase shift. As an alternative a laser-cut threefold symmetric mirror triplet on vertical piezo stages was developed. These techniques are shown to generate a discrete vortex field, with sufficiently low dispersion and higher field overlap with the waveguide array (see Figure 1 (d) and (e)).

EXPERIMENTAL SETUP & RESULTS

After excitation of the VLB with a vortex pulse with $T_{\mathrm{FWHM}} \approx 50\,\mathrm{fs}$ and $\lambda = 1500\,\mathrm{nm}$, the light which leaves the fibre array is analyzed with an imaging cross correlator. For details see [5]. This device generates 3D intensity traces with 40 fs temporal and 1µm spatial resolution, thus giving insight into the spatiotemporal state of the light leaving the sample (see Figure 2).

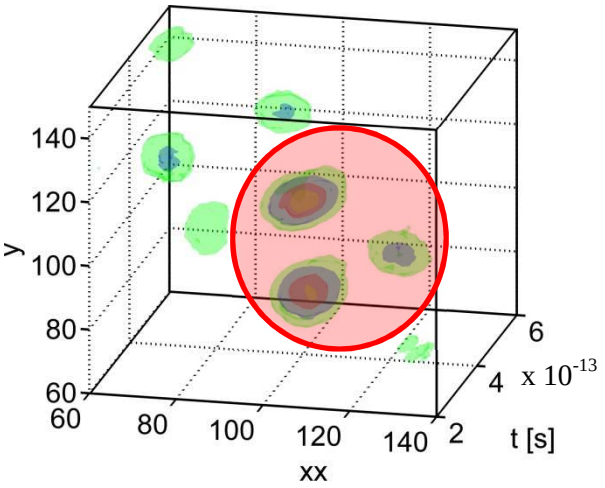

Figure 2 3D cross correlation trace in the transition region between LB and VLB propagation after a 30 mm fibre array. The red circle marks the VLB position.

Variation of the input power clearly shows the excitation of linear waves, ordinary LBs and VLBs, depending on the input power. The VLBs phase structure is preserved during propagation, as predicted by simulation results. Preliminary data shows that the evolution dynamics is similar to the dynamics of ordinary LBs [3, 5]. Self-redshift due to the intrinsic Raman effect increases the minimum energy for VLB propagation until it grows larger than the energy contained in the VLB, forcing it to decay.

In conclusion we present evidence for the first observation of stable high-dimensional solitary waves of higher order: VLBs in waveguide arrays. We have identified regimes of stability, established an understanding of propagation dynamics, successfully developed experimental excitation strategies, and characterized VLBs in an experiment.

[1] J. M. Dudley, G. Genty, and S. Coen, Rev. Mod. Phys. **78**, 1135 (2006).
[2] D. Solli, C. Ropers, P. Koonath, and B. Jalali, Nature **450**, 1054 (2007).
[3] S. Minardi *et al.*, Phys. Rev. Lett. **105**, 263901 (2010).
[4] Y. Silberberg, Opt. Lett. **15**, 1282 (1990).
[5] F. Eilenberger *et al.*, Phys. Rev. A **84**, 013836 (2011).
[6] F. Eilenberger *et al.*, Opt. Express **19**, 23171 (2011).
[7] H. Leblond, B. A. Malomed, and D. Mihalache, Phys. Rev. A **83**, 063825 (2011).

Properties of titanium oxide deposited by atomic layer deposition as a coating for highly efficient transmission grating

S. Ratzsch*[1], F. Fuchs[2], E.-B. Kley[1], A. Tünnermann[2], A. Szeghalmi[1]

[1]*Friedrich Schiller University Jena, Institute of Applied Physics (IAP), Albert-Einstein-Straße 15, 07745, Jena Germany*

[2]*Fraunhofer-Institut für Angewandte Optik und Feinmechanik, Albert-Einstein-Str. 7, 07745 Jena, Germany*

*Corresponding Author: *Stephan.Ratzsch@uni-jena.de*

Abstract

We present a new approach for realization of a highly efficient transmission grating for TM polarized light operating at 1030 nm wavelength. It had been theoretically shown that transmission efficiency for TM-polarized light of 100% in the -1st diffraction order can be reached. Therefor a fused silica binary grating is embedded within a high refractive index material. High quality, homogenous and void free coatings are required to achieve high optical efficiency. Atomic layer deposition (ALD) meets the enormous demands posed by these embedded gratings; however, film thickness homogeneity (2% non-uniformity) and low surface roughness are essential. Titanium dioxide (TiO_2) with its very high refractive index and no extinction in the near infrared spectral range is a potential candidate for the embedding material. The grating parameters (period, height, line width, etc.) have been optimized by rigorous coupled wave analysis (RCWA). These parameters depend on optical properties of the titania layer. Therefore the refractive index and extinction should be precisely controlled.

INTRODUCTION

Highly efficient gratings are used in many optical applications, e.g. as transmission grating in a chirped pulse amplification system (CPA). Therefore small period and high transmission efficiency of the grating are required. Unfortunately a small grating period means a high incident angle of the light which causes undesired Fresnel reflection at the grating surface [1]. Our new approach called embedded grating can overcome this problem. Therefor a fused silica grating will be embedded in a high index material. Theoretically it is possible to achieve 99.95% transmission efficiency for TM-polarized light, whereas conventional open binary gratings with the same period can only reach 94.05% at maximum.

Such an embedded grating offers additional advantages since the embedding layer will protect the grating against pollution or damage. Furthermore, cleaning of the embedded gratings is possible [2]

In order to realize a highly efficient grating with respect to high power lasers a high index material with nearly no absorption in the wavelength range between 1000 nm up to 1060 nm is needed. This is the range of the solid state laser the grating targeted for future development. The embedding layer should have a high quality and no air inclusion. Besides it is important to know the exact optical and deposition properties of the deposited layer. For this purpose we measured the homogeneity, surface roughness, refractive index and the extinction coefficient at different process parameter.

EXPERIMENTAL

One of the most promising technologies to deposit conformal layers on high aspect ratio grating is thermal or plasma enhanced atomic layer deposition (ALD) [2]. The main advantages of ALD are defect-free and conformal coatings with well-defined film thickness [3, 4]. The precise control of the layer thickness is reached because ALD is a cyclic self-limiting process. One ALD cycle consists in general of four major steps: First a self-terminated reaction of the first reactant, Second a purge or evacuation to remove the non-reacted reactants and

the gaseous reaction by-products, Third a self-terminated reaction of the second reactant - or another treatment to activate the surface for the reaction of the first reactant, Forth a purge or evacuation to remove the non-reacted reactants and the gaseous reaction by-products. Because the reactions are self-terminating each ALD cycle adds a specific amount of material on the surface. The reaction is independent of the shape of the surface. Therefore it is possible to coat even structures with high aspect ratios [5, 6]. Wang et al. showed that one can fill homogenously a grating with a high index using ALD [2].

High refractive index materials such as HfO_2, Ta_2O_5, Nb_2O_5 or Al_2O_3 are conceivable. In this paper, we will focus on the optical constants of titanium dioxide (TiO_2). TiO_2 is one of the dielectric materials with the highest refractive index.

The refractive index of TiO_2 deposited by thermal ALD processes is generally highly sensitive to the temperature of the substrate [5]. In contrast, the TiO_2 films produced by plasma enhanced ALD between 80°C and 150°C have a high and substrate temperature independent refractive index.

The refractive index as well as the layer thickness was ellipsometrically determined. The refractive index is 2.33 ± 0.05 at 1030 nm. The extinction coefficient was measured with a spectrometer. At 1030 nm wavelength the extinction coefficient is 3.08 e^{-5} nm^{-1} at 120°C and 1.47e^{-5} nm^{-1} at 150°C. The reduction is caused by the higher deposition temperature and thereby the promoted reaction of the precursors.

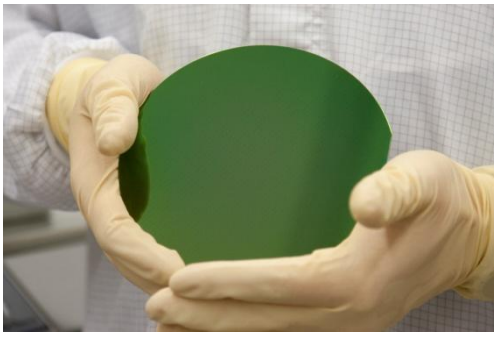

Figure 1 6'' Si wafer caoted homogeneously with TiO_2 at an 120°C deposition temperature by plasma enhanced atomic layer deposition. The homogenity is 2.1%.

Fig. 1 displays a coated 6'' Si wafer. The color distribution over the entire wafer is very homogeneously green which indicate a good homogeneity in the layer thickness. The homogeneity was measured with an ellipsometer in mapping mode over 69 measurement points. The Homogeneity achieved was ±2.1%.

Conclusion

Thermal or plasma enhanced atomic layer deposition is proposed to embed the grating. It could be shown that the achievable layer properties, homogeneity, refractive index and the extinction coefficient satisfy the requirements set on the deposition as an optical coating.

[1] T. Clausnitzer, T. Kämpfe, E. B. Kley, A. Tünnermann, A. V. Tishchenko, and O. Parriaux, Opt. Express **16** (2008)

[2] JJ. Wang, XG. Deng, R. Varghese, A. Nikolov, P. Sciortino, F. Liu, and L. Chen, Opt. Lett. **30** (2005).

[3] Steven M. George, Chem. Rev. **110** (2010).

[4] A. Szeghalmi, M. Helgert, R. Brunner, F. Heyroth, U. Goesele, and M. Knez, Appl.Opt. **48** (2009).

[5] H. C. M. Knoops, E. Langereis, M. C. M. van de Sanden, and W. M. M. Kessels, ` J. Electrochem. Soc. **12** (2010).

[6] J-Y. Kim, J-H. Kim, J-H. Ahn, P-K. Park, and S-W. Kang, J. Electrochem. Soc. **154** (2007).

Illustration of the Ewaldsphere with a twodimensional fs pulse written volume Bragg grating (VBG)

Daniel Richter[1,*], Christian Voigtländer[1], Jens Thomas[1], Andreas Tünnermann[1], and Stefan Nolte[1]

[1]*Institute of Applied Physics, Friedrich-Schiller-University Jena, Albert-Einstein-Str. 15, 07745 Jena, Germany*

[*]Corresponding Author: *daniel.richter.1@uni-jena.de*

Abstract

We present a VBG written by a three beam interference of fs pulses. The thereby generated twodimensional grating structure exhibits a discrete diffraction pattern and the observed reflections can be described by the Ewald sphere.

Introduction

Volume Bragg gratings are volume holograms with a periodic refractive index structure inside the sample bulk. Due to their properties and geometrical size they have a broad range of applications like frequency stabilization of laser diods, beam combiners or frequency filters ([1, 2, 3, 4]). The common fabrication method is based on the interference of UV-laser beams inside of photosensitive materials ([5, 6]) which suffers from limitations to a few materials and fabrication inflexibilites. Using femtosecond laser pulses a broad (transparent) material range can be processed and a higher flexibility is supplied inherently due to the modification method of the material ([7]). Furthermore, with our technique large core fibers can be structured easily ([8]).

In this paper we want to show the ability of our phase mask inscription method (fig. 1a) to generate twodimensional grating patterns by only using the $+1.$ and $-1.$ diffraction order of the phase mask for three beam interference.

Experimental results

In our VBG experiments we employed a commercial Ti:Sapphire-CPA laser system (Spectra Physics, Spitfire) to generate up to 700μJ - 50fs pulses at a central wavelength of 800nm with a repetition rate of 1kHz. These pulses were focused with a cylindrical lens (e.g. 20mm focal length) through a phase mask into the bulk sample (e.g.fused silica). The interference pattern is produced by the $+1.$ and $-1.$ diffraction orders of the phase mask. Due to the short coherence length of the laser pulses no interference with the 0. order is observed (order walk-off) which leads to pure two beam interference. In the focal volume the intensity is high enough to create a permanent refractive index modification due to nonlinear absorption processes.

Concerning our experiments we want to present here the overlap between the laser spot and the bulk is not 100% but around 70%. Due to this condition a part of the light that is diffracted into the $+1.$ diffraction order of the phase mask shines on the side surface of the bulk and is refracted into it (fig. 1b).

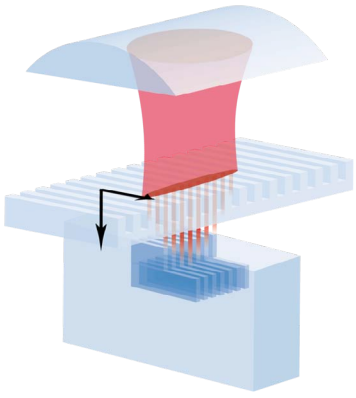

(a) Inscription of a VBG.

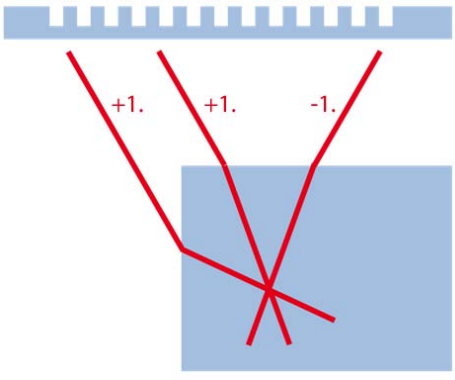

(b) Three beam interference due to refraction.

Figure 1: Illustration of the inscription of a VBG with a phase mask and realization of a three beam interference.

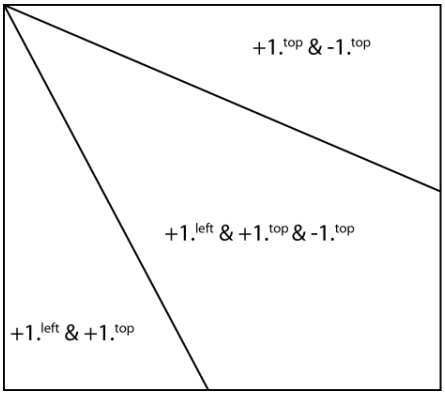

(a) Overlap sections inside the glass bulk.

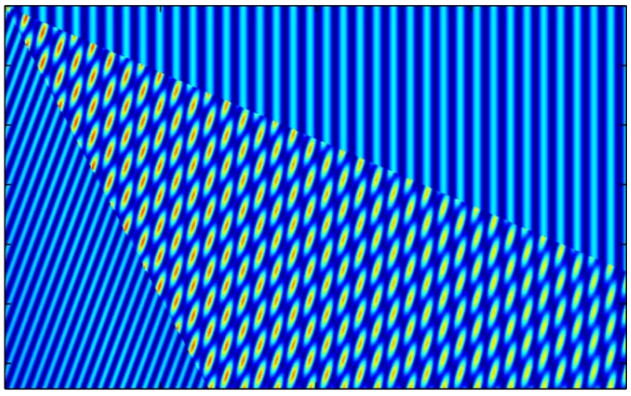

(b) Simulated interference pattern near the edge inside the glass bulk.

Figure 2: Illustration of the interference areas inside the glass bulk near the upper left edge (a) and the related interference pattern (b).

Due to Snell's law the orientation of the refracted light of the $+1.$ order after passing the side surface is different to the light that passed the upper surface. This creates an area wherein three beams interfere: the two $+1.$ diffraction orders and the $-1.$ order (fig. 2a). The diffraction behaviour of the thereby imprinted interference pattern (fig. 2b) can be described by the Ewald sphere. The measured and calculated discrete spots of a certain wavelength and orientation in space are in a good agreement and support our thesis on the developement of the inscribed grating.
With this inscription method as a model system ,e.g., a more detailed understanding of the diffraction process of x-rays by crystal unit cells is possible due to the fact that commonly no wavelength differentiation of the certain recorded spots is possible. Furthermore, one is able to realize 5 out of the 17 plane symmetry groups by only changing the angle of the side surface ([9]).

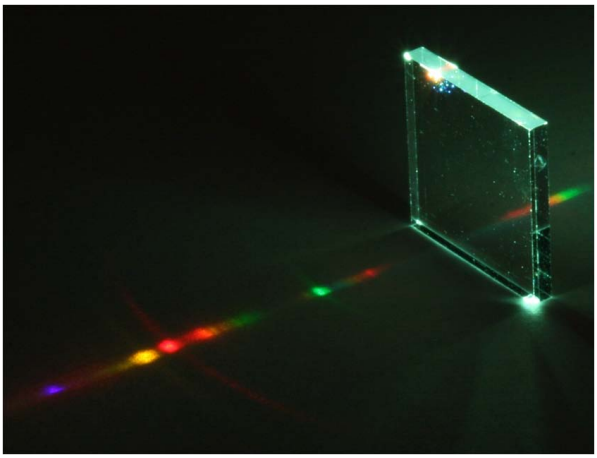

Figure 3: Diffraction pattern for the lower space region of one of the three-beam-VBGs when illuminated with a bright white light source.

[1] I. V. Ciapurin, L. B. Glebov, V. I. Smirnov, *Proc. SPIE* **5335** (2004).
[2] G. B. Venus, A. Sevian, V. I. Smirnov, L. B. Glebov, *Opt. Lett.* **31**, 1453 (2006).
[3] L. B. Glebov, *Proc. SPIE* **6216**, 621601 (2006).
[4] J. Lumeau, L. B. Glebov, V. Smirnov, *Opt. Lett.* **31**, 2417 (2006).
[5] J. J. Amodei, D. L. Staebler, *Appl. Phys. Lett.* **18**, 540 (1971).
[6] O. M. Efimov, L. B. Glebov, L. N. Glebova, K. C. Richardson, V. I. Smirnov, *Applied Optics* **38**, 619 (1999).
[7] C. Voigtländer, D. Richter, J. Thomas, A. Tünnermann, S. Nolte, *Appl. Phys. A: Materials Science & Processing* **102**, 35 (2011).
[8] J. Thomas, *et al.*, *Laser & Phot. Reviews* **6** (2012).
[9] J. L. Stay, T. K. Gaylord, *Appl. Opt.* **47**, 3221 (2008).

Fabrication of a Faraday Isolator by plasma-activated bonding

Carolin Rothhardt[*1, 2], Miroslaw Rekas[2], Gerhard Kalkowski[2], Ramona Eberhardt[2], Andreas Tünnermann[1, 2]

[1]*Institute of Applied Physics, Friedrich Schiller University, Albert-Einstein-Straße 15, 07745 Jena, Germany*

[2]*Fraunhofer Institute for Applied Optics and Precision Engineering, Albert-Einstein-Straße 7,07745 Jena, Germany*

[*]Corresponding Author: *carolin.rothhardt@iof.fraunhofer.de*

Abstract

We present the results of direct bonding of components for a faraday isolator for high power laser applications. Terbium Gallium Garnet single crystals have been joint with sapphire disks without any auxiliary materials at high bond strengths. After extensive cleaning, samples with high flatness and low roughness were subjected to a plasma activation process before bonding took place under compressive forces in a high vacuum environment at moderate temperature. With this process bonds with a very low fraction of defects were obtained. Bonded samples showed satisfactory performance under thermal as well as laser load.

INTRODUCTION

Optical contacting originating from the 200 years old technique known as “Ansprengen” is interesting for laser application, because it leads to virtually no absorption of the interlayer and shows high thermal stability compared to gluing. With the ongoing miniaturization of integrated circuits “direct wafer bonding” evolved. By use of plasma treatment or annealing of contacted surfaces at high temperature strong connections based on covalent bonds are formed [1]. Despite its advantages such as absence of creeping or outgassing and high transparency, plasma activated bonding is still barely used for optical [2] or laser applications [3]. Here we describe the use of plasma activated bonding for fabrication of components for a Faraday isolator for high power laser application ($P \approx 1$ kW, $\lambda = 1080$ nm).

DESIGN OF THE FARADAY ISOLATOR

The use of Faraday rotating materials at high power implies serious challenges. The Verdet constant and the depolarization ratio are sensitive to temperature [4]. With increasing power the thermal lensing and temperature gradients increase. We designed a faraday isolator assembly based on FEM simulations. As Faraday rotating material we chose TGG with its high Verdet constant ($V = 38$ rad/Tm at $\lambda = 1060$ nm [4]). Sapphire with its high thermal conductivity and transparency is employed as intermediate layer. To extract heat from TGG efficiently and prevent thermal lensing, a stack of alternating TGG (diameter = 10 mm; height = 2 mm) and sapphire disks (diameter = 12 mm; height = 2 mm) is fabricated by direct bonding. To reduce reflection losses the surfaces to be bonded were coated with an anti-reflective coating in an evaporation process. A symmetric three layer coating system, consisting of two different oxide compounds is considered appropriate to match the indices. The layer system is divided along the symmetry plane, and one half is applied to each surface to facilitate bonding.

SAMPLE CHARACTERIZATION

Prior to bonding of the surfaces of the samples were characterized with regard to roughness and flatness. Roughness was examined by white light interferometry (ZYGO NewView 600 S). All surfaces showed a root-mean-square roughness of 0.5 nm. In view of the thickness and related stiffness

of the samples, flatness is an issue and was measured with a Fizeau-type interferometer (50 mm aperture FISBA with reference flat of better than λ/15 PV at λ = 633 nm). The peak-to-valley (PV) flatness values of sapphire samples ranged from 500 nm to 770 nm PV. Considering only the inner part, the flatness values improves by a factor of 2 to 3 (to about 200 nm PV). Flatness measurement of TGG revealed values in the range of 60 nm to 200 nm PV.

SAMPLE PREPARATION AND ACTIVATION

Prior to bonding the samples underwent thorough cleaning and activation. Starting with an ultrasonic assisted bath cleaning process to remove residuals from polishing and lapping, the samples were then cleaned with a commercial spin cleaner, similar to the semiconductor RCA cleaning process. Afterwards the samples were activated by a low-pressure nitrogen plasma and subsequently rinsed in de-ionized water and spun dry.

BONDING

Two series of TGG-sapphire samples (coated and uncoated) were bonded. Instantly after cleaning and activating, the surfaces were brought into contact. Bonding took place in a vacuum environment at about 10^{-4} mbar by applying compressive forces in the kN range, to adjust for different flatness of the surfaces. Heating up to temperatures of around 200°C supports water diffusion and prevents excessive stresses originating from the mismatch in coefficients of thermal expansion of both materials (TGG: $\alpha = 7.8 \cdot 10^{-6}\ K^{-1}$; sapphire: $\alpha = 5.3 \cdot 10^{-6}\ K^{-1}$ [5]). For both series the bonding process was successful and yielded bonding interfaces with only small defects. A stack consisting of two TGG and sapphire disks each was successfully produced.

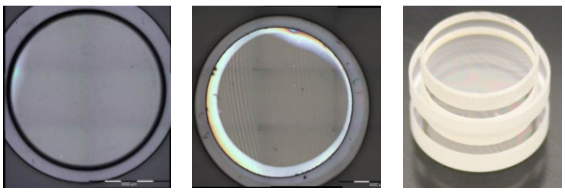

Figure 1: left: microscope picture of bonded uncoated sample; middle: microscope picture of coated bonded sampple; right: picture of stack (2x TGG, 2x sapphire)

PROPERTIES OF THE BONDED INTERFACE

To evaluate absorption behavior of the bonded interface, the samples were measured by spectral photometry (Perkin Elmer Lambda 950) before and after bonding. At the target wavelength (λ = 1080 nm) the absorption is very low.

To estimate the bonding strength, the uncoated bonded sample was subjected to a heat stress test. Heating took place in a vacuum environment up to 700°C stepwise beginning at 300°C in steps of 100 K. After every step, the samples were controlled for damage visually. After heating to 700°C cracking occurred in the TGG sample. Debonding took place only partially. From characterization with a birefringence analyzer (ILIS strainmatic) o significant change in the stress pattern is visible before cracking.

A laser damage threshold test was conducted to examine the performance of coated and uncoated bonded samples as well as single substrates under laser load. A setup consisting of JenLas fiber laser (λ = 1070 nm; P_{out} = 260 W), a Shack-Hartmann Sensor working with a probe laser to detect the wave front error and several power meters were used. The values of the reflected power are as expected from the calculation. From the diagram Figure 2 the improvement in minimizing the wavefront error under thermal load by bonding sapphire to TGG is visible. The circles show PV wavefront deformation of a single TGG substrate, whereas the triangles show the deformation of the bonded samples.

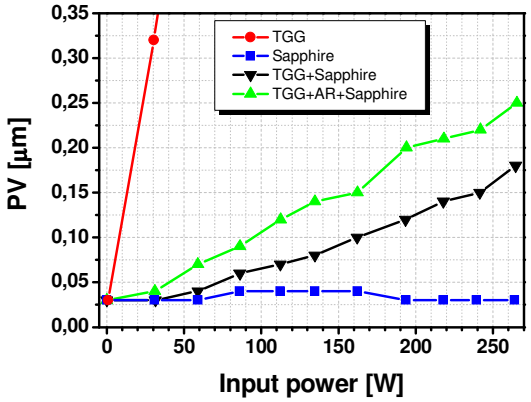

Figure 2: wavefront deformation PV depending on Input Power

CONCLUSIONS AND OUTLOOK

Plasma activated direct bonding is a useful technology for bonding TGG and sapphire crystals. Strong bonds were obtained as verified by the heat test. No influence on the absorption was observed. Testing under laser load revealed and increasing wavefront error by bonding sapphire to TGG as well as thermal stability up to 260 W at λ = 1070 nm. Next steps are to quantify the mechanical bonding strength and to fabricate and test a complete isolator.

ACKNOWLEDGEMENTS

We greatly acknowledge work of Charlotte Jahnke on sample cleaning, Dr. Peter Munzert on coating design and manufacturing, Paul Johannes Jobst on spectral photometry measurements, Dr. Thomas Peschel on FEM simulation, Uta Schmidt and Gerd Harnisch on mechanical design, Nicoletta Haarlammert, Marco Plötner and Michael Appelfelder on laser damage testing and Dr. Stefan Risse for fruitful discussions. This work is supported by the European Union within the Project "LIFT" under grant agreement no. NMP2-LA-2009-228587.

[1] U. Gösele, Semiconductor Wafer Bonding, Annual Review of Materials Science 28, 215 – 241 (1998).

[2] G. Kalkowski, U. Zeitner, T. Benkenstein, J. Fuchs, C. Rothhardt, R. Eberhardt, Direct wafer bonding for encapsulation of fused silica optical gratings, 37th International Conference on Micro and Nano Engineering, Berlin (2011)

[3] M. Kawaji, K. Imura, T. Yaguchi, and I. Shoji, Fabrication of quasi-phase-matched devices by use of the room-temperature-bonding technique, in Advanced Solid-State Photonics, OSA Technical Digest Series (CD), paper TuB24 (2009).

[4] E. Khazanov, Advances in Solid-State Lasers: Development and Applications, InTech, Croatia (2010).

[5] Kyocera Cooperation, "Single crystal sapphire," tech. rep., (2010).

Slow light in lithium niobate photonic crystal slab waveguides

Sina Saravi*, Séverine Diziain, Reinhard Geiss, Thomas Pertsch

Friedrich-Schiller-Universität Jena, Institute of Applied Physics, Albert-Einstein-Strasse 15, 07745 Jena, Germany

*Corresponding Author: *sina.saravi@uni-jena.de*

Abstract

We investigate light propagation with low group velocity in lithium niobate photonic crystal slab waveguides. We focus on designs which provide low group velocity dispersion over a large bandwidth. Band diagrams are calculated with RSoft Bandsolve. Group indices around 50 over a few nanometer bandwidth are reached.

INTRODUCTION

Because of their band gap effects, photonic crystal slab waveguides (PCSW) can confine and guide light in micro meter scale [1]. As a result, they offer a very promising platform for integrated optics. Slowing down the group velocity of light provides an effective way to enhance optical nonlinearities by increasing the light-matter interaction [2].

Lithium niobate (LN), a highly nonlinear material widely used for electro- and acousto-optic modulators, is a promising candidate for future integrated optical devices based on photonic crystals.

In this work, we investigate light propagation with low group velocity in lithium niobate PCSW. We focus on designs that will allow low group indices with both low dispersion and large bandwidth. Band diagrams of the studied structures are calculated with the Bandsolve engine of RSoft [3].

SLOW LIGHT IN LITHIUM NIOBATE PHOTONIC CRYSTAL SLAB WAVEGUIDES

LN PCSW consists of a LN membrane with a triangular lattice of holes drilled in it. The W1 photonic crystal waveguide is formed by removing one row of holes in the ΓK direction (Fig. 1). The guided mode is propagating in the *x* direction. It is confined in the *z* direction by the band gap effect and in the *y* direction by total internal reflection. The band diagram of a typical W1 PCSW is shown in Fig. 2 (a). The group index of a mode is defined by:

$$n_g = \frac{c}{v_g} = \frac{c}{d\omega/dk} \quad , \qquad (1)$$

where c is the speed of light in vacuum, v_g is the group velocity of the guided mode, and ω and k are the frequency and wave vector.

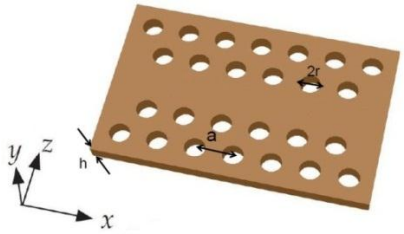

Figure 1: Schematic of a W1 photonic crystal slab waveguide.

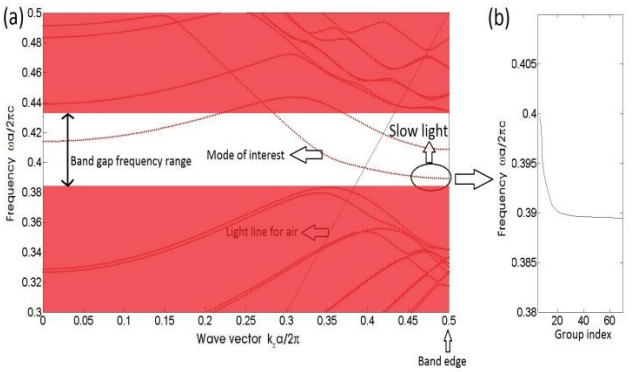

Figure 2: (a) Band diagram of the guided mode of interest. (b) Group index of the guided mode.

As can be seen in Fig. 2, n_g increases rapidly as the band edge is approached, which naturally provides low v_g. However, this rapid change of n_g causes large group velocity dispersion, which can cause a drawback for pulse propagation. Therefore, we look for designs that provide slow light with a constant n_g over a wide spectral bandwidth. The mode of

such a structure should be a straight line, as schematically shown in Fig. 3.

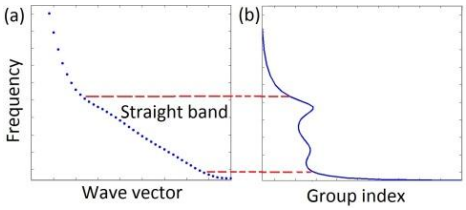

Figure 3: Schematic (a) band diagram and (b) group index spectra of a low dispersion slow light mode.

RESULT OF SIMULATION

A way to reach low group velocities with a low dispersion is to engineer the dispersion relation of the W1 waveguide by modifying the geometry of the structure. There are numerous ways for doing so [4-8]. We focus on a design which consists of shifting the first and second rows of holes adjacent to the defect line (Fig. 5), because it provides low dispersion slow light over a wide bandwidth and also is less sensitive to fabrication imperfection. Band diagrams have been calculated using the Bandsolve engine of RSoft. An operation wavelength of $1.55\,\mu m$ was assumed for implementing the refractive indices of LN. The group index of the desired mode is calculated from the band diagram using Eq. (1) (Fig. 6). It exhibits two regions of slow light with low dispersion. The first one is characterized by $n_g \approx 53$ over a bandwidth of $3.4\,nm$, while the second one has $n_g \approx 270$ over a limited bandwidth of $0.3\,nm$. The bandwidths are derived using the criteria of $\pm 7\%$ change in n_g.

Nevertheless, it would be difficult to achieve experimentally a mode with a group index as high as 270, because of losses caused by disorder in fabrication.

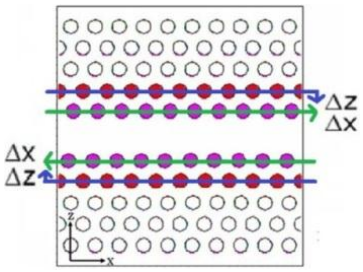

Figure 5: Engineering the dispersion relation of the guided mode by shifting the neighboring rows of holes and changing their radius.

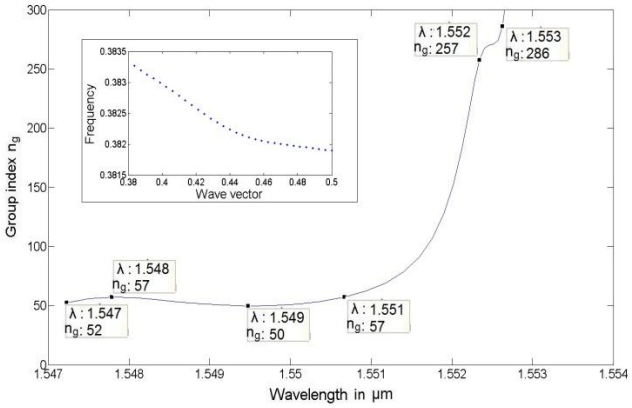

Figure 6: Group index for $\Delta Z/a = 0.11$ and $\Delta X/a = 0.04$ with $h/a = 0.8$ and $r/a = 0.3$. Periodicity, $a = 593\,nm$. Inset is the band diagram of the mode.

CONCLUSION

We have demonstrated designs for low dispersion slow light in LN W1 PCSWs, by shifting the first and second rows of holes adjacent to the defect line. It is possible to reach a group index as high as 53 over a bandwidth of $3.4\,nm$, centered around $1.55\,\mu m$. Another possible design would be to increase the radius of the second row of holes adjacent to the defect line.

[1] J.D. Joannopoulos, et al. Photonic Crystals: Molding the Flow of Light (Second Edition). Princeton University Press, 2008.
[2] T. F. Krauss, Journal of Physics D Applied Physics, **40**, 2666 (2007).
[3] RSoft Photonics CAD Suite, version 7.0.2.
[4] L. H. Frandsen, et al. Opt. Express, **14(20)**, 9444 (2009).
[5] Y. Hamachi, et al. Opt. Lett., **34(7)**, 1072, (2009).
[6] J. Hou, et al. Photon. Technol. Lett. **21**, 1571, (2009).
[7] J. Li, Opt. Express **16**, 6227, (2008).
[8] J. Liang, et al. Journal of Applied Physics, **110**, 063103 (2011).

Recent advances in laser speckle based structured illumination stereophotogrammetry

Martin Schaffer*[1], Marcus Große[1], Bastian Harendt[1] and Richard Kowarschik[1]

[1]*Institute of Applied Optics, Fröbelstieg 1, 07743 Jena, Germany*

*Corresponding Author: *martin.schaffer@uni-jena.de*

Abstract

Typical structured illumination techniques for 3D shape measurements use white light sources for pattern creation. The most common way to project patterns onto an object scene for shape reconstruction is an off-the-shelf DLP projector. We use coherent sources, mainly DPSS lasers at 532 nm, to illuminate the object under test with structures. They offer advantages and potential for new applications. However, novel difficulties coming along with the new light sources need to be addressed to get comparable results regarding accuracy and measurement time. We compare coherent with non-coherent pattern projection and outline new applications. Both are quantitatively compared in the same stereophotogrammetric setup. Media that substantiates the experimental results will be shown.

Introduction

Stereophotogrammetry has been invented and used already more than a century ago. Even with structured illumination and computer-based reconstruction algorithms it has been used for decades now and in industry, although tactile measurements outweigh, they are used for dense shape recovery in quality control already. While it seems that research is done there are still difficulties and the concept can be extended. Enabling new applications, measurement speeds and accuracies possible.

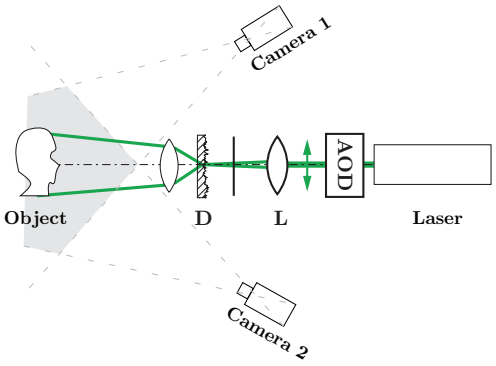

Figure 1: Basic experimental setup for 3D shape measurement with laser-speckle projection. Laser, AOD, focussing lens, diffuser and condensing lens.

Most structured light techniques, like stripe projection, use a DLP projector to project one or more desired patterns on the object. After acquiring the object illuminated with every pattern from at least two perspectives, one can reconstruct the object's shape. The pattern sequence is used to simplify the finding of corresponding pixels on featureless surfaces and increase subpixel accuracy.

The desired patterns are typically fringes [1] but can be different for various reasons, e.g. [2, 3, 4, 5]. The latter [5] uses laser speckles for fast pattern projection to allow highspeed 3D shape measurement with up to 200 3D frames per second. This approach has several other features that can be employed for various applications. A sketch of the used setup can be seen in Fig. 1.

Experimental setup

It mainly consists of a laser, an acousto-optical deflector (AOD), lens and diffuser. The idea is to create objective laser-speckles coming from the diffuser. The laser is focussed on the rough surface and the forward propagating statistical diffraction pattern is determined by the statistical roughness within the laser spot field. By changing the laser spot position one can change the diffraction field and therefore the laser-speckle pattern that illuminates the object under test.

Typically fast mechanical displacements are difficult to achieve. Therefore a non-mechanical displacement was introduced. An acoustic wave travels through a crystal leading to a refractive index change depending on the acoustic tension. The forming diffraction grating diffracts the incident laser beam to a desired angle depending on the applied frequency.

As the acousto-optical phenomena has a short fall and rise time, speckles and therefore illumination patterns can be switched at unprecedented 205.000 Hz.

CORRELATION TECHNIQUE

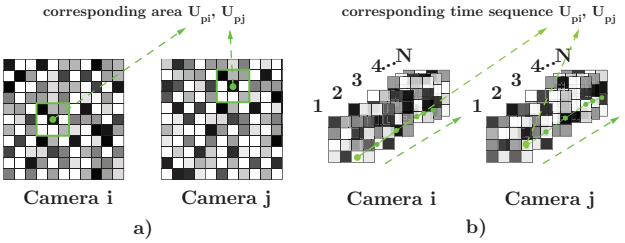

Figure 2: Comparing schemes of both correlation techniques; a) areal correlation b) temporal correlation

The pattern sequence of statistical objective laser-speckles result in two image stacks of the illuminated object, one of each camera (compare Figure 2). For every pixel one gets the gray value history over time. The goal now is to establish as much pixel correspondences between the to views as possible. This is done by using temporal correlation (eqn. 1) for every pixel of the first view. After calculating typically $\approx$ 100.000 point correspondences (the exact value depends strongly on camera resolution and object visibility) one can triangulate the 3D points, knowing intrinsic and extrinsic parameters of the setup.

$$\rho(p_i,p_j) = \frac{\sum_{t=1}^{N}\left(g(p_i,t)-\overline{g}_{U_{p_i}}\right)\cdot\left(g(p_j,t)-\overline{g}_{U_{p_j}}\right)}{rmsd(p_i,U_{p_i})\cdot rmsd(p_j,U_{p_j})} \tag{1}$$

RESULTS AND FURTHER APPLICATIONS

The overall brightness with laser-based illumination is much higher than what common 3D sensors achieve. Although 2 W light power sounds less than 250 W of DLP projectors, all the light power goes into the pattern due to diffractive pattern formation. Halogen lamps furthermore omit most of their power in heat and pattern formation is done by absorption. In experiments we could show, that with 2 W laser power shutter times of 600 μs are possible. With white-light projectors 3 times longer exposures are necessary. For highspeed applications therefore, laser-speckle illumination is preferable.

In experimental work we could show that additional subjective speckles that overlay the object images affect the measurement accuracy and the amount of reconstructible points. For two VGA cameras with a 60 degree triangulation angle at F-number of 1.4 one had a relative uncertainty (point noise divided by measurement volume diameter) of $\approx 1\cdot 10^{-4}$ without subjective speckles and $\approx 2\cdot 10^{-4}$ with. These results were obtained with an adapted setup introducing subjective speckle suppression by averaging over time. The loss in reconstructible point without suppresion was at higher F-numbers, e.g. 8, 30 %. The loss becomes larger when the subjective speckles size increases. This occurs when the with increasing focal length decreasing aperture size of the camera lenses.

Another advantage of the laser-speckle approach is the possibility to filter the illumination pattern from the light shining from extraneous light sources. This was implemented in an outdoor 3D shape measurement setup. The filters with 1 nm spectral width were placed in front of the camera lenses. With filtering the contrast reduction in the cameras' images was low. Hence, similar accuracies were achieved indoors and outdoors. This simple idea is not possible with common 3D sensors that use white-light sources for object structuring. We hope, this technique will contribute nicely to outdoor applications, like cultural heritage or art and archaeology in the future.

[1] S. S. Gorthi, P. Rastogi, *Optics and Lasers in Engineering* **48**, 133 (2010).

[2] Y. Wang, S. Zhang, *Opt. Express* **19**, 5149 (2011).

[3] J. P. Siebert, S. J. Marshall, *Sensor Review* **20**, 218 (2000).

[4] M. Grosse, M. Schaffer, B. Harendt, R. Kowarschik, *Optical Engineering* **50**, 100503 (2011).

[5] M. Schaffer, M. Grosse, B. Harendt, R. Kowarschik, *Opt. Lett.* **36**, 3097 (2011).

Characteristics of optical modes in coupled disk microresonators

Carsten Schmidt*[1], Mattes Liebsch[1], Angela Klein[1], Norik Janunts[1], Arkadi Chipouline[1], Thomas Käsebier[1], Ernst-Bernhard Kley[1], Andreas Tünnermann[1,2], and Thomas Pertsch[1]

[1] *Institute of Applied Physics, Abbe Center of Photonics, Friedrich-Schiller-Universität Jena, Max-Wien Platz 1, 07743 Jena, Germany*

[2] *Fraunhofer Institute for Applied Optics and Precision Engineering, Albert-Einstein-Strasse 7, 07745 Jena, Germany*

*Corresponding Author: *ca.schmidt@uni-jena.de*

Abstract

We report on the experimental characterization of optical modes in coupled disk microresonators excited by a tapered optical fiber using an adapted scanning near-field optical microscope (SNOM) technique. The SNOM-tip, which is placed in the evanescent tails of modes supported by the structure influences their coupling conditions to the tapered fiber, which leads to altered transmission and reflection signals. Correlation of SNOM-tip position and transmission signal results in intensity maps of the excited mode. The knowledge of spectrum and intensity distribution of the coupled disk structures together with thermal nonlinear effects observable in such systems allows for advanced tunable filters as well as optical sensors.

Introduction

Coupled optical microresonators have been attracting considerable attention in recent years. A combination of the advantageous properties of single microresonators [1] (especially, high Q-factor and strong field confinement) with the evanescent coupling by placing such resonators very close to each other results in systems of specific properties. For a few coupled resonators, effects like electromagnetically induced transparency [2], slow light [3], and optical bistability [4, 5] were observed. The coupling of a larger number of resonators forms a new class of optical waveguides, namely, coupled resonator optical waveguides (CROW [6]), which can be used, for example, as optical delay lines [7] and high-order filters [8]. Extending the coupling of the resonators to two-dimensional arrays allows the formation of photonic molecules [9], which can be used as optical sensors [10] or active lasing elements [11].

Especially for sensor applications, which are based on a resonance shift due to the interaction of the measured quantity (e.g. nanoparticles or physical quantities like temperature) with the cavity mode, the mode's intensity distribution is of particular interest. Due to the different spatial distributions of excited modes in coupled arrays of microresonators, it is possible to constrain the position of the perturbation across the array just by looking at changes in the spectrum.

Samples and experimental methods

The system of coupled microresonators under investigation consists of freestanding fused silica microdisks on a silicon pedestal, which are fabricated by direct electron beam writing and subsequent etching steps for processing the silica and the silicon layer. A detailed description of the sample fabrication can be found in [5]. The microdisks under investigation have radii of about $R = 15\ \mu$m and a thickness of $h = 1\ \mu$m and for the coupled samples they are arranged linearly or triangular with a gap size of $d_{\mathrm{gap}} \approx 300$ nm between them. In Fig. 1(a) scanning electron micrographs (SEM) of different samples are shown. In Fig. 1(b) a sketch of the setup is shown which also illustrates the mode mapping principle. The wavelength of the pump laser source, which is coupled to one of the disks of the sample, was fixed to a resonance resulting in a certain transmission and reflection signal measured at both ends of the fiber. By scanning a SNOM tip across the sample surface it perturbs the resonance when it reaches the mode's near field. The polarizability of the tip changes the effective refractive index of the environment, which has influences on the resonance

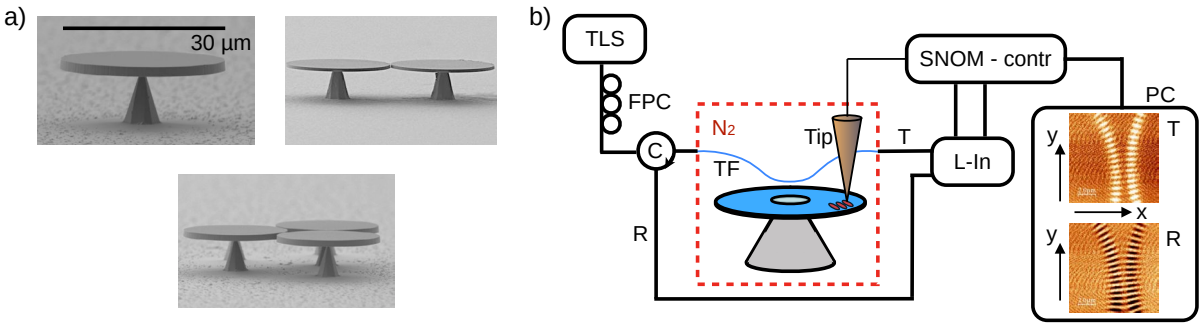

Figure 1: (a) SEM images of coupled microdisk samples under investigation. (b) Experimental setup illustrating the measurement principle and showing some obtained intensity mode maps in (T) transmission and (R) reflection (TLS - tunable laser source, FPC - fiber polarization controller, C - circulator, N_2 - nitrogen purged box, TF - tapered fiber, L-in - lock-in amplifier, PC - computer controlled setup and data aquisition).

condition and leads to a shift of the mode's resonance wavelength. Another effect of the tip is that it acts as a scatterer which introduces additional losses and also can couple different modes of the structure. All effects result in a change of the transmission and reflection signal depending on the position of the tip.

Results

As the measured signals described above actually display a map of interaction strength between tip and resonator mode, a theoretical model was used to extract the intensity distribution of the mode. This model uses a combination of theoretical field calculations of the structure and coupled mode equations taking into account the interaction of the tip, which is approximated by a dipole and couples different modes of the structure an leads to additional losses. From this the expected transmission and reflection signals depending on the mode distribution can be calculated and compared to the measurements. As a result the distinct characteristics of different modes can be determined (an example is shown in Fig. 1(b) for the gap region of two coupled disks). Together with previous results [5] investigating thermal nonlinear effects in such systems it allows for selective resonance tuning for advanced tunable filters or applications as versatile optical sensors.

[1] K. Vahala, *Nature* **424**, 839 (2003).

[2] A. Naweed, G. Farca, S. I. Shopova, A. T. Rosenberger, *Physical Review A* **71**, 043804 (2005).

[3] K. Totsuka, N. Kobayashi, M. Tomita, *Physical Review Letters* **98**, 213904 (2007).

[4] I. S. Grudinin, K. J. Vahala, *Optics Express* **17**, 14088 (2009).

[5] C. Schmidt et al., *Applied Physics B* **104**, 503 (2011).

[6] J. Poon, J. Scheuer, Y. Xu, A. Yariv, *Journal of the Optical Society of America B* **21**, 1665 (2004).

[7] A. B. Matsko et al., *IEEE Photonics Technology Letters* **17**, 136 (2005).

[8] M. A. Popovic et al., *Optics Letters* **31**, 2571 (2006).

[9] S. V. Boriskina, *Optics Letters* **31**, 338 (2006).

[10] S. V. Boriskina, *Journal of the Optical Society of America B* **23**, 1565 (2006).

[11] A. Nakagawa, S. Ishii, T. Baba, *Applied Physics Letters* **86**, 041112 (2005).

Measuring wavefronts using modal decomposition

Christian Schulze*[1], Daniel Flamm[1], Oliver Schmidt [2], and Michael Duparré[1]

[1]*Institute of Applied Optics, Fröbelstieg 1, 07743 Jena, Germany*

[2]*Max Planck Institute for the Science of Light, Günther Scharowsky Straße 1, 91058 Erlangen, Germany*

*Corresponding Author: *christian.schulze@uni-jena.de*

Abstract

Modal decomposition depicts an elegant approach to characterize optical fields. Measuring corresponding modal expansion coefficients yields amplitude and phase of the investigated beam. This work presents the use of computer-generated holograms to perform the modal decomposition and outlines a recipe to retrieve the beams wavefront. The principle is demonstrated using beams emerging from optical fibers and comparing the results to those of a Shack-Hartmann wavefront sensor.

Introduction

Wavefront reconstruction of optical fields is common in many domains of optics, including astronomy [1], microscopy [2, 3], ophthalmology [4, 5] and laser material processing [6, 7].
Different wavefront measurement techniques have been developed, such as laser ray tracing [8], pyramid sensors [9], interferometric approaches [10] and the widely used Shack-Hartmann sensor (SHS) [11]. Additionally, computer-generated holograms (CGHs) are studied to encode wavefront aberration modes [12].
In this work we consider a different approach making use of a CGH to perform a modal decomposition of the investigated beam. To demonstrate the principle we applied our method to beams emerging from multimode optical fibers and compared the results with the above mentioned Shack-Hartmann technique to check for reliability.

Experimental Setup

The experimental setup (Fig. 1) consists of laser seed source ($\lambda = 1064\,\mathrm{nm}$), multimode optical fiber, and analyzing system, which consists of a modal decomposition branch, including CGH and two cameras, and a second branch with a Shack-Hartmann wavefront sensor that serves as a reference.
A positioning stage provides precise control of the coupling situation at the front facet of the fiber, allowing to excite distinct mode mixtures. A beam splitter is used to analyze the beam with the wavefront sensor and with the modal decomposition setup at the same time. Two 4f-setups image the fiber end facet to the wavefront sensor and to the CGH. Via a second beam splitter, the fiber end face is simultaneously imaged onto the CGH and a CCD camera for recording the near field intensity (CCD_1, cf. Fig. 1) directly. Thereby, a polarizer (P) and an optional quarter-wave plate (QWP) enable the measurement of polarization in addition to the modal information achieved with the hologram. The CGH diffraction pattern is observed with a second CCD camera (CCD_2) in the Fourier plane of the hologram (2f-setup), which provides modal powers and phases of the beam.

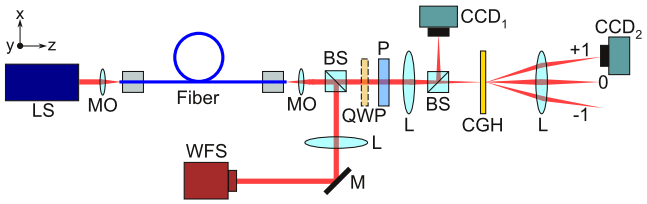

Figure 1: Measurement setup: LS laser source, MO microscope objectives, QWP quarter-wave, P polarizer, L lenses, BS beam splitter, $CCD_{1,2}$ CCD cameras, CGH computer-generated hologram, M mirror, WFS wavefront sensor.

Measurement Results

The combination of modal decomposition and polarization measurement enables the calculation of the beams Poynting vector. Accordingly, the wavefront w is defined to be a continuous surface perpendicular to

the direction of energy propagation, which is given by the Poynting vector **P** [13, 14]:

$$w(\mathbf{r},z) \perp \mathbf{P}(\mathbf{r},z), \tag{1}$$

Using Eq. (1), the wavefront can be reconstructed. One measurement example is depicted in Fig. 2. The illustrated beam was generated by exciting a mode mixture within a step-index fiber that according to its geometry specifications and the used wavelength potentially guides three transverse modes. The corresponding mode content consists of 49% fundamental mode as well as 9% and 42% next higher order modes. The comparison of intensities and wavefronts measured with CGH and Shack-Hartmann sensor (Fig. 2) reveal good agreement between the two techniques, prooving the modal decomposition ansatz to be suitable for wavefront measurements.

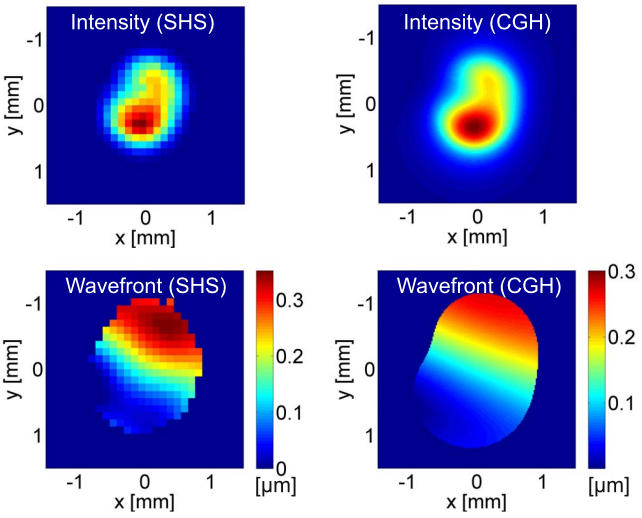

Figure 2: Intensity and wavefront of a multimode beam measured by modal decomposition (CGH) and with Shack-Hartmann sensor.

[1] F. Roddier, *et al.*, *Adaptive Optics in Astronomy* (Cambridge, 1999).

[2] M. A. A. Neil, *et al.*, *Journal of Microscopy* **200**, 105 (2000).

[3] M. Booth, M. Neil, T. Wilson, *Journal of Microscopy* **192**, 90 (1998).

[4] B. Hermann, *et al.*, *Opt. Lett.* **29**, 2142 (2004).

[5] A. Roorda, *et al.*, *Opt. Express* **10**, 405 (2002).

[6] R. Paschotta, *Encyclopedia of Laser Physics and Technology* (Wiley, 2008).

[7] M. Paurisse, M. Hanna, F. Druon, P. Georges, *Opt. Lett.* **35**, 1428 (2010).

[8] R. Navarro, E. Moreno-Barriuso, *Opt. Lett.* **24**, 951 (1999).

[9] S. R. Chamot, C. Dainty, S. Esposito, *Opt. Express* **14**, 518 (2006).

[10] M. P. Rimmer, J. C. Wyant, *Appl. Opt.* **14**, 142 (1975).

[11] R. G. Lane, M. Tallon, *Appl. Opt.* **31**, 6902 (1992).

[12] L. Changhai, X. Fengjie, H. Shengyang, J. Zongfu, *Appl. Opt.* **50**, 1631 (2011).

[13] B. Neubert, B. Eppich, *Optics Communications* **250**, 241 (2005).

[14] ISO, ISO 15367-1: 2003 lasers and laser-related equipment – test methods for determination of the shape of a laser beam wavefront – part 1: Terminology and fundamental aspects (2003).

Fluorescence based DNA detection of pathogens with magnetic beads

Barbara Seise[1,2], Susanne Pahlow[1,2], Martin Klapper[1,2], Dana Cialla[1,2], Karina Weber[1,2] and Jürgen Popp[*1,2]

[1]*Institute of Photonic Technologies, Albert-Einstein-Straße 9, 07745 Jena, Germany*

[2]*Friedrich Schiller University Jena, Institute of Physical Chemistry and Abbe Centre of Photonics, Helmholtzweg 4, 07743 Jena, Germany*

[*]Corresponding Author: *juergen.popp@uni-jena.de*

Abstract

Within this contribution we present a method combining magnetic beads and fluorescence spectroscopy for the detection of pathogens. Within a polymerase chain reaction (PCR) the region of interest of the pathogen DNA is amplified and labelled. Subsequently the amplicon is attached to magnetic beads. Via DNA hybridization reaction fluorescence dye labelled probe DNA is bound to the amplicons. Magnetic beads are used due to easy handling in DNA detection.

INTRODUCTION

For clinical biological diagnosis there is an emerging need of fast, robust and easy analysis assays. For this reason magnetic beads with different modifications were used during the last years leading to new and fast methods for biological detection techniques. [1, 2].

These techniques possess high potential for prevention and health care by exploiting interactions between antibody and antigen [3], detection of viruses or bacteria [4] and DNA or RNA hybridization reactions [5].

The readout of the techniques utilizes fluorescence spectroscopy [6, 7], Surface Enhanced Raman Scattering (SERS) [8], Surface Enhanced Resonance Raman Scattering (SERRS) [9] or combinations of chemo luminescence reactions [10, 11].

MAGNETIC BEADS

Magnetic beads are micro particles with a unique size contribution [12] which can vary from several hundred nanometres to some microns with lots of applications in biological assays [3, 13].

In general, magnetic beads contain super paramagnetic magnetite nanoparticles (Fe_3O_4) which are per se not magnetic. By applying a magnetic field, these super paramagnetic magnetite nanoparticles are more magnetisable than other paramagnetic material [14] and thus easier to separate [15].

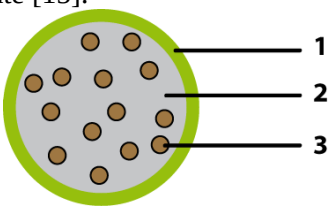

Figure 1: schematic view of magnetic bead. 1: functionalized polymer coating. 2: polymeric matrix. 3: magnetite particle.

The used magnetic beads were functionalized with streptavidin which allows the immobilization of biotin labelled biomolecules. By using a magnetic separator, these streptavidin functionalized magnetic beads are suited for a fast separation, purification and enrichment of biomolecules from complex media.

EXPERIMENTAL SETUP

A specific region of pathogen DNA is amplified and biotin labelled via PCR. The magnetic beads possess a streptavidin coating, so biotin labelled amplicons are bound to the magnetic beads via biotin streptavidin interaction. After the linking of amplicons to the magnetic beads, a fluorescence dye labelled probe DNA, which is complementary to the amplicon, is added.

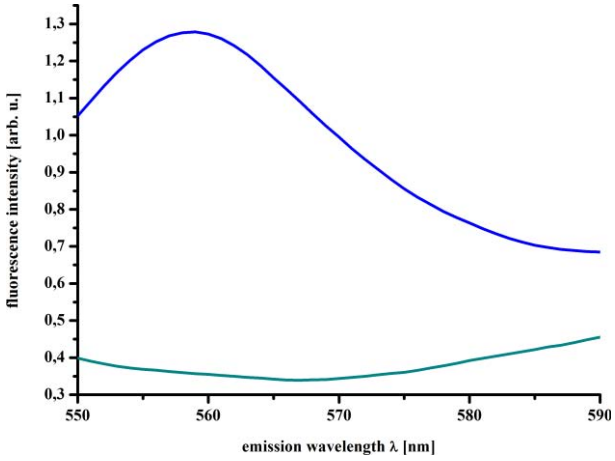

Figure 2: fluorescence spectra of Cy3 labelled probe DNA hybridized to the amplicons using the distant end binding probe (blue). A fluorescence spectrum of the blank sample shows no signal (green).

Via DNA hybridization reaction to the probe DNA is sequence specific bound to the amplicon. Two different probes were used, whereas one probe binds to the distant end of the amplicons relating to the magnetic bead and the other probe binds to a proximal position on the amplicons relating to the magnetic bead. Both probes were labelled with Cy3 as fluorescence dye and the readout was carried out with a fluorescence spectroscope, recording fluorescence spectra. For every analysis, the measurement of the blank containing no amplicons compared to the sample was done.

ACKNOWLEDGEMENT

The research project "NAWION" with the supporting ID 16SV5386K and V4MNI014 and the research project "JBCI 2.0" within the framework "InnoProfile - Transfer" are financially supported by the Federal Ministry of Education and Research (BMBF) Germany. We gratefully acknowledge support from the European Network of Excellence Photonics4Life.

[1] G. Amagliani, E. Omiccioli, A. del Campo, J Appl Microbiol **100**, 375 (2006)

[2] J. Wang, Q. Wang, L. Ren, Colloids and Surfaces B: Biointerfaces **72**, 112 (2009)

[3] B.-I. Haukanes, C. Kvam, Nat Biotech **11**, 60 (1993)

[4] O. Olsvik, T. Popovic, E. Skjerve, Clinical Microbiology Reviews **7**, 43 (1994)

[5] M. Uhlen, Nature **340**, 733 (1989)

[6] G. K. Kouassi, J. Irudayaraj, Analytical Chemistry **78**, 3234 (2006)

[7] L. Jiang, D. Duan, Y. Shen, Biosensors and Bioelectronics **34**, 291 (2012)

[8] Y. Liang, J.-L. Gong, Y. Huang, Talanta **72**, 443 (2007)

[9] C. Feuillie, M. M. Merheb, B. Gillet, PLoS ONE **6**, e17847 (2011)

[10] Z. Cao, Z. Li, Y. Zhao, Analytica Chimica Acta **557**, 152 (2006)

[11] H. Li, Z. He, Analyst **134**, 800 (2009)

[12] T. Lea, F. Vartdal, K. Nustad, Journal of Molecular Recognition **1**, 9 (1988)

[13] I. M. Hsing, Y. Xu, W. Zhao, Electroanalysis **19**, 755 (2007)

[14] A.-H. Lu, E. L. Salabas, F. Schüth, Angewandte Chemie International Edition **46**, 1222 (2007)

[15] A. J. Kell, K. Somaskandan, G. Stewart, Langmuir **24**, 3493 (2008)

Optimisation and application of the second-harmonic waveguiding in lithium niobate nanowires.

Anton Sergeyev*, Reinhard Geiß, Thomas Pertsch, Ernst-Bernhard Kley, and Rachel Grange

Institute of Applied Physics, Friedrich Schiller University, Albert-Einstein-Straße 15, 07745 Jena, Germany

*Corresponding Author: *anton.sergeyev@uni-jena.de*

Abstract

In this work, we study generation and waveguiding of the second-harmonic (SH) signal through $LiNbO_3$ nanowires which are fabricated by ion beam enhanced etching method (IBEE). We test different designs of the nanowires for optimising the guided SH signal by varying the length and facets of the nanowire. Finally, we demonstrate the efficiency of SH waveguiding by locally exciting dyes with the guided SH signal.

Introduction

Thanks to a two-dimensional confinement and a free third dimension, nanowires differ from other types of nanomaterials and provide characteristic optical effects such as waveguiding [1] and lasing [2]. Even more properties of nanowires can be found when nonlinear optics is taken into consideration. For example, the use of the second-harmonic generation (SHG) can help to study new effects. In order to observe such kind of effects, materials with efficient SHG are required. The $LiNbO_3$ nanowires have already been shown to generate efficient SH [3] and even to support SH waveguiding [4]. This effect can be used for local excitation of fluorescent material and be applied for biological study of cells [5, 6]. Nevertheless, the amount of the guided SH is not enough for an efficient excitation of dyes for further applications.

In this paper, we report the generation and propagation of the SH in $LiNbO_3$ nanowires which have been fabricated with the use of IBEE method [7]. We discuss the ways of increasing the propagated SH signal by modifying nanowires' facets and lengths. In the end, we demonstrate dye excitation with the use of generated and guided SH signal.

Experimental results and discussion

For the experiments, a home-made setup has been built. A pulsed laser beam is focused on a sample slide by a 10x objective. The generated SH or dye fluorescence signal is collected by a 100x magnification objective and imaged with a lens onto an electron-multiplying coupled charge device (EMCCD). In order to observe the required spectral range, corresponding filters are used in front of the EMCCD. A Ti:Sapphire oscillator is used as a source, delivering a pulsed beam of 820 nm with repetition rate of 80 MHz and pulse duration of 285 fs (FWHM) at the sample position. In order to optimise the generated SH signal, the polarization of the incident beam is manipulated with a half-wave plate.

By focusing the laser beam of 820 nm onto one of the ends of the $LiNbO_3$ nanowire and using a bandpass filter at 410 nm, a signal at the unilluminated end of the nanowire is observed (Fig. 1a). Moreover, the signal shows quadratic dependence on the incident beam power (Fig. 1b). Thus, the signal is probably the SH which is generated and guided through the nanowire.

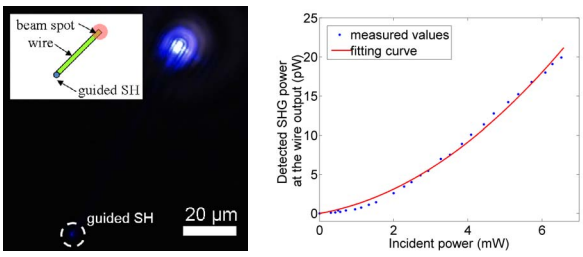

(a) (b)

Figure 1: a) Propagation of the SH through the wire with a length of 80 µm and a width and a height of approximately 500 nm. b) The power dependence of the signal at the output facet of the wire.

In this work, we have studied the ways of optimisation of the amount of the propagated SH by manipulating the length and the shape of input facets of the nanowires.

First, we decrease the length of the wire stepwise

with focused ion beam (FIB). After each cutting procedure, the waveguiding experiment is performed with the same power and polarization of the beam and the amount of the guided SH signal on the output wire is measured (Fig. 2).

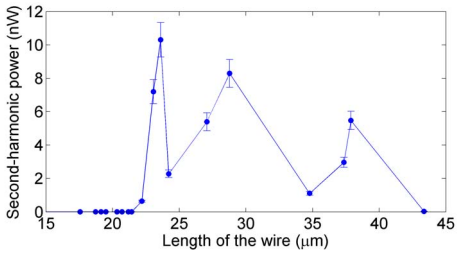

Figure 2: The SH power versus the length of a nanowire.

In Fig. 2, the power of the guided SH vary from 30 pW up to 10 nW for different length of the nanowire. We attribute the variation to the phase-matching effect. Thus, by varying the length of a nanowire, the amount of the obtained SH signal can be increased.

In order to study the influence of the shape of an input facet, a nanowire is cut first in two pieces of equal length. The input facets of the pieces are cut with angles of 45° and 135°. After performing the waveguiding experiment, the facet of one of the pieces is cut with an angle of 90° and the experiment is repeated. The shape of the facets is found out to have a considerable influence on the amount of the guided SH signal. Thus, the nanowires with facets of angles 45°, 90 ° and 135° provide 4.647 nW, 0.410 nW and 0.149 nW, respectively.

Finally, we demonstrate a possibility of exciting dyes (Coumarin 30) with the guided SH signal which is generated by a nanowire. The dyes do not exhibit direct absorption in the infrared range [8]. As a result, employing a laser beam of 820 nm, Coumarin can be excited through either direct excitation with generated SH signal or two-photon absorption process (TPA) of the fundamental wavelength.

In the experiment, a bandpass filter at 530 nm is used to filter out the infrared pump beam and the generated SH signal. Thus, only the fluorescence signal at 530± 10 nm is detected. The fact of dye excitation with the guided light is checked by performing waveguiding experiments before and after adding the dyes to the sample at the same beam parameters.

Moreover, further experiments have also shown that the dyes get excited much stronger with the use of propagated SH signal than when a laser beam is focused onto the dyes. Thus, the dyes are excited mostly by the guided SH but not by the fundamental wavelength due to the TPA process. Excitation of dyes with the use of nonlinear light sources has already been reported in [5, 9]. Nevertheless, the source of the excitation has never been clearly identified.

As a conclusion, we have studied the generation and propagation of the SH signal inside of the $LiNbO_3$ nanowires. We have discussed the influence of nanowire's input facet and length on the amount of the propagated SH signal. In addition, we have demonstrated that the $LiNbO_3$ nanowire can be used for an efficient local excitation of dyes with guided SH.

[1] T. Voss, *et al.*, *Nano letters* **7**, 3675 (2007).

[2] J. C. Johnson, *et al.*, *Nature materials* **1**, 106 (2002).

[3] R. Grange, *et al.*, *Applied Physics Letters* **95**, 143105 (2009).

[4] F. Dutto, C. Raillon, K. Schenk, A. Radenovic, *Nano Letters* **11** (2011).

[5] Y. Nakayama, *et al.*, *Nature* **447**, 1098 (2007).

[6] R. Grange, F. Dutto, A. Radenovic, *Niobates nanowires: Synthesis, Characterization and Applications* (Intec, 2011), pp. 509–524.

[7] H. Hartung, *et al.*, *Optical Materials* **33**, 19 (2010).

[8] G. Jones, W. R. Jackson, C. Y. Choi, W. R. Bergmark, *The Journal of Physical Chemistry* **89**, 294 (1985).

[9] S. Palomba, L. Novotny, *Nano Letters* **9**, 3801 (2009).

Equivalent step-index model of multifilament core fibers

Ron Spittel, Adrian Lorenz, Sylvia Jetschke, Matthias Jäger and Hartmut Bartelt

Institute of Photonic Technology Jena, Albert-Einstein-Straße 9, 07745 Jena, Germany

*Corresponding Author: *ron.spittel@ipht-jena.de*

Abstract

We present a semi-analytical model for the description of multifilament core (MFC) fibers by substituting the microstructured core with a circular equivalent step index (ESI) core with an effective radius and refractive index. We show that the model is very accurate for the prediction of the effective V-parameter, the fundamental mode and its effective area. It is therefore a very convenient tool for the design of such fibers.

Introduction

Multifilament core (MFC) fibers are characterized by a microstructured core consisting of a number of (identical) circular waveguides in a hexagonal lattice [1]. As an example, figure 1 illustrates a MFC fiber consisting of $N = 19$ filaments spaced by a pitch Λ and defined by the V-parameter of the filaments $V_{\mathrm{fil}} = \frac{2\pi}{\lambda} a \sqrt{n_{\mathrm{fil}}^2 - n_{\mathrm{bg}}^2}$, where λ is the wavelength, $a = d/2$ is the filament radius, n_{fil} and n_{bg} are the refractive indices of the filaments and the background, respectively. The refractive index of the cladding which surrounds the filamented core is denoted as n_{cl}.

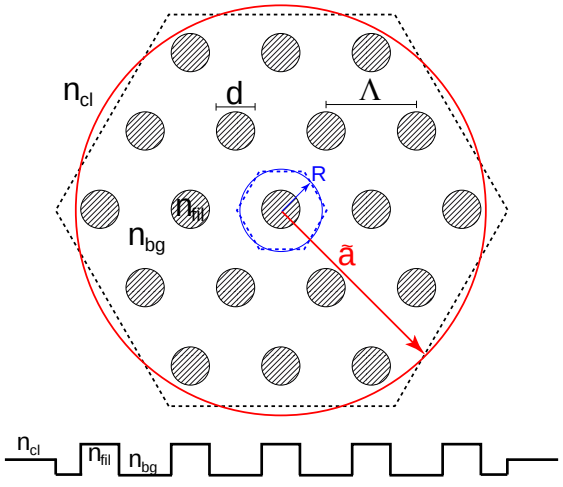

Figure 1: Schematic cross section of a MFC fiber with 19 filaments. The blue and red circle represent the circular unit cell and equivalent core, respectively.

We distinguish a MFC fiber from a multicore fiber by the number of modes which are able to propagate. While latter usually guides at least a few supermodes, a MFC fiber is designed to support only the fundamental (in-phase) supermode. Similar to the simplified description of the microstructured cladding of photonic crystal fibers (PCFs), we substitute the filamented core with a homogeneous equivalent material. The refractive index of this material is given by the fundamental space-filling mode (FSM), which is the solution of Maxwell's equations in an infinite extended lattice of filaments [2].

The Fundamental Space-Filling Mode

In contrast to PCFs, MFC fibers contain a microstructured core with small index differences embedded in a homogeneous cladding medium. This allows us to use an approximate semi-analytical approach based on the transformation of the hexagonal into a circular unit cell of radius $R = \sqrt{\frac{\sqrt{3}}{2\pi}}\Lambda$ with the same area (see figure 1). By applying appropriate boundary conditions we obtain the dispersion relation for the FSM [3]:

$$(\Phi + \Psi)\left(n_{\mathrm{fil}}^2 \cdot \Phi + n_{\mathrm{bg}}^2 \cdot \Psi\right) = n_{\mathrm{FSM}}^2 \cdot V^4. \qquad (1)$$

Here the functions Φ and Ψ are given by

$$\Phi = W^2 \left(1 - U \frac{J_2(U)}{J_1(U)}\right), \qquad (2)$$

$$\Psi = U^2 \left(1 - W \frac{I_1(W\frac{R}{a})K_2(W) + I_2(W)K_1(W\frac{R}{a})}{I_1(W\frac{R}{a})K_1(W) - I_1(W)K_1(W\frac{R}{a})}\right), \qquad (3)$$

with the parameters $U = \frac{2\pi}{\lambda} a \sqrt{n_{\mathrm{fil}}^2 - n_{\mathrm{FSM}}^2}$, $W = \frac{2\pi}{\lambda} a \sqrt{n_{\mathrm{FSM}}^2 - n_{\mathrm{bg}}^2}$ and $V = \frac{2\pi}{\lambda} a \sqrt{n_{\mathrm{fil}}^2 - n_{\mathrm{bg}}^2}$. $J_m(U)$, $I_m(W)$ and $K_m(W)$ are the Bessel function and

the modified Bessel functions of first and second kind, respectively. Please note, that the dispersion equation (1) is an implicit expression and cannot be solved analytically. Thus, we use Matlab to solve the equation and obtain n_{FSM}, which is the effective refractive index of the FSM and is the equivalent refractive index of the filamented core.

Eigenmodes of the ESI Fiber

After the calculation of the equivalent refractive index of the filamented core, we need to define an equivalent core radius. We chose a circle with the same area as the sum of all N (7, 19, 37,...) hexagonal unit cells, which results in an equivalent radius $\tilde{a} = \sqrt{\frac{N\sqrt{3}}{2\pi}}\Lambda$ (see figure 1). We then can define the V-parameter of the ESI fiber $\tilde{V} = \frac{2\pi}{\lambda}\tilde{a}\sqrt{n_{\mathrm{FSM}}^2 - n_{\mathrm{cl}}^2}$, which should be below $\tilde{V}^* = 2.405$ to fulfill our definition of a MFC fiber and guide only the fundamental supermode.

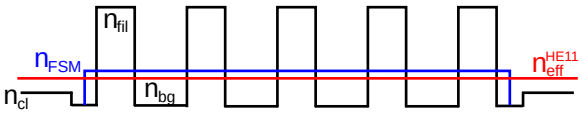

Figure 2: Refractive index profile of a MFC fiber, its ESI core (defined by the FSM and $\tilde{a}$) and n_{eff} of the fundamental mode.

Similar to the preceding section, we can derive the dispersion equation for the ESI fiber

$$\left(\tilde{\Phi}_m + \tilde{\Psi}_m\right)\left(n_{\mathrm{FSM}}^2\tilde{\Phi}_m + n_{\mathrm{cl}}^2\tilde{\Psi}_m\right) = m^2 n_{\mathrm{eff}}^2 \tilde{V}^4, \qquad (4)$$

with m being the azimuthal mode order and

$$\tilde{\Phi}_m = \tilde{W}^2 \cdot \left(m - \tilde{U}\cdot\frac{J_{m+1}(\tilde{U})}{J_m(\tilde{U})}\right), \qquad (5)$$

$$\tilde{\Psi}_m = \tilde{U}^2 \cdot \left(m - \tilde{W}\cdot\frac{K_{m+1}(\tilde{W})}{K_m(\tilde{W})}\right). \qquad (6)$$

The new parameters of the FSM-based equivalent step-index fiber are given by $\tilde{U} = \frac{2\pi}{\lambda}\tilde{a}\sqrt{n_{\mathrm{FSM}}^2 - n_{\mathrm{eff}}^2}$ and $\tilde{W} = \frac{2\pi}{\lambda}\tilde{a}\sqrt{n_{\mathrm{eff}}^2 - n_{\mathrm{cl}}^2}$. The dispersion equation (4) also has to be solved numerically and yields the effective refractive index n_{eff} of the eigenmodes of the ESI fiber. Figure 2 qualitatively shows the equivalent core and the effective refractive index of the fundamental (HE_{11}) mode.

Comparison with Finite Element Method

We will now compare the results from the ESI model using equations (1) and (4) with highly accurate numerical simulations of the MFC fibers done with a commercial finite element method (FEM). For simplicity, we have chosen $\tilde{V} = \tilde{V}^* = 2.405$ to analyze the error around the edge of the single-mode regime. The solid lines in figure 3 show the relative percentage error of n_{eff} for the fundamental mode (m=1). As one can see it is smaller than 10% for all considered ratios d/Λ and numbers N of filaments. The deviation decreases significantly for increasing number of filaments, falling to values below 1% for $N = 37$. The dashed lines represent the relative error of the effective area A_{eff}. Here, the deviations are in the magnitude of 5%, 0.5% and 0.05% for N=7, N=19 and N=37, respectively.

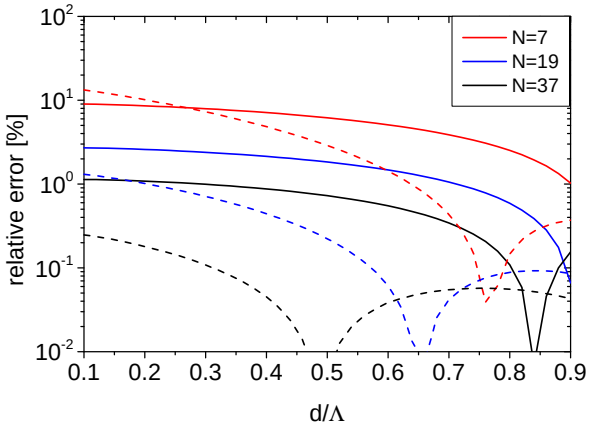

Figure 3: Relative percentage error of $n_{\mathrm{eff}}^{\mathrm{HE}_{11}}$ (solid lines) and $A_{\mathrm{eff}}^{\mathrm{HE}_{11}}$ (dashed lines) between the ESI model and FEM simulations for $\tilde{V} = 2.405$.

[1] G. Canat, *et al.*, *Optics Letters* **33**, 2701 (2008).

[2] G. Canat, R. Spittel, S. Jetschke, L. Lombard, P. Bourdon, *Optics Express* **18**, 4644 (2010).

[3] M. Midrio, M. P. Singh, C. G. Someda, *Journal of Lightwave Technology* **18**, 1031 (2000).

Superballistic transport and anomalous diffusion in inhomogeneous lattices

S. Stützer*[1], T. Kottos[2], U. Naether[3], S. Nolte[1], D.N. Christodoulides[4] and A. Szameit[1]

[1] *Institute of Applied Physics, Abbe Center of Photonics, Friedrich-Schiller-Universität Jena, Max-Wien-Platz 1, 07743 Jena, Germany*

[2] *Department of Physics, Wesleyan University, Middletown, Connecticut 06459, USA*

[3] *Departamento de Fisica, Facultad de Ciencias, Universidad de Chile, Santiago, Chile*

[4] *College of Optics and Photonics, University of Central Florida, Orlando, FL 32816, USA*

*Corresponding Author: *simon.stuetzer@uni-jena.de*

Abstract

We present the experimental proof for superballistic as well as anomalous diffusive transport in time-independant one-dimensional periodic structures.

Introduction

Understanding the dynamics of an evolving wave packet is a basic requirement for the interpretation of wave effects occurring in all fields of physics. There exist two common wisdoms on wave dynamics in time-independent one-dimensional (1D) periodic systems that are generally agreed on: (1) The spreading of a wave packet (either dispersive in time or diffractive in space) cannot exceed the ballistic limit, and (2) the wave transport cannot be diffusive. In our work, we provide for the first time experimental evidence for the existing of both a superballistic regime as well as a diffusive-like regime for the wave transport.

In a periodic system, translational symmetry is present. In this case the eigenmodes of the system are extended Floquet-Bloch modes [1], and the width of an evolving wave packet increases quadratically in time. As the wave packet transport is usually characterized by a so-called diffusion constant γ, in this case - commonly referred to as ballistic spreading - one finds $\gamma = 2$. In contrast, in disordered systems with no translational symmetry, all eigenmodes are localized [2] and the broadening of wave packets is fully suppressed - they are "Anderson-localized"[3], and $\gamma = 0$. It is commonly believed that, as translational symmetry either holds or not, wave packet dynamics in 1D systems can either be ballistic or localized.

Superballistic Transport

Recently it was found that a particular sophisticated hybrid setting allows for a spreading of a wave packet that exceeds the virtual limit of $\gamma = 2$ [4]. In this work, it was proposed that embedding a finite disordered lattice region into an infinite periodic lattice should result in superballistic spreading.

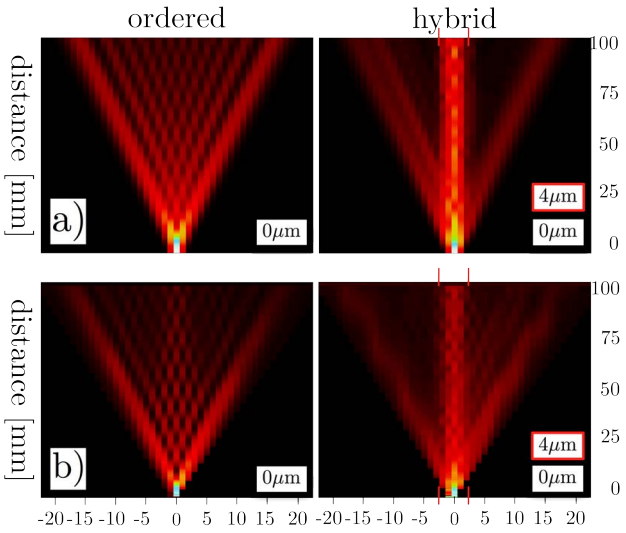

Figure 1: a) Simulations of the light propagation in the ordered (left) and the hybrid array (right). b) Experimental fluorescence images of the light propagation in an ordered (left) and the hybrid array (right).

In our work, we transfer the dynamics into a lattice of evanescently coupled waveguides, where the spatial evolution of the light directly corresponds to the temporal evolution of a quantum wave packet [5]. The lattice is fabricated using the laser direct-writing technology [6]. Light at $\lambda = 633$nm is launched into the lattice using fiber butt coupling, and the light evolution is directly monitored using a fluorescence microscopy

technique [6]. The hybrid lattice consists of 5 central waveguides with disordered spacing, and additional 10 ordered waveguides on each side. In Fig. 1, the light evolution in a periodic and a hybrid waveguide array are shown, in simulations (Fig. 1(a)) and experiment (Fig. 1(b)). From the experimental data, we extract the variance as a function of distance and plot the results in Fig. 2 to determine the diffusion coefficient in dependence on the positioning disorder in the central part of the lattice.. The spreading clearly exceeds the ballistic limit of $\gamma = 2$, with a maximum of $\gamma \approx 2.4$.

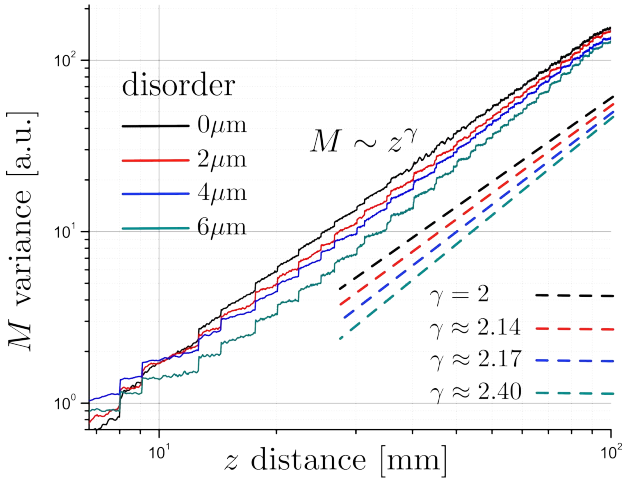

Figure 2: The spreading in the hybrid lattice (red, blue, green) exhibits a slope that is larger than in the ballistic case (black).

Anomalous Diffusion

Since Anderson considered in his seminal work only disordered systems without any correlations [2], there exist a few theoretical counter-examples where lattices with intrinsic long-range correlations may facilitate a intermediate regime of transport between localization and ballistic - a "diffusive" spreading. The prototypical case is that of the Random Dimer Model (RDM) [7] where (in the context of a tight-binding Hamiltonian) pairs of adjacent energy levels are assigned at random, leading to two-site correlations in an otherwise random model. Below a certain disorder threshold, a number of transparent states for finite samples emerge, and their existence results in a diffusive and super-diffusive wave propagation. Indirect experimental evidences of delocalized eigenstates in such short-range correlated systems were found using the electronic properties of GaAs-AlGaAs superlattices [7]. However, a direct experimental proof of (super-)diffusive transport in such systems is still missing. In our work, the theoretical predictions of the localization-delocalization transition are proven experimentally in RDM-arrays of coupled waveguides. Our measurements reveal a diffusive-like wavepacket spreading which is suppressed once the disorder contrast between dimers exceeds a critical value.

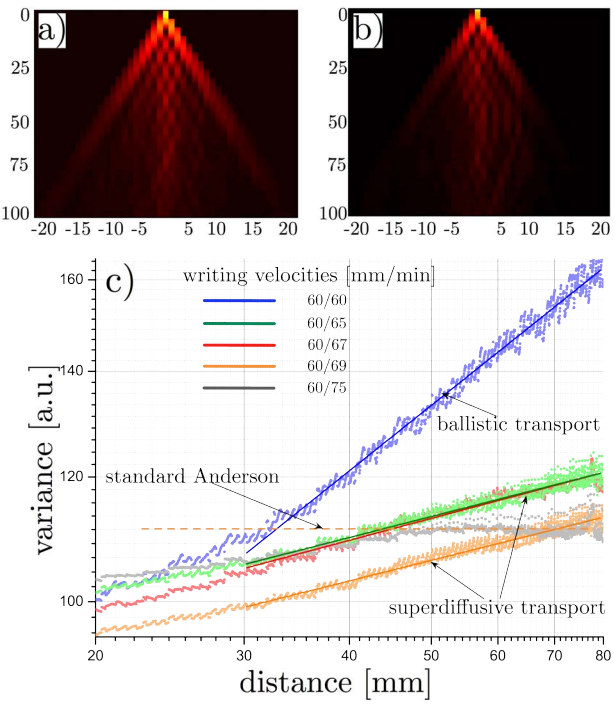

Figure 3: a), b) Experimental averaged output for diffusive-like transport and localization, respectively. c) Experimental variance as a function of distance for arrays prepared with different writing velocities of the two dimers. For a waveguide detuning $0 < \delta < 2$ the diffusion coefficient is $\gamma = 1.5$.

[1] N. W. Ashcroft and N. D. Mermin, *Solid State Physics Brooks* Cole (1976)

[2] P. W. Anderson, *Phys. Rev. 109, 1492* (1958)

[3] T. Schwartz et al., *Nature 446, 52* (2007); Y. Lahini et al., *Phys. Rev. Lett.100, 013906* (2008)

[4] L. Hufnagel et al., *Phys. Rev. E 64, 012301* (2001)

[5] D.N. Christodoulides, F. Lederer, and Y. Silberberg, Nature 424, 817 (2003)

[6] A. Szameit and S. Nolte, *J. Phys. B 43, 163001* (2010)

[7] P. Phillips and H.L. Wu, *Science 252*, 1805(1991)

[8] V. Bellani et. al., *Phys. Rev. Lett.82, 2159* (1999)

Femtosecond-Laser Induced Nanogratings
A versatile Platform for Birefringent Polarization Control

Christian Vetter*[1], Sören Richter[1], Felix Zimmermann[1], Matthias Heinrich[1], Felix Dreisow[1] and Stefan Nolte[1]

[1] *Institute of Applied Physics*
Albert-Einstein-Straße 15
07745 Jena

*Corresponding Author: *Christian.Vetter@uni-jena.de*

Abstract

We report on the generation of fs-laser induced nanogratings in fused silica and their intrinsic form-birefringent behavior. Based on that birefringence, it is shown, that nanogratings allow for the fabrication of intricately shaped and locally varying wave plates. More complicated structures can be used for optical mode conversion and other applications.

Introduction

In almost every field of modern technology, the precise control of light and its physical properties is a crucial step towards an actual application. Since light is not able to resolve structures much smaller than its own wavelength, novel optical materials, whose properties are mainly determined from their nano-geometry have been developed. The discovery of fs-laser induced sub-wavelength structures offers new approaches for laser-based material processing on a nanometer scale.

In 1999, Sudrie *et al.* discovered a distinct optically anisotropic behavior of fs-laser generated structures in fused silica [1]. Just three years later, Miller and coworkers suggested that self-assembled periodic sub-wavelength structures might be responsible for the observed anisotropic behavior [2]. Shimotsuma *et al.* provided the first experimental evidence for the existence of those nanogratings [3].

Until now, no model could be found, which explains the nanograting formation process in full agreement with the experimental observations. To this date, the following is known: Nanogratings are permanent refractive index modifications based on a modulated material density [3]. Their period scales with the employed laser wavelength as well as number of applied pulses [4, 5]. Moreover, the orientation of the grating planes is always perpendicular to the electric field direction [3] as depicted in Figure 1. Since the typical grating period is smaller than the wavelengths of the visible spectral range, they can act as an effective medium with anisotropic optical properties [1]. Hence, nanogratings are an alternative to natural birefringent media and allow for the fabrication of nanostructure based wave plates [6].

In contrast to naturally birefringent media, the fs-laser writing technique enables a spatially resolved nanograting control and three-dimensional structuring of the bulk material. That allows to fabricate wave plates with locally varying optical properties. The resulting spatially variable states of polarization are of great practical importance for optical mode conversion, beam shaping, improved material processing and other fascinating fields of application.

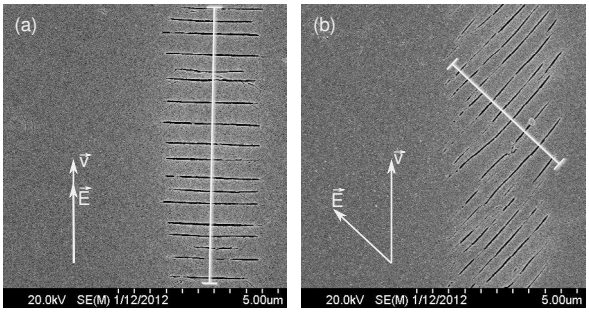

Figure 1: Scanning electron micrographs of individually written lines for (a) parallel and (b) oblique orientation of the laser polarization.

Experimental Setup

For the fabrication of the samples, a standard fs-laser writing setup has been employed. The laser pulses (515 nm wavelength, 170 nJ pulse energy, 500 fs pulse duration, up to 10 MHz repetition rate) were focused inside a fused silica sample using either microscope objectives or aspheric lenses with a typical numerical aperture of about 0.3 to 0.7. The position of the focal point can be controlled three-dimensionally using a precise positioning system (Aerotech). The two-dimensional structures were generated by writing multiple lines (with some overlap) next to each other.

RESULTS / APPLICATIONS

Based on the ability to locally modify the material, wave plates with nearly arbitrary shape might be fabricated. Figure 2 shows two polarization contrast images of a half-wave plate in form of the IAP logo. Since the nanogratings are aligned vertically in subfigure (a), no polarization altering due to form-birefringence can be observed. In (b), the nanogratings are set at about 45° towards the polarization of the incident light. Hence, the light will be rotated by 90° and the logo becomes visible.

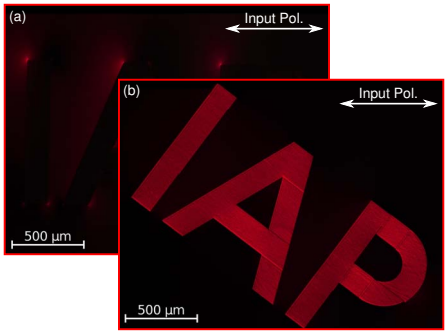

Figure 2: Polarization contrast images of an intricately shaped half-wave plate.

Classical wave plate manufacturing methods are only partially suited for the fabrication of locally varying wave plates. Nanograting based wave plates on the other hand can be controlled regarding their retardance (various parameters, *e.g.* pulse energy) and orientation (writing polarization) with very high precision and resolution. To achieve a grid-like polarization pattern for example, the polarization of the writing laser has just to be rotated during the manufacturing process. Figure 3 shows a scanning electron micrograph of such a grid-pattern wave plate.

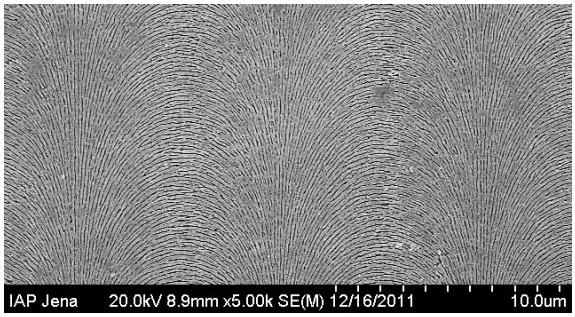

Figure 3: Scanning electron micrograph of the nanograting alignment in a grid-pattern wave plate.

Beyond that, it is possible to develope more complex structures which can be used for optical mode conversion. This way, a circularly polarized Gaussian mode can easily be transformed into a radially polarized donut mode as illustrated in Figure 4.

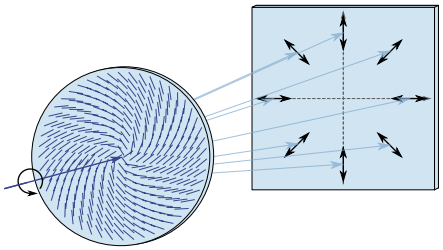

Figure 4: Simplified illustration of radially polarizing quarter-wave plate

ACKNOWLEDGEMENTS

The authors gratefully acknowledge the financial support from Deutsche Forschungsgemeinschaft DFG (priority program 1327). Mr. Sören Richter was supported by the Hans L. Merkle Stiftung.

References

[1] L. Sudrie, M. Franco, B. Prade, A. Mysyrewicz, *Optics Communications* **171**, 279 (1999).

[2] J. D. Mills, P. G. Kazansky, E. Bricchi, J. J. Baumberg, *Applied Physics Letters* **81**, 196 (2002).

[3] Y. Shimotsuma, P. G. Kazansky, J. Qiu, K. Hirao, *Physical Review Letters* **91**, 247405 (2003).

[4] V. R. Bhardwaj, *et al.*, *Physical Review Letters* **96**, 057404 (2006).

[5] S. Richter, *et al.*, *Journal of Laser Applications* (2012). Submitted.

[6] L. Ramirez, *et al.*, *Applied Physics A-materials Science & Processing* **100**, 1 (2010).

Femtosecond laser inscribed mode filter for few mode fibers

Christian Voigtländer[*1], Ria G. Krämer[1], Robert J. Williams[2], Michael J. Withford[2], Jens U. Thomas[1], Andreas Tünnermann[1], and Stefan Nolte[1]

[1]*Institute of Applied Physics, Abbe Center of Photonics, Friedrich-Schiller-Universität Jena, Max-Wien-Platz 1, 07743 Jena, Germany.*
[2]*Centre for Ultrahigh-bandwidth Devices for Optical Systems (CUDOS), MQ Photonics Research Centre, Department of Physics and Astronomy, Macquarie University, New South Wales 2109, Australia.*

[*]Corresponding Author: *ch.voigtlaender@uni-jena.de*

Abstract

Here we demonstrate a femtosecond induced mode filter, which can be used to suppress higher order modes in few mode fibers. The mode filter is based on a local refractive index increase around the fiber core. To demonstrate the functionality we used a homogeneous inscribed fiber Bragg grating.

Introduction

Fiber lasers have become an important tool for many applications as they provide very stable, compact and efficient laser sources. This triumphal procession was only possible because hampering nonlinear effects due to high intensities inside the fiber core could be decreased by introducing large mode area (LMA) fibers. With increasing core diameter the fibers are not strictly single mode anymore, but can be seen as few mode fibers. However, this mixture of modes is not always desired, and it degrades the beam quality in many applications.

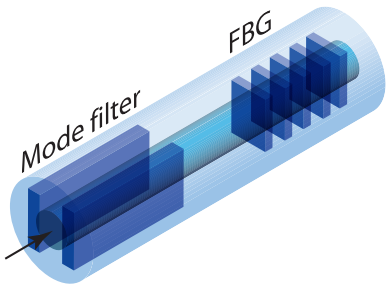

Figure 1: Mode filter in combination with a FBG. The modes pass the mode filter first before they are reflected by the FBG.

We present an all-integrated mode filter based on changing the guidance of the modes. Over a short distance the refractive index of the cladding is increased to the level of the fiber core (see Figure (1)). By propagating into the filter the modes from the fiber core will expand into the increased refractive index region. At the end of the filter the cross-section of the core goes back to the origin. Here the fundamental mode has a better overlap to the original core as the higher order modes. Thus, the losses for the higher modes are bigger and they couple out of the core.

Experiments

The mode filter was fabricated by focusing a femtosecond laser beam along the edge of the fiber core. To achieve a long smooth structure a cylindrical lens with 20 mm focal length was used as illustrated in Figure (2). By translating the fiber underneath the laser beam with a high precession air bearing system two modifications were inscribed on both sides of the fiber.

Since the measurement of the propagation through the modifications is quite complex, we used a fiber Bragg grating (FBG) for characterizing the mode filter (see Fig. (1)). A FBG is a periodic modification of the refractive index along the fiber core. Typically, FBGs are used as reflectors in single mode fibers. The reflection at specific wavelength is given by $\lambda = 2n_{eff}/\Lambda m$ with the grating period Λ, the effective refractive index n_{eff} and the order of reflection m. In non-single mode fibers every mode has a slightly different n_{eff} and therefore a different reflection wavelength. For our experiments we used a single mode fiber for 1.3 μm (SMF28). At a wavelength of 1 μm the fiber provides two modes.

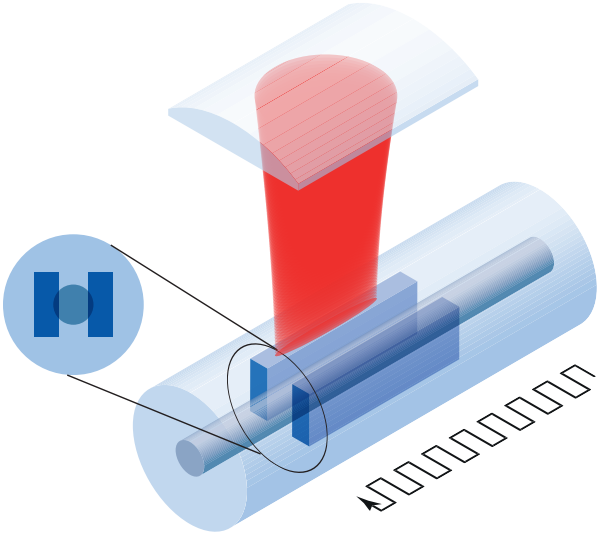

Figure 2: Inscription of the mode filter with a femtosecond laser and a cylindrical lens.

First a grating was inscribed by the phase mask scanning technique [1]. The FBG was investigated by coupling a supercontinuum source into the fiber. The reflected light was coupled to an optical spectrum analyzer. The grating has reflection peaks at $\lambda_{LP01} = 1036.3\,\text{nm}$ and $\lambda_{LP11} = 1034.8\,\text{nm}$. The black line in Figure (3) shows a qualitative reflection spectrum of the grating. A quantitative measurement was not possible as the excitation of the modes were unknown. However, it is not necessary, because the strength of the modes stay constant during the inscription.

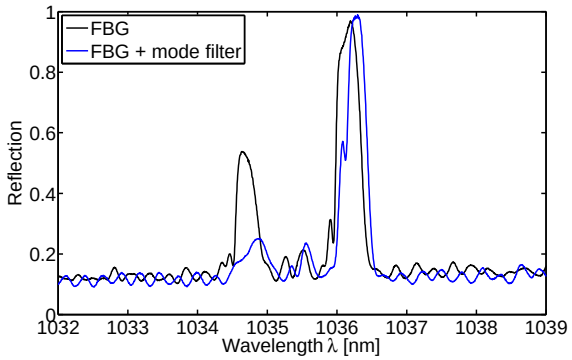

Figure 3: Reflection spectrum of a FBG without mode filter (black line) and with mode filter (blue line).

Afterwards the mode filter was inscribed in front of the FBG without the phase mask. The blue line in Figure (3) illustrates the difference of the spectrum after passing the mode filter twice. It can be seen, that the higher order mode is suppressed by about 50% after passing the filter twice compared to the reflection spectrum without mode filter. The reflection of the fundamental mode stays almost constant.

This shows the potential of the mode filter for all-integrated fiber lasers. The advantage of using femtosecond laser pulses are, that a mode filter can also be realized in the active fiber. In a monolithic fiber laser the FBG can act as a high reflective end mirror while the mode filter suppresses the higher order modes of the LMA fiber.

[1] J. Thomas, E. Wikszak, T. Clausnitzer, U. Fuchs, U. Zeitner, S. Nolte and A. Tünnermann, "Inscription of fiber Bragg gratings with femtosecond pulses using a phase mask scanning technique," Appl. Phys. A **86,** 153 (2007).

Multi-wavelength holograms made of plasmonic metamaterials

Benny Walther*[1], Carsten Rockstuhl[2], Christian Helgert[1], and Thomas Pertsch[1]

[1]*Institute of Applied Physics*
[2]*Institute of Condensed Matter Theory and Solid State Optics*
Abbe Center of Photonics, Friedrich-Schiller-Universität Jena,
07743 Jena, Germany

*Corresponding Author: *benny.walther@uni-jena.de*

Abstract

The dispersive properties of plasmonic metamaterials and the ability to tailor their optical response by variation of their geometry makes them promising candidates for versatile optical elements. Computer-generated holograms (CGH) based on plasmonic metamaterials can be used to shape wavefronts by simultaneously affecting the light's amplitude and phase. Moreover, due to the resonant behaviour of metamaterials, the hologram's response depends strongly on the illumination wavelength. Using a specific CGH design algorithm this allows for encoding multiple sheets of information in a single holographic structure for different wavelengths. Applications like multicolor holographic projections come into reach.

Diffractive optical elements are devices that are used to shape light waves. As computer-generated holograms (CGH) they have their applications in the field of holographic image projection. In contrast to an optically recorded hologram, a CGH is computed by an algorithm and then manufactured such as to produce the desired projection image. A great variety of encoding schemes and algorithms has been developed based on the physical properties of the medium the CGH is composed of [1, 2]. While pure amplitude holograms work with gradually attenuating media to encode the holographic information, classical phase holograms usually employ dielectric materials to locally affect the phase of the transmitted light. This is achieved by variations of the material thickness or effective refractive index variations induced by sub-wavelength microstructuring [3].

For the classical amplitude and phase holograms the element's response is rather insensitive to changes of the illuminating wavelength, which is due to vanishing or negligible inherent dispersion of the used materials. This non-dispersive behaviour constitutes a drawback when attempting to create multicolour elements. Such wavelength-multiplexed CGHs are convenient for the projection of colour images adapted to the perception of the human eye, i.e. providing separate responses for red, green and blue light from a single structured element. Several concepts to obtain such dielectric multicolour holograms have been developed, using polarization state and other tricks [4, 5, 6, 7]

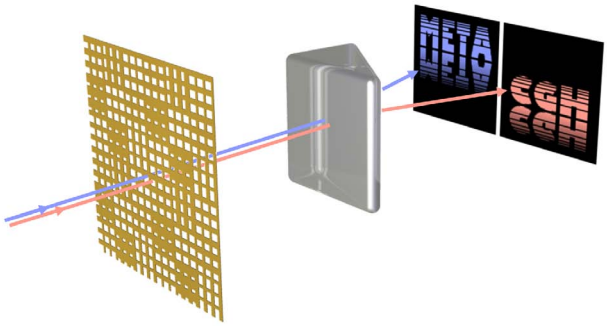

Figure 1: Schematic illustration of a metamaterial CGH operating at two wavelengths simultaneously.

In this work we introduce concepts for wavelength-multiplexed optical elements based on plasmonic metamaterials. We show that by employing a single holographic layer, which is composed of a proper arrangement of metamaterial unit cells, it is possible to produce different, predefined optical responses at two and more wavelengths. As previously shown on a numerical basis, metamaterial CGHs are able to selectively manipulate both amplitude and phase of transmitted or reflected light in order to form a specified intensity distribution in the far field [8]. Fig. 1 illustrates the geometry of such a pixel-based CGH. Each of the pixels comprises a few unit cells of the metamaterial, e.g., the fishnet structure, while from pixel to pixel the geometry parameters of this metamaterial are tuned in an appropriate manner in order to adjust the local transmission or reflection properties. Since the

metamaterial's complex-valued transmission and reflection coefficients are strongly affected by plasmonic resonant behaviour, it is appealing to use this spectral vividness to encode multiple sheets of information as depicted in Fig. 1. We propose ways on how this can be achieved.

A possible encoding scheme shall be demonstrated for the fishnet metamaterial, which is shown in Fig. 2a. In this three-layer stack of gold, magnesia and gold the lateral geometry parameters W_x and W_y can be conveniently varied. The lateral period of the structure is 600 nm in both directions and fabrication with state-of-the-art nanolithography, e.g. the lift-off technique, is well understood. As indicated in Fig. 2b, the parameters W_x and W_y are varied across the sample, forming a pixelated hologram. Properly designing the distribution of the complex-valued transmission coefficients t in these pixels by means of W_x and W_y allows to manipulate incident and transmitted light wave such, that a predefined image is generated in the far field.

Moreover, the strong dispersion of t induced by the plasmonic resonances of the metamaterial creates constellations that allow for implementation freedom at

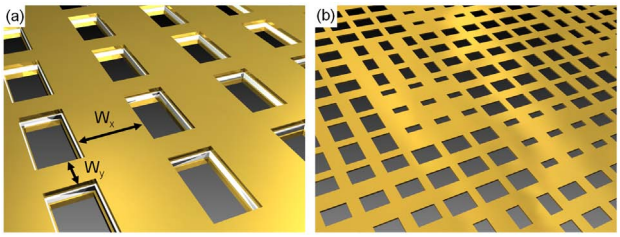

Figure 2: (a) Fishnet metamaterial with variable lateral parameters W_x and W_y. (b) Assembled hologram consisting of pixels, each comprising a limited number of fishnet unitcells.

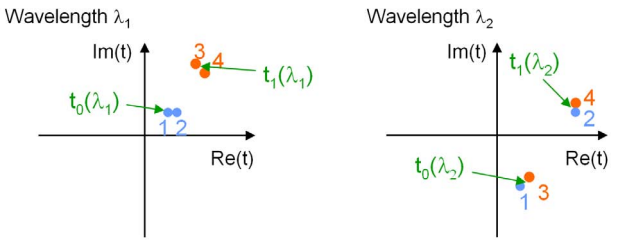

Figure 3: Constellation in the complex transmission coefficient t allowing for simultaneous encoding of binary holograms at two distinct wavelengths.

multiple wavelengths. What this means, is illustrated in Fig. 3, which schematically shows the transmission coefficients of four different fishnet implementations, i.e. parameter sets W_x, W_y, labeled with numbers 1 to 4. Note that the points in the complex plane, forming pairs, change their partner when transiting from wavelength λ_1 to wavelength λ_2. With this kind of arrangement binary holograms can be encoded at two distinct wavelengths using transmission values $t_0(\lambda_1)$ and $t_1(\lambda_1)$ at wavelength λ_1, and $t_0(\lambda_2)$ and $t_1(\lambda_2)$ at wavelength λ_2, respectively. The encoding utilizes the methods from [8] and can be done independently at each of the two wavelengths.

The approach can be extended to multiple wavelengths. Hence, with the availability of metamaterials working in the visible wavelength range true-colour holographic image projection could be achieved. Moreover, as these metamaterical CGHs do not only allow for spatial light modulation, but also give access to the spectral degree of freedom, applications in spatio-temporal pulse-shaping come to mind.

[1] F. Wyrowski, O. Bryngdahl, *Rep. Prog. Phys.* **54**, 1481 (1991).

[2] R. W. Gerchberg, W. O. Saxton, *Optik* **35**, 237 (1972).

[3] W. Freese, T. Kämpfe, E. Kley, A. Tünnermann, *Opt. Lett.* **35**, 676 (2010).

[4] I. Barton, P. Blair, M. R. Taghizadeh, *Opt. Express* **1**, 54 (1997).

[5] W. Yu, *et al.*, *Appl. Opt.* **41**, 96 (2002).

[6] S. Borgsmüller, S. Noehte, C. Dietrich, T. Kresse, R. Männer, *Appl. Opt.* **42**, 5274 (2003).

[7] T. Kämpfe, E.-B. Kley, A. Tünnermann, *J. Opt. Soc. Am. A* **25**, 1609 (2008).

[8] B. Walther, C. Helgert, C. Rockstuhl, T. Pertsch, *Applied Physics Letters* **98**, 191101 (2011).

Front and rear side photonic structures in silicon solar cells

Samuel Wiesendanger*[1], Carsten Rockstuhl[1], and Falk Lederer[1]

[1] *Institut für Festkörpertheorie und -optik, Helmholtzweg 4, 07743 Jena, Germany*

*Corresponding Author: *samuel.wiesendanger@uni-jena.de*

Abstract

We numerically investigate the light trapping properties of photonic structures at the front and rear side of a silicon solar cell. By analyzing the scattering and diffraction power of these photonic structures, we show that the absorption can be enhanced considerably by a proper choice of the geometric dimensions compared to an unstructured absorbing slab. Our optimized geometry shows an absorption enhancement of about 43%.

INTRODUCTION

In order to replace nuclear power plants after these reached the end of their terms renewable energy sources have gained a lot of interest. Among these are concepts using the sun as an energy source either by using a direct conversion of the incident solar power to produce electricity in photovoltaic cells or by boiling water with concentrated solar radiation in solar thermal power plants. However, to compete with nuclear power and energy sources based on fossil fuels, the prices of photovoltaic cells have to be lowered. One way to reduce the cost of a solar cell would be to use less of the absorbing material, since this high purity materials are very energy demanding to be produced. But the volume reduction of the absorbing material comes at the cost of a lower absorption. Therefore, light trapping concepts are mandatory to keep the absorption at a high level but using only a part of the absorber volume. Light trapping increases the path length of the light in the absorber and as a result enhances the absorption. Several approaches have been proposed. They are based either on a reduced fresnel reflection at the input side using randomized textures [1] or on the diffraction into higher order modes using gratings [2]. At the rear side, flat interfaces to the metal back contacts were replaced by photonic structures such as Bragg mirrors or photonic crystals [3]. For some materials it may also be advantageous to use metallic particles integrated into the solar cells to benefit from plasmonic effects [4]. In previous studies it was suggested to use inverted zinc oxide (ZnO) opals as back reflectors, which consist of air voids in a ZnO host. In this work randomly textured surfaces at the front side were used. However, at the rear side, not only perfect inverted opals were considered, but also opals applied conformally to the texture, such that they do not show the perfect symmetry of a face centered cubic (fcc) lattice. These more sophisticated photonic elements were investigated with respect to their absorption enhancement.

DEVICE STRUCTURES

To compare different configurations the short circuit current density I_{sc} was used, which is the integral of the absorption spectrum weighted by the incident solar power over all wavelengths given by

$$I_{sc} = e_0 \int \Phi_{AM1.5}(\lambda) A(\lambda) d\lambda ,$$

where e_0 is the elementary charge, $\Phi_{AM1.5}$ is the incident solar radiation at the earth's surface and A is the calculated absorption spectrum. Starting point was a homogeneous slab of micro-crystallin silicon (μSi) of a thickness of 1μm and complexity was successively increased. The randomly textured ZnO surface at the front side shows a crater-like height profile with an average crater diameter of about 1μm and a crater height of about 400nm. The purpose of this random texture is to provide a smoother transition from the low refractive index glass on top of the solar cell to the high refractive index absorbing material. At the rear side several photonic structures, all based on spherical air voids in ZnO were used. First, the optimal radius for the inverted opal was determined. Fig. 1 (a) shows the absorption spectra of a homogeneous μSi layer for various thicknesses. The thicker a layer is, the more light is absorbed and therefore the absorption edge

shifts to longer wavelengths. Light not absorbed after one pass through should be reflected by the inverted opal at the rear side. From Fig. 1 (a) the spectral position where high reflection should occur can be determined, namely where the intrinsic absorption of μSi starts to decrease. The solid line in Fig. 1 (b) shows the reflection spectrum of a 4-layer inverted opal for a radius of 325nm. Varying the radius allows the reflection peaks to be shifted. A proper choice of the radius leads to a high reflection in the desired spectral region. Several reflection maxima appear in the spectrum. The first one at lower energies is attributed to a high reflection into the zeroth order, where a band gap in the Γ-L direction of the fcc lattice exists, as shown by the dotted lines in Fig. 1 (b). Whereas the peaks at higher energies correspond to a diffraction of the light into higher orders.

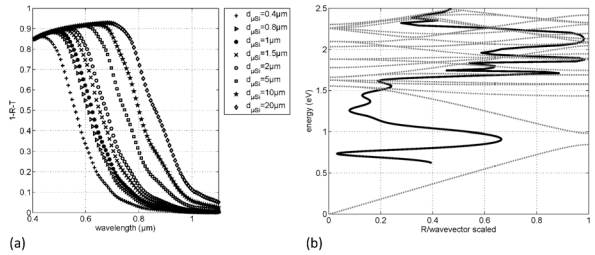

Figure 1: Absorption spectra for various thicknesses of a homogeneous μSi layer (a) and reflection spectrum of a 4-layer inverted ZnO opal (b). The dotted grey lines in (b) show the bandstructure of a fcc lattice along the Γ-L direction

Combining the information from Fig. 1 (a) and Fig. 1 (b) a certain radius can be determined for each given thickness. This very radius was used in what follows for the characterization of the investigated geometries. The simplest possible geometry is the homogeneous layer whose short circuit current serves as a reference value. Apart from perfectly arranged spheres at the rear side, which cannot reproduce the randomized texture, also randomly arranged spheres were considered. These spheres do not show the symmetry of a fcc lattice and therefore the rather sharp features in the reflection spectrum of Fig. 1 (b) are smeared out. However, focussed ion beam cuts of inverted opals on randomly textured surfaces revealed that after a few layers of random distribution, the spheres tend to build up a perfect opal even on textured surfaces. For this reason, randomly arranged spheres in combination with a perfect fcc lattice were also simulated. The short circuit current increases going from textured surfaces only to perfectly arranged spheres and finally to randomly arranged spheres. The best result was obtained for a combination of the last two. Fig. 2 shows summarized the results of the different geometries. The highest absorption enhancement is achieved if the properties of a random distribution and a crystal-like lattice are combined. The overall enhancement is about 43% compared to the unstructured geometry.

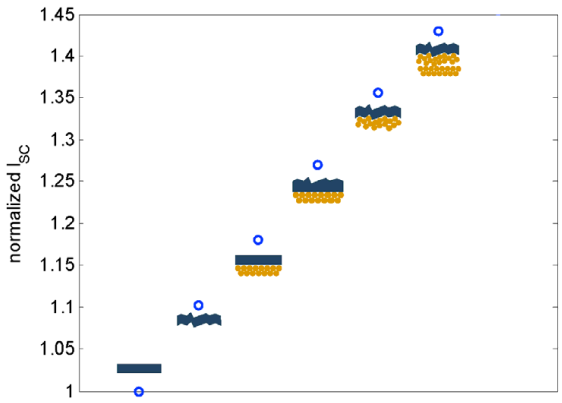

Figure 2: Normalized short circuit currents for the investigated geometries shown by the blue circles. For each point the drawings show the corresponding geometry

In conclusion, we have shown that properly dimensioned air voids in ZnO arranged randomly in combination with perfectly arranged voids lead to an absorption enhancement of more than 40%.

[1] P. Campbell, M. A. Green, *J. Appl. Phys.* **62**, 243 (1987).

[2] S. Zanotto, M. Liscidini, L. C. Andreani, *Optics Express* **18**, 4260 (2010).

[3] P. Bermel, C. Luo, L. Zeug, L. C. Kimerling, J. D. Joannopoulos, *Applied Physics Letters* **15**, 16986 (2007).

[4] V. E. Ferry, *et al.*, *Optics Express* **18**, A237 (2010).

Filter-based spectrometer for optical wavelength shift sensors

Roland Wuchrer*[1], Robert Brückner[2], Hartmut Fröb[2] and Thomas Härtling[1]

[1] *Fraunhofer Institute for Nondestructive Testing, Dresden Branch, Maria-Reiche-Strasse 2, 01109 Dresden, Germany*

[2] *Institute for Applied Photophysics, Technische Universität Dresden, George-Bähr-Straße 1, 01069 Dresden, Germany*

*Corresponding Author: *Roland.Wuchrer@izfp-d.fraunhofer.de*

Abstract

We present a filter-based spectrometer for the detection of wavelength shifts. By using a dielectric thin film filter with a lateral gradient and a position detector we set up a interrogator with pm resolution. The optical filter serves as wavelength selecting element and make it possible to miniaturize the device.

Introduction

Optical sensors which detect external influences on the basis of wavelength shifts very accurately receive big interest in structural and human health monitoring. Examples of such sensors are Fiber-Bragg-Gratings (FBGs), surface plasmon resonance sensors, photonic crystals and ring resonators. They are small, robust, electrically passive and easily integratable into structures of e.g. fiber composite materials. However, their applicability is limited due to the size of the interrogator. Conventional interrogations units such as grating spectrometers or interferometers can not be miniaturized without loss of spectral resolution. Furthermore they need ambitious data processing techniques to resolve small wavelength shifts, which causes long integration time.

In our contribution we report on a filter-based spectrometer, which solves the miniaturization problem. With the use of an optical filter the manufactured size and the spectral resolution of the interrogator are decoupled.

Principles

The filter-based spectrometer consists of a linear variable optical filter (LVF/LVOF) and a position detector. The LVF converts the spectral distribution of the incoming light into a spatial intensity distribution whose centroid is determined by the detector with high accuracy.

The LVF has a thin film Fabry-Pérot-structure with a tapered cavity layer. Through the wedge-shaped cavity thickness $d(x)$ the resonance condition for the wavelength

$$m\lambda_x = 2n_R d(x)cos\theta \tag{1}$$

is position depending (m order of resonance, n_R refractive index of the cavity layer, θ angle of incidence light). A wavelength shift therefore leads to a linear position change of the transmission spot behind the LVF. The optical behavior of the LVF is characterized by the full width half maximum (FWHM) δ_{LVF} [nm] and the spectral gradient g [nm/mm], which describes how large the spectral shift of the transmission maximum is compared to the spatial distance of two points on the LVF. The spatial width of the distribution w behind the LVF can be described by [1]

$$w = \frac{\delta_{ges}(\delta_0, \delta_{LVF})}{g} \tag{2}$$

with δ_0 the FWHM of the incident light and δ_{ges} the FWHM behind the LVF.

The position of the centroid is measured by a differential readout of two photo currents I_1 and I_2 of the detector (see Fig. 1)

$$\lambda_x \sim x \sim \frac{I_2 - I_1}{I_2 + I_1}. \tag{3}$$

Thus, a position change results in an increase of one photo current and the decrease of the other. Division by the total photo current makes the centroid calculation independent from intensity fluctuations of the light spot.

Experimental Setup

Fig.1 shows the experimental setup used to measure the wavelength shift resolution of the filter-based spectrometer [2].

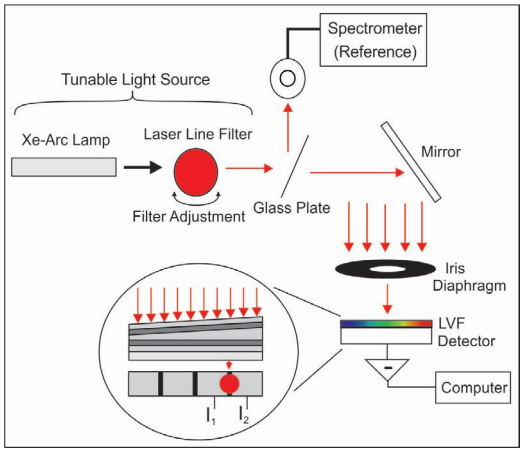

Figure 1: Experimental Setup.

For the simulation of the wavelength shift a tunable light source consisting of a Xe-arc lamp (collimated light) and a laser line filter is used. By rotating the laser line filter its resonance condition is intentionally changed (see Eq. 1) and the transmission wavelength shifts to shorter wavelengths. A small fraction of the light is directed to a grating spectrometer by the glass pate. Thus, a reference spectrum can be acquired which is needed to correlate the wavelength shift of the light source and the position change at the filter-based spectrometer. The monochromatic light transmitted through the glass plate then approaches the filter-based spectrometer and passes the LVF to reach the position detector. An iris diaphragm is located in front of the arrangement which allows us to adjust the light spot size on the spectrometer. The generated photo current on the detector is amplified and analyzed by a differential operational amplifier. The voltage signal characterizing the lateral position is sent to a display unit and a computer for further analysis.

Results

In this setup we obtain optimum results by using a photodiode pair as detection unit. We implemented a 16 Si-photodiode array (PDA), at which one photodiode is 0.9 mm x 1.45 mm in size and the diode pitch is 0.1 mm wide. The laser line filter has a central wavelength of 800 nm and a $\delta_0 = 10$ nm. The light spot on the LVF amounts to 2 mm. The spectral resolution of a LVF with $g = 5$ nm/mm and $\delta_{LVF} = 5$ nm is determined. The acquired data obtained upon rotating the laser line filter are depicted in Fig. 2.

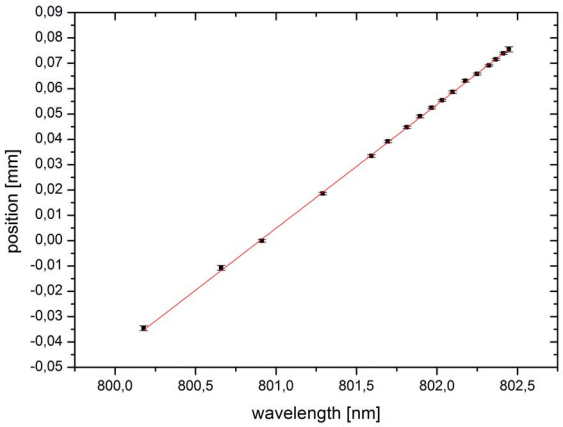

Figure 2: Measured wavelength shifts for a PDA and a LVF with $g = 5$ nm/mm and $\delta_{LVF} = 5$ nm.

A highly linear curve results which allow us to determine the spectral resolution to 50 pm. If one considers the position noise, an accuracy of the wavelength shift of at least 10 pm can be reached with a more sensitive tunable light source.

Conclusion and Future Scope of Work

In our work we demonstrated that with the combination of a LVF and a position detector a small interrogation unit can be set up which resolves pm wavelength shifts. Our latest research is aimed at reading out a fiber Bragg grating sensor both in reflection and in transmission mode. Furthermore, we will design a robust package for the entire spectrometer setup which allows its application in harsh environments.

[1] O. Schmidt, P. Kiesel, S. Mohta und N. M. Johnson, *Appl. Phys. B 86* pp. 593–600 (2007).

[2] R. Wuchrer, Aufbau eines filterbasierten Spektrometers und Untersuchungen zu dessen Zuverlässigkeit, Diploma thesis, TU Dresden (2012).

Surface enhanced Raman spectroscopy (SERS) for the detection of ecological harmful arrearages of sewage water

Sophie Zierbock[1], Dana Cialla[1,2], Patrick Bräutigam[3], Karina Weber[1,2], and Jürgen Popp*[1,2]

[1] *Institute of Physical Chemistry and Abbe Center of Photonics*
Friedrich-Schiller-University Jena,
Helmholtzweg 4, 07743 Jena, Germany

[2] *Institute of Photonic Technology (IPHT)*
Albert-Einstein-Strasse 9, 07745 Jena, Germany

[3] *Institute of Technical Chemistry and Environmental Chemistry*
Friedrich-Schiller-University Jena
Lessingstrasse 12, 07743 Jena, Germany

* Corresponding author: *juergen.popp@uni-jena.de*

Abstract

Drugs and disinfectants are one of the most serious pollution of sewage water, especially from hospitals and nursing homes. Consequently, the growth of multi resistant bacteria increases and threatens human, animal and the whole nature. To prevent the environment from this setting, it is searched for fast, easy and cheap methods to detect and eliminate these hazardous substances. Due to its high molecular specificity and sensitivity surface enhanced Raman spectroscopy (SERS) is our method of choice to detect low molecular weight substances like hormones and antibiotics in the micro-molar region.

INTRODUCTION

Due to its molecular specificity and high sensitivity [**1**], surface enhanced Raman spectroscopy (SERS) is a powerful tool to detect low-molecular weight substances like drugs and hormones. The enhancement is based on the excitation of plasmon polaritons of metallic nanoparticles. The resulting high electromagnetic field in the vicinity of the nanoparticle increases the Raman signal. Due to its plasmonic resonance in the NIR or visible region, gold and silver are preferred metals [**2**].

The metallic nanoparticles can be prepared as colloidal solution or as substrates, whereas sharp edges, thin needles or other spiky and rough surfaces show highest enhancement factors. Diverse top down, like electron beam lithography (EBL), and bottom up techniques, like deposition of colloids, can be used to prepare the required nanoparticles.
A fast and easy method, using SERS to detect contaminants in sewage water, is under development and will be presented within this contribution.

HORMONES AND DRUGS IN SEWAGE WATER

The contamination of sewage water with drugs and disinfectant is due to the massive application of antibacterial dilutions, antibiotics and hormones in hospitals and nursing homes. Of course it is important to work clean and sterile in such establishments; however this leads also to the evolution of multi resistant bacteria which are a big threat for patients. Thus it is important, to clean sewage water before it comes in contact with other effluent and also other bacteria.

The pollution of the environment with drugs from the sewage water is another aspect, because clarification plants mostly cannot filter out low-molecular weight substances. The so contaminated ground water is assimilated in the biological cycle of plants, animals and humans. To prevent the nature from this setting

it is important to clean the sewage water before it comes out of the hospital area. However, it is crucial to know which contaminant is in the sewage water and has to be taken out of it.

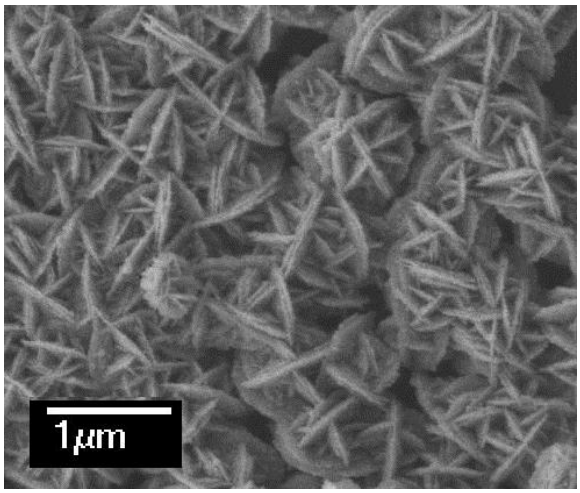

Figure 1: SEM image of enzymatically generated silver nanoparticles. The rough surface is clearly visible.

SERS APPLICATION

Here we present enzymatically generated silver nanoparticles (EGNP) used as SERS substrate in our studies, generating a homogenous signal enhancement [**3**]. In Figure 1 a SEM image is depicted, which illustrate the sharp and spiky desert rose-like morphology [**4**]. Fingerprint spectra of various solid and water-solved drugs or disinfectant can be shown.

ACKNOWLEDGEMENT

Funding of the research projects 'QuantiSERS' and 'Jenaer Biochip Initiative 2.0' within the framework 'Unternehmen Region – InnoProfile Transfer' from the Federal Ministry of Education and Research, Germany (BMBF) is gratefully acknowledged.

[1] D. Cialla, A. Maerz, Analytical Bioanalytical Chemistry **403**, 27 (2012)

[2] B. Shama, R.R. Frontiera, Materials Today **15**, 16 (2012)

[3] K. Hering, R. Moeller, Chemical Physics and Chemistry **9(6)**, 867 (2008)

[4] K.K. Strelau, A. Brinker, Journal of Raman Spectroscopy **42**, 243 (2011)

Ultrashort pulse induced nanogratings and their fundamental structure

Felix Zimmermann*[1], Sören Richter[1], Anton Plech[2], and Stefan Nolte[1]

[1]*Institute of Applied Physics, Abbe Center of Photonics, Friedrich-Schiller-Universität Jena, Max-Wien-Platz 1, 07743 Jena,Germany*

[2]*Institute for Synchrotron Radiation,Karlsruhe Institute of Technology, PO box 3640, 76021 Karlsruhe, Germany*

*Corresponding Author: *Felix.Zimmermann@uni-jena.de*

When intense femtosecond laser pulses are focused into a glass substrate, self-organized periodic nanostructures, so-called nanogratings, are generated in a certain parameter regime. To clarify the ultimate nanogratings we employed focused ion beam (FIB) milling and small angle X-ray scattering (SAXS). The results considerably show that voids are the primary constituents and their number increases with ongoing exposure to laser pulses.

INTRODUCTION

About ten years ago grating like structures with periods smaller than the laser wavelength were observed in fused silica via tightly focusing ultrashort laser pulses [1]. These modifications called "nanogratings" result of a self-organized process and show a strong form birefringence due to their anisotropic structure. Emerging after several laser pulses [2] they are oriented perpendicular to the laser polarization. By tuning the laser parameters the structural properties and thus the birefringence can be controlled [3]. Consequently, there are numerous potential applications from phase elements controlling the laser polarization [3] to devices enabling the generation of optical vortices [4]. Nevertheless the self organized formation process is not yet fully understood. One reason is that the underlying surface structure is difficult to explore. Due to the small feature size optical microscopy cannot be used and electron microscopic (SEM) investigations require sample preparations leading to bluring and distorting essential structure details. Recent work on cleaved samples revealed nanoporous fine structures and planar nanocracks within nanogratings [5].

We employed small angle X-ray scattering (SAXS) as well as focused ion beam (FIB) milling and scanning electron microscopy (SEM) to determine the principal constituents of nanogratings.

METHODOLOGY

Nanogratings are inscribed using the frequency doubled (515 nm) light of a mode locked laser oscillator (Amplitude t-pulse 500). This laser provides pulses with durations of about 450 fs, pulse energies up to 200 nJ at repetition rates up to 10 MHz. The repetition rate was reduced by an external acusto-optical modulator in order to avoid heat accumulation effects. For focusing we used an aspheric lens (New Focus 5722) with a numerical aperture of 0.55.

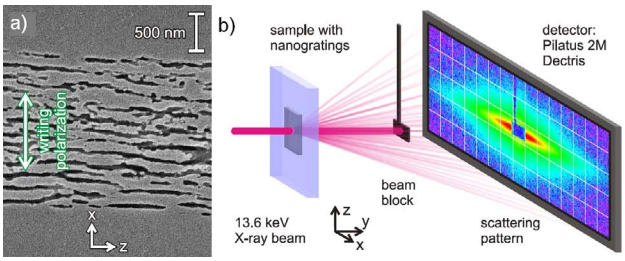

Fig.1 SEM micrograph of gratings after etching with hydrofluoric acid (a) and schematic of the SAXS measurement (b).

X-ray patterns were studied in order to investigate nanogratings in a nondestructive way. Thereby no preparation steps are required for embedded structures. Samples with nanogratings were illuminated with a probe beam (photon energy 13.6 keV, cSAXS beamline at the Swiss Light Source (Villigen, CH)) that is scattered and the pattern is recorded with a large direct converting pixel converter (see Fig. 1(a)). FIB has been used whereby

a volume containing nanogratings was dissected in 12 nm slices and analysed per SEM imaging.

RESULTS

Due to the different dimensions in the nanograting samples along the x and z direction the scattering patterns show strongly anisotropic behaviour. The evaluation along x (direction of laser polarization) showed a broad distribution whereby two distinct populations with different diameters exist. As it can be seen in Fig. 2(a) these are roughly independent on pulse energy and number of laser pulses. This indicates that once the structure is formed no further growth along the laser polarization takes place. Furthermore an increasing structure size during the first ≈ 100 pulses along the z direction was detected. Fig. 2(b) shows the aspect ratio between the structure size along the x and z axis.-

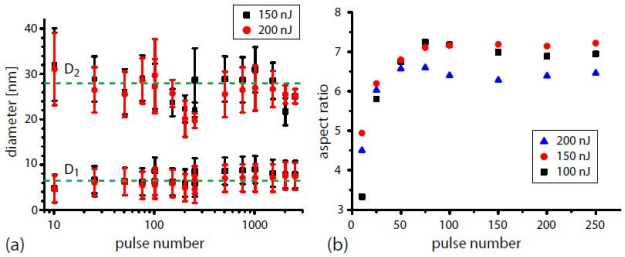

Fig. 2 Results of the SAXS measurements.

The measured increase of the characteristic scattering parameter with rising pulse number can be attributed to a growing number of pores that corresponds well to the observed decrease in the grating period during prolonged laser exposure [3]. To get an insight of the real structure of nanogratings we performed FIB measurements.

Figure 3(a) shows an SEM micrograph of a FIB slice that depicts the micro porous character of the grating. With an appropriate Fourier filtering algorithm we isolated the pores from hundred FIB slices in order to obtain a 3D view of their size (see Fig. 3(b)).

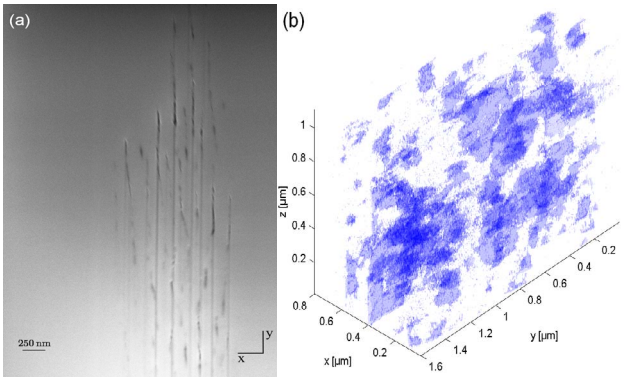

Fig. 3 SEM micrograph of a FIB-slice in the x-y-plane (a) and 3D plot of nanogratings constructed out of many FIB slices (b).

In accordance to the SAXS measurements, the transverse dimensions of the pores (200-300 nm) are significantly larger than their thickness (30 nm). The unidirectional anisotropy is confirmed by the small feature sizes of the pores along y and z.

ACKNOWLEDGEMENTS

We thank Swiss Light Source (cSAXS beamline at Paul Scherrer Institut Villigen, CH) for the beamtime. Furthermore the authors gratefully acknowledge financial support from Deutsche Forschungsgemeinschaft DFG (priority program 1327). Sören Richter was supported by the Hans L. Merkle Stiftung.

[1] Y. Shimotsuma, P.G. Kazansky, J. Qiu and K. Hirao, "Nanostructuring of transparent materials by ultrashort light pulses," Phys. Rev. Lett. **91**, 247405 (2003).

[2] Richter S., Heinrich M., Döring S., Tünnermann A.. „Formation of femtosecond laser-induced nanogratings at high repetition rates" Appl. Phys. **A 104(2)**, 503-507 (2011).

[3] Ramirez L.P.R., Heinrich M. Richter S., et al.." Tuning the structural properties of femtosecond-laser-induced nanogratings", Appl. Phys. A **100(1)**, 1-6 (2010).

[4] Beresna M., Gecevičius M., Kazansky P.G., and Gertus T.. "Radially polarized optical vortex converter created by femtosecond laser nanostructuring of glass", Appl. Phys. Lett. **98**, (2011).

[5] *Taylor R., Hnatovsky C., and Simova E.."*Applications of femtosecond laser induced self-organized planar nanocracks inside fused silica glass", Laser & Photon Rev. **2(1-2)**, 26-46 (2008).

Highly nonlinear interaction of laser beams with orbital angular momentum

M. Zürch[1,2 *], C. Kern[1,2], P. Hansinger[1,2], A. Dreischuh[3], and Ch. Spielmann[1,2,4]

[1] *Institute of Optics and Quantum Electronics, Friedrich-Schiller-University Jena, Max-Wien-Platz 1, 07743 Jena, Germany*
[2] *Abbe Center of Photonics, 07743 Jena, Germany*
[3] *Department of Quantum Electronics, Faculty of Physics, Sofia University, 5, J. Bourchier Blvd., BG-1164 Sofia, Bulgaria*
[4] *Helmholtzinstitut Jena, Helmholtzweg 4, 07743 Jena, Germany*

[*]Corresponding Author: *michael.zuerch@uni-jena.de*

Abstract

Light beams carrying an isolated point singularity with a screw-type phase distribution are called an optical vortex (OV). The fact that in free space the Poynting vector of the beam gives the momentum flow leads to an orbital angular momentum of the photons in such a singular beam independent on the spin angular momentum. To exploit the applications of such beams carrying angular momentum it is necessary to produce them in various wavelength regimes. In previous studies it was observed that nonlinearities, which are commonly used to produce new wavelengths of light, lead to breaking up of these OVs and therefore it is challenging to extend the range of useable wavelengths. Here we show for the first time that OVs can be produced in the extreme ultra-violet (XUV) using high-harmonic generation (HHG) driven by ultra-short laser pulses. We found that beams carrying angular momentum can survive high nonlinearities as they are present in HHG.

INTRODUCTION

The real and the imaginary parts of the field amplitude (i.e. also the field intensity) are zero at the point of phase dislocation, which is a singularity. The characteristic helical phase profiles of OVs are described in terms of $\exp(im\theta)$ multipliers, where θ is the azimuthal coordinate and the integer number m is their topological charge (TC).

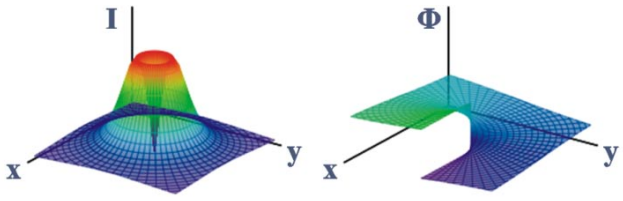

Figure 1: Intensity (left) and phase (right) distribution that characterize an optical vortex.

Since the Poynting vector gives the momentum flow in free space, for helical phase fronts it has an azimuthal component that produces an orbital angular momentum parallel to the beam's axis. An m-fold charged OV beam carries an orbital angular momentum of $m\hbar$ per photon. This is independent on the spin angular momentum (i.e. on the polarization state). There are many applications of OVs shown in literature, including particle micro-manipulation, imaging, interferometry, quantum information and high-resolution microscopy and lithography [1]. This makes research on this field of extending the usable wavelength range for OVs desirable.

HIGH HARMONIC GENERATION

The process that we use to obtain wavelengths as short as 20nm out of a common ultrashort laser pulse in the IR is called High Harmonic Generation (HHG) [2].

This highly nonlinear process is microscopically described by tunnel-ionization of a noble gas, followed by propagation of the free electron in the laser field and finally recombination with the parent ion, accompanied by the emission of an XUV photon. The macroscopic build-up of the XUV radiation is governed by coherent superposition and limited by phase-mismatch and re-absorption. HHG based XUV-sources are nowadays widely used for spectroscopic applications due to their ultrashort pulses in the attosecond range and the high spatial and temporal coherence.

EXPERIMENTAL SETUP

The setup is shown in detail in Fig. 1. A femtosecond laser system producing pulses with sub-30fs duration at 800nm wavelength and energies up to 1mJ at a repetition rate of 1kHz was used. By reflection on a spatial light modulator the helical phase is imprinted on the beam. The laser pulses are then focused (f=300mm, f/#=15) into a gas jet to a diameter of roughly 40µm, resulting in peak intensities of approximately 2×10^{15}Wcm^{-2}. The XUV beam emerges from there, and is subsequently filtered by an aluminum foil to suppress the fundamental light. The XUV light is recorded by a 2048x2048 pixel XUV camera. A thin tungsten wire can be placed shortly behind the gas jet for phase evaluation by wave front splitting.

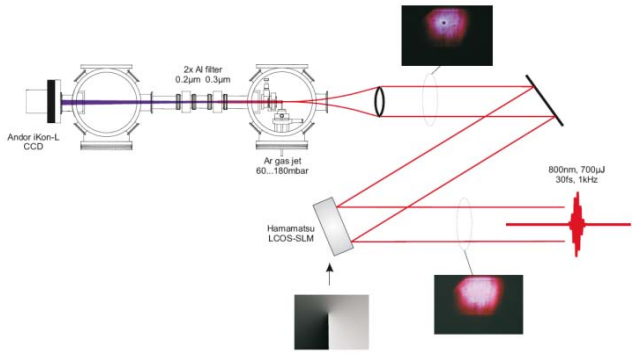

Figure 2: The experimental setup of the XUV vortex experiment. A spatial light modulator introduces a helical phase onto the laser beam, which is then focused into an argon jet for HHG.

EXPERIMENTAL RESULTS

We were able observe an OV in the XUV when the singularity was carefully placed at the centre of the Gaussian input mode. We were expecting a doughnut mode, as common for OVs, but instead saw two intensity lobes (Fig. 3b) with zero intensity in the center. We attribute that to the non-perfect IR-focus (Fig. 3a). A wave-front splitting measurement with a thin tungsten wire (Fig. 3c) revealed that the phase jump from one side of the mode to the other is π, which indicates for a TC of one. This is confirmed by simulation (Fig. 3d). This is in contradiction to theory, where a multiplication of the phase by the harmonic order is expected. We explain this by decay of the highly charged OVs within the generation medium, such that only a single charged OV propagates behind the gas jet.

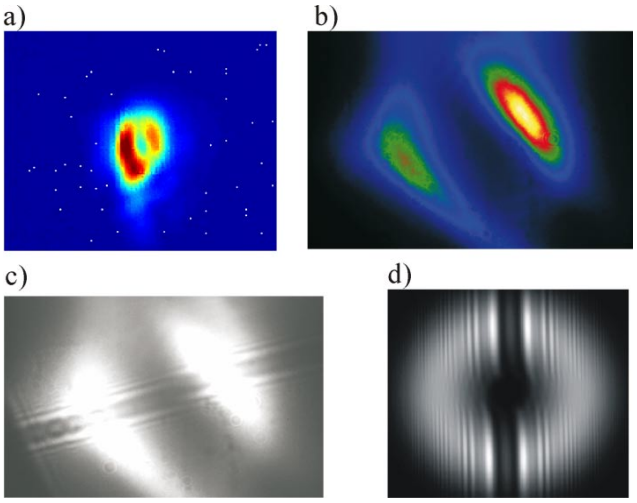

Figure 3: (a) Measurement of the focus of the IR-beam shows non-perfect OV structure in the focus which is due to aberrations on the input beam. (b) Typical observed OV on the XUV featuring two lobes. (c) Interference measured by wavefront splitting at a thin tungsten wire shows shifted interference lines which indicates for single charged OV, as is confirmed by simulation (d).

OUTLOOK

We showed that optical vortex beams can be converted to shorter wavelengths by HHG. Thus high energetic photons carrying orbital angular momentum can be produced with table top systems. For further use of these beams more work has to be put into optimizing the IR focus in order to get a fully featured OV in the XUV.

All results of the experiment along with more extended explanations and further literature can be found elsewhere [3] and will be reported on the conference.

[1] L. Allen, S. M. Barnett, M. J. Padget, *Optical Angular Momentum* (Institute of Physics, Bristol, 2004).

[2] T. Brabec, F. Krausz, Reviews of Modern Physics **72**, 545 (2000).

[3] M. Zürch, et al., Nature Physics, accepted (2012), DOI:10.1038/nphys2397

List of Contributors

ALAEE, RASOUL

Complete light absorption in extremely coupled plasmonic nanostructure (poster)
Institute of Condensed Matter Theory and Solid State Optics, Friedrich-Schiller-Universität, Jena, Germany

BIERBACH, JANA

Intense Attosecond Pulses from Relativistic Surface Plasmas (talk)
Institute of Optics and Quantum Electronics, Friedrich-Schiller-Universität, Jena, Germany

CHEMNITZ, MARIO

Parametric fiber optical amplifier for spectrally high-resolved coherent anti-Stokes Raman spectro-microscopy (talk)
Institute of Applied Physics, Friedrich-Schiller-Universität, Jena, Germany

DIETRICH, KAY

Chiral Nanomaterial Fabrication by means of On-Edge Lithography (poster)
Institute of Applied Physics, Friedrich-Schiller-Universität, Jena, Germany

DÖRING, SVEN

Analysis of the hole formation in ultrashort pulse laser deep drilling (talk)
Institute of Applied Physics, Friedrich-Schiller-Universität, Jena, Germany

EILENBERGER, FALK

Imaging Cross Correlator FROG: Space-Time Retrieval of Ultrashort Complex Electric Fields (talk)
Institute of Applied Physics, Friedrich-Schiller-Universität, Jena, Germany

ELSMANN, TINO

Inscription of first order Volume-Bragg-Gratings in a non-photosensitive material by using femtosecond-pulses with a wavelength of 400 nm (talk)
Institute of Photonic Technology, Friedrich-Schiller-Universität, Jena, Germany

FALKNER, MATTHIAS

How to characterize comprehensively highly dispersive metamaterials with optical activity (talk)
Institute of Applied Physics, Friedrich-Schiller-Universität, Jena, Germany

FASOLD, STEFAN

Plasmonic Moiré Magnifier (poster)
Institute of Applied Physics, Friedrich-Schiller-Universität, Jena, Germany

FILTER, ROBERT

Controlling Light-Matter-Interactions using Nanoantennas (talk)
Institute of Condensed Matter Theory and Solid State Optics, Friedrich-Schiller-Universität, Jena, Germany

FLAMM, DANIEL

Selective excitation of higher-order modes in optical fibers using a spatial light modulator (talk)
Institute of Applied Optics, Friedrich-Schiller-Universität, Jena, Germany

FUCHS, SILVIO

Optical Coherence Tomography using broad-bandwidth XUV and soft x-ray radiation (talk)
Institute of Optics and Quantum Electronics, Friedrich-Schiller-Universität, Jena, Germany

GEISS, REINHARD

Lithium Niobate Nanowaveguides fabricated by IBEE (poster)
Institute of Applied Physics, Friedrich-Schiller-Universität, Jena, Germany

GERMER, SUSETTE

Basic structures of integrated photonic circuits for smart biosensor applications (poster)
Institute of Ion-Beam Physics and Materials Research, Helmholtz-Center Dresden-Rossendorf , Dresden, Germany

GRÄFE, MAXIMILIAN

Design of ultrafast fluorescence spectroscopy for axial resolution of fluorophore distribution with low numerical apertures for ophthalmologic application (poster)
Institute of Applied Optics, Friedrich-Schiller-Universität, Jena, Germany

HARTUNG, ALEXANDER

Applicability of input coupling taper transitions for supercontinuum generation (poster)
Institute of Photonic Technology, Friedrich-Schiller-Universität, Jena, Germany

HASAN, SHAKEEB BIN

Quadratic Frequency Conversion In Plasmonic Slot Waveguides (talk)
Institute of Condensed Matter Theory and Solid State Optics, Friedrich-Schiller-Universität, Jena, Germany

HEISEL, PER-CHRISTIAN

UV fs-laser pulse durations from autocorrelation measurements in CaF2 (poster)
Institute of Photonic Technology, Friedrich-Schiller-Universität, Jena, Germany

JAHN, MARTIN

Lipophilic sensor layers for SERS-based detection of water-insoluble substances (poster)
Institute of Physical Chemistry, Friedrich-Schiller-Universität, Jena, Germany

JANSEN, FLORIAN

Ytterbium-doped large-pitch fibers (talk)
Institute of Applied Physics, Friedrich-Schiller-Universität, Jena, Germany

JOST, AURELIE

Fast Structured Illumination Microscopy (talk)
Institute of Photonic Technology, Friedrich-Schiller-Universität, Jena, Germany

JUST, FLORIAN

Powder sintering process for the manufacturing of novel, highly efficient laser fibers (talk)
Institute of Photonic Technology, Friedrich-Schiller-Universität, Jena, Germany

KAISER, THOMAS

Light propagation in plasmonic nanoparticle loaded waveguides (talk)
Institute of Applied Physics, Friedrich-Schiller-Universität, Jena, Germany

KARRAS, CHRISTIAN

The impact ionization coefficient in dielectric materials revisited (poster)
Institute of Photonic Technology, Friedrich-Schiller-Universität, Jena, Germany

KIELHORN, MARTIN

Spatio-angular microscopy (talk)
Institute of Photonic Technology, Friedrich-Schiller-Universität, Jena, Germany

KLEIN, ANGELA

Controlling plasmonic hot-spots by interfering Airy beams (talk)
Institute of Applied Physics, Friedrich-Schiller-Universität, Jena, Germany

KLINER, ANDREA

Adiabatic Tapers (poster)
Fraunhofer Institute for Applied Optics and Precision Engineering, Friedrich-Schiller-Universität, Jena, Germany

KRÄMER, RIA

Inscription of fiber Bragg gratings in a 120 core fiber with ultrashort pulses (poster)
Institute of Applied Physics, Friedrich-Schiller-Universität, Jena, Germany

KRÖSEN, SEBASTIAN

Integration of Functional Optical Devices in Lithium Niobate Wafers by Direct Femtosecond Laser Writing (talk)
Institute for Applied Physics, Westfälische Wilhelms- Universität, Münster, Germany

LORENZ, ADRIAN

Comparison of different design concepts for large mode area optical fibers (poster)
Institute of Photonic Technology, Friedrich-Schiller-Universität, Jena, Germany

LU, HUI WEN

Fast High-Resolution Fluorescence Microscopy by Nonlinear Structured Illumination (poster)
Institute of Photonic Technology, Friedrich-Schiller-Universität, Jena, Germany

MAASS, JACQUELINE

Flexible Simulation Tool for Talbot - Lithography to Fabricate Various Three-dimensional Microstructures (poster)
Carl Zeiss Jena GmbH, , Germany

MÖLLER, MAX

Single-shot carrier-envelope phase measurement based on stereographic above-threshold ionization in the multi-cycle regime (talk)
Institute of Optics and Quantum Electronics, Friedrich-Schiller-Universität, Jena, Germany

MÖRBITZ, JULIA

Fabrication and characterization of a "continuous Fiber Bragg Grating fiber" using Draw Tower Grating Technology (talk)
FBGS Technologies GmbH, Jena, Germany

OTT, JOHANNES

Development of an Optical System to Monitor a Cell Based Lab-On-A-Chip In Vitro Assay (talk)
Department of Medical Engineering and Biotechnology, Ernst-Abbe-University of Applied Sciences, Jena, Germany

OTTO, HANS-JÜRGEN

Mode instabilities in high-power fiber-laser systems (talk)
Institute of Applied Physics, Friedrich-Schiller-Universität, Jena, Germany

PRATER, KARIN

Vortex Light Bullets: a Discrete Revolution (poster)
Institute of Applied Physics, Friedrich-Schiller-Universität, Jena, Germany

RATZSCH, STEPHAN

Properties of titanium oxide deposited by atomic layer deposition as a coating for highly efficient transmission grating (poster)
Institute of Applied Physics, Friedrich-Schiller-Universität, Jena, Germany

RICHTER, DANIEL

Illustration of the Ewaldsphere with a twodimensional fs pulse written volume Bragg grating (VBG) (talk)
Institute of Applied Physics, Friedrich-Schiller-Universität, Jena, Germany

ROTHHARDT, CAROLIN

Fabrication of a Faraday Isolator by plasma-activated bonding (talk)
Fraunhofer Institute for Applied Optics and Precision Engineering, Friedrich-Schiller-Universität, Jena, Germany

SARAVI, SINA

Slow light in lithium niobate photonic crystal slab waveguides (poster)
Institute of Applied Physics, Friedrich-Schiller-Universität, Jena, Germany

SCHAFFER, MARTIN

Recent advances in laser speckle based structured illumination stereophotogrammetry (talk)
Institute of Applied Optics, Friedrich-Schiller-Universität, Jena, Germany

SCHMIDT, CARSTEN

Characteristics of optical modes in coupled disk microresonators (talk)
Institute of Applied Physics, Friedrich-Schiller-Universität, Jena, Germany

SCHULZE, CHRISTIAN

Measuring wavefronts using modal decomposition (talk)
Institute of Applied Optics, Friedrich-Schiller-Universität, Jena, Germany

SEISE, BARBARA

Fluorescence based DNA detection of pathogens with magnetic beads (talk)
Institute of Photonic Technology, Friedrich-Schiller-Universität, Jena, Germany

SERGEYEV, ANTON

Optimisation and application of the second-harmonic waveguiding in lithium niobate nanowires (talk)
Institute of Applied Physics, Friedrich-Schiller-Universität, Jena, Germany

SPITTEL, RON

Equivalent step-index model of multifilament core fibers (talk)
Institute of Photonic Technology, Friedrich-Schiller-Universität, Jena, Germany

STÜTZER, SIMON

Superballistic transport and anomalous diffusion in inhomogeneous lattices (talk)
Institute of Applied Physics, Friedrich-Schiller-Universität, Jena, Germany

VETTER, CHRISTIAN

Femtosecond-Laser Induced Nanogratings - A versatile Platform for Birefringent Polarization Control (talk)
Institute of Applied Physics, Friedrich-Schiller-Universität, Jena, Germany

VOIGTLÄNDER, CHRISTIAN

Femtosecond laser inscribed mode filter for few mode fibers (talk)
Institute of Applied Physics, Friedrich-Schiller-Universität, Jena, Germany

WALTHER, BENNY

Multi-wavelength holograms made of plasmonic metamaterials (talk)
Institute of Applied Physics, Friedrich-Schiller-Universität, Jena, Germany

WIESENDANGER, SAMUEL

Front and rear side photonic structures in silicon solar cells (talk)
Institute of Condensed Matter Theory and Solid State Optics, Friedrich-Schiller-Universität, Jena, Germany

WUCHRER, ROLAND

Filter-based spectrometer for optical wavelength shift sensors (talk)
Fraunhofer Institute for Nondestructive Testing, Dresden, Germany

ZIERBOCK, SOPHIE

Surface enhanced Raman spectroscopy (SERS) for the detection of ecological harmful arrearages of sewage water (poster)
Institute of Physical Chemistry, Friedrich-Schiller-Universität, Jena, Germany

ZIMMERMANN, FELIX

Ultrashort pulse induced nanogratings and their fundamental structure (talk)
Institute of Applied Physics, Friedrich-Schiller-Universität, Jena, Germany

ZÜRCH, MICHAEL

Highly nonlinear interaction of laser beams with angular orbital momentum (poster)
Institute of Optics and Quantum Electronics, Friedrich-Schiller-Universität, Jena, Germany

Board of Organizers

Institute of Applied Physics, Friedrich-Schiller-Universität Jena:

- Angela Klein
- Daniel Richter
- Falk Eilenberger
- Matthias Falkner
- Reinhard Geiss
- Ria Krämer
- Thomas Kaiser

Institute of Applied Optics, Friedrich-Schiller-Universität Jena:

- Martin Schaffer

Institute for Condensed Matter Theory and Solid State Optics, Friedrich-Schiller-Universität Jena:

- Robert Filter

First row: Martin, Ria, Falk, Robert. Second row: Thomas, Daniel, Reinhard.
Last row: well you should know *that* guy. . . Not in the picture: Angela, Matthias.

Notes

"... denn was man schwarz auf weiß besitzt, kann man getrost nach Hause tragen!"
Goethe, Faust I